Rediscovering the ancient maritime Silk Road *p. 1440*

Illuminating valleys in the electron landscape *p. 1489*

Lassa virus reveals a new paradigm in viral entry *p. 1506*

Science

$10
27 JUNE 2014
sciencemag.org

AAAS

SPECIAL ISSUE

The great gas boom

An energy revolution holds promise and peril *p. 1464*

CONTENTS

1446 & 1481
Human decisions combine inference and creativity

27 JUNE 2014 • VOLUME 344 • ISSUE 6191

SPECIAL SECTION

The gas surge

INTRODUCTION

1464 Fracking has ignited an energy revolution, with still-uncertain consequences for climate and the environment

NEWS

1468 Will fracking put too much fizz in your water?
By E. Stokstad

1470 Searching for life in the deep shale
By E. Pennisi

1472 Hunting a climate fugitive
By E. Kintisch

1474 The bond breaker
By R. Service

SEE ALSO

▸ REPORT P. 1500

ON THE COVER

Natural gas extracted from a deep shale formation by hydraulic fracturing ("fracking") technology burns at a well in Bradford County, Pennsylvania. Fracking is enabling a shale gas production boom, remaking energy markets, and stoking environmental concerns. See page 1464. *Photo: © Les Stone/Corbis*

NEWS

IN BRIEF

1432 Roundup of the week's news

IN DEPTH

1435 SCRIPPS AND USC CONSIDER UNION, FOR MONEY AND PRESTIGE
Negotiations with university spark opposition from biomedical institute's scientists *By R. Service*

1436 NOT-SEEING IS BELIEVING
"Zero knowledge" tests could let inspectors identify a nuclear weapon without learning the secrets of its design *By R. Stone*

1437 FREE WILLY? DOLPHIN DRAMA RILES AQUARIA
Proposal to remove captive dolphins draws ire *By D. Grimm*

1439 DARING TO LIVE ON THE EDGE
Tracking the house sparrow's spread yields secrets of the invaders—a taste for novel foods, for example *By E. Pennisi*

FEATURE

1440 SAILING SINBAD'S SEAS
Archaeologists are rediscovering the ancient Maritime Silk Road, which once powered more commerce than the famed Central Asian land route *By A. Lawler*

INSIGHTS

PERSPECTIVES

1446 EXPLOITING AND EXPLORING THE OPTIONS
How does the human brain reason when to change strategies? *By T. Hare*
▸ RESEARCH ARTICLE P. 1481

1448 PREDICTING MICROBIAL GROWTH
Integration of a plethora of genomic and biochemical data enables large-scale prediction of cellular functions *By J. Monk and B. O. Palsson*

1449 TARGETING VASCULAR SPROUTS
Manipulating metabolism could control angiogenesis *By L. B. Rivera and G. Bergers*

1451 PHASE-TRANSFORMING ELECTRODES
Structural studies suggest a route to improve the performance of rechargeable batteries *By J. Owen and A. Hector*
▸ RESEARCH ARTICLE P. 1480

1452 ANTICIPATING THE NEXT CENTURY OF WASTEWATER TREATMENT
Advances in activated sludge sewage treatment can improve its energy use and resource recovery *By M. C. M. van Loosdrecht and D. Brdjanovic*

1454 FOLLOW THE ODOR
How do moths and other insects find their way to food sources in the presence of other odors? *By P. Szyszka*
▸ REPORT P. 1515

1455 HARNESSING DNA TO IMPROVE ENVIRONMENTAL MANAGEMENT
Genetic monitoring can help public agencies implement environmental laws *By R. P. Kelly* et al.

Science Staff 1430
AAAS News & Notes 1462
New Products 1526
Science Careers 1527

Published by AAAS

CONTENTS

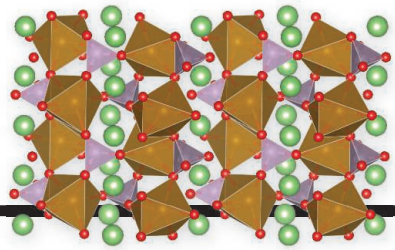

1451 & 1480
How iron phosphate stores lithium in batteries

27 JUNE 2014 • VOLUME 344 • ISSUE 6191

1457 GERALD M. EDELMAN (1929–2014)
A great biologist made fundamental discoveries and conceived a selectionist theory of the brain *By G. Tononi*

BOOKS *ET AL.*

1458 MORE THAN NATURE NEEDS
By D. Bickerton,

A NATURAL HISTORY OF HUMAN THINKING
By M. Tomasello, reviewed by S. Levinson

LETTERS

1460 EDITORIAL EXPRESSION OF CONCERN
By M. McNutt

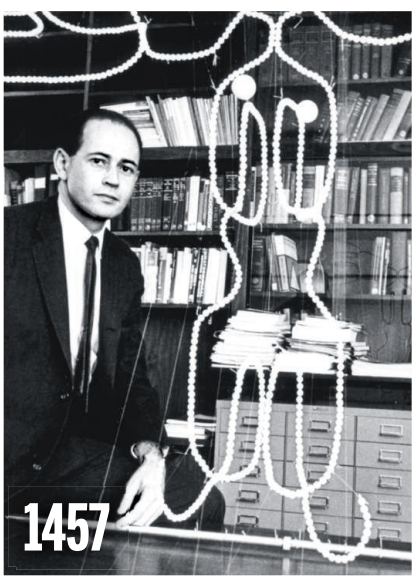

1460 CARBON MARKETS: EFFECTIVE POLICY?
By D. Cullenward and M. Wara

1460 RESPONSE
By R. G. Newell et al.

1461 A CARBON CODE OF CONDUCT FOR SCIENCE
By B. Favaro

RESEARCH

IN BRIEF

1476 From *Science* and other journals

RESEARCH ARTICLES

1480 BATTERIES
Capturing metastable structures during high-rate cycling of $LiFePO_4$ nanoparticle electrodes *H. Liu* et al.
RESEARCH ARTICLE SUMMARY; FOR FULL TEXT: HTTP://DX.DOI.ORG/10.1126/SCIENCE.1252817
▸ PERSPECTIVE P. 1451

1481 HUMAN COGNITION
Foundations of human reasoning in the prefrontal cortex *M. Donoso* et al.
▸ PERSPECTIVE P. 1446

REPORTS

1486 QUANTUM METROLOGY
Optically measuring force near the standard quantum limit
S. Schreppler et al.

1489 VALLEYTRONICS
The valley Hall effect in MoS_2 transistors
K. F. Mak et al.

1492 MACHINE LEARNING
Clustering by fast search and find of density peaks *A. Rodriguez and A. Laio*

1496 NANOFLUIDICS
Observing liquid flow in nanotubes by 4D electron microscopy
U. J. Lorenz and A. H. Zewail

1500 GAS FORMATION
Formation temperatures of thermogenic and biogenic methane
D. A. Stolper et al.
▸ THE GAS SURGE SECTION P. 1464

1504 EARLY ANIMALS
Ediacaran metazoan reefs from the Nama Group, Namibia
A. M. Penny et al.

1506 VIRUS ENTRY
Lassa virus entry requires a trigger-induced receptor switch
L. T. Jae et al.

1510 MEMBRANE TRAFFICKING
Nucleoside diphosphate kinases fuel dynamin superfamily proteins with GTP for membrane remodeling
M. Boissan et al.

1515 SENSORY BIOLOGY
Flower discrimination by pollinators in a dynamic chemical environment
J. A. Riffell et al.
▸ PERSPECTIVE P. 1454; PODCAST

1519 MICROBIAL EVOLUTION
Global epistasis makes adaptation predictable despite sequence-level stochasticity
S. Kryazhimskiy et al.

1522 NONHUMAN GENETICS
Genomic basis for the convergent evolution of electric organs
J. R. Gallant et al.

DEPARTMENTS

1431 EDITORIAL
Negative-emissions insurance
By Sally M. Benson

1534 WORKING LIFE
Brewing a career
By Trisha Gura

PHOTO: (RIGHT) FLORIS VAN BREUGAL, ART IN NATURE PHOTOGRAPHY

SCIENCE (ISSN 0036-8075) is published weekly on Friday, except the last week in December, by the American Association for the Advancement of Science, 1200 New York Avenue, NW, Washington, DC 20005. Periodicals mail postage (publication No. 484460) paid at Washington, DC, and additional mailing offices. Copyright © 2014 by the American Association for the Advancement of Science. The title SCIENCE is a registered trademark of the AAAS. Domestic individual membership and subscription (51 issues): $153 ($74 allocated to subscription). Domestic institutional subscription (51 issues): $1282; Foreign postage extra: Mexico, Caribbean (surface mail) $55; other countries (air assist delivery) $85. First class, airmail, student, and emeritus rates on request. Canadian rates with GST available upon request, GST #1254 88122. Publications Mail Agreement Number 1069624. **Printed in the U.S.A.**
Change of address: Allow 4 weeks, giving old and new addresses and 8-digit account number. **Postmaster:** Send change of address to AAAS, P.O. Box 96178, Washington, DC 20090–6178. **Single-copy sales:** $10.00 current issue, $15.00 back issue prepaid includes surface postage; bulk rates on request. **Authorization to photocopy** material for internal or personal use under circumstances not falling within the fair use provisions of the Copyright Act is granted by AAAS to libraries and other users registered with the Copyright Clearance Center (CCC) Transactional Reporting Service, provided that $30.00 per article is paid directly to CCC, 222 Rosewood Drive, Danvers, MA 01923. The identification code for *Science* is 0036-8075. *Science* is indexed in the *Reader's Guide to Periodical Literature* and in several specialized indexes.

Published by AAAS

Science
AAAS
1200 New York Avenue, NW, Washington, DC 20005
Bateman House, 82-88 Hills Road, Cambridge, UK CB2 1LQ

Editor-in-Chief Marcia McNutt
Executive Editor Monica M. Bradford **News Editor** Tim Appenzeller
Managing Editor, Research Journals Katrina L. Kelner
Deputy Editors Barbara R. Jasny, Andrew M. Sugden(UK), Valda J. Vinson, Jake S. Yeston

Research and Insights

SR. EDITORS Caroline Ash(UK), Gilbert J. Chin, Lisa D. Chong, Maria Cruz(UK), Julia Fahrenkamp-Uppenbrink(UK), Pamela J. Hines, Stella M. Hurtley(UK), Paula A. Kiberstis, Marc S. Lavine(Canada), Kristen L. Mueller, Ian S. Osborne(UK), Beverly A. Purnell, L. Bryan Ray, Guy Riddihough, H. Jesse Smith, Peter Stern(UK), Phillip D. Szuromi, Brad Wible, Nicholas S. Wigginton, Laura M. Zahn **ASSOCIATE EDITORS** Brent Grocholski, Melissa R. McCartney, Margaret M. Moerchen, Jelena Stajic, Sacha Vignieri **BOOK REVIEW EDITOR** Sherman J. Suter **ASSOCIATE LETTERS EDITOR** Jennifer Sills **EDITORIAL MANAGER** Cara Tate **SR. COPY EDITORS** Jeffrey E. Cook, Chris Filiatreau, Cynthia Howe, Harry Jach, Lauren Kmec, Barbara P. Ordway, Trista Wagoner **SR. EDITORIAL COORDINATORS** Carolyn Kyle, Beverly Shields **EDITORIAL COORDINATORS** Ramatoulaye Diop, Joi S. Granger, Lisa Johnson, Anita Wynn **PUBLICATIONS ASSISTANTS** Aneera Dobbins, Jeffrey Hearn, Dona Mathieu, Le-Toya Mayne Flood, Shannon McMahon, Scott Miller, Jerry Richardson, Rachel Roberts(UK), Alice Whaley(UK), Brian White **ADMINISTRATIVE SUPPORT** Janet Clements(UK), Joan Cuthbert(UK), Maryrose Madrid, John Wood(UK)

News

NEWS MANAGING EDITOR John Travis **INTERNATIONAL EDITOR** Richard Stone **DEPUTY NEWS EDITORS** Daniel Clery(UK), Robert Coontz, Elizabeth Culotta, David Grimm, David Malakoff, Leslie Roberts **CONTRIBUING EDITORS** Martin Enserink(Europe), Mara Hvistendahl (Asia) **SR. CORRESPONDENTS** Jeffrey Mervis, Elizabeth Pennisi **NEWS WRITERS** Yudhijit Bhattacharjee, Adrian Cho, Jennifer Couzin-Frankel, Carolyn Gramling, Eric Hand, Jocelyn Kaiser, Kelly Servick, Robert F. Service, Erik Stokstad, Emily Underwood **CONTRIBUTING CORRESPONDENTS** Pallava Bagla(South Asia), Michael Balter(Paris), John Bohannon, Jon Cohen, Ann Gibbons, Sam Kean, Richard A. Kerr, Eli Kintisch, Kai Kupferschmidt(Berlin), Andrew Lawler, Christina Larson(Beijing), Mitch Leslie, Charles C. Mann, Eliot Marshall, Virginia Morell, Dennis Normile(Tokyo),Heather Pringle, Tania Rabesandratana(Brussels), Gretchen Vogel(Berlin), Lizzie Wade(Mexico City) **CAREERS** Jim Austin(Editor), Donisha Adams **COPY EDITORS** Kara Estelle, Nora Kelly, Jennifer Levin **ADMINISTRATIVE SUPPORT** Scherraine Mack

Executive Publisher Alan I. Leshner
Publisher Beth Rosner **Chief Digital Media Officer** Rob Covey

BUSINESS OPERATIONS AND ADMINISTRATION DIRECTOR Deborah Rivera-Wienhold **BUSINESS SYSTEMS AND FINANCIAL ANALYSIS DIRECTOR** Randy Yi **MANAGER OF FULFILLMENT SYSTEMS** Neal Hawkins **SYSTEMS ANALYST** Nicole Mehmedovich **ASSISTANT DIRECTOR, BUSINESS OPERATIONS** Eric Knott **MANAGER, BUSINESS OPERATIONS** Jessica Tierney **BUSINESS ANALYSTS** Cory Lipman, Cooper Tilton, Celeste Troxler **FINANCIAL ANALYST** Jeremy Clay **RIGHTS AND PERMISSIONS: ASSISTANT DIRECTOR** Emilie David **PERMISSIONS ASSOCIATE** Elizabeth Sandler **RIGHTS, CONTRACTS, AND LICENSING ASSOCIATE** Lili Kiser

MARKETING DIRECTOR Ian King **MARKETING MANAGER** Julianne Wielga **MARKETING ASSOCIATE** Elizabeth Sattler **SR. MARKETING EXECUTIVE** Jennifer Reeves **SR. ART ASSOCIATE, PROJECT MANAGER** Tzeitel Sorrosa **ART ASSOCIATE** Seil Lee **ASSISTANT COMMERCIAL EDITOR** Selby Frame **MARKETING PROJECT MANAGER** Angelissa McArthur **SR. WRITER** Bill Zimmer **PROGRAM DIRECTOR, AAAS MEMBER CENTRAL** Peggy Mihelich **FULFILLMENT SYSTEMS AND OPERATIONS** membership@aaas.org **MANAGER, MEMBER SERVICES** Pat Butler **SPECIALISTS** LaToya Casteel, Javia Flemmings, Latasha Russell **MANAGER, DATA ENTRY** Mickie Napoleoni **DATA ENTRY SPECIALISTS** JJ Regan, Jaimee Wise, Fiona Giblin

DIRECTOR, SITE LICENSING Tom Ryan **DIRECTOR, CORPORATE RELATIONS** Eileen Bernadette Moran **SR. PUBLISHER RELATIONS SPECIALIST** Kiki Forsythe **PUBLISHER RELATIONS MANAGER** Catherine Holland **PUBLISHER RELATIONS, EASTERN REGION** Keith Layson **PUBLISHER RELATIONS, WESTERN REGION** Ryan Rexroth **MANAGER, SITE LICENSE OPERATIONS** Iquo Edim **FULFILLMENT ANALYST** Lana Guz **ASSOCIATE DIRECTOR, MARKETING** Christina Schlecht **MARKETING ASSOCIATES** Thomas Landreth, Minah Kim

DIRECTOR OF WEB TECHNOLOGIES Ahmed Khadr **SR. DEVELOPERS** Jumoke Adekanmi, Chris Coleman **DEVELOPER** Dan Berger **SR. PROJECT MANAGER** Trista Smith **SYSTEMS ENGINEER** Luke Johnson **PRODUCT MANAGER** Walter Jones

CREATIVE DIRECTOR, MULTIMEDIA Martyn Green **DIRECTOR OF ANALYTICS** Enrique Gonzales **SR. WEB PRODUCER** Sarah Crespi **WEB PRODUCER** Alison Crawford **VIDEO PRODUCER** Nguyen Nguyen **SOCIAL MEDIA PRODUCER** Meghna Sachdev

DIRECTOR OF OPERATIONS PRINT AND ONLINE Lizabeth Harman **ASSISTANT MANAGER** Lisa Stanford **PRODUCTION SPECIALISTS** Amy Hardcastle, Antoinette Hodal, Nichele Johnston, Yuse Lajiminmuhip, Lori Murphy, Kimberley Oster **PRODUCTION DIRECTOR** Wendy K. Shank **ASSISTANT MANAGER** Rebecca Doshi **SR. SPECIALISTS** Steve Forrester, Anthony Rosen **SPECIALIST** Jacob Hedrick **PREFLIGHT MANAGER** Marcus Spiegler **SR. SPECIALISTS** Jason Hillman, Tara Kelly

DESIGN DIRECTOR Beth Rakouskas **ASSOCIATE ART DIRECTOR** Laura Creveling **SR. ILLUSTRATORS** Chris Bickel, Katharine Sutliff **ILLUSTRATOR** Valerie Altounian **SR. ART ASSOCIATES** Holly Bishop, Preston Huey **ART ASSOCIATES** Kay Engman, Garvin Grullón, Chrystal Smith **SR. PHOTO EDITOR** William Douthitt **PHOTO EDITOR** Leslie Blizard

DIRECTOR, GLOBAL COLLABORATION, CUSTOM PUBLICATIONS, ADVERTISING Bill Moran **EDITOR, CUSTOM PUBLISHING** Sean Sanders: 202-326-6430 **ASSISTANT EDITOR, CUSTOM PUBLISHING** Tianna Hicklin: 202-326-6463 **ADVERTISING MARKETING MANAGER** Justin Sawyers: 202-326-7061 science_advertising@aaas.org **ADVERTISING SUPPORT MANAGER** Karen Foote: 202-326-6740 **ADVERTISING PRODUCTION OPERATIONS MANAGER** Deborah Tompkins **SR. TRAFFIC ASSOCIATE** Christine Hall **SALES COORDINATOR** Shirley Young **ASSOCIATE DIRECTOR, COLLABORATION, CUSTOM PUBLICATIONS/CHINA/TAIWAN/KOREA/SINGAPORE** Ruolei Wu: +86-186 0822 9345, rwu@aaas.org **EAST COAST/E. CANADA** Laurie Faraday: 508-747-9395, FAX 617-507-8189 **WEST COAST/W. CANADA** Lynne Stickrod: 415-931-9782, FAX 415-520-6940 **MIDWEST** Jeffrey Dembksi: 847-498-4520 x3005, Steven Loerch: 847-498-4520 x3006 **UK EUROPE/ASIA** Roger Goncalves: TEL/FAX +41 43 243 1358 **JAPAN** Makiko Hara: +81 (0) 3 6802 4616, FAX +81 (0) 3 6802 4615, ads@sciencemag.jp **CHINA/TAIWAN** Ruolei Wu: +86-186 0822 9345

WORLDWIDE ASSOCIATE DIRECTOR OF SCIENCE CAREERS Tracy Holmes: +44 (0) 1223 326525, FAX +44 (0) 1223 326532 tholmes@science-int.co.uk **CLASSIFIED** advertise@sciencecareers.org **U.S. SALES** Tina Burks: 202-326-6577, Nancy Toema: 202-326-6578 **SALES ADMINISTRATOR** Marci Gallun **EUROPE/ROW SALES** Axel Gesatzki, Sarah Lelarge **SALES ASSISTANT** Kelly Grace **JAPAN** Yuri Kobayashi: +81 (0)90-9110-1719, careerads@sciencemag.jp **CHINA/TAIWAN** Ruolei Wu: +86-186 0822 9345 rwu@aaas.org **MARKETING MANAGER** Allison Pritchard **MARKETING ASSOCIATE** Aimee Aponte

AAAS BOARD OF DIRECTORS RETIRING PRESIDENT, CHAIR Phillip A. Sharp **PRESIDENT** Gerald R. Fink **PRESIDENT-ELECT** Geraldine (Geri) Richmond **TREASURER** David Evans Shaw **CHIEF EXECUTIVE OFFICER** Alan I. Leshner **BOARD** Bonnie L. Bassler, May R. Berenbaum, Carlos J. Bustamante, Claire M. Fraser, Laura H. Greene, Elizabeth Loftus, Raymond Orbach, Inder M. Verma

SUBSCRIPTION SERVICES For change of address, missing issues, new orders and renewals, and payment questions: 866-434-AAAS (2227) or 202-326-6417, FAX 202-842-1065. Mailing addresses: AAAS, P.O. Box 96178, Washington, DC 20090-6178 or AAAS Member Services, 1200 New York Avenue, NW, Washington, DC 20005

INSTITUTIONAL SITE LICENSES 202-326-6755 **REPRINTS:** Author Inquiries 800-635-7181 **COMMERCIAL INQUIRIES** 803-359-4578 **PERMISSIONS** 202-326-6765, permissions@aaas.org **AAAS Member Services** 202-326-6417 or http://membercentral.aaas.org/discounts

Science serves as a forum for discussion of important issues related to the advancement of science by publishing material on which a consensus has been reached as well as including the presentation of minority of conflicting points of view. Accordingly, all articles published in *Science*—including editorials, news and comment, and books reviews—are signed and reflect the individual views of the authors and not official points of view adopted by AAAS or the institutions with which the authors are affiliated.

INFORMATION FOR AUTHORS See pages 680 and 681 of the 7 February 2014 issue or access www.sciencemag.org/about/authors

SENIOR EDITORIAL BOARD
A. Paul Alivisatos, *Lawrence Berkeley Nat'l. Laboratory,* **Ernst Fehr,** *U. of Zürich*
Susan M. Rosenberg, *Baylor College of Medicine,* **Michael S. Turner,** *U. of Chicago*

BOARD OF REVIEWING EDITORS
Adriano Aguzzi, *U. Hospital Zürich*
Takuzo Aida, *U. of Tokyo*
Leslie Aiello, *Wenner-Gren Foundation*
Judith Allen, *U. of Edinburgh*
Sonia Altizer, *U. of Georgia*
Virginia Armbrust, *U. of Washington*
Sebastian Amigorena, *Institut Curie*
Kathryn Anderson, *Memorial Sloan-Kettering Cancer Center*
Peter Andolfatto, *Princeton U.*
Meinrat O. Andreae, *Max-Planck Inst. Mainz*
Paola Arlotta, *Harvard U.*
Johan Auwerx, *EPFL*
David Awschalom, *U. of Chicago*
Jordi Bascompte, *Estación Biológica de Doñana CSIC*
Facundo Batista, *London Research Inst.*
Ray H. Baughman, *U. of Texas, Dallas*
David Baum, *U. of Wisconsin*
Mark Bear, *Massachusetts Inst. of Technology*
Kamran Behnia, *ESPCI-ParisTech*
Yasmine Belkaid, *NIAID, NIH*
Philip Benfey, *Duke U.*
Stephen J. Benkovic, *Penn State U.*
Gabriele Bergers, *U. of California, San Francisco*
Christophe Bernard, *Aix-Marseille U.*
Bradley Bernstein, *Massachusettes General Hospital*
Gregory C. Beroza, *Stanford U.*
Peer Bork, *EMBL*
Bernard Bourdon, *Ecole Normale Supérieure de Lyon*
Chris Bowler, *École Normale Supérieure*
Ian Boyd, *U. of St. Andrews*
Emily Brodsky, *U. of California, Santa Cruz*
Christian Büchel, *U. Hamburg-Eppendorf*
Joseph A. Burns, *Cornell U.*
William P. Butz, *Population Reference Bureau*
Gyorgy Buzsaki, *New York U. School of Medicine*
Blanche Capel, *Duke U.*
Mats Carlsson, *U. of Oslo*
David Clapham, *Children's Hospital Boston*
David Clary, *U. of Oxford*
Joel Cohen, *Rockefeller U., Columbia U.*
Jonathan D. Cohen, *Princeton U.*
James Collins, *Boston U.*
Robert Cook-Deegan, *Duke U.*
Alan Cowman, *Walter & Eliza Hall Inst.*
Robert H. Crabtree, *Yale U.*
Janet Currie, *Princeton U.*
Jeff L. Dangl, *U. of North Carolina*
Tom Daniel, *U. of Washington*
Frans de Waal, *Emory U.*
Stanislas Dehaene, *Collège de France*
Robert Desimone, *MIT*
Claude Desplan, *New York U.*
Ap Dijksterhuis, *Radboud U. of Nijmegen*
Dennis Discher, *U. of Pennsylvania*
Gerald W. Dorn II, *Washington U. School of Medicine*
Jennifer A. Doudna, *U. of California, Berkeley*
Bruce Dunn, *U. of California, Los Angeles*
Christopher Dye, *WHO*
Todd Ehlers, *U. of Tuebingen*
David Ehrhardt, *Carnegie Inst. of Washington*
Tim Elston, *U. of North Carolina at Chapel Hill*
Gerhard Ertl, *Fritz-Haber-Institut, Berlin*
Barry Everitt, *U. of Cambridge*
Ernst Fehr, *U. of Zurich*
Anne C. Ferguson-Smith, *U. of Cambridge*
Michael Feuer, *The George Washington U.*
Peter Fratzl, *Max-Planck Inst.*
Elaine Fuchs, *Rockefeller U.*
Daniel Geschwind, *UCLA*
Andrew Gewirth, *U. of Illinois*
Karl-Heinz Glassmeier, *TU Braunschweig*
Julia R. Greer, *Caltech*
Elizabeth Grove, *U. of Chicago*
Kip Guy, *St. Jude's Children's Research Hospital*
Taekjip Ha, *U. of Illinois at Urbana-Champaign*
Christian Haass, *Ludwig Maximilians U.*
Steven Hahn, *Fred Hutchinson Cancer Research Center*
Michael Hasselmo, *Boston U.*
Martin Heimann, *Max-Planck Inst. Jena*
Yka Helariutta, *U. of Finland*
James A. Hendler, *Rensselaer Polytechnic Inst.*
Janet G. Hering, *Swiss Fed. Inst. of Aquatic Science & Technology*
Michael E. Himmel, *National Renewable Energy Lab.*
Kai-Uwe Hinrichs, *U. of Bremen*
Kei Hirose, *Tokyo Inst. of Technology*
David Hodell, *U. of Cambridge*
David Holden, *Imperial College*
Lora Hooper, *UT Southwestern Medical Ctr. at Dallas*
Thomas Hudson, *Ontario Inst. for Cancer Research*
Raymond Huey, *U. of Washington*
Steven Jacobsen, *U. of California, Los Angeles*
Kai Johnsson, *EPFL Lausanne*
Peter Jonas, *Inst. of Science & Technology (IST) Austria*
Matt Kaeberlein, *U. of Washington*
William Kaelin Jr., *Dana-Farber Cancer Inst.*
Daniel Kahne, *Harvard U.*
Daniel Kammen, *U. of California, Berkeley*
Masashi Kawasaki, *U. of Tokyo*
Joel Kingsolver, *U. of North Carolina at Chapel Hill*
Robert Kingston, *Harvard Medical School*
Alexander Kolodkin, *Johns Hopkins U.*
Roberto Kolter, *Harvard Medical School*
Alberto R. Kornblihtt, *U. of Buenos Aires*
Leonid Kruglyak, *UCLA*
Thomas Langer, *U. of Cologne*
Mitchell A. Lazar, *U. of Pennsylvania*
David Lazer, *Harvard U.*
Thomas Lecuit, *IBDM*
Virginia Lee, *U. of Pennsylvania*
Stanley Lemon, *U. of North Carolina at Chapel Hill*
Ottoline Leyser, *Cambridge U.*
Marcia C. Linn, *U. of California, Berkeley*
Jianguo Liu, *Michigan State U.*
Luis Liz-Marzan, *CIC biomaGUNE*
Jonathan Losos, *Harvard U.*
Ke Lu, *Chinese Acad. of Sciences*
Christian Lüscher, *U. of Geneva*
Laura Machesky, *CRUK Beatson Inst. for Cancer Research*
Anne Magurran, *U. of St. Andrews*
Oscar Marin, *CSIC & U. Miguel Hernández*
Charles Marshall, *U. of California, Berkeley*
C. Robertson McClung, *Dartmouth College*
Graham Medley, *U. of Warwick*
Yasushi Miyashita, *U. of Tokyo*
Richard Morris, *U. of Edinburgh*
Sean Munro, *MRC Lab. of Molecular Biology*
Thomas Murray, *The Hastings Center*
James Nelson, *Stanford U. School of Med.*
Karen Nelson, *J. Craig Venter Institute*
Daniel Neumark, *U. of California, Berkeley*
Timothy W. Nilsen, *Case Western Reserve U.*
Pär Nordlund, *Karolinska Inst.*
Helga Nowotny, *European Research Advisory Board*
Ben Olken, *MIT*
Luke O'Neill, *Trinity College, Dublin*
Joe Orenstein, *U. of California Berkeley & Lawrence Berkeley National Lab*
Harry Orr, *U. of Minnesota*
Andrew Oswald, *U. of Warwick*
Steve Palumbi, *Stanford U.*
Jane Parker, *Max-Planck Inst. of Plant Breeding Research*
Donald R. Paul, *U. of Texas, Austin*
John H. J. Petrini, *Memorial Sloan-Kettering Cancer Center*
Joshua Plotkin, *U. of Pennsylvania*
Philippe Poulin, *CNRS*
David Randall, *Colorado State U.*
Colin Renfrew, *U. of Cambridge*
Trevor Robbins, *U. of Cambridge*
Jim Roberts, *Fred Hutchinson Cancer Research Ctr.*
Barbara A. Romanowicz, *U. of California, Berkeley*
Jens Rostrup-Nielsen, *Haldor Topsoe*
Mike Ryan, *U. of Texas, Austin*
Mitinori Saitou, *Kyoto U.*
Shimon Sakaguchi, *Kyoto U.*
Miquel Salmeron, *Lawrence Berkeley National Lab*
Jürgen Sandkühler, *Medical U. of Vienna*
Alexander Schier, *Harvard U.*
Randy Seeley, *U. of Cincinnati*
Vladimir Shalaev, *Purdue U.*
Robert Siliciano, *Johns Hopkins School of Medicine*
Joseph Silk, *Institut d'Astrophysique de Paris*
Denis Simon, *Arizona State U.*
Alison Smith, *John Innes Centre*
John Speakman, *U. of Aberdeen*
Allan C. Spradling, *Carnegie Institution of Washington*
Jonathan Sprent, *Garvan Inst. of Medical Research*
Eric Steig, *U. of Washington*
Paula Stephan, *Georgia State U. and National Bureau of Economic Research*
Molly Stevens, *Imperial College London*
V. S. Subrahmanian, *U. of Maryland*
Ira Tabas, *Columbia U.*
Sarah Teichmann, *Cambridge U.*
John Thomas, *North Carolina State U.*
Christopher Tyler-Smith, *The Wellcome Trust Sanger Inst.*
Herbert Virgin, *Washington U.*
Bert Vogelstein, *Johns Hopkins U.*
Cynthia Volkert, *U. of Göttingen*
Douglas Wallace, *Dalhousie U.*
David Wallach, *Weizmann Inst. of Science*
Ian Walmsley, *U. of Oxford*
David A. Wardle, *Swedish U. of Agric. Sciences*
David Waxman, *Fudan U.*
Jonathan Weissman, *U. of California, San Francisco*
Ian A. Wilson, *The Scripps Res. Inst.*
Timothy D. Wilson, *U. of Virginia*
Rosemary Wyse, *Johns Hopkins U.*
Jan Zaanen, *Leiden U.*
Kenneth Zaret, *U. of Pennsylvania School of Medicine*
Jonathan Zehr, *U. of California, Santa Cruz*
Len Zon, *Children's Hospital Boston*
Maria Zuber, *MIT*

BOOK REVIEW BOARD
David Bloom, *Harvard U.,* **Samuel Bowring,** *MIT,* **Angela Creager,** *Princeton U.,* **Richard Shweder,** *U. of Chicago,* **Ed Wasserman,** *DuPont*

Published by AAAS

EDITORIAL

Negative-emissions insurance

In its April 2014 report, the Intergovernmental Panel on Climate Change (IPCC) recognized that reducing greenhouse gas (GHG) emissions by 40 to 70% by mid-century will require more than just implementing emission-free solutions. Many scenarios for stabilizing GHG concentrations that were evaluated by the panel included removing carbon dioxide (CO_2) from the atmosphere: so-called "negative emissions" or carbon dioxide removal (CDR). Among the most promising CDR methods are reforestation, afforestation (planting new forests), and bioenergy with carbon capture and storage (BECCS). However, for BECCS strategies to succeed, major hurdles must be overcome.

All BECCS approaches rely on removal of CO_2 from the atmosphere by plants during photosynthesis. In nature, as a plant decays, it releases CO_2 back into the atmosphere. But with BECCS, CO_2 is captured and permanently stored underground, resulting in a net negative reduction in atmospheric carbon. At least three BECCS technologies are being investigated today. CO_2 released during the microbial fermentation of plant sugars to ethanol can be captured. CO_2 can also be captured during the gasification of biomass to synthetic gas for conversion to transportation fuels, chemicals, or electricity generation. And CO_2 from the combustion of biomass, either with or without coal, can be captured.

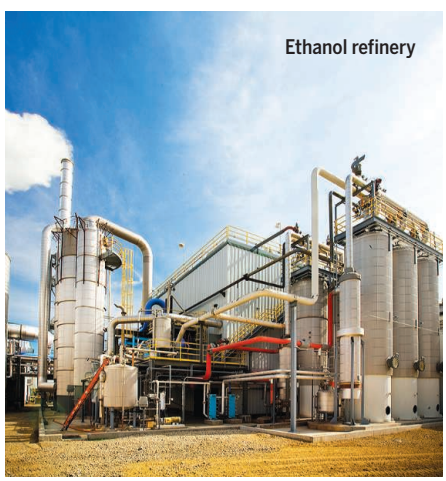

Ethanol refinery

"This approach still leaves unanswered questions, but to not consider it carefully would be too risky."

Since 2009, a consortium supported by the U.S. Department of Energy has successfully operated a BECCS test facility in Illinois. CO_2 emitted during the fermentation of corn is captured and stored in a sandstone formation about 7000 feet underground. The project removes 300,000 metric tons of CO_2 per year from the atmosphere—the equivalent of removing about 70,000 cars from the road annually. But that's just a fraction of the amount of CO_2 that will have to be removed to curb global warming, and of the estimated 2 to 10 gigatons (Gt) of CO_2 per year that could be removed from the atmosphere with BECCS by 2050.*

For either conventional CCS or BECCS, the cost must come down. Right now, CCS costs range from about $30 to $140 per ton of CO_2, depending on the source from which it is captured, the capture technology, and the form of storage.† Improving energy-conversion efficiency would address the cost hurdles, but this requires further research and development. Increased confidence in long-term geological storage security is also needed to better understand the risks of BECCS strategies. Capturing and storing 1 Gt of CO_2 from the atmosphere using BECCS would require about 0.5 to 1 Gt of biomass (equivalent to 10 to 20 exajoules of primary energy). Concerns about whether this much biomass could be practically and sustainably harvested, dried, and collected at this scale without interfering with food production or negatively affecting other ecosystem services must be examined.

Combined with sustainably managed reforestation and afforestation, the potential cobenefits of habitat creation, carbon mitigation, and renewable energy make BECCS an attractive choice. Rigorous research and development are needed so that the potential of BECCS is clear to scientists, policy-makers, and the public.

Negative-emissions technologies such as BECCS can be thought of as part of an insurance policy for climate change mitigation. This approach still leaves unanswered questions, but to not consider it carefully would be too risky.

– Sally M. Benson

Sally M. Benson is director of the Precourt Institute for Energy and the Global Climate and Energy Project, and a professor in the department of Energy Resources Engineering, at Stanford University, Stanford, CA. E-mail: smbenson@stanford.edu

PHOTO: (RIGHT) STANFORD UNIVERSITY; (INSET) TADPHOTO/ISTOCKPHOTO.COM

*http://report.mitigation2014.org/drafts/final-draft-postplenary/ipcc_wg3_ar5_final-draft_postplenary_technical-summary.pdf. †https://www.ipcc.ch/pdf/special-reports/srccs/srccs_chapter8.pdf and http://decarboni.se/sites/default/files/publications/24202/costs-ccs-and-other-low-carbon-technologies.pdf.

10.1126/science.1257423

Published by AAAS

Downloaded from www.sciencemag.org on June 28, 2014

NEWS

> “The titles are horrible. ... The public gets the impression that all NSF funds are these silly studies.”
>
> **Representative Donna Edwards (D–MD)**, urging scientists to write better headlines for their National Science Foundation–funded projects, last week at the American Geophysical Union’s Science Policy Conference in Washington, D.C.

IN BRIEF

Ebola outbreak sets sobering record

Protective clothing used by workers treating Ebola victims dries in Guéckédou, Guinea.

The outbreak of Ebola virus disease in West Africa has surpassed a grim milestone: It is now the largest and deadliest outbreak of its kind. According to a 24 June report from the World Health Organization (WHO), 599 people have been infected and 338 have died in the outbreak, which likely started in Guinea in December 2013 and has spread to Liberia and Sierra Leone. Those numbers are a significant undercount, says Robert Garry, a virologist at Tulane University in New Orleans, Louisiana, who this month helped trace the outbreak in Sierra Leone. “There have been many, many deaths, most of them unrecorded,” he says. The main organizations that have been working to stop the outbreak—WHO, Doctors Without Borders, the U.S. Centers for Disease Control and Prevention, and national health ministries—are stretched to the limit, Garry says. There is no vaccine or specific treatment for Ebola. The only way to stop the outbreak is to convince patients to come to medical centers and families to bury the dead without directly touching the body. “We need to think about nontraditional ways” to fund and ramp up the containment effort, Garry adds, because the virus is “not going away anytime soon.”

AROUND THE WORLD

Chemist, prosecutors settle suit

LOS ANGELES, CALIFORNIA | Federal prosecutors and a chemistry professor at the University of California, Los Angeles (UCLA), have settled a long-running case arising from the 2009 death of research assistant Sheharbano Sangji in a laboratory fire. Chemist Patrick Harran and UCLA had faced criminal charges. The university settled and accepted responsibility in 2012. Harran, who faced up to 4.5 years in prison, admitted no wrongdoing but agreed to pay a $10,000 fine and do 800 hours of community service, according to a 20 June statement. He will brief incoming UCLA students on “the importance of lab safety” and teach a chemistry course for inner-city students. In a statement, Sangji’s family said they were “extremely disappointed. ... We do not understand how this man is allowed to continue running a laboratory.”
http://scim.ag/labfire

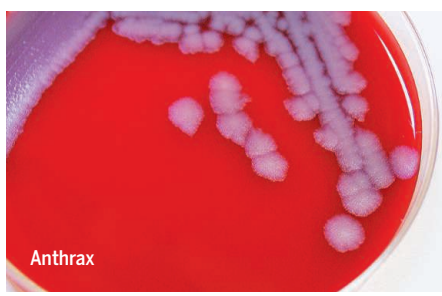

Anthrax

Anthrax accident at CDC

ATLANTA | The U.S. Centers for Disease Control and Prevention (CDC) is treating or monitoring 84 staff members for possible anthrax exposure after workers botched a new protocol for killing the dangerous bacteria. “[E]stablished safety practices were not followed” at the agency’s Bioterror Rapid Response and Advanced Technology Laboratory, officials said in a 19 June statement. In the incident, which occurred between 6 and 13 June, researchers used a chemical alternative to radiation to “inactivate” anthrax in a biosafety level 3 laboratory before transferring it to less secure level 2

PHOTOS: (TOP TO BOTTOM) SEYLLOU/AFP/GETTY IMAGES; CDC/MEGAN MATHIAS AND J. TODD PARKER

Downloaded from www.sciencemag.org on June 28, 2014

Published by AAAS

BY THE NUMBERS

87.1

Percent of people who inject drugs who are infected with HIV in Tripoli, according to a study published on 17 June in *PLOS Medicine*.

500

Percent increase since 2011 in orders for exome sequencing, which helps clinicians identify potentially important DNA mutations, according to Allen Bale, director of the DNA Diagnostics Laboratory at the Yale School of Medicine. But insurance companies are balking at paying.

60

Years ago that 12 nations launched CERN, the European Organization for Nuclear Research. Today, CERN has 21 member nations and collaborates with many more.

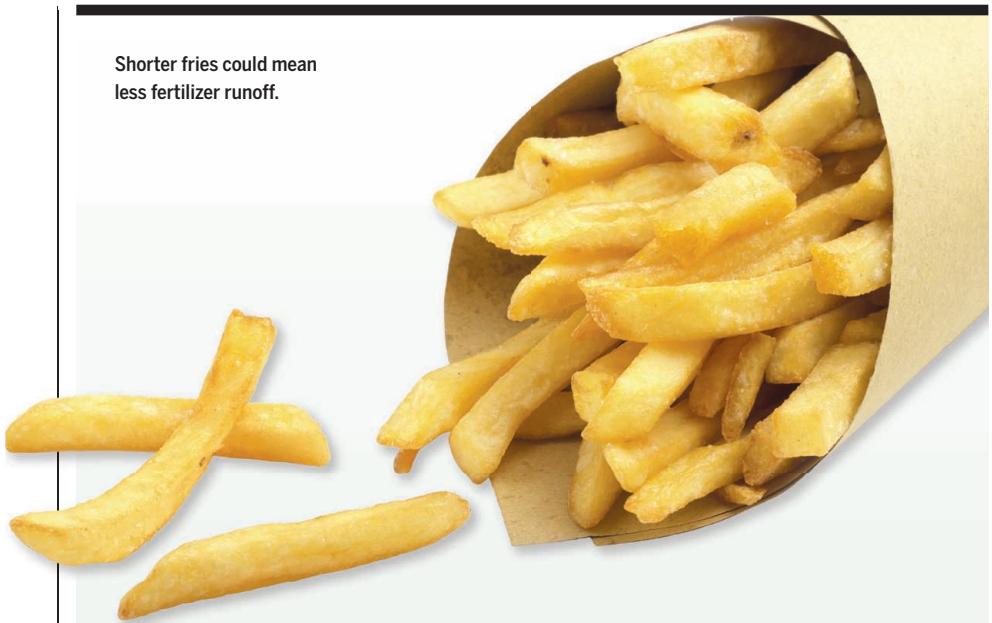

Shorter fries could mean less fertilizer runoff.

A cleaner, greener french fry

WASHINGTON, D.C.—Prince Edward Island (PEI) has a nitrogen pollution problem—and shorter french fries could be a solution. PEI's farmers are Canada's biggest potato producers, and they use a lot of fertilizer, which leaks nitrates into ground water and the nearby Northumberland Strait. One way to soak up the pollutants: Sow a fast-growing "catch crop," such as oil seed radishes, after the potatoes are harvested, suggested geochemist Martine Savard of the Geological Survey of Canada and George Somers of PEI's environment department at last week's American Geophysical Union Science Policy Conference. But there's a hitch: Demand for longer fast-food fries has farmers planting longer, slower growing tubers, reducing the window for a catch crop. Persuading consumers that a shorter fry is a greener fry, however, could reopen the door to stubbier taters—and cleaner waters.

laboratories. Days later, workers raised the alarm after finding live anthrax flourishing in growth plates. CDC has reassigned the lab's director, Michael Farrell, and the accident has led to renewed media scrutiny of facilities working with dangerous "select agents." **http://scim.ag/CDCanthrax**

Dieting mouse colony to close

BETHESDA, MARYLAND | The National Institute on Aging (NIA) at the U.S. National Institutes of Health has announced it will shutter its colony of calorie-restricted mice. Slashing rations for mice and many other kinds of animals dramatically extends their lives, and for nearly 20 years NIA has provided the hungry rodents to researchers. Just eight to 10 researchers, however, request animals from the colony each year, says NIA's Nancy Nadon, chief of the Biological Resources Branch. "The way the usage has changed over the last few years, it wasn't the best way to go about using NIA funds," she says. Most researchers who are investigating aging don't use the rodents, so they won't be affected. Scientists who depend on NIA's animals will have to adapt. **http://scim.ag/mousecolony**

Blast clears way for telescope

CHILE | Workers on 19 June blasted away part of the top of Cerro Armazones, a 3000-meter peak, preparing for construction of the world's largest telescope: the 39-meter European Extremely Large Telescope. Construction of a road leading to the summit began in March; first light on the completed telescope is expected in 2024. Construction won't begin in earnest, however, until Brazil's National Congress ratifies an agreement to join the European Southern Observatory (ESO), which oversees the project. In 2010, Brazil's science ministry signed the agreement—which would make Brazil ESO's first non-European member—but it has languished ever since. Under the agreement, Brazil would contribute €270 million over 10 years to ESO's budget, or one-quarter of the telescope's €1.083 billion cost.

Big bang for a big telescope.

Criminal charges in AIDS case

DES MOINES | An AIDS researcher who has admitted to research misconduct is now facing four felony criminal charges of misusing U.S. government funds. Federal prosecutors on 19 June alleged that Dong Pyou Han, a former researcher at Iowa State University (ISU) in Ames, made false statements related to millions

PHOTOS: (TOP TO BOTTOM) GETTY IMAGES/ISTOCKPHOTO; EUROPEAN SOUTHERN OBSERVATORY

Published by AAAS

of dollars in grant funding. Han left ISU this past September after investigators suggested he had added chemicals to rabbit blood in order to make it appear that an experimental AIDS vaccine was working. The case attracted the attention of U.S. Senator Charles "Chuck" Grassley (R–IA), who expressed concern that the government was not acting strongly enough to punish Han and recover misspent funds. Each charge Han faces carries a maximum prison sentence of 5 years.

Rocket launches wildlife tracker

YASNY, RUSSIA | A Russian rocket carried 37 satellites into space on 19 June, including Iraq's first spacecraft, which will track dust storms, and the cube-shaped DTUsat, which is designed to track small animals, such as the common cuckoo, that have been outfitted with tiny tags. It's about

Common cuckoo

"solving the mysteries of migrations," says zoologist Kasper Thorup of the University of Copenhagen, which built the craft with the Technical University of Denmark. The goal is to test technologies for an ambitious effort to track wildlife from the International Space Station.
http://scim.ag/wildlifetrack

Bill would nix Chu's brainchild

WASHINGTON, D.C. | Lawmakers in the U.S. House of Representatives moved to kill a signature project of former Secretary of Energy Steven Chu. In their version of the proposed 2015 budget for the Department of Energy (DOE), released 18 June, House appropriators zeroed out funding for the Joint Center for Artificial Photosynthesis (JCAP), which seeks ways to convert sunlight to fuels such as hydrogen. Chu championed such work and in 2010 launched JCAP, headquartered at the California Institute of Technology in Pasadena, as one of five Energy Innovation Hubs. JCAP's original funding expires this year and DOE must decide whether to continue it for five more years. But the White House requested only a 1-year, $24 million extension. The Senate and the White House would have to agree to kill JCAP. http://scim.ag/DOEartphoto

Europe leads partnership push

Consortia launched in three regions, by year

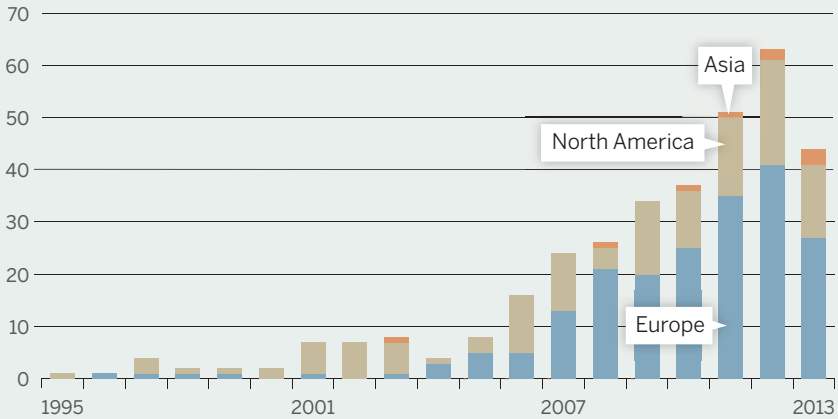

Source: M. D. Lim, *Science Translational Medicine* **6**, 242 (25 June)

Come together now

The last decade has seen a boom in biomedical consortia—collaborations between academic researchers, industry, disease advocacy groups, and others aimed mainly at speeding drug development. At least 369 such alliances have emerged since the mid-1990s, according to Mark Lim of FasterCures in Washington, D.C., who scoured press releases, the Internet, and other sources for data. Most are in Europe, followed by North America and Asia, Lim reports this week in *Science Translational Medicine*. Many aim to generate shared tools, such as transgenic mice and biomarkers for predicting vaccine safety, and they often focus on specific diseases, with cancer, Alzheimer's disease, diabetes, and rare diseases topping the list. It's too soon to assess the effectiveness of consortia, but Lim says the growing number launched by industry "is one indicator that competing research organizations are not waiting" for proof of principle before partnering with other groups to "solve unmet needs."

NEWSMAKERS

Three Q's

In her new novella *The Collapse of Western Civilization: A View from the Future*, Harvard University science historian **Naomi Oreskes** describes a planet devastated by centuries of global warming. The book, co-written with science historian Erik Conway of NASA's Jet Propulsion Laboratory, helped Oreskes win an outreach award last week from the American Geophysical Union.

Q: Why fiction?
A: I struggle with finding the right emotional tenor for talking about this issue. With fiction, I can sound an alarm … be emotional … [and] upset about things that are upsetting.

Q: You write as a Chinese historian looking back 4 centuries to the present.
A: I'm a scientist but also a historian, so a humanist. I got to thinking—what would a historian in the future say about us?

Q: How did you choose which climate scenario to depict?
A: The book is a worst-case scenario, but not a made-up scenario. What if it turns out that something—like sea level rise—is at the top of the error bars from the projections of the Intergovernmental Panel on Climate Change? Everything [in the story] that happens before 2013 is true, and everything that happens after is from the high end of the projections.

PHOTOS: (TOP TO BOTTOM) SHUTTERSTOCK; NAOMI ORESKES

Published by AAAS

IN DEPTH

Scripps Florida would be part of any deal.

BIOMEDICAL RESEARCH

Scripps and USC consider union, for money and prestige

Negotiations with university spark opposition from biomedical institute's scientists

By **Robert Service**

It's not just biomedical scientists who are struggling as federal research spending declines—entire research institutions are increasingly fighting for their existence. Last week, the Scripps Research Institute in San Diego, California, the world's largest independent biomedical research institution, publicly confirmed a report in the *U-T San Diego* that it is in merger talks with the University of Southern California (USC).

Scripps officials insist that no deal is imminent, and researchers there are already protesting—a leaked e-mail from Scripps's faculty chairs to its president warns that "the proposed path with USC would destroy much of what has been built and what we and others in the community value so much."

Outsiders say that the possible marriage illustrates the tough times facing independent institutes that rely primarily on federal grants for support. "It's a serious concern for the whole community," says Sally Rockey, the deputy director for extramural research at the National Institutes of Health (NIH) in Bethesda, Maryland. "We're talking about major institutions that are doing whatever they can to survive."

Scripps's financial concerns stem in part from declining revenue from NIH. In constant dollars, NIH funding for all of biomedical research has fallen 12.5% since its peak in 2004. Factor in the high rate of inflation for biomedical research, and the decline amounts to 23% since 2001. Scripps's overall revenues—86% of which come from NIH, according to Fitch Ratings—reflect the drop, declining 12% in constant dollars between 2007 and 2013, the institute's annual financial statements reveal.

With a current operating budget of $310 million and 262 faculty members on its California and Florida campuses, Scripps is also weathering the loss of other previously lucrative funding streams. The pharmaceutical giant Pfizer paid Scripps $100 million over 5 years from 2006 through 2011 for the rights to commercialize drug candidates from the institute's labs. Another drug giant, Novartis, made a similar deal for $39 million over 9 years beginning in 2007. "Those types of deals have fallen out of favor as pharmaceutical companies have become less flush," says one Scripps official who requested anonymity in order to discuss the merger possibility.

Revenue from the state of Florida is also tapering off. Florida paid Scripps $310 million over 10 years, beginning in 2004, to help launch its Florida campus in Jupiter. Some are worried the outpost could be shut out of a potential Scripps-USC alliance. Last week, former Florida Republican Congressman Mark Foley, who helped lure Scripps, said he was "outraged" at the possibility of a deal that could cut the Florida campus loose. Scripps President Michael Marletta, however, issued a statement last week that any merger will involve the Florida campus. "Scripps is one institute with two campuses," Marletta wrote.

Scripps isn't the only independent research institution caught in the funding squeeze. In November 2012, trustees at the Boston Biomedical Research Institute voted to disband due to financial difficulties. And last year, the Marine Biological Laboratory (MBL) in Woods Hole, Massachusetts, merged with the University of Chicago. According to MBL President Joan Ruderman, the merger has stabilized the historic institution's finances, by giving

Scripps's shrinking NIH support

NIH funding and approved projects, by year

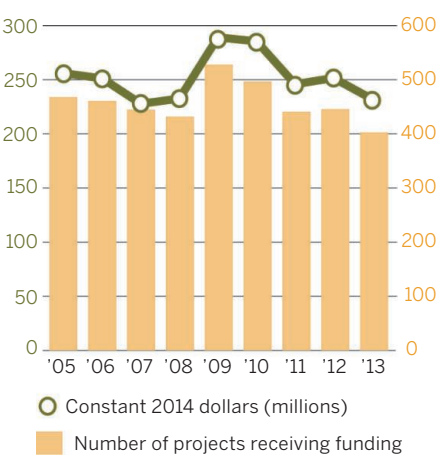

Source: NIH RePORT

PHOTO: JULIANVA AT EN.WIKIPEDIA [CC-BY-SA-3.0 (HTTP://CREATIVECOMMONS.ORG/LICENSES/BY-SA/3.0)], VIA WIKIMEDIA COMMONS

Downloaded from www.sciencemag.org on June 28, 2014

Published by AAAS

it support for research and faculty salaries while allowing MBL to shed overhead costs, including administration, facilities management, and legal fees. A merger with USC, which is in the middle of a $6 billion fundraising campaign to increase its endowment, could benefit Scripps in much the same manner, she says.

But some suggest USC is trying to get Scripps too cheaply. (*The Palm Beach Post* reports USC's offer was $15 million annually for 40 years.) "The terms of the proposed merger with USC are not even close to what it would take to build faculty support. … [A]bsent a far better arrangement than what is currently proposed, faculty are willing to make personal sacrifices to work for and maintain independence," the faculty chairs' e-mail concludes.

It's unclear whether Scripps first approached USC or vice versa, but the institute has considered other merger options before, a Scripps official says. If the union does occur, USC stands to bolster its scientific stature considerably. According to statistics from the National Science Foundation, the much bigger USC outranks Scripps in the total amount of federal funds received for science and engineering research. But in the main disciplines Scripps researchers practice, such as biochemistry and immunology, their impact considerably outweighs that of their USC colleagues, according to a Thomson Reuters Web of Science analysis of citation statistics from 2008 to 2013 conducted for *Science*. In the eight disciplines examined, USC's citation impacts outperform the world average, but Scripps has a higher, and often significantly higher, citation impact than does USC.

A merger "would be a very positive situation for both Scripps and USC," says Bruce Stillman, president of the Cold Spring Harbor Laboratory, a biomedical research facility in New York. USC may have competition for Scripps, however. Some see its coastal neighbor, the University of California, San Diego, as a more natural partner and an official there this week expressed interest in such an alliance.

Ruderman notes that independent research institutions are among the most vulnerable to slowdowns in federal funding, because they can't rely on undergraduate tuition dollars or on income from affiliated hospitals to help pay for their overhead. To make matters worse, she says, the cost of doing cutting-edge basic research continues to climb. As a result, other research institutes may soon find themselves looking for partners. "I think it's very likely we're going to see this trend continue," Ruderman predicts. ■

ARMS CONTROL

Not-seeing is believing

"Zero knowledge" tests could let inspectors identify a nuclear weapon without learning the secrets of its design

By **Richard Stone**

In nuclear arms control, the catchphrase "trust, but verify" gets you only so far. It's simple to count nukes deployed on intercontinental ballistic missiles, heavy bombers, or submarines: Just tally up the delivery systems. But verifying the number and types of nuclear warheads in storage—as future accords will require—is another story. No nuclear power would permit verification tests that reveal secret warhead designs.

Now, there may be a solution to this conundrum. Researchers have devised a way to verify a nuclear warhead's identity without laying eyes on it. Known as a zero-knowledge protocol, a name adopted from a technique used in cryptography, their proposal is setting the arms control community abuzz. It's an "ingenious solution," says physicist James Acton, a nonproliferation expert at the Carnegie Endowment for International Peace in Washington, D.C.

"This is a useful invention, and if it facilitates the arms reduction process, I favor it," says hydrogen bomb designer Richard Garwin, now an éminence grise at IBM's Thomas J. Watson Research Center in Yorktown Heights, New York. But the approach, published this week in *Nature*, is not quite ready for prime time, he cautions.

Nuclear armed

Estimated number of warheads, 2014

Russia	8,000
United States	7,315
France	300
China	250
United Kingdom	225
Israel	80
Pakistan	100–120
India	90–110
North Korea	<10
Total:	~16,400

Source: Federation of American Scientists

Efforts to verify warheads have focused on crafting "information barriers": electronic sensors and software that digest a claimed warhead's secret specs but spit out only an unclassified "yes"—the real deal—or a "no." But these methods are prone to tampering. A host nation might devise a trapdoor that tricks an inspector into confusing a prop for a warhead, or an adversary might engineer a side channel that leaks secret data during the inspection.

The inspiration for a radical new approach came at a regular Monday lunch at Princeton University to which David Dobkin, the outgoing dean of the faculty, invites professors from various departments to chat about what they are working on. At one such lunch in December 2010, Alexander Glaser, a physicist, said he hoped to devise a warhead verification system that divulges no sensitive information—but confessed that he had no idea how to get there. Dobkin, a computer scientist, saw an analogy in the digital world: zero-knowledge proofs, invented in the 1980s, that allow one to prove that a statement is true without revealing why it is true. They have become an indispensable tool in cryptography and are now used in such applications as electronic voting, online auctions, and privacy-protected data mining.

Intrigued, Glaser set to work with Princeton plasma physicist Robert Goldston and Boaz Barak, an expert on zero-knowledge proofs at Microsoft Research New England in Cambridge, Massachusetts. They hit on using high-energy neutrons to image nuclear warheads just as x-rays image bones; bombs of the same design would have virtually identical radiographs. However, these "fingerprints" would be suffused with classified data and would be off-limits to inspectors.

The solution: a neutron detector that can be preloaded with the radiographic negative for the design of its warhead. An inspector would randomly select the preload from a set provided by the host nation. A warhead to be verified would then be scanned with neutrons; the resulting image would add to the negative. If it matched the weapon being tested, inspectors would see a uniform signal—"what you would expect to see as if nothing was there," Goldston says—conveying no details

Published by AAAS

Warheads from retired Peacekeeper missiles in storage at F. E. Warren Air Force Base in Cheyenne, Wyoming. A new verification technique could pave the way for cuts in nuclear stockpiles.

PHOTO: PAUL SHAMBROOM

of the weapon itself. Scanning a warhead repeatedly with different preloads or testing multiple warheads in parallel should make verification ironclad. "The inherent simplicity of the principle is enormously pleasing," says John Finney, a condensed matter physicist at University College London, who was not involved in the work.

Glaser's group devised a proof of principle with the British Test Object (BTO), a disk used for radiographic testing in unclassified research. The BTO has a ring of tungsten, which gives a good approximation of fission induced when high-energy neutrons slam into plutonium or uranium-235. (The verification test doesn't increase a radioactive material's natural fission enough to affect a warhead.) For experimental tests, the team plans to blast the BTO with neutrons from a deuterium-tritium generator and align the resulting radiograph with the radiographic negative. The team anticipates that it will be able to reliably spot mismatches and discern the true BTO from a fraudulent one.

If a future accord were to mandate elimination of excess warheads, a state might be tempted to cheat by trying to pass off a fake as an authentic warhead slated for dismantlement, "allowing the real thing to be diverted to a clandestine stash," Acton notes. The zero-knowledge approach would readily unmask common real-world frauds, the researchers say. For example, if a nuclear power tried to get credit for decommissioning a harmless warhead loaded with nonfissile uranium-238 or reactor-grade plutonium, a skewed fission rate would reveal that the device wasn't bomb-ready.

In March, Glaser's group invited seven nuclear jocks to Princeton to "poke holes in our idea," Glaser says. "If there was a flaw, we needed to find out before it was too late." Garwin saw some chinks, including the potential for a host nation to rig the system to fake a scan. Adding a second set of detectors tuned to a different neutron generator—for instance, beryllium shorn of neutrons by a gamma ray source—would make the system more robust, Garwin says. "Fission neutrons detected in the side detectors will then be sure evidence of fissile material."

Before nuclear powers embrace the technology, they will have to jointly iron out any more kinks that might undermine trust in a verification system, says Raymond Jeanloz, a nuclear weapons policy expert at the University of California, Berkeley, who also visited Princeton in March for the review. "It's a great idea, and I'm cheering them on," Jeanloz says. But to implement this, "the devil is in the details."

He and others note that a nonproliferation payoff may be years off. Even if nuclear powers agree on a foolproof verification system, they must still negotiate how many stored nukes to eliminate. ■

ANIMAL WELFARE

Free Willy? Dolphin drama riles aquaria

Proposal to remove captive dolphins draws fire

By **David Grimm,** ***in Baltimore, Maryland***

John Racanelli gazes at his eight bottlenose dolphins as if he might be looking at them for the last time. The CEO of the National Aquarium here, he sits on bleachers in a circular amphitheater as the animals glide around a giant concrete tank, some grasping small orange basketballs in their mouths, others blowing bubbles. One peeks his head out of the water and stares back at the CEO. "He's spying on us," Racanelli laughs.

Last month, the aquarium announced that it is considering moving these animals to a marine sanctuary, citing concerns that it is cruel to keep such cognitively advanced creatures in captivity. The move has deepened a schism in the research community that studies dolphins and whales, collectively known as cetaceans. Scientist-turned-animal-advocate Lori Marino calls the aquarium's announcement "a giant step forward" and predicts the National Aquarium's reputation will put pressure on other facilities to reconsider captivity. But this week, the Dolphin Research Center (DRC) in Grassy Key, Florida, sent a letter to the National Aquarium denouncing the potential plan as bad for both science and public engagement. "It's misguided in a number of ways," says DRC Research Director Kelly Jaakkola.

Cetacean researchers have wrestled for years with the ethics of confining whales and dolphins; about 600 of the animals are kept in 34 facilities in North America today. In 2010, Marino, then a biopsychologist at Emory University in Atlanta, helped draft a "Declaration of Rights for Cetaceans: Whales and Dolphins," which argued that captivity spells cruelty for these intelligent animals, because no facility can reproduce the cognitive and social environment of the open ocean. She hoped her work on dolphin cognition—showing, for example, that the animals are self-aware enough to recognize themselves in mirrors—would convince colleagues that cetaceans should be studied only in the wild. Instead, many fired back

Downloaded from www.sciencemag.org on June 28, 2014

Published by AAAS

with a series of papers arguing that captive cetacean research remained crucial (*Science*, 29 April 2011, p. 526).

Then came *Blackfish*. The popular 2013 documentary, in which Marino appears, cast a pall on captivity by focusing on the travails of a SeaWorld orca named Tilikum, which was implicated in the deaths of three people. Racanelli says public opinion fed into the National Aquarium's announcement, but he also has personal reasons. He began interacting with dolphins 40 years ago as a tank cleaner at Marine World in San Francisco, and says premature deaths of captive dolphins shaped his views. Shortly after he arrived at the National Aquarium in 2011, he stopped the facility's dolphin shows (*Science*, 30 May, p. 951). Today, visitors can view the animals, but they won't see them perform tricks. "No music, no monitors," Racanelli says. "They just get to goof around."

Still, he's not satisfied with the current setup. The dolphin tank is small, chemically treated, and bereft of other marine life. "This is still a stadium," he says, glancing around the amphitheater. "It does not feel like a dolphin habitat."

Last fall, Racanelli gathered a group of marine biologists, veterinarians, and structural engineers to map out a new mission for the National Aquarium, including deciding the fate of its eight dolphins. If the animals do move, they won't go to the open ocean, an environment most have never encountered. Instead, the group is considering the feasibility of a dolphin sanctuary, perhaps a large, fenced-off area of the sea. The animals would continue to get regular medical care, but otherwise would have almost no interaction with humans. No such sanctuary exists today, so the team would start from scratch.

The working group, known as BLUEprint, hopes to make a preliminary decision about the dolphins by April of next year, Racanelli says. A sanctuary would take anywhere from another 3 to 10 years to become reality, and no cost estimates have been given.

Such a plan would face stiff opposition from other cetacean facilities such as the DRC, a nonprofit funded with admissions and public donations that houses dolphins in sea pens and has conducted studies of dolphin behavior and cognition. In its letter to the National Aquarium this week, the DRC states that it and other facilities adhere to "extremely high standards of animal care and training" and that Racanelli is advancing "opinions that are either factually inaccurate and/or that do a great disservice … to the very animals themselves."

Jaakkola, the center's scientific director, worries that if dolphins are out of the public's sight, they'll also be out of mind and support for protecting them will drop. "Before aquariums, humans didn't know or care about these animals," she says. "Now people care about them because they can get up close and personal with them. That's why we have things like dolphin-safe tuna."

Others fret that our understanding of cetaceans will stall without access to captive animals. Shawn Noren, a physiologist at the University of California, Santa Cruz, who has studied whales and dolphins for nearly 20 years, testified in April against a California bill that would have banned orca shows in the state and phased out captivity. Her studies on dolphins kept in natural lagoons (where they also perform shows and swim with the public) has involved attaching heart rate monitors to the animals, for example, to determine why they are susceptible to decompression sickness when startled by Navy sonar; this study was funded by the Office of Naval Research, which has not taken a public position on the issue of captive cetaceans. "None of this work could have been done in the wild," she says.

Sanctuaries are not viable, Noren says, because dolphins that have spent most or all of their lives in sterile environments would face pollution and disease. Plus, she says, "these animals are used to human stimulation and interaction. They'd be bored out of their minds." Jaakkola adds, "Sanctuaries are not necessarily a Disney type of place."

Nevertheless, Noren says, the die may have already been cast. Even though the California bill she fought didn't pass, the press coverage of it placed aquariums on the spot, and the National Aquarium's plan, if it goes forward, "would put even more pressure on them." There are other signs of changing attitudes. A biannual marine mammal research conference in New Zealand last year hosted a panel discussion on the ethics of captivity, the first such forum at this meeting that researchers can remember. Marino left Emory this year to head the Kimmela Center for Animal Advocacy, which aims to inject more science into the animal advocacy movement. She's also advising the Nonhuman Rights Project, which last year filed a series of lawsuits in an attempt to free four New York chimpanzees from captivity (*Science*, 6 December 2013, p. 1154) and may set its sights on cetaceans.

If chimpanzee research is any parallel, those who support studying captive cetaceans have reason to worry: Similar concerns spurred the National Institutes of Health to phase out most of its captive chimp studies and move the animals to sanctuaries (*Science*, 5 July 2013, p. 17).

Back at the National Aquarium, one little girl has toddled into the amphitheater and stares, mouth agape, at the dolphins. "Whoa!" she says. Racanelli looks over at her. "I worry about losing that," he says. "But at the end of the day we have to figure out if these dolphins are part of our true mission: changing the way humanity views and cares for the ocean." ■

For now, dolphins enchant at the National Aquarium.

PHOTO: COURTESY OF THE NATIONAL AQUARIUM

Captive cetaceans

607

Whales and dolphins are kept in captivity in North America*

506	76	25
Dolphins	Beluga	Killer whales

*NUMBERS EXCLUDE THOSE HELD BY THE U.S.NAVY, WHICH DOES NOT RELEASE SUCH DATA

Source: CETA-BASE

Published by AAAS

ECOLOGY

Daring to live on the edge

Tracking the house sparrow's spread in Africa yields secrets of these invaders—a taste for novel foods, for example

By **Elizabeth Pennisi**

When Lynn "Marty" Martin first visited Kenya in 2002 as a graduate student, he saw just a single house sparrow. By 2009, these birds—originally from Europe—were so plentiful that he was easily catching them in a hotel parking lot in Nairobi. "They went from almost nothing to being abundant," says Martin, an ecological physiologist at the University of South Florida, Tampa.

The house sparrow, *Passer domesticus*, has done this before, spreading to almost all parts of the world over the past few hundred years. But by analyzing the bird's recent advances in Kenya, Martin and his colleagues have watched one of those invasions unfold almost in real time—and have gained a unique opportunity to pinpoint the traits that define a successful invader. They've documented differences in the immune system and stress responses in birds on the leading edge of the expansion. And last month, they reported finding another clue to the birds' success: a penchant for novel foods.

The discovery helps round out the picture of an ideal invasive animal, according to scientists impressed with Martin's work. "It adds new evidence for the hypothesis that developing new behaviors is key for animals to succeed in novel environments," says ecologist Daniel Sol of the Centre for Ecological Research and Forestry Applications in Cerdanyola del Vallès, Spain. With invasive species transforming ecosystems worldwide, "learning about traits that make a species a successful invader is of great importance," adds Claudia Mettke-Hofmann, a behavioral ecologist at Liverpool John Moores University in the United Kingdom.

Biologists already know that invaders eat a varied diet, aren't too picky about where they live, and reproduce lots. More recently, they've begun to look for cognitive and molecular attributes that define invasive species. Martin's previous work added a further twist by suggesting that invaders gain an edge not just from species-wide traits, but also from traits found only in individuals at the vanguard. About a decade ago, for example, he compared house sparrows in two invasive populations, in Panama and New Jersey. The birds from Panama, where house sparrows invaded only about 30 years ago, happily ate novel foods, whereas the New Jersey birds, established for 150 years, showed no such plasticity.

In 2010, drawing on such data, Tim Wright of New Mexico State University in Las Cruces and his colleagues proposed that flexibility benefits an invasive species only as it settles into a new place. A willingness to try new foods, for example, has risks, potentially exposing an animal to new toxins or pathogens. "In established populations, it may be better to stick with the known, good resources," Wright says.

The house sparrows spreading through Kenya allowed Martin and his colleagues to explore such trade-offs. Sparrows first gained a foothold in the Kenyan coastal city Mombasa in the 1950s, arriving as stowaways in freighters from South Africa. Subsequent generations spread westward 850 kilometers to the Ugandan border and now are thriving in cities across Kenya. In 2012, Martin, Andrea Liebl, now a behavioral physiologist at the University of Exeter in the United Kingdom, and their colleagues measured hormonal responses to stress in birds captured at varying distances from Mombasa, along with the density of two related stress-hormone receptors in the brains of some of the birds. Sparrows farthest from Mombasa—at the leading edge of the invasion—release more stress hormone, the researchers reported in 2012. And to cope, their brains have a higher ratio of certain hormone receptors. In theory, a faster stress response should benefit the birds leading the invasion. But likely because it's costly energetically to maintain a strong stress response, the more settled birds on the back end of the invasion lose some of their edge, Liebl notes.

A 2013 study showed that the active invaders also have sharper immune systems. Toll-like receptors are immune surveillance molecules that trigger responses to pathogens, from bacteria to parasites. The amount of those receptors in sparrows on the range edge is "huge," Martin says, in comparison with the number in Mombasa birds. Birds moving into new territory will encounter new parasites, making the additional immune receptors worthwhile in spite of the energetic costs of the revved-up immune response that results, Martin says. Once the birds' immune systems have had a chance to coevolve with the new pathogens, those energetic costs become a liability and the number of toll-like receptors decreases, he hypothesizes.

Liebl and Martin also used the Kenyan birds to follow up on the earlier work on novel food preferences. In the initial study, the Latin and North American birds had a lot of genetic diversity that could account for their willingness to try new foods. But the Kenyan sparrows were introduced so recently that their genetic diversity is lower. Yet the same behavioral differences emerged when Liebl presented birds from eight cities with frozen strawberries and dog food mashed with hard-boiled eggs—two foods she was sure they had not encountered in the wild. Even after an hour, hungry Mombasa birds had not approached the food, she and Martin reported online on 26 May in *Behavioral Ecology*. In contrast, leading-edge birds "approached and ate it in a matter of seconds," she says.

Now, investigators want to learn whether recent genetic change or other factors underlie the special features of sparrows on the leading edge. "Doing so will give us a case study of what defines a successful invasive species," says David Reznick, an ecologist at the University of California, Riverside. ■

House sparrow invasion of Kenya

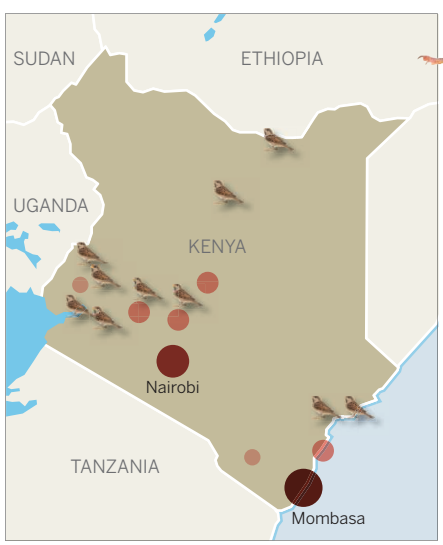

Source: Martin *et al.*, *Proc. R. Soc. B* (7 January)

PHOTO: GETTY IMAGES

Downloaded from www.sciencemag.org on June 28, 2014

Published by AAAS

FEATURES

Sailing Sinbad's seas

Archaeologists are rediscovering the ancient Maritime Silk Road, which once powered more East-West commerce than the famed Central Asian land route

By **Andrew Lawler**

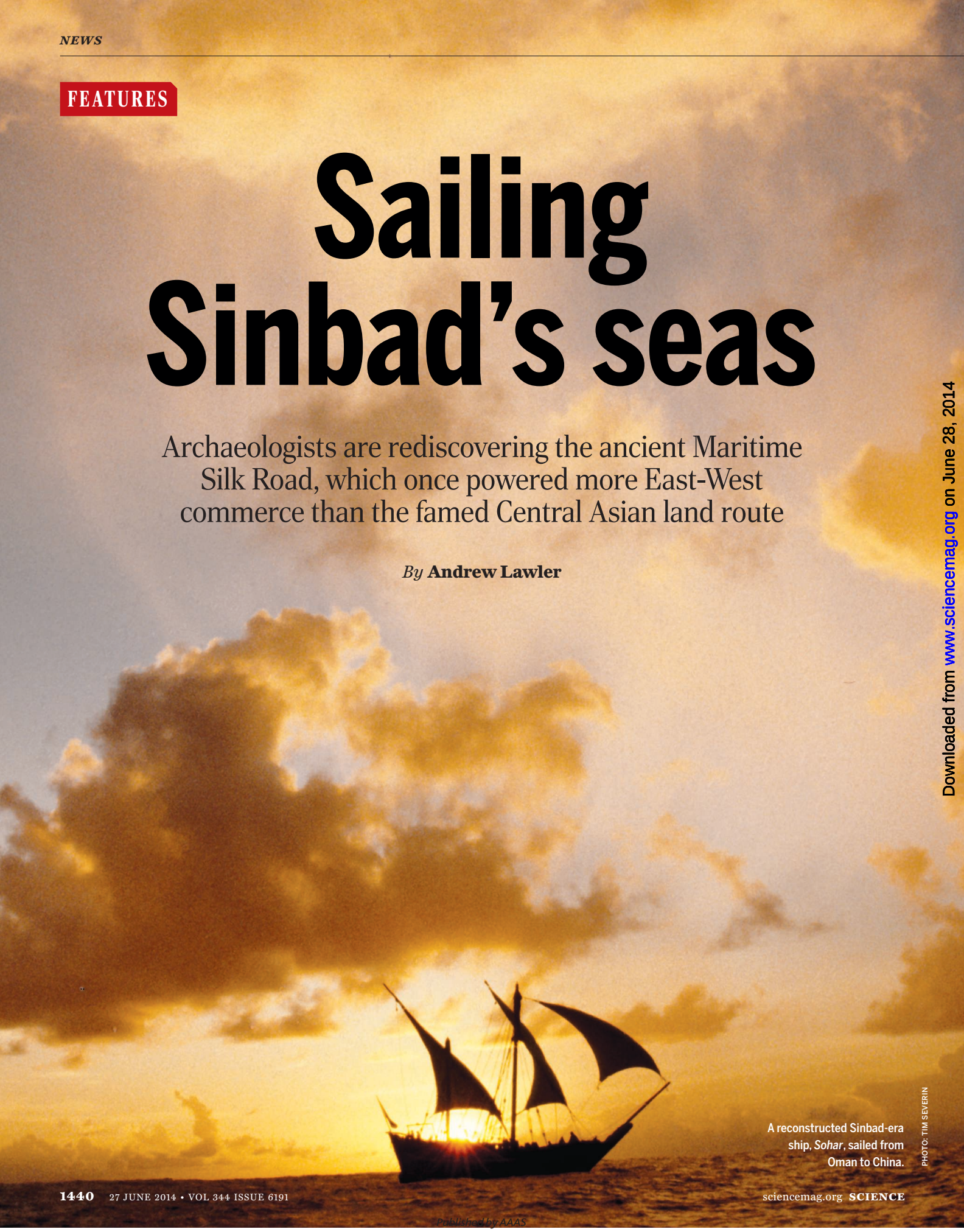

A reconstructed Sinbad-era ship, *Sohar*, sailed from Oman to China.

PHOTO: TIM SEVERIN

Downloaded from www.sciencemag.org on June 28, 2014

Published by AAAS

Shipping lanes of the Maritime Silk Road

Intensive trade around the Indian Ocean developed in distinct phases

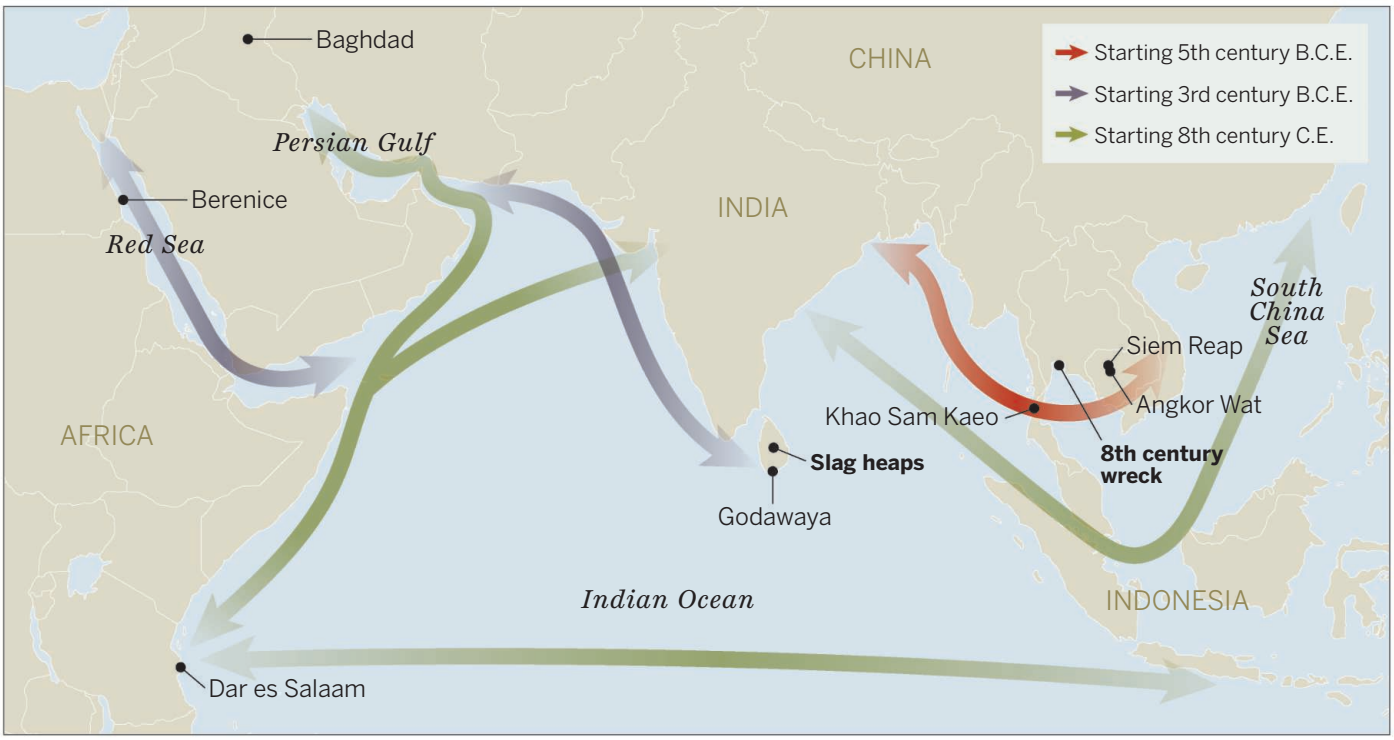

"One day, the old desire entered my head to visit far countries and strange people, to voyage among the isles and curiously regard things hitherto unknown to me," recalls Sinbad the Sailor in *The Thousand and One Nights*, first compiled in the 9th century C.E. "Also, the trading habit rose in me again." This wily Odysseus of the Indian Ocean told fantastic stories of shipwrecks, cannibals, and exotic lands rich with gems and heady spices.

Until recently, Sinbad's tall tales held little interest for scholars of ancient and medieval East-West relations. They focused instead on the more than 6000-kilometer Silk Road far to the north, made famous by Venetian merchant Marco Polo, who traveled across the Central Asian steppes from Europe to China in the 13th century. Most researchers ignored the fact that Polo returned to Europe via the Indian Ocean, in the waters plied by real-world Sinbads. Glimpsed only in the odd Roman coin found in an Indian village or in medieval Chinese ceramics washed up on a Kenyan shore, the southern maritime road was easy to overlook.

Now, this busy trading route is emerging from the shadows. Researchers are picking through Southeast Asian swamps, diving off Sri Lankan reefs, and digging on African beaches. The artifacts they are finding—glass beads, potsherds, seeds, animal bones—reveal a lost story of Indian Ocean trade that went far beyond the simple exchange of gems and spices. "Finally we are moving beyond just talking about trade to the making of cultural identity," says archaeologist and historian Himanshu Prabha Ray of New Delhi's Jawaharlal Nehru University.

The work, still in the early stages, is shifting archaeologists' focus from the great empires at either end of the Silk Road—Rome and China—to the trade and influence of the vibrant societies in between. Until recently, many historians would have agreed with a 20th century French scholar who dismissed the world's third largest ocean as "scarcely more than an extension of the eastern Mediterranean." A paucity of ancient texts and archaeological digs reinforced this parochial view.

But the new evidence shows that from 2000 B.C.E. until the arrival of Europeans in 1498, the Indian Ocean network linked diverse societies on three continents, catalyzing industrial development and cultural changes from early Southeast Asia to medieval coastal Africa. It all sounds unexpectedly modern, says J. D. Hill, an archaeologist at the British Museum in London. "The surprise is that the world was interconnected long ago."

In 2008, archaeologist Nicole Boivin of the University of Oxford in the United Kingdom and colleagues won a $1.5 million, 5-year grant from the European Research Council to piece together the neglected history of Indian Ocean trade. They have since been expanding collaborations, applying new methods to existing artifacts, and conducting small digs around the rim of the ocean. Their ambitious goal is to track how plants, animals, trade goods, people, and ideas moved across the ocean over more than 3 millennia, and they shared progress reports at a November 2013 meeting in Oxford on protoglobalization in the region. Says archaeologist Greger Larson of Britain's Durham University, with a touch of Sinbad swagger: "We are a new generation of explorers."

ARTISANS ARRIVE: East Indian Ocean, 5th century B.C.E. to 2nd century B.C.E. The Indian Ocean is defined by the monsoon, an Arabic word for season. Blowing southwest from May to September and northeast from November to March, this wind reliably propels ships across large stretches of open sea. As early as 2000 B.C.E., Indian merchants traveled to Arabia on these winds, according to finds made in the 1980s (*Science*, 28 May 2010, p. 1101). Such ancient trade shaped the distribution

Published by AAAS

of domesticated plants and animals: Grains like sorghum and millet made their way from Africa to India; zebu cattle went from India to Africa; and cinnamon and nutmeg moved from South Asia all the way to Israel and Egypt—although it is unclear who carried this bounty from continent to continent, and how.

Now, a second phase of international trade, in the early centuries B.C.E., is coming to light in the eastern half of the ocean. In this period, India and China were urbanizing but Southeast Asia was long considered a rural backwater until its first empires arose, such as the Khmer empire based at Angkor Wat. Now, archaeologists are discovering that by 400 B.C.E., Southeast Asians were making iron, supporting an elite, and building large moated settlements of their own design, says Charles Higham of the University of Otago, Dunedin, in New Zealand, who has excavated extensively in Thailand and Cambodia.

This new Southeast Asian elite would have prized luxury goods—and new finds suggest that trade with distant north India helped provide them. Between 2005 and 2009, a French-Thai expedition uncovered what may be the oldest known city in Southeast Asia, at the narrowest point of the Malay Peninsula that separates the Indian Ocean from the South China Sea. The site of Khao Sam Kaeo was an early and important trading link between India and Southeast Asia, argues Bérénice Bellina-Pryce, an archaeologist from the French national research agency CNRS in Paris who led the dig.

Located 500 kilometers south of Bangkok, Khao Sam Kaeo is now a remote swamp. But millennia ago, it was a convenient point to unload goods from the Indian Ocean for overland transport to Southeast Asia (see map, p. 1441), avoiding a longer voyage through the treacherous, pirate-plagued Strait of Malacca to the south. The dig revealed that from the 4th century B.C.E. to the 1st century B.C.E., Khao Sam Kaeo was a sprawling city of walled neighborhoods surrounded by a ditch-and-palisade rampart. The finding was so unexpected that "it took me years to convince colleagues that we had an early form of urbanization," Bellina-Pryce says. Later cosmopolitan coastal towns in this region probably resembled Khao Sam Kaeo.

Working in dense forest and beset by looters, the team found metal vessels and stone and glass beads linking the site to India to the west and to Vietnam and China to the east. Bronze and iron workers at the site used copper alloys similar to those in Vietnam and China. But the beads, although made locally, were crafted using

Drawing a bead on trade

Indo-Pacific beads offer clues to ancient trading patterns.

By **Andrew Lawler**

In a small laboratory tucked into the Field Museum in Chicago, Illinois, Laure Dussubieux carefully positions a tiny bead so that a laser can drill a microscopic pit into its surface, releasing a puff of gas. A mass spectrometer then reads the gas's composition, including the trace elements. The result is a unique signature that often can reveal how, where, and even when the glass was formed, Dussubieux explains. And that has turned humble glass beads into tools for tracing long-lost trade routes in the Indian Ocean (see main story).

"I think it's pretty great that you can take a simple glass bead, shoot a laser at it, crunch some numbers, and then get the recipe used to make the glass," says Alison Carter, an archaeologist at the University of Wisconsin, Madison, and one of many researchers who show up regularly at Dussubieux's door with their own colorful bits of glass.

Around the vast Indian Ocean, peoples spoke different languages, ate different foods, and worshiped different gods. But they shared a love of glass beads, which typically were strung together to make colorful bracelets and necklaces. Enormous effort and skill went into making huge numbers of baubles as small as 3 millimeters in diameter in a dazzling array of colors. Difficult to date and organize into types, the artifacts were long neglected by archaeologists.

Then, in the 1990s, archaeologist Bernard Gratuze of the French national research agency CNRS in Orléans began to pioneer bead analysis using lasers and a mass spectrometer; Dussubieux learned the technique as a Ph.D. student in his lab. Beads were often made locally of raw glass ingots that had been shipped great distances, and the new technique made it possible to trace the glass to its origin, revealing shipping and trade routes.

For example, bead studies have shown that a glass formula using mineral soda appears to have originated around the 5th century B.C.E. in the Ganges plain of northern India and then spread south and east. When Dussubiex analyzed about 200 beads excavated at Khao Sam Kaeo, which emerged as a trading city on the Malay Peninsula beginning in the 4th century B.C.E., she found that many were made of this soda-rich glass. Thus, the raw glass was likely made in India and shipped more than 2000 kilometers east.

In a study of Cambodian beads, Carter discovered that 1st century C.E. beads from the southeast of the country were made using potash—an indigenous Cambodian method—whereas beads in the northwest consisted of mineral soda glass from India. In later centuries, however, soda glass spread to southeastern Cambodia, perhaps a sign of rising Indian influence.

Across the Indian Ocean, Marilee Wood of the University of the Witwatersrand in Johannesburg, South Africa, is using bead analysis to track trade routes along the southern coast of East Africa. Changing bead types reveal African ties to the Middle East starting around the 7th century C.E., followed by trade with distant Sumatra and then with India around 1000 C.E. "We have early glass coming from Southeast Asia," she says. "This is a very different pattern than you find in the north" coast, where Middle Eastern and Indian glass predominates.

Carter, like many of her colleagues, praises Dussubieux for her analyses and patient work training others to read beads. She's "a walking database of glass types," Carter says. "Combined with the body of work from Laure and others, the glass bead can be tied into a whole network of ancient glass production and trade." ■

PHOTO: SHINU ANNA ABRAHAM AND P. J. CHERIAN/KCHR

Published by AAAS

Tracing trade. At Khao Sam Kaeo, archaeologists discovered traces of an ancient city; 2000 kilometers away off Sri Lanka (*right*), divers examining a wreck found a pot from around 150 B.C.E.

PHOTOS: (LEFT TO RIGHT) BERÉNICE BELLINA-PRYCE; SUSANNAH H. SNOWDEN

Indian technologies and imported glass (see sidebar, p. 1442), evidently by Indian artisans fashioning goods for Southeast Asian elites.

Higham, who was not involved in the research, concludes "the work at Khao Sam Kaeo has revealed beyond reasonable doubt that Indian craft workers were settling coastal port towns in the [Malay] peninsula by the 4th century B.C.E., and fashioning beads there for local tastes."

Indian cotton weavers were also likely hawking their wares in Southeast Asia in the early centuries B.C.E. The cotton has long since disintegrated, but the artisans left behind iron biconical spindle whorls, distinctive little objects with a hole in the middle and tapered on two sides. These whorls show up first in India as early as 400 B.C.E. and spread as far east as Vietnam in the following centuries, says Judith Cameron of the Australian National University in Canberra. There's no reason to transport a spindle whorl unless you're creating a textile yourself, she notes. "These are hard to use without knowledge and have no intrinsic value," she says.

The whorls and beads shed light on a heretofore unknown migration of artisans and merchants. They suggest that in the early centuries B.C.E., Indian people as well as goods landed in Southeast Asia, where they met a complex society with a wealthy elite. "This is not about the materials, but about the links formed by people," says archaeologist James Lankton of University College London, who has worked at Khao Sam Kaeo.

BUDDHIST STEEL: Indian subcontinent, 3rd century B.C.E. to 4th century C.E.

While Khao Sam Kaeo flourished in the east, a new era of trade began in the western half of the Indian Ocean. A unique Greek text offers a glimpse of it. Copied in the 10th century C.E. by a Byzantine scribe, the Periplus of the Erythraean Sea is based on a document likely written in the 1st century C.E. by a ship captain or merchant. In 66 short chapters, it describes the geographical, economic, and political landscape from East Africa to Malaysia. The manuscript describes cinnamon and slaves for sale in Somalia, mentions the best ports to buy Indian cotton and sesame oil, and cites the Ganges valley as a source of silks, ivory, and precious stones. Contemporary Roman writers add another detail: Hundreds of ships annually sailed the monsoon from Egypt to India carrying grain, silver, and other goods, and returned with Chinese silk and Asian spices, such as cinnamon and nutmeg.

Using these texts as guides, historians long assumed that Rome's appetite for luxury goods drove trade in this period. Roman coins and amphorae found from India to Vietnam reinforced this belief, which was "the culmination of Indian Ocean history as Roman history," as archaeologist Eivind Heldaas Seland of the University of Bergen in Norway wrote in a review earlier this year. Recent excavations at the Egyptian Red Sea port of Berenike have confirmed some of the goods mentioned in the Periplus: spices, wood, textiles, bamboo, and coconuts imported from the east as early as the 3rd century B.C.E.

But archaeological work now under way in Sri Lanka, the teardrop-shaped island off the southern coast of India, contradicts the idea that Westerners jumpstarted the Indian Ocean economy. Instead, Egyptian and Roman merchants were likely drawn to an already booming international trade, researchers say.

Clues come from the oldest known shipwreck in the Indian Ocean. A team of Sri Lankan and American researchers recently completed their second full season of work on the wreck, which lies 34 meters underwater just offshore from the estuary of Walawe River, one of the island's few navigable rivers. The boat itself appears

Published by AAAS

to have disintegrated, but may have been 25 meters or more in length. Recovered material has been dated by artifacts and radiocarbon to between 200 and 100 B.C.E., says archaeologist Deborah Carlson of Texas A&M University, College Station, who is co-leading the effort with Osmund Bopearachchi from Paris's CNRS (*Science*, 20 July 2012, p. 288). Among the artifacts are several glass ingots, likely made in India and on their way to be used in local production of beads and bangles. Divers also spotted remnants of cargo: Several solid masses of iron and rock, about 3 meters high and totaling about 20 meters long.

Carlson thinks she knows where the iron came from: hilly areas upriver, where other archaeologists are finding ancient mines and iron and steel production facilities dating to the centuries before and after the start of the common era. (Iron production began by 1500 B.C.E. on the nearby Indian subcontinent, centuries before it caught on in the Middle East and Europe.) Researchers have identified a giant slag heap—as big as four school buses parked end to end—along the Walawe River in Sri Lanka's interior and dated it to 400 to 200 B.C.E., reported Mats Mogren of the Swedish National Heritage Board in Lund at the Oxford meeting. This single site could have produced thousands of tons of finished iron as well as high-carbon steel, smelted in 2-meter-high furnaces fired by ranks of monsoon-powered windmills. "The technological knowledge is very high," says Mogren, who estimates that hundreds of such sites may exist. "This has fantastic implications" for long-distance trade in metals, he adds.

The Sri Lankan wreck confirms that metals were made for export, not just small-scale domestic consumption. Thus, an island once considered a rural society was also an industrial powerhouse. "Hinduwane," the Arab term for steel in the 6th and 7th centuries C.E., may reflect that role, Mogren notes: "Wane" is the word for steel in Sri Lanka's native tongue, Sinhalese.

PHOTO: © ANURUDDHA LOKUHAPUARACHCHI/REUTERS

THE BIRTH OF SWAHILI: East African coast, 800 C.E. to 1400 C.E.

In the early centuries of Indian Ocean trade, "East Africa is the missing story," says Mark Horton, an archaeologist at the University of Bristol in the United Kingdom. Few ancient texts clarify Africa's role, and archaeology there lags behind work on Asian coasts. The Periplus mentions extensive trade between Mediterranean and African ports. But excavators have yet to identify any ports predating 700 C.E., and "Greco-Roman" beads found on the African coast turned out to be medieval, according to analyses by archaeologist Marilee Wood of the University of the Witwatersrand in Johannesburg, South Africa. Evidence is growing that East Africa south of Somalia did not play a major role in Indian Ocean trade until after that time.

The Indian Ocean trade did eventually leave one of its most enduring legacies on the African coast from Kenya to Mozambique: an entire culture based on the trading way of life. The Swahili way of life includes the Muslim faith, an Arabic-laced language, and culinary and mercantile traditions strongly reminiscent of the Middle East. The word "Swahili" itself is Arabic for "coastal dwellers."

Medieval texts describe ivory, gold, timber, and slave exports from Africa to the Middle East. Many historians therefore theorized that the Swahili culture was born when Persians and Arabs came to the East African coast in the 8th and 9th centuries to extract resources. But preliminary results of an unpublished genetic study in coastal Kenya suggest that the number of foreigners was few and that the Swahili are overwhelmingly of African lineage. Ryan Raaum, a biologist at Lehman College in New York City, sampled 150 men in 13 coastal communities and examined their maternal—X—and paternal—Y—chromosomes, as well as some preliminary genome-wide DNA. Just over half the paternal genes resembled those found among Arabs, Iranians, and South Indians, suggesting foreign fathers. By contrast, few of the maternal genes appeared foreign, and the genome-wide data are also chiefly African. Raaum suggests that a relatively small number of foreign men successfully introduced their genes into a mostly African population. He is now sequencing entire genomes to clarify this picture.

Research on plant and animal introductions supports the view that East Africa

Published by AAAS

Spice route. Even today, cinnamon is processed on Sri Lanka, and in ancient times, spices like Indonesian nutmeg (*right*) drew merchants across the Indian Ocean.

PHOTO: © YUSUF AHMAD/REUTERS

entered the Indian Ocean trade around 800 C.E. Archaeobotanical finds show that the cultivation of previously unknown grains like rice began in the region by 800 C.E., with the arrival of two separate strains, one from Southeast Asia and one from India, according to genetic studies by Erik Gilbert of Arkansas State University, Jonesboro. Cats, chickens, and rats also appear to have arrived in East Africa by ship starting in the 8th century. The use of foods like rice did not spread inland until much later, a sign that Swahili culture was oriented toward the Indian Ocean rather than interior Africa.

SINBAD'S SHIP What kind of vessels made these voyages? Based on the few wrecks found to date, Lucy Blue, a maritime archaeologist at the University of Southampton in the United Kingdom, says that a typical vessel of Sinbad's era carried 1000 times the weight a camel can bear and required far less human labor than a Silk Road caravan. One example, a 9th century ship wrecked off the coast of Indonesia in the Java Sea, epitomized the protoglobalization of the medieval Indian Ocean. The vessel was crafted in an Arab style, carried a load of Chinese goods, and was built with timbers from Africa, according to Horton. Another wreck turned up just last fall on a shrimp farm on the southwest outskirts of Bangkok. A team co-led by Erbprem Vatcharangkul, chief of Thailand's underwater archaeological division, began excavating and revealed a vessel at least 35 meters in length, built in Arab style and dating to about the 8th century. Sailors or looters have scavenged the cargo, but they left behind an ivory tusk, wood that likely comes from India, and Chinese ceramics.

The sailing culture that these ships spawned left its mark on the societies that ring the ocean. Southern Indian Tamil poetry from the first 3 centuries C.E. warns young men not to leave home for dreams of wealth in distant ports, notes archaeologist Veerasamy Selvakumar of Tamil University in Thanjavur. That's a sign of societal stress as people shifted from traditional farming and fishing to mercantile pursuits, he says. Later inscriptions and stone carvings suggest that ship owners grew into an influential and wealthy class, according to archaeologist Pierre-Yves Manguin of the National University of Singapore. A Javanese shipmaster, for example, served as ambassador from a Javanese kingdom to the Chinese court in 993 C.E. "They played a big role as cultural diplomats and in propagating" faiths like Buddhism and Islam, Manguin says.

The tales of Sinbad reflect this status. In his final voyage, the Iraqi-born merchant acts as a diplomat for the Baghdad caliph, carrying precious gifts to a distant ruler and earning the caliph's gratitude.

By 1400 C.E., the geopolitical dynamics in the Indian Ocean began to change as Chinese and European consumers tired of buying expensive foreign goods through Arab, Indian, and Southeast Asian middlemen. Fleets of massive Chinese ships, some carrying 500 people, cruised as far west as Arabia and Africa, rattling the locals (*Science,* 9 May, p. 572).

Less than a century later, Europeans followed suit, mastering the trip around Africa. Over the succeeding centuries, the Indian Ocean trade fractured into more local exchange as the Portuguese, French, Dutch, and British, equipped with better military technology than the regional powers, carved up the waters well into the 20th century. Today, however, the ocean is humming with international trade again; two-thirds of the world's trade goods move through it.

Sinbad retired comfortably to Baghdad after his seventh voyage, pledging never to set foot on a ship again. Archaeologists, however, are only at the beginning of their effort to recover the long-lost chronicle of the Indian Ocean. "We are rewriting history," Wood says. ■

Published by AAAS

Making water treatment more sustainable *p. 1452*

DNA monitoring for environmental policy *p. 1455*

PERSPECTIVES

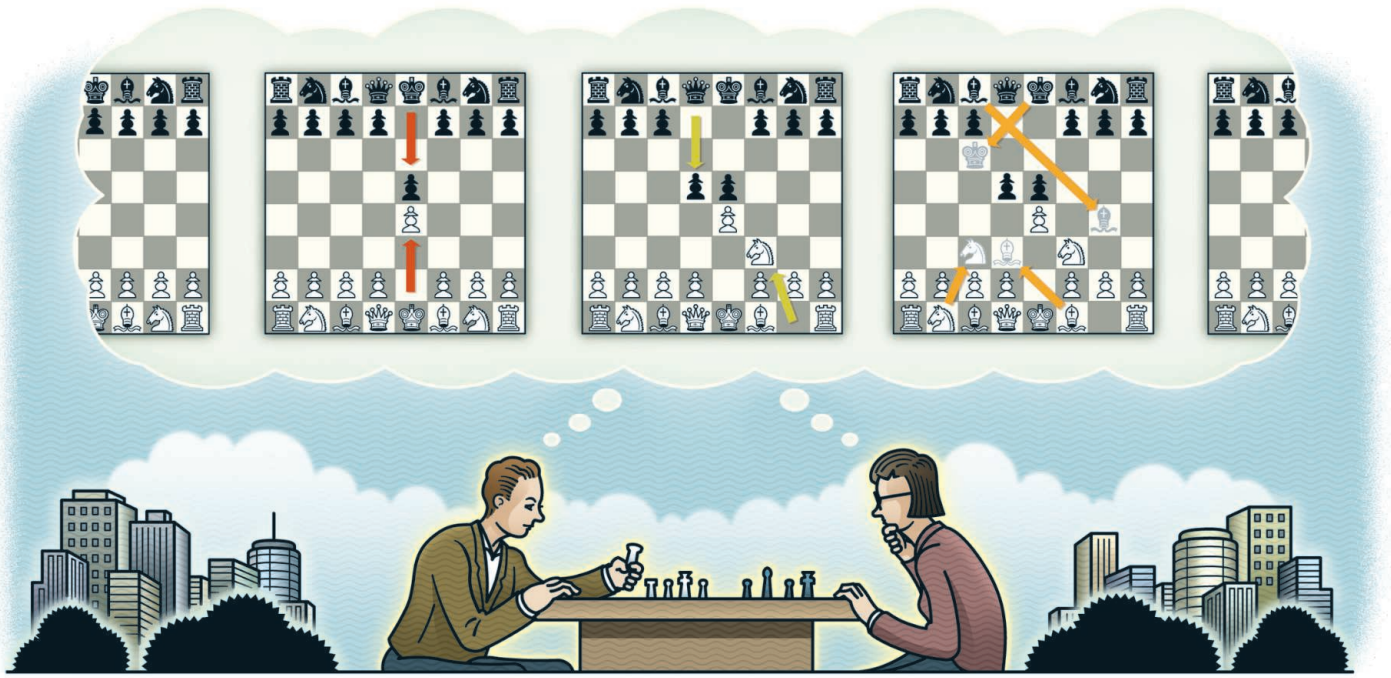

Decisions and outcomes. Reasoning in an uncertain environment is reflected in the game of chess. An individual may plan two to three different moves while also considering the opponent's possible responses to each of those moves, and then further plan counteractions to each one of those responses.

NEUROSCIENCE

Exploiting and exploring the options

How does the human brain reason when to change strategies?

By **Todd Hare**

In an ever-changing world, the brain must continually formulate, monitor, and adapt patterns of behavior to achieve the best outcome. Often, strategies that we have employed in the past to solve a problem or reach a specific result will work again when we are confronted with a similar situation. When this is the case, we can exploit such strategies for maximal gain. However, if important aspects of the environment or context have changed, we need to modify our behavior and explore new action strategies. How does the brain monitor and adapt our behavior or create altogether new strategies? On page 1481 of this issue, Donoso *et al.* (*1*) provide key algorithmic and neurobiological insights into how the human brain accomplishes such feats.

Inferring the best response from a large range of possible actions frequently involves difficult computations that the brain is unlikely to perform rapidly (*2*). Nevertheless, humans often do well in such situations. Donoso *et al.* demonstrate that a computational model designed to integrate reward learning with probabilistic inference (i.e., computing the odds) and a form of hypothesis testing can approximate the optimal solution in a neurobiologically plausible manner. Moreover, the model provides a good fit to human behavior and, as seen by functional magnetic resonance imaging (fMRI), is represented in the activity patterns of specific prefrontal and striatal brain regions.

Reward learning algorithms update our expectations about the benefits resulting from a stimulus or action. They do so on the basis of prediction error signals that quantify the mismatch between predictions and reality. These algorithms have been used in machine learning applications and in explaining many aspects of human and animal behavior (*3*). Furthermore, prediction error

SNS Lab, University of Zurich, Zurich, Switzerland. E-mail: todd.hare@econ.uzh.ch

ILLUSTRATION: PETER AND MARIA HOEY/WWW.PETERHOEY.COM

Published by AAAS

signals have been linked to dopamine neurons that are located in the midbrain and project to striatal and prefrontal learning and decision areas (*4*). These signals are present not only for executed actions, but also for alternative actions (*5*), suggesting that the brain can track the benefits of multiple action strategies concurrently (see the cartoon). When a decision is made, activity in regions of medial prefrontal cortex increases in proportion to the expected gains from chosen actions (*6*), whereas activity in more lateral regions of frontopolar cortex increases with the potential gains from possible alternative actions (*7*). This indicates that predictions over all monitored options are available to drive choices. Because the brain has a finite working memory capacity, there is a limit to the number of strategies or potential actions it can monitor at the same time (*8*). Also, reward learning algorithms do not provide any mechanism for determining when and how to formulate new strategies if none of the current options are acceptable.

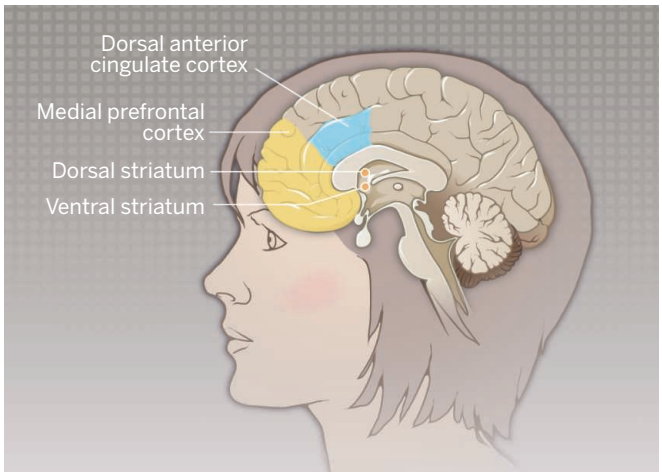

Reasoning regions. Activity in specific brain regions tracks the reliability of executed strategies (medial prefrontal cortex), alternative strategies (frontopolar cortex, not shown), the need to explore new strategies (dorsal anterior cingulate cortex), and the confimation of strategies as valid (ventral striatum).

The model of Donoso *et al.* combines aspects of reward learning algorithms with features designed to detect when to switch from exploiting current strategies to exploring new options by implementing a form of hypothesis testing pertaining to patterns of behavior and outcomes. Predictions derived from a hypothesis are tested against actual measurements, and then either maintained, revised, or rejected in light of the correspondence between the predictions and the measured data. Donoso *et al.* reveal that there is a similar process at work when we decide how to act in uncertain, variable environments. They studied the behavior and brain activity of participants who were trying to identify patterns as they were asked to link a number displayed on a screen to one of four possible buttons to press. Correct button presses earned monetary rewards. However, without warning, the experimenter would change what the correct button press should be, and participants had to update their associations between numbers and buttons on the basis of correct/incorrect feedback (i.e., by trial and error). These unannounced changes in the patterns are analogous to changes in the environment or state of the world that we may or may not be aware of. In the experimental setting of Donoso *et al.*, a participant might form a belief about the pattern based on previous trials, but the feedback on subsequent responses may cause the person to modify or reject his/her current hypothesis about the pattern. Further exploration and testing then proceeds until the participant finds an appropriate strategy.

If the brain implements such a model, then underlying model components such as value, hypothesis testing, rejection, and confirmation signals should be reflected in the brain's neural activity. The patterns of behavior observed by Donoso *et al.* suggest that participants actively monitored the currently executed strategy as well as two or three alternative strategies. Value signals for executed and alternative actions previously identified in the medial prefrontal and frontopolar cortex (*6*, *7*), respectively, were also noted by Donoso *et al.* (see the figure). In addition, activity in the dorsal anterior cingulate cortex and dorsal striatum increased when participants determined that no currently monitored strategies were valid and switched to exploring new cue-response patterns. These anterior cingulate signals are similar to those recorded in the anterior cingulate of rhesus macaques when they switched to a new reward patch in a laboratory foraging paradigm (*9*) and are consistent with the role of this brain region in monitoring the need to adjust or control behavior (*10*). Donoso *et al.* also observed neural signals in prefrontal and ventral striatal regions for events predicted by their model, including the rejection of previously executed strategies in favor of alternatives held in working memory, and confirmation of new patterns as valid strategies.

The links between model components and brain activity highlight a key advantage of incorporating mathematical modeling into behavioral and neuroscience research. Such modeling efforts permit the identification and testing of subjective beliefs and reasoning states that the experimenter could not otherwise observe. For example, without their algorithm, Donoso *et al.* would not have known precisely when participants rejected previously executed strategies, switched to exploratory states, or confirmed a strategy as valid. Although these events are all associated with changes in the cue-response mappings that are controlled by the experimenters, the point in time when participants realize these changes and adapt, their behavior varies as a function of trial sequence and individual differences. Without this timing information, it would not have been possible to link these reasoning states to activity in specific brain regions. Thus, not only does modeling help to formalize concepts, it also provides a means to identify and test specific aspects of reasoning and neurobiology.

One important aspect of the model of Donoso *et al.* is that it explains reasoning and behavior in cases for which one action is correct because it yields the desired outcome more often than deciding by chance (e.g., flipping a coin), and all other actions are no better than chance (i.e., incorrect). However, there are situations in which several actions could be considered correct because they all achieve the desired goal. A person seeking to make money might consider investing in one of two stocks (A, B), ultimately deciding to choose stock A. One month later, the price of stock A has risen by 15% and stock B is up by 20%. Choosing stock A achieved the goal of making money, but stock B would have made more. How then, does one decide to invest this month's excess earnings? It is possible to adapt the comparison criteria in the model of Donoso *et al.* to account for such cases, but such adaptations raise the question of how and when the brain sets comparison criteria for different decisions. Such questions represent likely aims of future work that build on this promising advance in understanding decision-making in uncertain and ever-changing environments. ■

ILLUSTRATION: ADAPTED FROM YANA HAMMOND

REFERENCES

1. M. Donoso *et al.*, *Science* **344**, 1481 (2014).
2. A. Collins, E. Koechlin, *PLOS Biol.* **10**, e1001293 (2012).
3. P. Dayan, Y. Niv, *Curr. Opin. Neurobiol.* **18**, 185 (2008).
4. W. Schultz, *Curr. Opin. Neurobiol.* **23**, 229 (2013).
5. T. Lohrenz, K. McCabe, C. F. Camerer, P. R. Montague, *Proc. Natl. Acad. Sci. U.S.A.* **104**, 9493 (2007).
6. O. Bartra *et al.*, *Neuroimage* **76**, 412 (2013).
7. E. D. Boorman *et al.*, *Neuron* **62**, 733 (2009).
8. N. Cowan, in *Human Learning and Memory: Advances in Theory and Applications*, C. Izawa, N. Ohta, Eds. (Erlbaum, Mahway, NJ, 2005), pp. 155–175.
9. B. Y. Hayde *et al.*, *Nat. Neurosci.* **14**, 933 (2011).
10. A. Shenhav *et al.*, *Neuron* **79**, 217 (2013).

10.1126/science.1256862

Published by AAAS

GENETICS

Predicting microbial growth

Integration of a plethora of genomic and biochemical data enables large-scale prediction of cellular functions

By **Jonathan Monk** *and* **Bernhard O. Palsson**

Cellular functions result from biochemical interactions among thousands of components within the cell. The growing availability of annotated genome sequences and a plethora of biochemical data allow these interactions to be assembled on a genome scale for model microorganisms. This detailed biochemical information can be converted into a computational model—a genome-scale model, or GEM (*1*)—that allows phenotypic functions to be predicted. Both environmental and genetic parameters are explicitly accounted for in GEMs, enabling increasingly accurate predictions of the genotype-phenotype relationship in a given environment.

The basis for a GEM is a quality-controlled reconstruction of the biochemical reaction networks that the organism's functions are based on. In a given environment where the nutritional inputs are defined, GEMs can be used to compute a phenotype. For example, the growth of a cell requires about 60 to 70 different metabolites (*2*). A GEM can compute a path from the available nutrients through the reaction network (or reactome) to each metabolite. It can also compute the balanced use of the reactome to form all metabolites simultaneously and in the correct relative amounts while accounting for the energetic, redox, and chemical interactions that must be balanced to enable growth.

Any such genome-scale accounting exercise is predicated on an accurate reconstruction of the reactome (*3*). Here, we focus on the prediction of possible cellular growth states, the power of this capability, and the implications of scaling up the number of such predictions. Similar considerations apply to other measureable phenotypes that are computable.

The simplicity of computing growth states as a function of nutritional inputs with the selective removal of genes has led to a number of studies that cross environmental parameters with gene deletions. This explicit relationship between a gene and a reaction makes the deletion of genes and their encoding reactions straightforward. Growth screens where the environment is crossed with a gene deletion have been performed with target organisms for which gene knockout strain collections exist, such as *Escherichia coli* (*4*), *Saccharomyces cerevisiae* (*5*), and *Bacillus subtilis* (*6*). GEMs can compute the outputs of such experiments, allowing prediction of growth based on biochemical mechanisms.

The number of phenotypic predictions with experimental validation from growth screens has grown steadily over the past 15 years (see the figure). The initial comparisons included less than 100 predictions, whereas the more recent ones exceed 100,000 predictions. How accurate are the predictions?

Computational predictions of outcomes fall into four categories: true positive, true negative, false positive, and false negative. For instance, a true positive is the prediction of growth and experimental measurement of growth. In contrast, a false positive is the prediction of growth and experimental measurement of no growth.

The accuracy of true-positive and true-negative predictions generally exceeds 80% to 90% for the organisms examined. For double knockouts, true-negative predictions are particularly important because they show that models can predict true genetic interactions. Highly curated models can predict up to 50% of true-negative cases. The missed predictions represent cases that are currently difficult for functional genomicists to understand (*7*).

False-negative predictions occur when a GEM predicts no growth, but the experiment results in growth. This discrepancy indicates that the reconstructed reactome is incomplete. In contrast, false-positive predictions occur when a GEM predicts growth but the experiment results in no growth. This difference indicates possible errors in the data that the reactome was based on, or a missing regulatory process; for example, regulation that prevents the function of an enzyme used in the GEM to compute the predicted growth state.

Reconciling such discrepancies between predicted and observed growth states provides an opportunity for biological discovery. Algorithms have been developed to compute the most likely reasons for failure of prediction, enabling model-guided experimental inquiry and discovery (*8*). This approach has, for example, led to the discovery of two new reactions carried out by the classical enzymes phosphofructokinase and aldolase

Department of Bioengineering, University of California, San Diego, CA 92093–0412, USA. E-mail: palsson@ucsd.edu

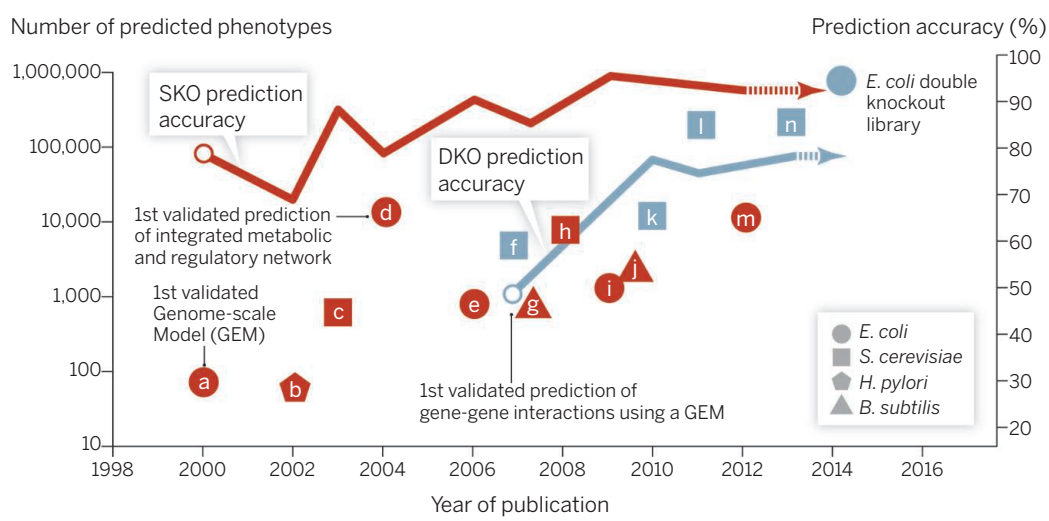

Predicting experimental outcomes of cellular growth screens. The number of predictions made on growth screens that cross environmental conditions with gene knockouts has grown steadily over the past 15 years. Over this time, both single-gene knockout (SKO) predictions (red line) and double-gene knockout (DKO) predictions (blue line) have become increasingly accurate. For a full list of references for these studies, see the supplementary materials.

Published by AAAS

in *E.* coli (*9*). Similarly, analysis of synthetic lethal screens in yeast led to corrections of the pathways leading to NAD synthesis (*7*). Also, reconciliation of prediction failure led to the description of gluconate kinase in human cells (*10*). Many false predictions can be resolved by fixing relatively few components in a model's reactome. For example, a recent study was able to reconcile 2442 false model predictions from the *E. coli* GEM by updating the function of just 12 genes (*11*).

A GEM thus provides a platform not only for formalizing and solidifying the understanding of a target organism but also for the systematic discovery of its missing parts and functions. Double-knockout collections being produced for *E. coli* (where highly quantitative measurements under defined growth conditions can be obtained) should lead to millions of possible growth predictions in just a few years. Such experiments and computational predictions would enable large-scale predictions of gene-gene interactions.

If such efforts for model organisms are successful and genetic manipulation techniques for less-characterized organisms become readily available, then we can foresee a massive scale-up in phenotypic predictions for a spectrum of organisms. For instance, experimentally constructed transposon libraries with sequencing (TnSeq) can now be used to examine the effect of gene knockouts in different environments for organisms with little to no existing biochemical data (*12*). A draft GEM for such an organism can thus be improved quickly using the same algorithms that reconcile the differences between predicted and observed growth states mentioned above. Such developments would hopefully make the fundamental underpinnings of microbial physiology as solid as our understanding of microbial genomics has become over the past 15 years. By strategically choosing target organisms from across the phylogenetic tree, this approach would allow the comprehensive discovery of the metabolic processes used by the many diverse organisms on our planet. ■

REFERENCES

1. A. Bordbar *et al.*, *Nat. Rev. Genet.* **15**, 107 (2014).
2. A. M. Feist, B. O. Palsson, *Curr. Opin. Microbiol.* **13**, 344 (2010).
3. J. Monk *et al.*, *Nat. Biotechnol.* **32**, 447 (2014).
4. T. Baba *et al.*, *Mol. Syst. Biol.* **2**, 2006.0008 (2006).
5. M. Costanzo *et al.*, *Science* **327**, 425 (2010).
6. K. Kobayashi *et al.*, *Proc. Natl. Acad. Sci. U.S.A.* **100**, 4678 (2003).
7. B. Szappanos *et al.*, *Nat. Genet.* **43**, 656 (2011).
8. J. D. Orth, B. Ø. Palsson, *Biotechnol. Bioeng.* **107**, 403 (2010).
9. K. Nakahigashi *et al.*, *Mol. Syst. Biol.* **5**, 306 (2009).
10. Ó. Rolfsson *et al.*, *Biochem. J.* **449**, 427 (2013).
11. D. Barua *et al.*, *PLOS Comput. Biol.* **6**, e1000970 (2010).
12. A. Deutschbauer *et al.*, *PLOS Genet.* **7**, e1002385 (2011).

SUPPLEMENTARY MATERIALS

www.sciencemag.org/content/344/6191/1448/suppl/DC1
References for figure

10.1126/science.1253388

ANGIOGENESIS

Targeting vascular sprouts

Manipulating metabolism could control angiogenesis

By **Lee B. Rivera** *and* **Gabriele Bergers**

Angiogenesis, the formation of new blood vessels, has long been recognized as a hallmark of cancer (*1*). Its functional importance for the manifestation and progression of tumors has been validated by the therapeutic effects of angiogenesis inhibitors. However, the overall effectiveness of several approved therapies that target the proangiogenic pathways controlled by vascular endothelial growth factor (VEGF) have had rather modest and transient effects in the clinic (*2*). This is because tumors can activate alternative pathways to adapt to vascular growth restrictions. Emerging evidence (*3*–*5*) indicates that targeting metabolic pathways in blood vessel endothelial cells may be a new and promising strategy because metabolism in these cells not only fuels vascular expansion, but also regulates the very formation of blood vessels.

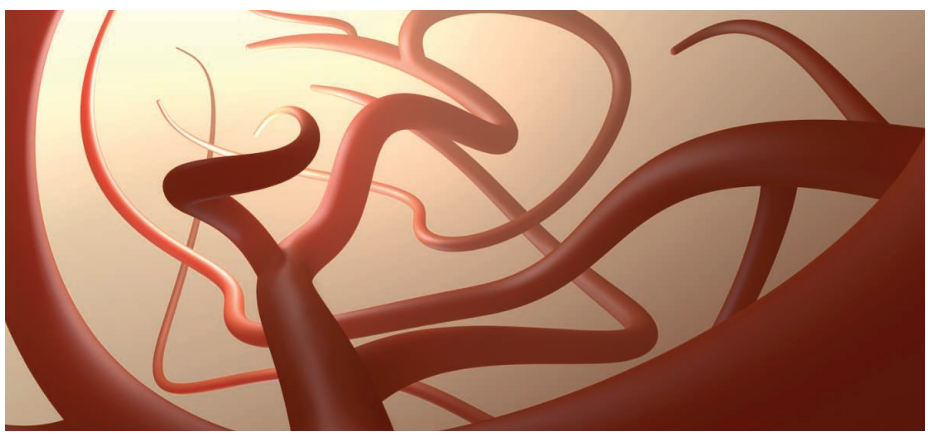

Endothelial cells that form the inner lining of blood vessels are in general quiescent in the adult but have to quickly become activated to form new vascular branches during normal physiological processes or upon injury. Much effort has been devoted to understanding the molecules that regulate the multiple steps of vessel formation, but how metabolic regulation in endothelial cells affects angiogenesis has remained largely unexplored. Glycolysis apparently provides the necessary energy for endothelial cells to switch from quiescence to angiogenesis, and in addition, directly controls several aspects of vascular sprouting (*3*). This metabolic pathway is much less efficient than oxidative phosphorylation, yet, surprisingly, endothelial cells rarely use the latter process (*6*, *7*), even when they proliferate and migrate to form new sprouts (*3*). Why would these cells choose an inefficient process to produce sufficient energy?

During glycolysis, glucose is metabolized to pyruvate, which is then either converted to lactate, yielding two molecules of adenosine 5′-triphosphate (ATP), or, in the presence of oxygen, fully oxidized in mitochondria to produce 36 ATP molecules. Therefore, it might be expected that endothelial cells would favor pyruvate oxidation as they have immediate access to oxygen in blood. But consider that the main purpose of neovascularization is to oxygenate areas that suffer from oxygen deprivation. If endothelial cells relied on pyruvate oxidation, they would deplete oxygen from the blood and thereby reduce the amount of oxygen available to diffuse into the surrounding hypoxic tissue.

De Bock *et al.* (*3*) investigated whether glycolysis not only fuels vessel growth but somehow regulates it. The study identified 6-phosphofructo-2-kinase/fructose-2,6-biphosphatase 3 (PFKFB3; also called PFK2) as the most abundantly expressed glycolytic enzyme in endothelial cells. PFKFB3 converts fructose-6-phosphate to fructose-2,6 bisphosphate, an allosteric activator of phosphofructokinase-1 (PFK-1). Therefore, inhibition of PFKFB3 led to only a partial reduction in glycolytic flux and resulted in cell quiescence. This is in contrast to other approaches for targeting glycolysis that

Department of Neurological Surgery, Brain Tumor Research Center, Helen Diller Family Comprehensive Cancer Center, University of California, San Francisco, San Francisco, CA 94158, USA. E-mail: gabriele.bergers@ucsf.edu

ILLUSTRATION: V. ALTOUNIAN/*SCIENCE*

Published by AAAS

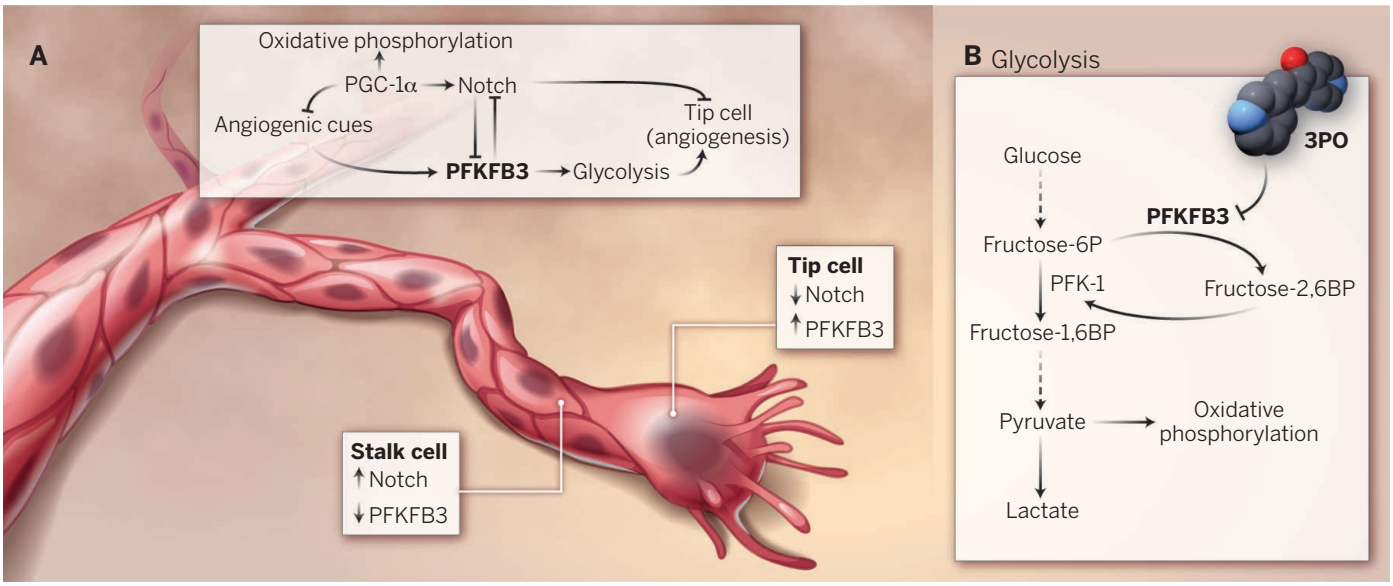

Metabolism regulates neovascularization. (**A**) The glycolysis enzyme PFKFB3, transcriptional coregulator PGC-1α, and the signaling protein Notch control metabolism and the formation of tip cells or stalk cells. Small molecules that induce PGC-1α expression have been identified but not tested for their capacity to inhibit angiogenesis. (**B**) The small molecule 3PO inhibits formation of angiogenic sprouts by blocking PFKFB3 activity. P (phosphate), BP (bisphosphate).

completely shut down the process and result in cell death (*8*).

Vascular sprouting is a dynamic process involving distinct types of endothelial cells. A tip cell that bears extending filipodia moves at the front of a sprouting vessel and is followed by proliferating stalk cells that elongate the sprout (*9*, *10*). VEGF activates tip cells, whereas the signaling protein Notch suppresses them and stimulates stalk cells (see the figure). Not only is PFKFB3 required for tip cell formation, it can override the ability of Notch to promote stalk cell behavior (*3*). Interestingly, although sprout-inducing signals like VEGF and fibroblast growth factor can induce PFKFB3 expression, glycolysis has no effect on signaling by VEGF receptor 2, suggesting growth factor signaling and glycolysis promote tip cell function independently. Yet another reason why endothelial cells favor glycolysis is that glycolytic enzymes are selectively compartmentalized within tip cell filipodia (*3*). Thus, tip cell protrusions extending into areas of low oxygen tension can rapidly generate local ATP for use in processes with high energy demand such as the assembly of cytoskeletal actin filaments.

In line with these findings, Sawada *et al.* (*5*) recently discovered a metabolic regulator in endothelial cells that blocks angiogenesis by inducing Notch activity while impeding angiogenic signaling. Peroxisome proliferator-activated receptor gamma coactivator 1–α (PGC-1α) is a transcriptional coactivator involved in mitochondrial biogenesis and activity, and it is highly expressed in endothelial cells of diabetic patients and mice. In contrast to the Notch-inhibitory effect exerted by PFKFB3, PGC-1α induced Notch activation, thereby presumably blocking sprout formation and, hence, promoting the stalk phenotype. Furthermore, PGC-1α blunted angiogenic signaling. Thus, PGC-1α activation may represent an additional metabolic approach to block pathologically angiogenic diseases.

Molecules that have the capacity to induce PGC-1α expression have already been identified in genetic screens and include microtubule inhibitors and agents that block protein synthesis (*11*). Importantly, these molecules can activate PGC-1α–mediated oxidative phosphorylation; however, whether or not pharmacological induction of PGC-1α expression can suppress angiogenesis has not been tested. Nevertheless, recent proof-of-principle experiments support the idea of targeting endothelial cell glycolysis to treat disease-associated angiogenesis. Schoors *et al.* (*4*) used the small molecule 3-(3-pyridinyl)-1-(4-pyridinyl)-2-propen-1-one (3PO) to block PFKFB3 and test this notion in preclinical models of psoriasis and colitis, where it successfully blocked angiogenesis. These inflammatory disorders are exacerbated by angiogenesis. Interestingly, targeting PFKFB3 also enhanced the efficacy of VEGF-pathway inhibitors in animal models of macular degeneration and retinopathy, two conditions in which angiogenesis causes the disease. Inadequate blockade of angiogenesis by VEGF-pathway inhibitors may be due to glycolysis that parallels VEGF signaling to drive neovascularization.

It will be very interesting to see whether blocking PFKFB3-driven glycolysis or activation of PGC-1α expression could represent a new opportunity to improve anti-angiogenic therapy in cancer (*2*). Importantly, inhibition of PFKFB3 or induction of PGC-1α expression skews the vasculature toward a homeostatic state; therefore, the manipulation of either factor affects endothelial cells only in the context of angiogenesis, leaving the quiescent vasculature unperturbed. Furthermore, tumor cells, like endothelial cells, favor glycolysis in the so-called Warburg effect, for a number of proposed reasons, from adapting to low-oxygen environments within tumors to shutting down mitochondria and its associated programmed cell death mechanism that would kill cancerous cells. Recent studies have identified targets to block tumor glycolysis with very promising results, but it remains to be determined whether such results are due to effects solely in tumor cells or if effects in the tumor vasculature are actually contributing factors (*12*). ■

REFERENCES

1. D. Hanahan, R. A. Weinberg, *Cell* **100**, 57 (2000).
2. G. Bergers, D. Hanahan, *Nat. Rev. Cancer* **8**, 592 (2008).
3. K. De Bock *et al.*, *Cell* **154**, 651 (2013).
4. S. Schoors *et al.*, *Cell Metab.* **19**, 37 (2014).
5. N. Sawada *et al.*, *Cell Metab.* **19**, 246 (2014).
6. A. Dobrina, F. Rossi, *Biochim. Biophys. Acta* **762**, 295 (1983).
7. A. Krützfeldt, R. Spahr, S. Mertens, B. Siegmund, H. M. Piper, *J. Mol. Cell. Cardiol.* **22**, 1393 (1990).
8. C. Granchi, F. Minutolo, *ChemMedChem* **7**, 1318 (2012).
9. P. Carmeliet, R. K. Jain, *Nature* **473**, 298 (2011).
10. R. Blanco, H. Gerhardt, *Cold Spring Harbor Perspectives in Medicine* **3**, a006569 (2013).
11. Z. Arany *et al.*, *Proc. Natl. Acad. Sci. U.S.A.* **105**, 4721 (2008).
12. F. L. Muller *et al.*, *Nature* **488**, 337 (2012).

10.1126/science.1257071

ILLUSTRATION: V. ALTOUNIAN/*SCIENCE*

Published by AAAS

MATERIALS SCIENCE

Phase-transforming electrodes

Structural studies suggest a route to improve the performance of rechargeable batteries

By **John Owen** *and* **Andrew Hector**

Lithium iron phosphate ($LiFePO_4$) is one of the cheapest and safest materials used as the positive electrode of the lithium ion battery. Since its discovery in 1996 (*1*), the material has been a subject of debate regarding its outstanding performance in high-rate discharge-charge cycling applications. The surprisingly high performance is attained despite the miscibility gap (the composition range at which solutions become supersaturated and tend to separate into concentrated and dilute phases—like clear honey that partially crystallizes in the refrigerator) and phase transformation that complicates lithium insertion and extraction in this material. Such properties are typically associated with slow rates of electrical charge and discharge and even structural damage during cycling. On page 1480 of this issue, Liu *et al.* (*2*) provide experimental evidence to support new theoretical models (*3*, *4*) that bypass the miscibility gap so that the phase transformation need not happen after all.

$LiFePO_4$ was first described as a material for low-power batteries because it is virtually an electrical insulator in its pristine form. Several years of research followed to speed up the delivery of charge into $LiFePO_4$ particles: carbon coatings (*5*), other coatings, or dopants were added to assist electron transport; likewise, optimized electrolyte conductance in the composite electrode structure facilitated ion transport (*6*), and the particles themselves were reduced to nanometer size to minimize the distance from the surface to the center of each particle. The result was a material that could discharge its stored electrical energy in just a few seconds.

The problem lies in understanding the discharging mechanism. Conventional theories describe the discharge process as a nucleation and growth of an almost pure $LiFePO_4$ phase into an almost unchanged $FePO_4$ initial phase, with an interfacial phase boundary moving with time. This is the conclusion of equilibrium thermodynamics, which dictates that only the lowest-energy states—that is, solid solutions outside the miscibility gap—should exist. Nonequilibrium thermodynamics allows for metastable states but predicts the nucleation and growth of stable phases, driven by a supersaturation caused by the overpotential applied during battery cycling. Furthermore, beyond the points of inflection in the free energy–composition profile (see the figure), nucleation and growth by spinodal (the rapid unmixing of a mixture of liquids or solids) disproportionation of phases would be spontaneous (*7*).

Although evidence for coexisting phases has been found to explain the slow discharge of large particles, it is difficult to obtain in nanoparticles, where different mechanisms could apply. Liu *et al.* report x-ray diffraction data indicative of a continuum of metastable compositions with structures intermediate between those of the two end phases: effectively single-phase behavior with a lattice parameter that varies according to Vegard's law (the observed linear relationship between the crystal lattice parameter and the relative concentration of constituent atoms in a solid solution).

Lithium extraction or insertion is usually observed as the growth of diffraction peaks of one phase while those corresponding to the other diminish. In true two-phase behavior, these peaks would retain their normal symmetric shapes. Liu *et al.* observed that the diffraction peaks of $LiFePO_4$ became asymmetric, with a distortion toward the position of the $FePO_4$ peaks as they grew in. This is consistent with a solid solution between the two phases (i.e., a $Li_{1-x}FePO_4$ composition). Extended solutions were observed even in the absence of the second phase, confirming that these observations are not due solely to mechanical strain caused by a coherent interface.

In powder diffraction, peak shape is affected by factors that include the instrumental resolution and geometry, crystallite size, and strain (lattice parameter variation). The x-ray diffraction data presented by Liu *et al.* could be fitted by using a microstrain-like broadening term to model the distribution of lattice parameters, allowing them to extract the variations and distributions of cell parameters during cycling. As further proof of the model, a fit to their data with a series of phases with symmetrical peaks required at least 10 phases to be present; that is, this was a genuine solid solution. Finally, Liu *et al.* also simulated the effect of a $LiFePO_4$-$FePO_4$ phase boundary within a single particle, as required by a nucleation and growth model,

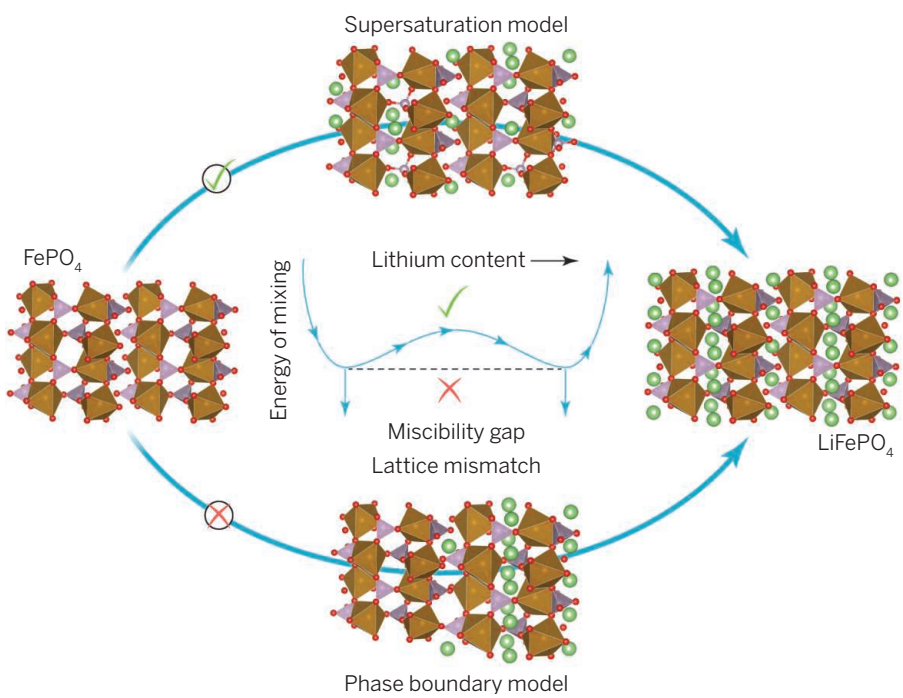

Charging through change. Schematic pathways for the discharge of $FePO_4$ (left) to form $LiFePO_4$ (right). The upper path and upper curve (center) show the high-energy path via a continuous solid solution that is confirmed by these structural studies. The lower path, predicted by equilibrium thermodynamics, requires less energy but involves a phase boundary and lattice mismatch.

Chemistry Department, University of Southampton, Highfield, Southampton SO17 1BJ, UK. E-mail: j.r.owen@soton.ac.uk

Published by AAAS

and the observed anisotropy could only be modeled if that boundary extended to the size of the crystallites.

Liu *et al.* therefore provide evidence that disproportionation is not the dominant mechanism during fast cycling of nanosized $LiFePO_4$. Instead, a metastable nonstoichiometric phase exists throughout the transition state accessed via the applied overpotential. Hence, instead of a local phase change, involving a progressive structural reorganization near a moving phase boundary, there exists a cooperative structural rearrangement across a wide region of compositional variation as the structure changes continuously from one form to the other with only a small degree of lattice strain. The latter fact explains why it is fast and reversible for thousands of cycles.

The above model seems reasonable; instead of a phase boundary, there are continuous variations in both the lithium concentration and the chemical potential (energy) of lithium in a one-phase material, as observed for normal electrodes. One problem remains: The spinodal region near the energy maximum still exists and can cause havoc—the diffusion coefficient can become negative, promoting rapid diffusion up concentration gradients and thereby forcing disproportionation. Maybe this effect is too weak or too slow to make a difference. However, there is another stabilizing influence, which is that the moving species is a charged lithium ion; as a result, the electric potential, which increases with the current during discharge, adds another energy term to the equation (*4*). If the current is high enough, the miscibility gap, spinodal region, and anomalous diffusion effect all vanish and the behavior returns to normal as for a non–phase-transforming electrode.

The value of the discovery by Liu *et al.* lies not only in the already optimized $LiFePO_4$ but also in the prediction of how it can be used to make better materials. The hope is that the single-phase transformation pathway can be enabled in other phase-transforming electrode materials with high energy density, to reap the associated benefits of higher power and longer cycle life. ■

REFERENCES

1. A. K. Padhi, K. S. Nanjundaswamy, J. B. Goodenough, *J. Electrochem. Soc.* **144**, 1188 (1997).
2. H. Liu *et al.*, *Science* **344**, 1252817 (2014); 10.1126/science.1252817.
3. R. Malik, F. Zhou, G. Ceder, *Nat. Mater.* **10**, 587 (2011).
4. P. Bai, D. A. Cogswell, M. Z. Bazant, *Nano Lett.* **11**, 4890 (2011).
5. N. Ravet *et al.*, *J. Power Sources* **97-98**, 503 (2001).
6. P. A. Johns, M. R. Roberts, Y. Wakizaka, J. H. Sanders, J. R. Owen, *Electrochem. Commun.* **11**, 2089 (2009).
7. J. W. Cahn, J. E. Hilliard, *J. Chem. Phys.* **28**, 258 (1958).

10.1126/science.1255819

WATER TREATMENT

Anticipating the next century of wastewater treatment

Advances in activated sludge sewage treatment can improve its energy use and resource recovery

By **Mark C. M. van Loosdrecht**[1] *and* **Damir Brdjanovic**[1,2]

Rapid urbanization and industrialization in the 19th century led to unhealthy environments and widespread epidemic diseases. In response, research was undertaken that led to the development of sanitation technology. Exactly 100 years since the activated sludge process was presented (*1*), it is still at the heart of current sewage treatment technology. Activated sludge is a mixture of inert solids from sewage combined with a microbial population growing on the biodegradable substrates present in the sewage. The settling and recycling of sludge inside treatment plants was the invention of Ardern and Lockett. The current demands from a rapidly growing human population and the need for a more sustainable society are pushing forward new developments for sewage handling. These developments have two main drivers: general process improvements and the contribution to the recycling of resources (*2*, *3*).

The activated sludge process, combined with a better drinking water supply, was the main factor behind the increase in average life span in the previous century and for minimizing the environmental impact of human activities. Wastewater treatment is in itself a relatively low-cost process (in the Netherlands, 50 to 70 EUR per person per year), consuming limited energy (<7 W per person); its main limitations are the large upfront investment costs (usually to be recovered from inhabitants within 20 years) and land area requirements (mainly needed for the gravity-based separation of flocculent activated sludge and treated wastewater). Attempts to intensify the separation process, e.g., by membrane separation of the sludge, have been technologically successful (*4*) but not widely used because of the additional energy demand and capital costs.

The morphogenesis of the microbial communities in activated sludge is a complex process based on the interaction of microbiological, chemical, and physical processes (*5*). Only in recent years has it become possible to engineer these microbial structures to allow bacteria to form a stable granular sludge instead of flocculent sludge (see the first figure) (*6*). This form of sludge makes gravity-based separation a compact process that can be integrated inside the treatment reactor and greatly reduces area requirements and costs (by roughly 75 and 25%, respectively) (*7*).

Activated sludge technology is based on a complex microbial ecology process, in

100 years of activated sludge—quo vadis?
Two reactors at the wastewater treatment plant Garmerwolde in the Netherlands (**A**) using aerobic granular sludge technology (**B**) are treating the wastewater of 235,000 persons.

Published by AAAS

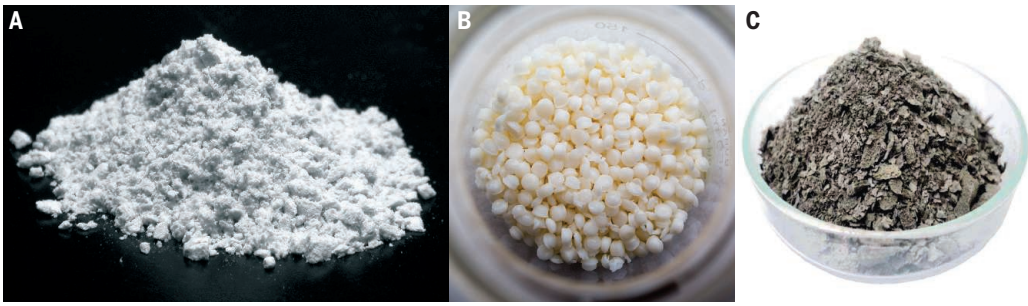

Struvite (**A**), polyhydroxyalkanonate bioplastic (**B**), and alginate biopolymers (**C**) are examples of recycled materials produced by wastewater treatment.

which sewage and microorganisms are recycled to different tanks with different redox conditions. Modern genomic tools (*8*) are improving the understanding of interactions among organic carbon-, nitrogen-, and phosphate-converting bacteria and have led to better process designs. Moreover, in granular sludge technology, these activities have been integrated inside the granules. With the different redox conditions present inside the granule, the transport of compounds occurs by diffusion, replacing transport by the pumping of sewage and activated sludge between different reactor compartments, thus minimizing energy needs.

Sewage treatment by activated sludge is a technology that allows for closing cycles and reuse of resources such as water (*3*), energy (*9*), and chemicals (*2*). With an increasing global population demanding more resources, this aspect is becoming even more important. Effective sewage treatment makes the recovery of water by the use of membrane technology feasible. Furthermore, water stress can be minimized by the use of alternative water sources, e.g., by using harvested rainwater or seawater for toilet flushing (*10*). Energy generation in the form of biogas produced from the sludge has been practiced since the early days of the activated sludge process. In the 1970s, a high-rate, two-stage activated sludge process was developed that maximized energy recovery in the form of biogas, but because of the need for organic carbon, the interest in this process ceased. With the recent advance of Anammox technology, a net energy-producing treatment plant, including effective nutrient removal, is becoming feasible (*11*).

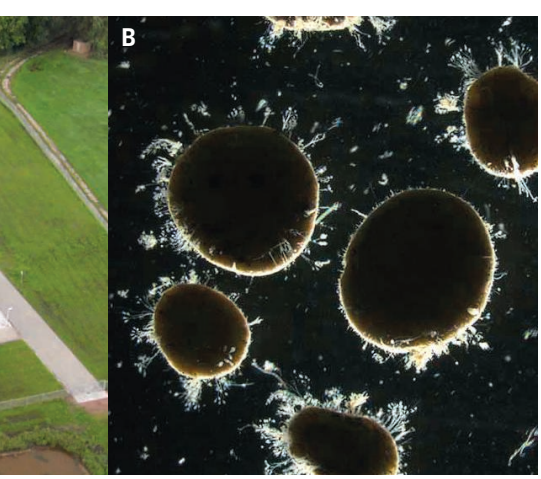

Although the recuperation and production of energy at sewage works is currently getting most attention, the resource recovery from wastewater and sludge should not be overlooked. It is even more important with respect to developing a more sustainable society. Phosphate recovery from sewage is increasingly being used, and other options for the production of valuable materials from sludge are also emerging, e.g., the recovery of cellulose fibers (*12*) and the production of bioplastics (*2*) and biopolymers (*13*). The initial results show that valuable products can be produced in quantities and at costs that match the current market demand and prices (see the second figure).

In contrast to high-income industrialized countries, where coverage by sewage facilities is high and practically all wastewater is treated at an advanced level (carbon, nitrogen, and phosphorus removal), the sewerage coverage and sewage treatment in developing countries and countries in transition are overall very low (less than 10%). In these regions, centralized conventional activated sludge (CAS) systems are competing with decentralized technology. Replicating CAS designs (mostly for solids and carbon removal) too often has not taken into account the differences in local conditions, such as sewage characteristics and temperature. Also, the dumping of large quantities of septic sludge in sewage works and lack of operator experience with CAS systems has limited successful applications.

The main constraint identified as contributing to or causing the numerous failures of CAS systems in the developing world is poor governance by the responsible institutions (*14*). However, most of these developing regions now have an economic and technical level well above those in Europe and the United States a century ago. Long-term investments in sanitation are economically favorable because of improved public health and thereby the increased productivity of society. Cost recovery structures and proper infrastructure asset management (i.e., governance) are the main prerequisites for the successful application of activated sludge technology.

The solutions for these issues may be the construction of smaller and simpler, decentralized systems that are community-managed, thus minimizing costs (e.g., anaerobic treatment or aerobic granular sludge needs much less mechanical equipment and fewer imports), or enhancing resource recovery (higher temperature-assisted biogas production, nutrients, and water). An illustrative example is Windhoek Goreangab in Namibia (*15*, *16*), where a 21,000 m^3/day water reclamation plant for the pioneering production of potable water from treated sewage (an activated sludge process followed by maturation ponds and advanced multibarrier treatment system) is used. Its realization confirms that advanced treatment technology combined with proper governance can be successfully applied in the developing world. ■

[1]*Department of Biotechnology, Delft University of Technology, Julianalaan 67, 2628 BC Delft, Netherlands.* [2]*UNESCO-IHE Institute for Water Education, Westvest 7, 2611 AX Delft, Netherlands. E-mail: m.c.m.vanLoosdrecht@tudelft.nl*

REFERENCES

1. E. Ardern, W. T. Lockett, *J. Soc. Chem. Ind.* **33**, 523 (1914).
2. J. S. Guest *et al.*, *Environ. Sci. Technol.* **43**, 6126 (2009).
3. S. B. Grant *et al.*, *Science* **337**, 681 (2012).
4. S. Judd, *Trends Biotechnol.* **26**, 109 (2008).
5. H. Daims, M. W. Taylor, M. Wagner, *Trends Biotechnol.* **24**, 483 (2006).
6. M. K. de Kreuk, J. J. Heijnen, M. C. M. van Loosdrecht, *Biotechnol. Bioeng.* **90**, 761 (2005).
7. A. Giesen, R. Niermans, M. C. M. van Loosdrecht, *Water* **21**, 28 (2012).
8. R. J. Siezen, M. Galardini, *Microb. Biotechnol.* **1**, 3330 (2008).
9. G. Olsson, *Water and Energy: Threats and Opportunities* (International Water Association, London, 2012).
10. M. C. M. van Loosdrecht, D. Brdjanovic, S. Chui, G. H. Chen, *Water* **21**, 17 (2012).
11. B. Kartal, J. G. Kuenen, M. C. M. van Loosdrecht, *Science* **328**, 702 (2010).
12. C. J. Ruiken, G. Breuer, E. Klaversma, T. Santiago, M. C. M. van Loosdrecht, *Water Res.* **47**, 43 (2013).
13. Y. Lin, M. de Kreuk, M. C. M. van Loosdrecht, A. Adin, *Water Res.* **44**, 3355 (2010).
14. K. Vairavamoorthy, D, Brdjanovic, "Engineering infrastructure: Water supply and sanitation," in UNESCO Report on Engineering: Issues, Challenges and Opportunities for Development, UNESCO, ISBN 978-92-3-104156-3 (2010).
15. I. B. Law, *Water* **30**, 31 (2003).
16. P. L. du Pisani, *Desalination* **188**, 79 (2006).

10.1126/science.1255183

Published by AAAS

ECOLOGY

Follow the odor

How do moths and other insects find their way to food sources in the presence of other odors?

By **Paul Szyszka**

We rely on our noses to notice that the milk has gone bad before we drink it, but disregard our sense of smell when it comes to finding food sources, instead using our eyes to track down the nearest supermarket. Most other animals, however, rely on olfaction to find the remote food sources. Tracking down an odor source poses a particular challenge: Odors occur in turbulent plumes and break into thin filaments, and target odors intermingle with background odors (see the figure). On page 1515, Riffell *et al.* (*1*) choose an excellent model system—a foraging sphinx moth, *Manduca sexta*, searching for its nectar resource, the flowers of *Datura wrightii*—to shed light on how insects track odors in complex odor environments.

Department of Neurobiology, University of Konstanz, 78457 Konstanz, Germany. E-mail: paul.szyszka@uni-konstanz.de

When animals recognize an attractive odor, they generally follow a simple but efficient strategy to find its source: They move upstream in the presence of the odor and move cross-stream in the absence of the odor (*2*). In insects, odor detection begins in olfactory receptor neurons on the antenna and continues in the antennal lobe in the brain. In the antennal lobe, receptor neurons with the same odor response profile converge on distinct subregions, called glomeruli. Each odor activates a unique pattern of glomeruli (*3*), and this "neural code" for the chemical identity of an odor is transmitted by projection (output) neurons to other brain areas.

Riffell *et al.* found that background odors alter projection neuron odor responses, thereby impairing the ability of moths to track a target odor (see the figure). When multiple odors mix, humans and insects often perceive them not as a group of individual components, but rather as a perceptual unit (*4*, *5*). This loss of odor component information in a mixture also occurs in the insect antennal lobe, where the neuronal response to an odor mixture often cannot be predicted from the responses to the single components (*6*). Nevertheless, insects can segregate concurrent odors from closely spaced sources based on millisecond differences in the arrival of odorants (*7*, *8*). The insect brain is likely to exploit fast stimulus dynamics for odor-background segregation, but the mechanisms are not yet known.

Riffell *et al.* were able to reproduce the disrupting effect of a background odor on odor tracking by interfering pharmacologically with the inhibitory network in the antennal lobe. Based on these results, they argue that odor tracking requires the right balance of excitation and inhibition and that a background odor disturbs this balance. The authors used a continuous odor background (see the figure, panel B). However, in nature background odors fluctuate (panel C). It will be revealing to investigate the effect of fluctuating background odors on odor tracking. It is possible that the insect olfactory system can exploit background fluctuations for odor-background segregation, similar to the way it exploits odor onset asynchrony to segregate two concurrent odors (*7*, *8*).

Experience may also contribute to odor-background segregation. In honeybees, learning modifies odor representations such that relevant odors become more salient, whereas less relevant odors are suppressed (*9*). This effect of odor learning might facilitate odor-background segregation. There is much yet to be discovered about odor-background segregation. Revealing its neural mechanisms could also aid the development of artificial sensor arrays capable of odor-background segregation and localization in natural environments. ■

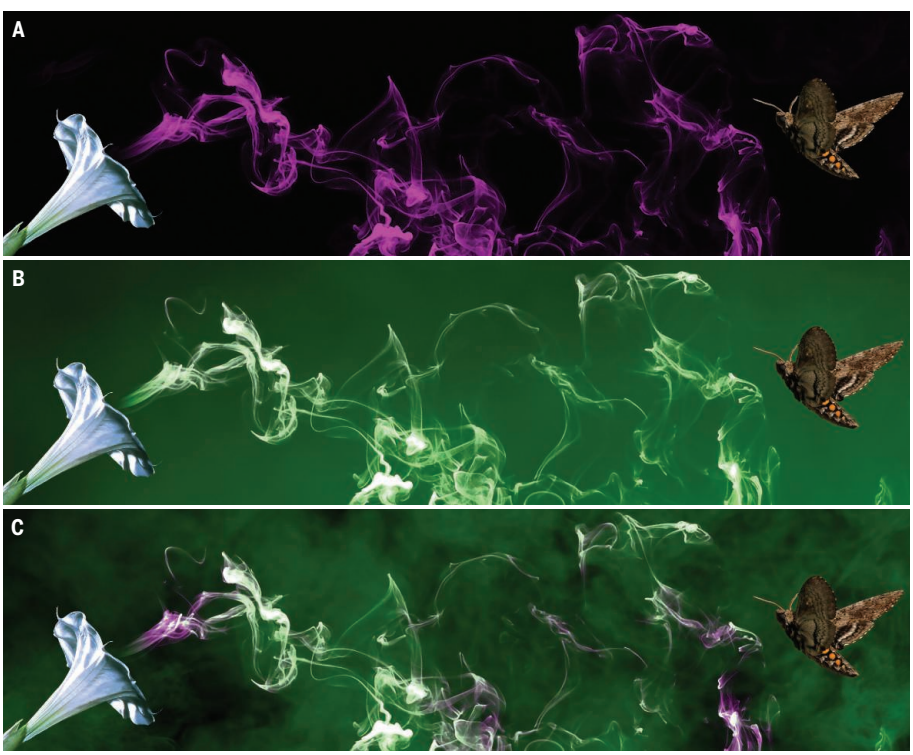

Navigating through turbulent odors. Sphinx moths rely on olfaction to find their preferred nectar sources, here the flower of the sacred datura. However, flower-odor plumes (magenta, monitored with smoke) break up into thin filaments (**A**) and mix with continuous (**B**) or fluctuating (**C**) background odors (green). Riffell *et al.* show that continuous background odors alter the neural representation of the flower odor and disrupt the ability of a moth to find the flower. It remains to be shown how fluctuating odor backgrounds affect the ability of moths and other insects to track down odor sources.

PHOTOS: SPHINX MOTH: A. J. HINTERWIRTH/WWW.AMPHIOXUS.ORG; DATURA: J. RIFFELL/UNIVERSITY OF WASHINGTON

REFERENCES AND NOTES

1. J. A. Riffell *et al.*, *Science* **344**, 1515 (2014).
2. N. J. Vickers, *Biol. Bull.* **198**, 203 (2000).
3. S. Sachse, A. Rappert, C. G. Galizia, *Eur. J. Neurosci.* **11**, 3970 (1999).
4. A. Jinks, D. G. Laing, *Physiol. Behav.* **72**, 51 (2001).
5. B. H. Smith, *Physiol. Behav.* **65**, 397 (1998).
6. A. F. Silbering, C. G. Galizia, *J. Neurosci.* **27**, 11966 (2007).
7. T. C. Baker, *et al.*, *Nature* **393**, 530 (1998).
8. P. Szyszka, J. S. Stierle, S. Biergans, C. G. Galizia, *PLOS ONE* **7**, e36096 (2012).
9. P. C. Fernandez, F. F. Locatelli, N. Person-Rennell, G. Deleo, B. H. Smith, *J. Neurosci.* **29**, 10191 (2009).

ACKNOWLEDGMENTS

I thank Th. Nowotny for reviewing this manuscript, and A. J. Hinterwirth and J. Riffell for providing photographs of a sphinx moth and a sacred datura flower, respectively.

10.1126/science.1255748

Published by AAAS

California's Big Sur coast, south of Monterey Bay, California. Monterey County is home to renowned marine biodiversity, as well as considerable human impacts to the marine environment, and is the site of eDNA field trials by several of the authors.

PHOTO: RYAN KELLY

ENVIRONMENTAL MONITORING

Harnessing DNA to improve environmental management

Genetic monitoring can help public agencies implement environmental laws

By **Ryan P. Kelly,[1,2]* Jesse A. Port,[2] Kevan M. Yamahara,[2] Rebecca G. Martone,[2] Natalie Lowell,[1] Philip Francis Thomsen,[3] Megan E. Mach,[2] Meredith Bennett,[2] Erin Prahler,[2] Margaret R. Caldwell,[2] Larry B. Crowder[2]**

Responsive environmental policy demands a constant stream of information about the living world, but biological monitoring is difficult and expensive. For many species and ecosystems—especially in aquatic and marine environments—practical monitoring methods are lacking; even where methods do exist, they may be inefficient, highly destructive, or dependent on diminishing taxonomic expertise.

The emerging science of environmental DNA (eDNA) monitoring is one promising path forward, with dozens of publications in the past 2 years defining its contours and with increasingly practical applications in environmental policy (table S1). DNA is ubiquitous in the environment, and eDNA refers to genetic material from whole microbial cells or shed from multicellular organisms via metabolic waste, damaged tissue, or sloughed skin cells. Species' shedding rates and the environmental context likely influence the spatial scale of detection for eDNA monitoring—flowing rivers might be quite different from soil samples, for example—but species have been detected within meters to kilometers of a monitoring site (*1*).

Genetic analysis has long been useful to identify source species for whale meat, sturgeon eggs, shark fins, and other high-value (and imperiled) species subject to illegal trade (*2*). But such applications require invasive or hard-to-obtain tissue samples and focus only on a single species; the potential to distill policy-relevant ecosystem-level information from a glass of seawater is new (*3*). The aims of this monitoring differ from the large-scale metagenomic sampling prevalent in the past decade (*4*), which primarily has focused on discovering unknown microbial life. The methods we outline here have the more practical aim of locating and quantifying species already of management concern.

These techniques are broadly applicable—for characterizing soil communities, identifying emerging plant pathogens, or even sensing human pathogens, such as those used in biological warfare (*5*)—but the first advances in practical monitoring with eDNA have come in large part from aquatic and marine environments (see the first photo). Because the DNA fragments of interest often degrade beyond detection in days to weeks in contemporary aquatic and marine ecosystems, eDNA provides the here-and-now view of the living world that policy decisions demand (*6*). Genetic methods are consequently beginning to allow us to collect high-resolution biological information from lakes, rivers, and bays; recent publications have reported surveys of species' distributions, which point the way toward assessing relative abundance or even numbers of key species (*7*). Takahara and colleagues, for example, used eDNA to estimate the biomass of common carp in freshwater lagoons (*8*).

eDNA monitoring has two strong advantages over conventional techniques: increased sensitivity and reduced cost. DNA-based detection outperforms other common biological survey techniques in terms of number of species detected (*3*) and does so with noninvasive sampling. As the costs of sequencing continue to plummet, generating genetic data from environmental samples becomes increasingly affordable. Per-sample costs depend on the depth and coverage of DNA sequencing, but genetic sampling is already less resource-intensive than manual censuses in some cases (*9*).

POLICY

Policy-relevant data often derive from management and compliance monitoring required by environmental laws worldwide (table S1). For example, establishing the presence of certain endangered species in a habitat triggers a suite of protections in the United States under the Endangered Species Act, and under equivalent laws in Canada, the European Union (EU), and elsewhere. Where eDNA can help underfunded public agencies perform these kinds of existing duties to implement data-hungry laws

Downloaded from www.sciencemag.org on June 28, 2014

Published by AAAS

concerning natural resources, agencies will have powerful incentives to adopt such techniques. New Zealand, for example, has begun developing molecular tools for early detection of harmful algal blooms and invasive species (*10*), and the U.S. Geological Survey is working along similar lines.

Whether eDNA alone—in the absence of traditional data—will drive environmental policy decisions remains to be seen (see the second photo). One hurdle to the regulatory use of eDNA is unknown false-positive or false-negative detection rates: for example, whether multiple vectors of invasive species' DNA may be conflated and how eDNA error rates compare with those of traditional monitoring (*11*). Recent work to assess eDNA error rates due to primer bias and variable eDNA concentrations in the field—key to making more sensitive techniques into more useful ones—has begun to establish the parameters of practical eDNA use (*12*), but acceptable error rates will differ across applications. In the interim, one value of eDNA is in supplementing existing monitoring for invasive species or public health threats. Two-tiered monitoring—genetic screening of environmental samples to guide subsequent conventional monitoring—can make use of eDNA even when error rates are unknown but where false-negative rates are likely to be lower than traditional monitoring techniques. The U.S. Fish and Wildlife Service has used two-tiered surveillance for invasive Asian carp in the Great Lakes basin, and California has similarly developed tiered monitoring at the intersection of environmental and public health by developing genetic detection methods for human pathogens along the state's beaches (*13*). Such monitoring is likely to reduce overall sampling time and cost, even as agencies work to validate molecular techniques for routine use.

Policy applications demand varying levels of quantitative information. Detecting an invasion front, for example, merely requires presence and/or absence data that eDNA studies already provide. Other applications require counts—for example, stock assessments under the Magnuson-Stevens and the Marine Mammal Protection Acts (U.S. Public Laws 94-265 and 92-522, respectively, with amendments). Although eDNA concentration is positively correlated with biomass or population density, estimates of absolute abundance remain elusive. If eDNA is to become a viable approach for stock assessments or other quantitative applications, multiple new molecular markers and further microcosm and mesocosm studies involving communities of known composition will be necessary to link recovered eDNA reads to some measure of organismal abundance. The use of multiple markers simultaneously allows researchers to correct for amplification bias, while replication and internal controls further improve reliability; these safeguards are increasingly common in eDNA studies (*14*). In the future, these methods could obviate the use of the polymerase chain reaction (with its attendant bias).

Finally, the dynamism of environmental settings (rivers and oceans, for example) makes it challenging to determine where recovered DNA has been generated and how stable its measurement is over time. Incorporating models of environmental dynamics and eDNA degradation into genetic surveys will be a further critical step toward independent validation of the emerging monitoring methods.

By using genetic information to link biological processes to existing physical and chemical data, we can better leverage existing investments in environmental observing systems and begin to disentangle the mechanisms that drive ecosystem dynamics. As genetic monitoring techniques become more quantitative, by addressing the challenges described above, it should become possible to simultaneously track many species in different trophic levels—measuring environmental change, comparing ecosystem-level shifts over time relative to natural or human-induced stressors, and determining whether the magnitude of change exceeds permissible limits. Quantifying the baselines of ecosystem structure and departures from those baselines are core questions underlying, for example, any environmental impact assessment required by the U.S. National Environmental Policy Act (Public Law 91–190).

In sum, eDNA is beginning to influence management and policy decisions, although current applications by management agencies remain relatively experimental. To animate regulations and accordingly influence human behavior, data must be reliable enough to satisfy legal standards and to justify public confidence. Working toward these goals will require careful and integrated effort by researchers in collaboration with local, state, and federal agencies but are more probably years (rather than decades) away because of growing interest worldwide. ■

Sampling water for eDNA analysis. Natalie Lowell samples water for eDNA analysis in the Lake Washington Ship Canal in Seattle, an area heavily affected by human uses.

PHOTO: KATHRYN GRAZIANO

[1]*School of Marine and Environmental Affairs, University of Washington, Seattle, WA 98103, USA.* [2]*Center for Ocean Solutions, Stanford University, Stanford, CA 94305, USA.* [3]*Centre for GeoGenetics, Natural History Museum of Denmark, University of Copenhagen, Copenhagen, Denmark*
**Corresponding author. rpkelly@uw.edu.*

REFERENCES AND NOTES

1. K. Deiner, F. Altermatt, *PLOS ONE* **9**, e88786 (2014).
2. C. S. Baker, S. R. Palumbi, *Science* **265**, 1538 (1994).
3. P. F. Thomsen *et al.*, *PLOS ONE* **7**, e41732 (2012).
4. J. C. Venter *et al.*, *Science* **304**, 66 (2004).
5. J. J. Gooding, *Anal. Chim. Acta* **559**, 137 (2006).
6. P. F. Thomsen *et al.*, *Mol. Ecol.* **21**, 2565 (2012).
7. C. L. Jerde, A. R. Mahon, W. L. Chadderton, D. M. Lodge, *Conserv. Lett.* **4**, 150 (2011).
8. T. Takahara, T. Minamoto, H. Yamanaka, H. Doi, Z. Kawabata, *PLOS ONE* **7**, e35868 (2012).
9. Y. Ji *et al.*, *Ecol. Lett.* 10.1111/ele.12162 (2013).
10. S. A. Wood *et al.*, *N. Z. J. Mar. Freshw. Res.* **47**, 90 (2013).
11. J. A. Darling, A. R. Mahon, *Environ. Res.* **111**, 978 (2011).
12. R. P. Kelly, J. A. Port, K. M. Yamahara, L. B. Crowder, *PLOS ONE* **9**, e86175 (2014).
13. J. F. Griffith *et al.*, *The California Microbial Source Identification Manual: A Tiered Approach to Identifying Fecal Pollution Sources to Beaches* (Technical Report 804, Southern California Coastal Water Research Project, Costa Mesa, CA, 2013).
14. M. De Barba *et al.*, *Mol. Ecol. Res.* **14**, 306 (2014).

ACKNOWLEDGMENTS

The authors gratefully acknowledge the support of the David and Lucile Packard Foundation, which funded this work. P.F.T. was funded by the Danish National Research Foundation. We thank A. Boehm and S. Palumbi for providing valuable feedback on the manuscript and for supporting related work.

SUPPLEMENTARY MATERIALS

www.sciencemag.org/content/355/6191/1455/suppl/DC1

10.1126/science.1251156

Published by AAAS

RETROSPECTIVE

Gerald M. Edelman (1929–2014)

A great biologist made fundamental discoveries and conceived a selectionist theory of the brain

By **Giulio Tononi**

Gerald M. Edelman, who was born in New York in 1929, died at his home in La Jolla, California, on 17 May 2014. With him, biology has lost a great scientist and something even rarer—a profound thinker. Edelman's work in the 1960s revealed the chemical structure of antibody molecules, for which he received the Nobel Prize in Physiology or Medicine in 1972 with Rodney Porter. In the 1970s, Edelman turned to studying how cells stick to each other, which led to the discovery of cell adhesion molecules (CAMs). Afterward, Edelman directed much of his efforts to understanding "how the brain gives rise to the mind" and formulated a general theory of brain function—the theory of neuronal group selection.

Gerald Edelman received his B.S. from Ursinus College in Pennsylvania in 1950 and an M.D. in 1954 at the University of Pennsylvania. He joined the Rockefeller Institute (now University) where he earned a Ph.D. in 1960. He remained at Rockefeller where, in 1981, he established the Neurosciences Institute. In 1993 Edelman moved with the institute to La Jolla.

While the discovery of the structure of the antibody and of CAMs are undisputed landmarks in biology, the theory of neuronal group selection, also known as *Neural Darwinism* from the title of Edelman's book and dubbed "neural Edelmanism" by Francis Crick, has remained controversial and not well understood. Yet there are good reasons to believe that *Neural Darwinism* represents Edelman's most important legacy and that it will endure as a classic. As Edelman himself liked to say, other scientists would have figured out antibodies and CAMs soon enough, but perhaps not neural Darwinism. And he showed where his passion lay, thinking about "how the brain works" for 35 years, a challenge he felt truly matched his intellectual power and ambition. Edelman knew all too well, of course, that in biology the structure of a tiny molecule often carries more weight than the grandest of theories. But some theories can change the way we look at the world, which is why Edelman's selectionist approach to the brain is important.

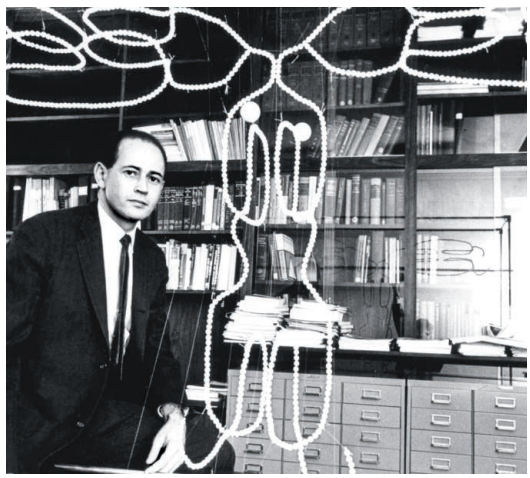

PHOTO: OMIKRON/SCIENCE SOURCE

As a tribute to Edelman's quest, it is worth briefly restating the essence of his theory, starting with the basic principles of selectionism: There must be mechanisms to generate diversity, mechanisms to sample a changing environment, and mechanisms to differentially amplify those variants that fit the environment well. It was long assumed that species are what they are immutably and by design, and it took Darwin to imagine that they may evolve by variation and selection. Similarly, it was first thought that antibodies had to be "instructed" by antigens into the appropriate shape, until Edelman and others proved that antibodies, too, are produced by variation and selection. And the same was thought true for the brain: Most people implicitly assume that the world comes prelabeled into fixed categories—whether faces, animals, objects, or anything else—and that the brain "processes information" about such inputs. Instead, insisted Edelman, "the world is an unlabeled place," and the brain, too, is a selectionist system: There is a preexisting repertoire of variations, albeit constrained by evolutionary history and developmental processes; there is the unique history of encounters of a brain with its environment; and there is the differential amplification, usually through the strengthening of synapses, of those brain circuits that work best in that environment. Of course, just as evolution includes sexual selection and immunity requires tolerance, neural selection too has its special features, such as neuronal groups and "reentry." These were discussed in *Neural Darwinism* and in later work that expanded the theory of neuronal group selection to address consciousness and higher brain functions.

When *Neural Darwinism* was published, the extent to which the brain is plastic was unclear. Today, demonstrations of plasticity fill neuroscience publications, vindicating Edelman's stance, and we now realize that almost any encounter with the environment during a waking day will strengthen many brain circuits. It is not so much that "instruction" never occurs; especially during development, synapses may form under the guidance of specific molecules (including CAMs) and specific patterns of activity. It is rather that neurons can combine into an immense repertoire of different circuits, out of which encounters with the environment will constantly select some that "resonate" better.

But then, if plasticity is so pervasive, Edelman realized, categories and concepts cannot be fixed. Just as every face is a face, but is also unique, so every individual's way to know the world, despite family resemblances, must also be unique: There must be as many ways to carve the world as there are people and animals, reflecting their particular histories and values. Edelman, who had a knack for mixing jokes with deep observations, often made the point by asking: "What do dogs think of automobiles, which had no place in their evolutionary history? Or, for that matter, what do they think of fire hydrants? A good place to raise one's leg?"

Edelman was a supreme conversationalist, endowed with a prodigious memory, a culture that was as vast as it was diverse, and powers of imagination that gave him insight equally well into molecular structures and human motives (although "nobody can smell one's nose," he liked to point out). Not surprisingly, he was also a remarkably intense and complex individual. But one could not spend time with him without absorbing some of the human richness that, like a great artist, he exuded in his own unique style. Which is just the way it should be, if indeed nature evolves and shapes our brain by variation and selection. An accomplished violinist, Edelman used to say this of obituaries: We begin as an artist, and we end as a paragraph. In his case, it will be more like a book. ■

10.1126/science.1257185

Department of Psychiatry, University of Wisconsin, 6001 Research Park Boulevard, Madison, WI 53719, USA. E-mail: gtononi@wisc.edu

Published by AAAS

BOOKS *et al.*

HUMAN EVOLUTION

Language and Wallace's problem

By **Stephen Levinson**

Alfred Russel Wallace, who with Darwin gave us the foundations of evolutionary theory, despaired of the power of natural selection to explain the intellectual and technological prowess of humans: "Natural selection could only have endowed the savage with a brain a little superior to that of an ape," he noted (*1*), pointing to intellectual, linguistic, and technological capabilities way beyond what would seem required for survival. What kind of improbable course of events yielded this excess of competences? In his wide-ranging *More Than Nature Needs*, Derek Bickerton takes this problem as the starting point for a novel inquiry into the evolution of language.

Bickerton dismisses many current approaches to the evolution of language with trenchant arguments. He contends that a standard comparative approach is misplaced: human prowess is not to be accounted for by the accumulation of elements exhibited among the apes or elsewhere in primates. Rather, extraordinary competences required extraordinary selective pressures, best understood by searching for analogies far away in phylogenetic space, like the signaling of pollen sources by bees. Bickerton suggests that the special pressure was a climate-induced switch to cooperative scavenging, which required a spatial signal system similar to that of the bees but more flexible about food types. Well over a million years ago, this "displacement" of message content from the here-and-now limitations typical of animal communication gave rise to "protolanguage," an unstructured string of wordlike symbols. That in turn provided a stimulus for brain reorganization, enabling the hierarchical organization of strings of words—the simple syntactic organization that Bickerton, like Chomsky, thinks is the essence of linguistic capacity. He assembles evidence for the nature of this core syntax from a wide range of sources, but especially from the structure of creoles, the stripped-down languages on which he is an expert. [Curiously, he ignores recent work on new sign languages (*2*) and "home sign" (*3*) that might have been better grist for his mill.] Unlike most of Chomsky's followers, however, Bickerton thinks the great complexity and diversity of modern languages is due wholly to cultural history.

A book this wide-ranging—surveying linguistic, developmental, evolutionary, and brain research—is bound to upset specialists, who will find fault with much detail. Neither the Chomskyans nor the functional linguists are likely to be happy with Bickerton's solution: His version of a minimal nativist syntax has no place for the elaborate structures beloved of the generativists, while it remains stubbornly at odds with the psycholinguistic facts that he correctly thinks should be central to the picture. (For example, language production is incremental and involves left-to-right processing, not the bottom-up merging of units that he favors.)

But the way that the problem is set up and the directions chosen for seeking solutions is deeply thought-provoking. Wallace's problem, Bickerton points out, is that humans went beyond an adequate, simple protolanguage. There must have been something inevitable about the road to excess once the process had begun.

Among this stimulating book's loose ends, one stands out. Darwin argued both that an evolved capacity for thought must have preceded language and that language is partly responsible for its development (*4*). So was it advanced cognition that made language possible? Or did language enable our complex thinking? Bickerton wrestles with the same dilemma but comes down on the side of language enabling thought: The displacement of messages gave us "offline" thinking, and core grammar gave us the syntax of thought.

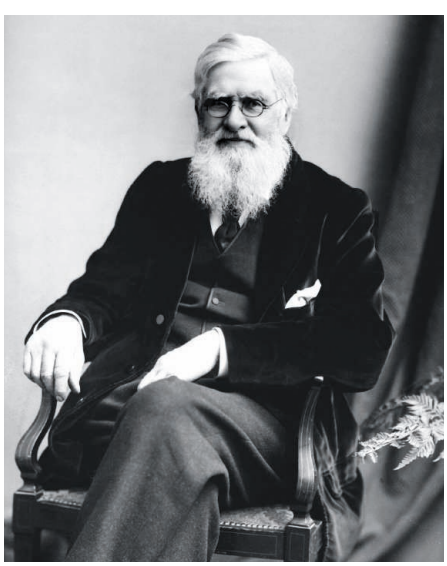

Alfred Russel Wallace.

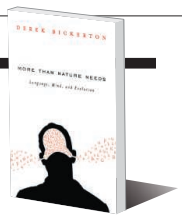

More Than Nature Needs
Language, Mind, and Evolution
Derek Bickerton
Harvard University Press, 2014. 334 pp.

Here, *A Natural History of Human Thinking* makes compelling reading. Michael Tomasello argues that it was a change in the mode of thinking that opened the great gulf between humans and the other great apes and that language developed from that new mode. Like Bickerton, Tomasello thinks it must have taken extraordinary conditions to provoke the evolution of human capacities, and he similarly imagines cooperative foraging as the main selective force. But in a reassessment of his earlier work, Tomasello argues that apes are cognitively much closer to humans than had been thought only a decade ago. Apes reason as if using conditionals, disjunction, and negation; appear to use abstract representations exploited productively for inferences; and have advanced abilities to understand others' goals. Interestingly for Bickerton's argument, apes clearly think with "displacement," planning for the future (e.g., retaining tools). Moreover, they are able to control their impulses and sustain attention, displaying a level of meta-awareness roughly comparable to a three-year-old child. Apes thus behave in a "flexible, intelligent, self-regulated way" similar to humans. The crucial difference is that the domains in which they exercise these inferences are largely competitive, not cooperative.

Unlike Bickerton, Tomasello thinks comparative psychology reveals that the cognitive launch pad was already present in our common ancestor with the chimpanzees. Tomasello imagines two big steps to get from apelike to our mental capacities. The first, fully realized by perhaps 400,000 years ago, was the evolution of joint cooperative action, requiring recursive "mind reading" to establish common goals and assumptions. It also requires a reciprocity of perspectives in the joint enterprise and so a meta-analysis of the cooperative activity. Evidence for this stage is only indirect, but Tomasello argues that the cooperative ability of prelinguistic infants as young as one year gives us insight into our early ancestors, since they share the lack of elaborated language and developed culture.

The reviewer is at the Max Planck Institute for Psycholinguistics, Wundtlaan 1, 6525 XC Nijmegen, Netherlands. E-mail: stephen.levinson@mpi.nl

PHOTO: © WORLDPHOTOS/ALAMY

Downloaded from www.sciencemag.org on June 28, 2014

Published by AAAS

Lucas Cranach the Elder's *The Golden Age* (1530).

CREDIT: ALTE PINAKOTHEK, MUNICH/PHOTO: WWW.BRIDGEMANART.COM

With the advantages of cooperatively shared information, this advance provided the niche for the development of a protolanguage (primarily gestural), which crucially added an informative mode to the ape-level imperative mode. Pointing plus intonation would soon have been supplemented with an open-ended system of iconic gestures and pantomime, allowing the depiction of the not-here-and-now, so exercising human spatial imagination. While having structured strings and predicate-argument structure, this protolanguage lacked a developed repertoire of shared conventions.

The second giant step, prompted by increasing intergroup competition, was the development of sanctioned group norms. These formed the basis for shared conventions and for cross-generational transmission, thus producing the ratchet effect of increasing cultural complexity. Norms brought conformity, internalized measures of performance, a sense of objectivity, and the need for persuasive reasoning. They gave us social institutions and also the cumulative conventionalizations of lexicon and grammar, requiring no cognitive capacities special to language. Grammar is therefore an outcome of the normative domestication of the species, not the great catalyst to human thought that it is on Bickerton's account.

The two stages seem to inevitably overlap (for example, a protolanguage will also rely on microconventions of precedence and parity between sender and receiver). Still, the book's great virtue is its conceptual analysis of the cumulative steps in cognition required to get us from ape to human. For empirical illustration of each step, Tomasello draws largely on his group's work on apes and children. He sees no innate program for the development of all these cognitive, cultural, and linguistic skills, but rather the cooperative predisposition to construct them.

So here are two alternative solutions to Wallace's problem: the acquisition of a powerful mental algorithm as a side effect of acquiring the capacity for symbolic communication, or the fundamental switch toward cooperative motivations and the deep recursive computations required for joint action, which then provided the basis for language. Bickerton's account actually presupposes something like Tomasello's fundamental cooperative turn of mind. But can Tomasello's account stand alone? Can grammar emerge just from cooperative conventions for communication, through the slow cultural acquisition of constructions? How can we account for the specialized neural circuitry associated with language, e.g., the extended wiring of the *arcuate fasciculus*, which connects Broca's and Wernicke's areas (*5*)? Tomasello's explanation seems to need extension.

For one, both books neglect speech. Humans are almost unique among the primates in our ability to mimic whatever sound we hear. We have developed an elaborate vocal apparatus, with reconfigured vocal tract, and greatly enhanced voluntary neural control of the tract and breathing that animates it (*6*). Modern human language use is multimodal, with speech, gesture, face, and gaze all involved, and the roots of this system must be ancient (*7*). The generation of messages in such a system is part of the action system, and many commentators have thought that the origins of hierarchical, recursive syntax can be found in action (*8*). Tomasello's emphasis on joint action and the recursive propositional thinking that lies behind it makes this all the more plausible (*9*) and has the advantage of making some evolutionary connection between our technological intelligence and linguistic abilities. Current linguistic opinion is divided on whether, as Bickerton assumes, something extra, more specifically grammatical, is part of our native endowment.

Oddly, neither book engages seriously with the new data from paleontology, archaeology, and ancient DNA. The development of the vocal tract, the control of breathing, and fast input-output mapping (in which the gene FOXP2 seems to play a role) can all be traced in the archaeological record (*10*). Despite some skepticism about the evidence (*11*), it seems probable that our vocal skills evolved much earlier than either author imagines, and they are likely to have had a causal role in all the other developments.

Darwin described language as "an instinctive tendency to acquire an art" (*4*). Neither book fully captures Darwin's insight—although Tomasello comes close—because both concentrate on the "cold" abstract cognitive prerequisites rather than the "hot" motivational and interactional instincts that lie behind the strongly universal patterns of multimodal communication (*12*). Nonetheless, both books are highly stimulating, especially in conjunction. ■

A Natural History of Human Thinking
Michael Tomasello
Harvard University Press, 2014
192 pp.

REFERENCES AND NOTES

1. A. R. Wallace, *Q. Rev.* **126**, 359 (1869).
2. U. Zeshan, C. De Vos, Eds., *Sign Languages in Village Communities: Anthropological and Linguistic Insights* (de Gruyter, Berlin, 2012).
3. S. Goldin-Meadow, *Hearing Gesture: How Our Hands Help Us Think* (Harvard Univ. Press, Cambridge, MA, 2012).
4. C. Darwin, *Descent of Man, and Selection in Relation to Sex* (John Murray, London, 1871).
5. J. K. Rilling *et al.*, *Nat. Neurosci.* **11**, 426 (2008).
6. W. T. Fitch, *The Evolution of Language* (Cambridge Univ. Press, Cambridge, 2010).
7. S. C. Levinson, J. Holler, *Philos. Trans. R. Soc. London Ser. B*, in press, 10.1098/rstb.20B.0302.
8. P. M. Greenfield, *Behav. Brain Sci.* **14**, 531 (1991).
9. S. C. Levinson, *Language* **89**, 149 (2013).
10. D. Dediu, S. C. Levinson, *Front. Lang. Sci.* **4**, 397 (2013).
11. N. D. Hauser *et al.*, *Front. Psychol.* 10.3389/fpsyg.2014.00401 (2014).
12. S. C. Levinson, in *Roots of Human Society: Culture, Cognition, and Interaction*, N. J. Enfield, S. C. Levinson, Eds. (Berg, Oxford, 2006), pp. 39–69.

10.1126/science.1252988

Published by AAAS

LETTERS

Edited by **Jennifer Sills**

Editorial expression of concern

IN THE 16 SEPTEMBER 2011 issue, *Science* published the Report "Unclicking the click: Mechanically facilitated 1,3-dipolar cycloreversions" by J. N. Brantley *et al.* (*1*).

After concerns were raised in an e-mail to the editors from a reader, the corresponding author supervised a comprehensive evaluation of all data presented in the original manuscript by tracing all figures back to their raw data files. In over 50% of the figure parts, the authors deemed the data unreliable due to uncertainty regarding the origin of data or the manner in which the data were processed. A confidential investigation that is relevant to these concerns is currently being conducted by the University of Texas at Austin.

Pending the conclusion of the investigation, *Science* is publishing this Editorial Expression of Concern to alert our readers to the fact that serious questions have been raised about the validity of findings in the Brantley *et al.* paper.

Marcia McNutt

Editor-in-Chief

REFERENCE

1. J. N. Brantley, K. M. Wiggins, C. W. Bielawski, *Science* **333**, 1606 (2011).

Carbon markets: Effective policy?

IN THEIR POLICY FORUM "Carbon market lessons and global policy outlook" (21 March, p. 1316), R. G. Newell and his colleagues present an optimistic—but ultimately misleading—picture of existing carbon markets. Citing the expanded use of carbon markets, Newell *et al.* use economic theory to calculate the extent to which these policies are reducing net greenhouse gas emissions. In our view, it would be more realistic to look at how carbon markets are performing in practice, not theory. This distinction matters because actual markets are not producing the net emissions reductions for which they were designed.

One key problem is leakage, which refers to emissions that leave a jurisdiction because of the carbon price. Newell *et al.* claim that leakage has been small, but fail to address problems specific to subnational policies. Both the Regional Greenhouse Gas Initiative (RGGI) (*1*) and the California market (*2*, *3*) allow companies to swap emissions-intensive power contracts with neighbors in linked electricity markets not subject to carbon limits. Inadequate information precludes any conclusion on the Chinese pilot markets at this time; however, just as in RGGI and California, China's grids are larger than its carbon markets.

The authors also gloss over the European Union's problematic experience with international carbon offsets. Many of these offsets came from refrigerant factories that artificially generated extra emissions in order to destroy them for credit; their use in the EU Emissions Trading System has been substantial and came at the expense of actual emissions reductions (*4*).

Newell *et al.* close with a research agenda focused on the growth and consolidation of carbon markets. A more realistic research agenda would ask: Are existing carbon markets reducing net emissions as intended? If not, what policy reforms are required; and how effectively will these instruments, if left unaltered, scale to larger regions and stricter emissions targets?

Danny Cullenward*[1] *and* ***Michael Wara*[2]**

[1]University of California, Berkeley, Berkeley, CA 94720, USA. [2]Stanford Law School, Stanford University, Stanford, CA 94305, USA.

*Corresponding author. E-mail: dcullenward@berkeley.edu

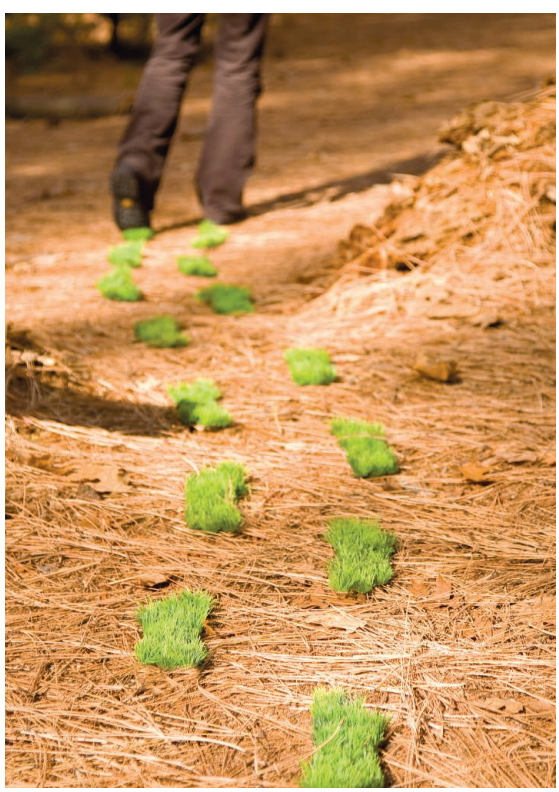

PHOTO: JAMES TUTOR/ISTOCKPHOTO

REFERENCES

1. I. Sue Wing, M. Kolodziej, "The Regional Greenhouse Gas Initiative: Emission leakage and the effectiveness of interstate border adjustments" (Harvard Kennedy School Working Paper RPP-2008-03, 2008).
2. Y. Chen, *Energy Econ.* **31**, 667 (2009).
3. D. Cullenward, D. Weiskopf, "Resource shuffling and the California carbon market" (Stanford Law School ENRLP Working Paper, 2013).
4. M. Wara, *UCLA Law Rev.* **55**, 1759 (2008).

Response

CULLENWARD AND WARA raise two main issues: (i) Are carbon markets delivering the reductions they were designed to deliver? (ii) Can we use economic theory to calculate the extent to which carbon markets are reducing emissions? They then highlight two problems—leakage and offsets—that suggest carbon markets are not performing as designed.

Emission targets and programs are often designed with some understanding of potential problems. The Regional Greenhouse Gas Initiative (RGGI) was fully aware of the potential for leakage to neighboring regions, and intentionally designed their program to operate with low prices that limit leakage (*1*). California may have believed that it could successfully address leakage, but it also implemented a price floor that largely protects the rest of the program if it occurs (*2*). The European Union placed strict limits on the use of offsets, in turn limiting the potential for their abuse (*3*). Similarly, the Bonn and Marrakech conferences after the Kyoto Protocol largely renegotiated the original targets through limits on credits for carbon sinks, highlighting how even credit provisions that are widely acknowledged to influence environmental effectiveness can be part of an intentional program design (*4*). We believe that although leakage and problematic offsets are never desirable, they are often occurring in a way that was anticipated at the time the program was designed.

To answer Cullenward and Wara's second question, we do not think that leakage and offsets negate the mitigation effects of the observed carbon price. We argue that carbon markets—even if flawed—are working and are reducing emissions. Leakage and certain offsets can yield reduction credit where it has not actually occurred in aggregate. Such reductions, however, are in addition to all of the real

Downloaded from www.sciencemag.org on June 28, 2014

Published by AAAS

abatement activities that will occur at a given market price. We can certainly imagine subtleties that caution us from being too precise about our rough calculations, but our review suggests these issues are not problematic.

Richard G. Newell,[1]* William A. Pizer,[2] Daniel Raimi[3]

[1]Nicholas School of the Environment, Duke University, Durham, NC 27708, USA. [2]Sanford School of Public Policy, Duke University, Durham, NC 27708, USA. [3]Duke University Energy Initiative, Duke University, Durham, NC 27708, USA.

*Corresponding author.
E-mail: richard.newell@duke.edu

REFERENCES

1. RGGI Emission Leakage Multi-State Staff Working Group, "Potential emissions leakage and the Regional Greenhouse Gas Initiative (RGGI): Evaluating market dynamics, monitoring options, and possible mitigation mechanisms" (2007); www.rggi.org/docs/il_report_final_3_14_07.pdf.
2. H. G. Fell, D. Burtraw, R. D. Morgenstern, K. L. Palmer, L. Preonas, "Soft and hard price collars in a cap-and-trade system: A comparative analysis" (Resources for the Future Discussion Paper 10-27-REV, 2010).
3. D. A. Ellerman, F. J. Convery, C. de Perthius, *Pricing Carbon* (Cambridge Univ. Press, Cambridge, 2010).
4. C. Bohringer, *Oxford Rev. Econ. Pol.* **19**, 451 (2003).

A carbon code of conduct for science

MANY SCIENTISTS SUPPORT emissions reductions, but struggle with the fact that our research programs can produce a substantial amount of greenhouse gas pollution. When our personal emissions are greater than those of an average citizen (*1*–*5*), we are faced with a credibility gap in advocating for others to reduce their carbon footprint.

It is unreasonable for modern scientists to avoid emitting carbon entirely—such an action could grind research to a halt. However, it is difficult to determine when and where we should consider carbon usage to be appropriate, as there are no broadly accepted guidelines for ethical emissions in research. Since emissions are globally harmful (*6*), this issue requires attention and debate within the scientific community.

The dilemma of how to conduct research that causes harm has been thoroughly explored in medical research, where experimentation on animals is critical to the conduct of the discipline (*7*). Guidelines in modern science are based on three Rs: replacement with less sentient animals (e.g., replacing vertebrates with invertebrates); reduction in the number of animals used; and refinement of the research methods used such that pain and distress are minimized (*8*). This decision process can permit the conduct of research that is painful or lethal to

Scientists should take a page from animal research guidelines to minimize carbon emissions.

highly sentient animals, such as primates, provided that researchers can demonstrate that they ruled out all other options, and that the research is necessary. However, it establishes expectations for researchers to minimize the harm caused by their activities and to adopt alternatives where possible. These expectations are then enforced by institutional and national animal ethics bodies.

Science should adopt a carbon code of conduct, based on the three Rs. For scientific activities that require the emission of carbon, researchers should replace with less carbon-intensive activities, reduce the scope of the activity, and refine their research plan to maximize the scientific return for each unit of carbon emitted.

If the researcher concludes that their activity is essential and cannot be replaced, reduced, or refined, then a fourth requirement should be to mitigate carbon impacts through the purchase of reputable offsets (*9*) or by mitigating their emissions in a tangible and defensible manner (e.g., supporting community-based initiatives, such as tree planting). This requirement to offset would need to be initiated by funders, who would have to make such payments allowable within their granting programs.

It may be argued that the contribution of the science community to global emissions is too small to warrant such attention. However, the magnitude of our emissions is less important than the harm associated with the activity. It would not be acceptable to cause undue, unregulated pain to a single animal in the name of research, despite the fact that this harm would represent a tiny contribution to the collective suffering of animals around the world. Carbon emissions threaten the integrity of the global ecosystem, so we should treat them with a similar level of seriousness.

There is no debate within the scientific community that climate change is dangerous and that emissions must be dramatically and immediately reduced to avoid catastrophic warming (*6*). Therefore, our actions and behaviors should match our messages. If broadly adopted, a carbon code of conduct would not restrict the advancement of knowledge any more than adopting ethical standards in animal research restricted medical science. However, it would provide accountability, help us reduce our carbon consumption, and ultimately facilitate our ability to engage the public on the issue of reducing emissions across society. We have little to lose and much to gain in seriously considering this most important environmental issue of our time.

Brett Favaro

Centre for Sustainable Aquatic Resources, Fisheries and Marine Institute of Memorial University of Newfoundland, St. John's NL, A1C 5R3, Canada.
E-mail: brett.favaro@mi.mun.ca

REFERENCES

1. C. Synolakis, S. Foteninis, *Nature* **461**, 167 (2009).
2. L. Fahrni, Y. Rydin, S. Tunesi, M. Maslin, "Travel related carbon footprint: A case study using the UCL Environment Institute" (UCL Environment Institute, London, 2009).
3. W. M. J. Achten, J. Almeida, B. Muys, *Ecol. Indic.* **34**, 352 (2013).
4. I. C. Burke, *Science* **330**, 1476 (2010).
5. D. Spinellis, P. Louridas, *PLOS ONE* **8**, e66508 (2013).
6. IPCC, Climate change 2014: Impacts, adaptation, and vulnerability. Contribution of working group II to the fifth assessment report of the Intergovernmental Panel on Climate Change (Cambridge Univ. Press, Cambridge, 2014).
7. C. Palmer, P. Sandøe, in *Animal Welfare*, M. C. Appleby, J. A. Mench, I. A. Olsson, B. O. Hughes, Eds. (CABI, Cambridge, 2011), chap. 1.
8. W. M. S. Russell, R. L. Burch, *The Principles of Humane Experimental Technique* (Methuen, London, 1959).
9. A. Brohé, N. Eyre, N. Howarth, *Carbon Markets: An International Business Guide* (Earthscan, London, 2009).

PHOTO: RF ZOONAR/THINKSTOCK

Published by AAAS

Evacuating after Typhoon Haiyan. Scientists in a new fellowships program will analyze policy issues such as whether Vietnam's early warning system can be improved.

New effort seats scientists at the policy table in Southeast Asia

Inspired by a AAAS program, a pilot project aims to inject more science and technology into the region's policy-making

By **Ginger Pinholster**

Every year, the tropical monsoon region surrounding Vietnam generates about 27 to 28 tropical storms, according to Nga Thi Thanh Pham, a scientist with expertise in meteorology and weather forecasting who is spending a year at Vietnam's Ministry of Science and Technology. A handful of those storms inevitably make landfall in Vietnam, where a long coastline, mountainous terrain, and many rivers can exacerbate their impacts, with deadly results. Between 1980 and 2010, natural disasters—mostly storms and floods—killed 16,099 people in the country, according to PreventionWeb, a disaster-risk reduction Web site.

Preparation is critical for minimizing this toll. In her new position with the government, Nga will assess the effectiveness of the country's early warning system, which relies on the Voice of Vietnam and Vietnam Television to help the public prepare for natural disasters. She will study how updates to a disaster-prevention law, implemented this year, are being carried out at the regional and district levels, and she will review lessons learned in other regions.

"This type of work is so important in Vietnam," she said. "Their living heavily depends on the natural environment and agriculture. Saving more lives and promoting economic development depends on being able to better prepare for natural disasters. I do hope that my knowledge will prove useful in supporting storm-related disaster prevention."

Nga is a member of the inaugural class of ASEAN-U.S. Science and Technology Fellows, a pilot project inspired by the 40-year-old Science & Technology Policy Fellowships program at AAAS. The new project aims to increase the use of science, technology, and objective analysis in the political decision-making process in five Southeast Asian nations: Indonesia, Myanmar, the Philippines, Thailand, and Vietnam.

The initiative, announced by the Association of Southeast Asian Nations (ASEAN), has tasked eight scientists and engineers to work for 1 year on policy matters related to biodiversity, climate change, reducing disaster risks, health, and water management. The program, which is the first multi-nation effort to use the AAAS policy-fellows model, is managed by the U.S. Agency for International Development (USAID) in partnership with the United States Mission to ASEAN.

Other fellows include Anh Tung Pham, also in Vietnam, who will provide analysis to support policy-making decisions related to helping cities adapt to climate change. In the Philippines, fellow Maria Ruth B. Pineda will help set up a governance structure for the ASEAN-Network for Drugs, Diagnostics, Vaccines, and Traditional Medicines Innovation, an information-sharing initiative. In Indonesia, fellow Dyah Marganingrum will develop recommendations for improving water resource management. Other fellows in Indonesia, Myanmar, and Thailand will work on a variety of issues related to biodiversity and climate change.

"In any country, science, technology, and innovation can be an essential piece of the development process," said AAAS science diplomat Norman Neureiter, senior advisor to the AAAS Center for Science Diplomacy. "This experiment in Southeast Asia, based

PHOTO: © KHAM/REUTERS/CORBIS

Published by AAAS

on the AAAS model, will provide invaluable information on how best to leverage science to enhance regional development and promote scientific cooperation."

In April, Neureiter and Cynthia Robinson, director of the AAAS S&T Policy Fellowships, participated in a 4-day orientation event in Jakarta, Indonesia, for the first class of ASEAN fellows. Robinson conducted a session to help fellows maximize their opportunities and accomplishments, and she moderated sessions on strategies to leverage science in support of policy-making.

Over the years, she said, colleagues in Australia, Canada, Israel, Japan, New Zealand, Sweden, and Switzerland have expressed interest in the AAAS policy fellowships. A successful program with an environmental-policy focus was launched in Israel 4 years ago. In the United States, California and Massachusetts have programs in place that used the AAAS experience as a guide. "We're particularly excited about the effort in Southeast Asia because it's regional," Robinson said. "We hope that it will become a successful model for helping to inform policy in places where multiple countries face the same science-based problems."

At the Jakarta orientation event for the ASEAN fellows, Neureiter's presentation focused on the value of international science diplomacy as a mechanism for improving cross-border relations based on shared goals for advancing science. One of the first such examples of U.S science diplomacy took place in 1961, when Japanese Prime Minister Hayato Ikeda and U.S. President John F. Kennedy, at the urging of Edwin Reischauer, then the U.S. ambassador to Japan, announced the creation of three U.S.-Japan joint committees, including one on scientific cooperation. In 1972, Neureiter noted, President Richard M. Nixon also leveraged science diplomacy to help normalize relations with Russia.

"Science can be an important element of foreign policy," Neureiter said. "Taking advantage of that through programs such as this new ASEAN fellowship initiative can improve cooperation between countries and, we hope, result in better outcomes for their research."

The initiative was proposed by Montira Pongsiri, who was then the Science Advisor to the U.S. Mission to ASEAN and previously a mentor to AAAS S&T Policy Fellows at the Environmental Protection Agency, in collaboration with alumna AAAS policy fellow Teresa Leonardo, the Regional Science and Technology Advisor at the USAID Regional Development Mission for Asia.

PHOTO: CARLA SCHAFFER/AAAS

Swapping stories. Alumni reminisced about their internships at a 2 June gathering at AAAS.

Mass Media Fellows celebrate 40 years

By **Earl Lane**

Forty years ago, AAAS sent its first class of science-savvy students into the newsroom to learn first-hand about writing and reporting from working journalists. For some alumni, their summer as a AAAS Mass Media Science & Engineering Fellow was a life-changing experience.

"Without this fellowship, I swear I'd be selling aluminum siding somewhere in New Jersey," said Steve Mirsky, columnist and podcast editor for *Scientific American*. Mirsky was working fitfully toward his doctorate in chemistry when he went to work in 1985 as a fellow at WSVN-TV in Miami. He used that experience to get a job at a radio station in Syracuse, New York, where he developed broadcast skills that he now uses for his lively podcasts.

The fellows program has welcomed 620 participants since 1974, and many of them have gone on to distinguished careers in journalism and science communication. Those who have remained in the science professions have used their media skills to better communicate their work to colleagues and the wider public.

Dione Rossiter, the program's project director, has been conducting a survey of alumni to learn more about the fellowship's long-term impacts. Preliminary results show that 76% of the respondents said that the program was "extremely" or "very" important to their success, and 37% said that it completely changed the course of their career.

This summer also marks the 10th anniversary of the Minority Science Writers Internship program for undergraduates at *Science* magazine. Natalie Villacorta, a 2011 intern at the magazine, said that the program allowed her to answer an inner voice that said "tell stories." She is now a health care reporter for Politico, an online news site.

New dues rates approved for 2015

The AAAS Board of Directors has approved a dues increase for 2015. The new rates are effective for membership terms beginning after 31 December 2014 and do not include postage or taxes for international members, which is additional. For more information, contact the AAAS Membership Office at 202-326-6417.

Regular professional members	$155
Postdocs and K-12 teachers	$99
Emeritus members who receive print *Science*	$115
Students	$75
Patrons	$310
Institutional rate for print for high schools and public libraries	$360
All other institutions receiving print	$1397

Published by AAAS

The gas surge

Fracking has ignited an energy revolution, with still-uncertain consequences for climate and the environment

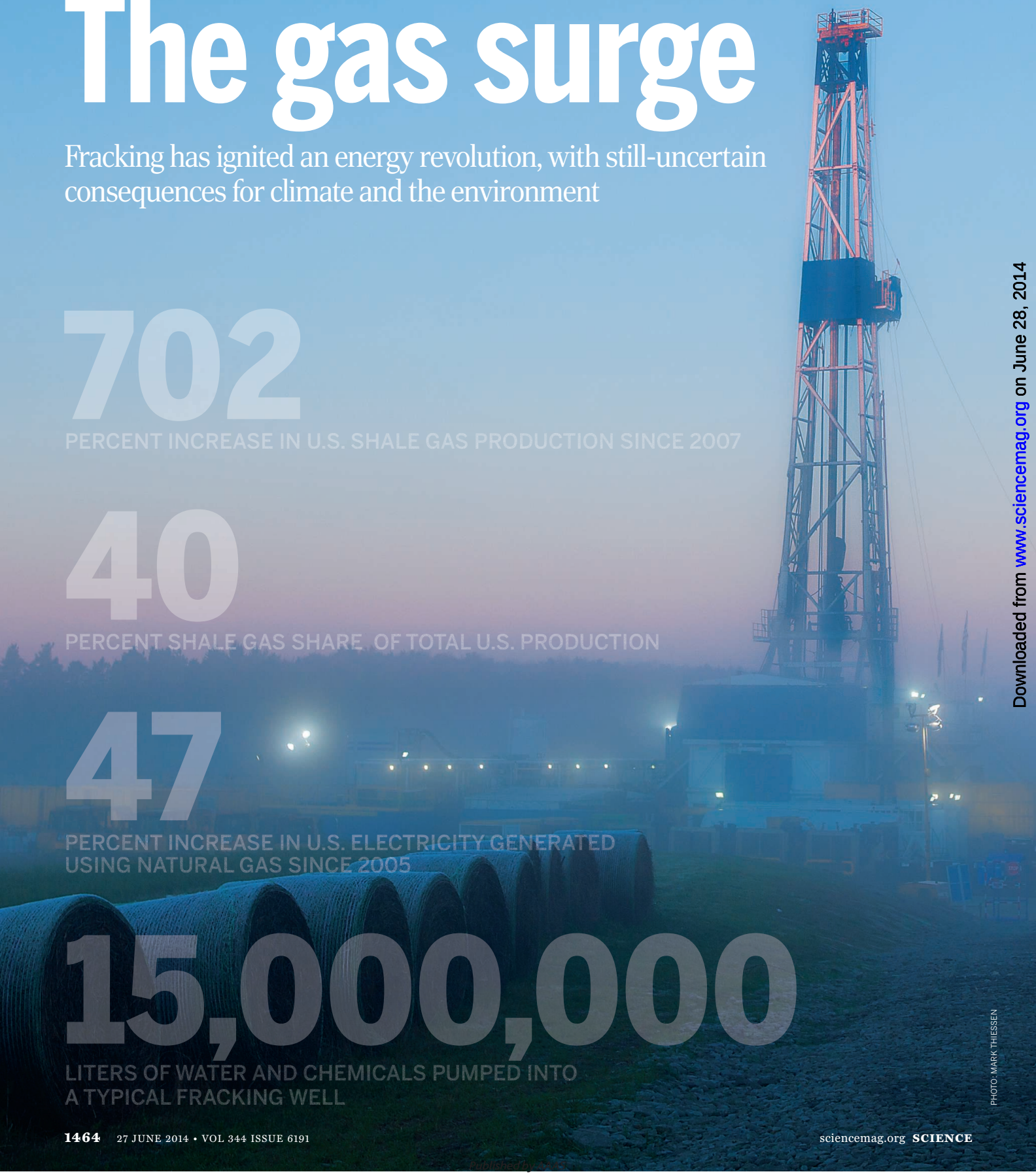

PHOTO: MARK THIESSEN

Downloaded from www.sciencemag.org on June 28, 2014

Published by AAAS

Nearly 70 years ago, a small group of engineers and geologists gathered at a dusty gas drilling site in southwestern Kansas to try an experiment. They pumped nearly 4000 liters of gelled gasoline and sand some 700 meters down a borehole into a thick bed of limestone, in hopes that the pressurized gunk would fracture the rock and release more natural gas. The "hydraulic fracturing" test failed. But success ultimately followed: Today, fracking, as it is known, is revolutionizing the energy industry, enabling firms to extract natural gas from a source once considered unpromising—vast deposits of shale, which is too dense for gas to flow freely (*Science*, 25 June 2010, p. 1624). By penetrating the shale with boreholes that bend horizontally, and then pumping in millions of liters of fluids and sand under high pressure, drillers can force open minute cracks that release valuable streams of gas.

Extensive shale gas deposits—or "plays" as they are

By **David Malakoff**

A fracking well in Pennsylvania taps shale gas deposits some 2 kilometers down.

Published by AAAS

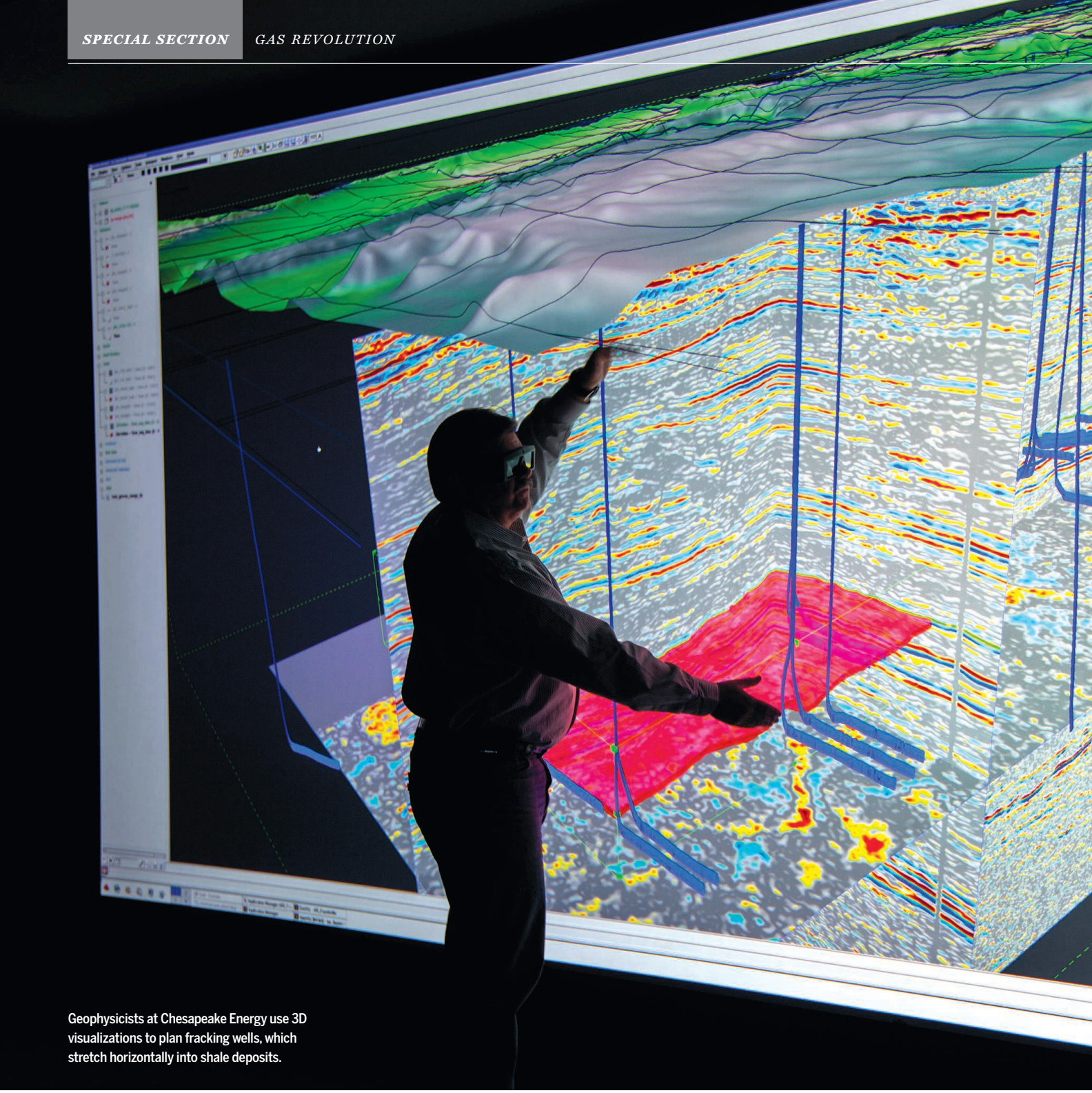

Geophysicists at Chesapeake Energy use 3D visualizations to plan fracking wells, which stretch horizontally into shale deposits.

PHOTO: MARK THIESSEN

known in the industry—are found around the world (see map, p. 1467). So far, however, the shale gas boom is largely confined to the United States, where over the past decade companies have drilled thousands of fracking wells into once obscure geological formations, including the Marcellus Shale in Pennsylvania, the Barnett in Texas, and the Haynesville in Louisiana. (In other shale plays, such as the Bakken in North Dakota, fracking is primarily used to produce oil.)

The resulting surge in natural gas is remaking U.S. energy markets—and causing economic ripple effects globally. Shale gas has made the United States the world's leading natural gas producer and now accounts for about 40% of U.S. production, up from less than 2% in 2001. The share is projected to grow to 53% by 2040, and natural gas prices have tumbled as abundance grows (see graphs, p. 1467). That's helped accelerate a shift away from coal to natural gas for generating electricity and prompted energy-intensive manufacturing firms to shift production from overseas factories to the United States, creating hundreds of thousands of jobs. The United States is also boosting natural gas exports to other nations—reversing its traditional role as an energy importer.

The shale gas shake-up has been accompanied by plenty of controversy—and new research—as the stories in this special section illustrate. Scientists are debating frack-

Published by AAAS

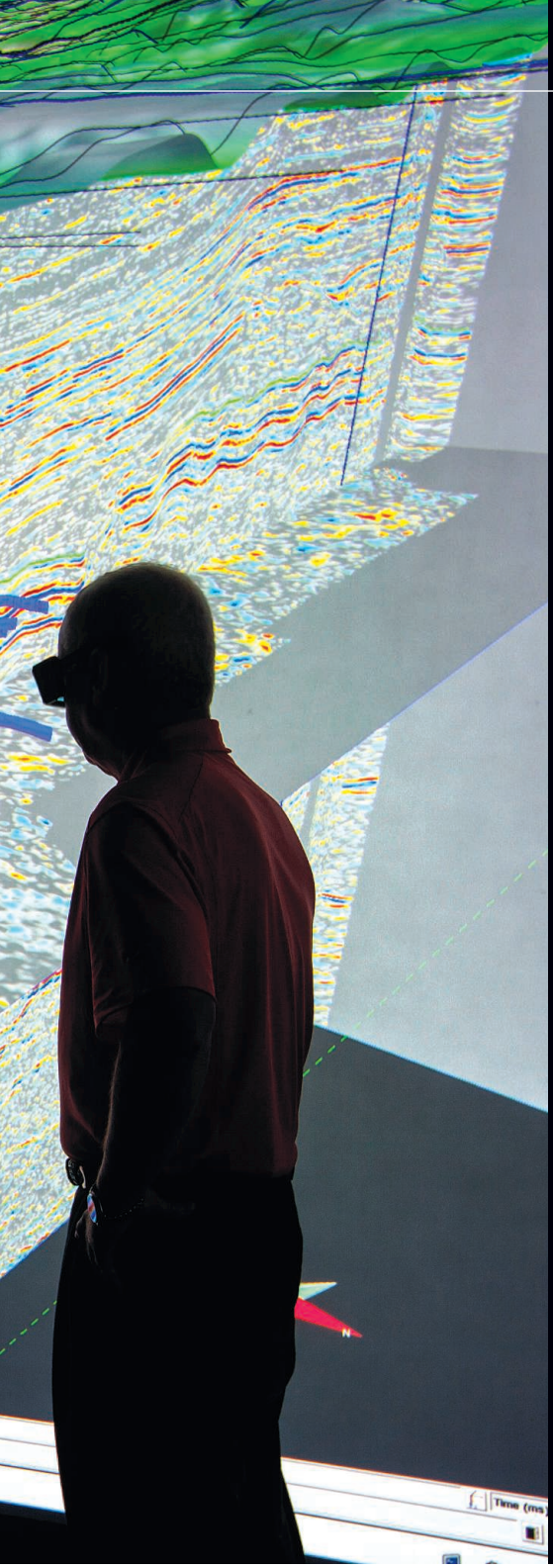

The world has vast deposits of gas-rich shale ...

Six nations—the United States, China, Argentina, Algeria, Canada, and Mexico—hold an estimated 80% of documented shale gas deposits.

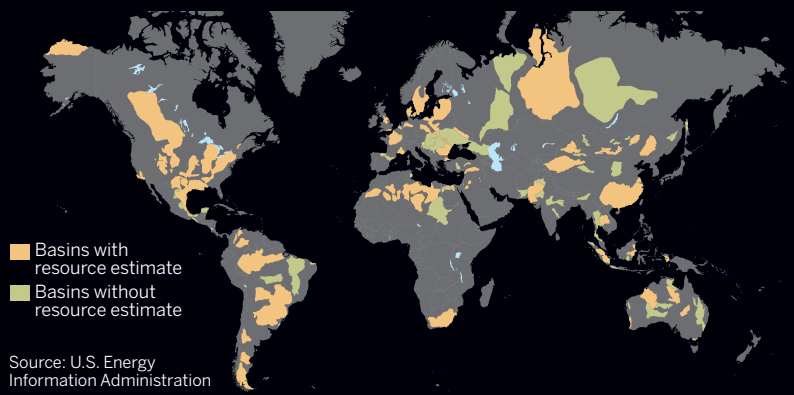

Source: U.S. Energy Information Administration

but so far shale gas has had the biggest impact in the United States ...

As other U.S. sources of natural gas decline, shale gas production is projected to expand and provide 53% of the total by 2040.

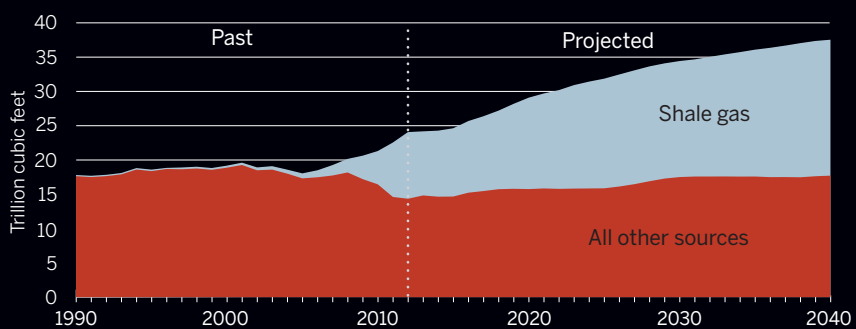

Source: U.S. Energy Information Administration, *Natural Gas Annual 2012*

where abundant supplies have helped reduce natural gas prices.

Future natural gas prices will depend, in part, on the future productivity of wells.

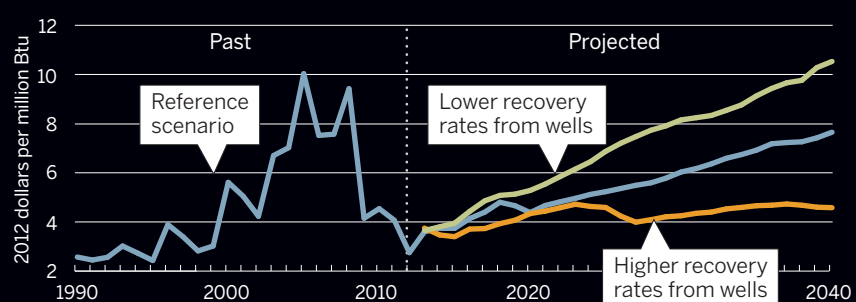

Source: U.S. Energy Information Administration, *Annual Energy Outlook 2012*

ing's impact on water quality (see p. 1468) and whether the shale gas boom will help or hurt efforts to curb climate change (see p. 1472). They are also exploring potential links to human-caused earthquakes (*Science*, 23 March 2012, p. 1436), air pollution, and habitat fragmentation.

Basic researchers are also sizing up this new resource. They are searching for life deep in shale deposits (p. 1470) and potentially transformative ways to convert the methane in natural gas into liquid fuels and other chemicals (p. 1474). Some are examining the origins of shale gas, trying to determine whether it is primarily the product of methane-producing microbes or thermal breakdown of organic matter (see p. 1500). And analysts continue to debate just how much shale gas is really out there—and how quickly the current boom could turn bust.

For the moment, any downturn seems distant. Canada, which already gets 15% of its natural gas from shale, is ramping up production. China, Europe, and Russia are eyeing their essentially untapped shale deposits. Public opposition to fracking is growing in some nations, however, and drilling technologies that have performed well in the United States may not work well overseas, where the shale can have very different properties. One thing is clear: The shale gas revolution is still in its infancy, with plenty of growing pains ahead. ■

Published by AAAS

Will fracking put too much fizz in your water?

Leaky gas wells loom large in debate over drilling's impact on water quality

By **Erik Stokstad**

On New Year's Day 2009, the well in Norma Fiorentino's backyard exploded. An electric pump ignited methane that had seeped into her water well, and the blast was powerful enough to tear apart a concrete pad. That was just the beginning of the fireworks. Nineteen families in rural Dimock Township, Pennsylvania, blamed well contamination on stray methane leaking from nearby boreholes. They had been rapidly drilled by Cabot Oil & Gas Corp., which was searching for natural gas in the deep Marcellus Shale. After a lawsuit and government investigations, Cabot agreed to provide the families with cash settlements and water purification systems, but insisted that the methane had come from natural sources, not its gas wells.

The Dimock controversy, featured in the popular movie *Gasland*, shone a spotlight on the potential risks associated with the U.S. shale gas boom. Around the world, media have highlighted dramatic ruptures of pipelines, waste spills, well blowouts, and tanker truck crashes. The problems helped persuade officials in nearby New York state to declare a moratorium on fracking—the hydraulic fracturing that cracks rocks and coaxes natural gas from the Marcellus and other shale formations (see p. 1464). France, Bulgaria, and other countries have also banned fracking.

Perhaps the biggest fear is the potential to pollute drinking water. Although the new wave of high-volume fracking typically targets geological formations that are more than a kilometer down—far deeper than most drinking water wells and aquifers—many communities worry that they could become the next Dimock, their water tainted with methane or chemicals. Fracking opponents point to widespread complaints of contamination near gas wells. But industry advocates claim that there has never been a documented case of fracking harming drinking water.

Who's right? A growing corps of researchers is trying to find out. Some are testing water wells, while others comb through state environmental records. One team is trying to take advantage of an unusual natural experiment, documenting water quality along the border between frack-free New York and frack-heavy Pennsylvania. Meanwhile, gas companies are funding their own vast surveys of predrilling water quality—if only to defend themselves against postdrilling lawsuits. And many eyes are on the Environmental Protection Agency (EPA), which later this year is expected to release a much anticipated national study of fracking's effect on water.

Big money is at stake. If fracking is shown to be a major threat to water quality, companies could face potentially expensive regulation and lawsuits that could keep them from tapping shale formations holding natural gas worth billions of dollars. If not, the finding could hasten the end of moratoriums in New York and elsewhere. The research "will impact what counties, states, and countries will do, whether they give incentives to drill or put bans in place," says Robert Jackson, a hydrogeologist at Stanford University in Palo Alto, California.

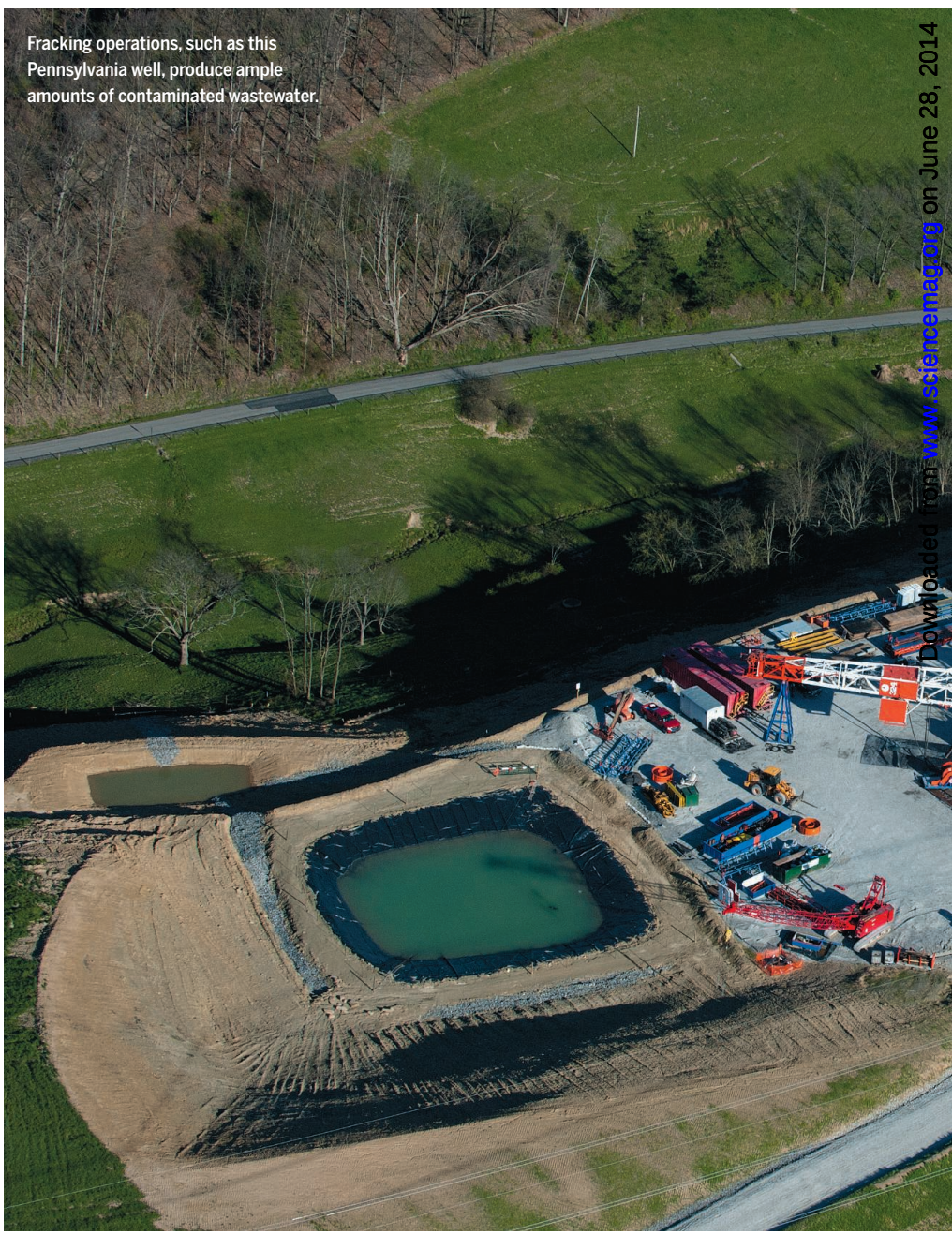

Fracking operations, such as this Pennsylvania well, produce ample amounts of contaminated wastewater.

Downloaded from www.sciencemag.org on June 28, 2014

Published by AAAS

WATER IS AN ESSENTIAL INGREDIENT in fracking. Once a company has drilled a deep horizontal borehole, workers pump in an average of 15 million liters of pressurized water to break open the shale—10 to 100 times more water than in a conventional, vertical gas well. About 20% of this fluid, which is mixed with sand and chemicals to keep the fractures open, then flows back out of the well. With it comes so-called produced water, the mildly radioactive brine that permeates the shale itself.

Improperly managed, flowback waste can cause serious pollution. In Pennsylvania, Marcellus well operators now recycle most of the flowback to frack new wells. (In other regions, they dispose of the fluid by pumping it deep underground.) But until 2011, some trucked the fluids to municipal sewage treatment plants, which weren't equipped to deal with them. Worse, onsite storage ponds failed and rogue contractors dumped the dregs into streams. Such problems are not unique to fracking; conventional oil and gas wells create waste, too, although in smaller amounts. But once the pace of Marcellus fracking slows, some analysts fear, companies may be faced with an excess and nowhere to put it. "We see this potential train wreck on the horizon," says Mark Brownstein of the Environmental Defense Fund in New York City.

PHOTO: MARTHA RIEL

One irony of the fracking controversy is that the fracturing itself doesn't worry scientists. Because it typically takes place at great depths, any larger cracks are quickly squeezed shut by the weight of the overlying rock. So experts have assumed that gas or fluids are unlikely to escape. A 2004 study by EPA, for example, concluded that fracking posed little threat to underground supplies of drinking water; the finding helped persuade Congress in 2005 to exempt the practice from regulation under the federal Safe Drinking Water Act.

More recent studies are also finding scant evidence that contaminants are migrating up through fractures created by fracking. In Pennsylvania, scientists at the Department of Energy (DOE) have spent 9 months monitoring tracers injected into six commercial wells drilled into the Marcellus Shale. So far, there is no sign that gas or fracking fluids are moving toward the surface, reported DOE's Richard Hammack and colleagues this past August at the Society of Petroleum Engineers Eastern Regional Meeting. (A lingering concern, however, is the presence of countless abandoned oil and gas wells, some dating back a century, which could also provide a conduit for gas or fluids.)

The greater risk—for all wells—is that fluids or gas will escape through a faulty casing into shallow aquifers. To prevent leaks, crews pump cement into the 2-centimeter space between the pipe and the surrounding rock. But if the cement has gaps, contaminants can bubble up. Rarely, the steel pipe fractures or its threaded joints leak.

Poor cementing is a well-known hazard in conventional wells. In one tragic incident in 2004, gas escaped from a conventional well in Jefferson County, Pennsylvania, collected in a home basement, and exploded, killing a couple and their grandson. But before the media attention to the fracking surge, few people heard of the disaster. "It barely got a mention in the newspaper," says Fred Baldassare of ECHELON Applied Geoscience Consulting in Murrysville, Pennsylvania.

Now, researchers are examining how often Pennsylvania's fracking wells encounter similar problems by analyzing a well inspection database assembled by the state's Department of Environmental Protection (DEP). One effort, led by Susan Brantley of Pennsylvania State University (Penn State), University Park, concluded that inspectors found well construction problems at 3.4%, or 219, of the 6466 wells examined between 2008 and 2013; 16 were cited for leaking methane into ground water, her team reported in a review in *Science* (17 May 2013, p. 826), updated this month in the *International Journal of Coal Geology*. "From what we can see," she says, "the frequency of big problems is pretty low."

Published by AAAS

That estimate is probably too low, says engineer Anthony Ingraffea of Cornell University, who has also been analyzing the DEP records. He and colleagues pored over some 75,000 records for 41,000 gas wells inspected between 2000 and 2012. Using statistical techniques to make up for variations in how thoroughly inspectors scrutinize wells and document their visits, they estimate that at least 6% of Pennsylvania's more than 7000 fracking wells have compromised casings, compared with 1% of conventional wells. The findings are in review at the *Proceedings of the National Academy of Sciences* (*PNAS*), but the team is already trying to figure out why fracking wells have the much higher rate of problems. The numbers also suggest that more than 45% of wells fracked in northeast Pennsylvania since 2009 will end up leaking.

And worse is yet to come, he fears. The number of wells is still climbing, despite a recent slowdown. Drillers may be just 8% of the way toward exhausting the Marcellus Shale, he notes, although estimates of the amount of recoverable gas vary. "The cumulative impact will be unbelievable," Ingraffea predicts.

Although methane itself isn't toxic, the gas can stir up metals and minerals, particularly in old water wells. The key question for most people is whether any of the leaking methane is reaching their drinking water.

In a heavily drilled part of northeastern Pennsylvania, one study suggests that the answer is yes. A team led by Stanford's Jackson, then at Duke University in Durham, North Carolina, measured concentrations of methane at 141 drinking water wells in six counties, an area that includes Dimock. Wells within 1 kilometer of a natural gas well had methane concentrations that were six times greater than those of more distant water sources, they reported in *PNAS* in July 2013. And the chemical signature of the gas (determined by isotopic studies) closely resembled that of gas from the Marcellus Shale. The problem, they believe, was defective casings in fracking wells.

Sherry Vargason can ignite her kitchen faucet.

Industry experts agree that the errant gas leaked from faulty well casings. But they doubt that the source was the Marcellus. Instead, they think it came from younger, shallower geological formations not touched by fracking. About 80% of water wells in the region have some level of this methane, they note, which may be leaking into water wells through natural fractures. This possibility is suggested by several studies, including work in the May/June 2013 issue of *Groundwater* by geochemist Lisa Molofsky and colleagues at Cabot and at GSI Environmental Inc. in Houston, Texas. After analyzing methane data from 1701 water wells in northeastern Pennsylvania, Molofsky's team concluded that higher concentrations were linked to water wells located in val-

Searching for life in the deep shale

By **Elizabeth Pennisi**

For energy developers, the geological formation known as the Marcellus Shale represents a rich new source of natural gas. For environmental engineer Paula Mouser and geochemist Shikha Sharma, it represents a potentially rich source of new microbes.

Following up on some tantalizing but unconfirmed clues, the pair is looking for life in the deep, hot layers of rock—and considering how the gas boom might affect long-isolated ecosystems. Drilling companies care, too, because deep-dwelling microbes could corrode equipment, clog pipes, and even contaminate the gas. Microbes can "really affect the bottom line," says Mouser, who works at Ohio State University, Columbus.

"Next to nothing is known about the biodiversity of shale deposits," says Simon Malcomber of the National Science Foundation (NSF) in Washington, D.C., which is funding the work. Indeed, it's hard to imagine a more inhospitable environment than the Marcellus and similar gas-bearing formations (see map, p. 1467). The beds typically sit a kilometer or more down, where pressures are 500 times greater than those found at the surface, and temperatures exceed 70°C. One study in the 1990s, however, was able to culture microbes from shallower deposits of shale, but it came before genomic technologies made a more comprehensive look possible.

In 2012, Sharma—who works at West Virginia University in Morgantown—began to think deeper shale also hosted microbes. She was analyzing carbon isotopes in water from various kinds of wells and aquifers, looking for clues that would distinguish water coming from different underground sources. While studying a fracking well in Pennsylvania's Marcellus Shale, Sharma noticed that the water flowing out of the well "had a very different signature" than what had been injected. The data suggested that the returning fluid had

PHOTO: MARK THIESSEN

Published by AAAS

Some landowners complain about leaks from pipes carrying wastewater from fracking sites.

leys, where abundant natural fractures allow gas to escape from shallow sources. In addition, Molofsky and others suspect that the study by Jackson's team may have been biased, because it focused on an atypical contamination incident.

Industry experts also argue that leak risks are going down as drilling companies better understand the complexities of local geology and fracking well design. They are using cements enhanced with latex and other additives to plug natural fractures in the rock, for instance. And they routinely run geophysical tests during drilling to check for problems. It's the kind of practical experience that can't be gained in a research lab or during a drilling moratorium, ECHELON's Baldassare notes. Ingraffea and others, however, remain dubious that leaks will decline.

RESOLVING WHETHER FRACKING is a serious threat to water quality will take time. EPA's ambitious nationwide study, which Congress requested in 2009, has been slowed by political controversies over its scope. It's also a technical and logistical challenge, involving far-flung field studies. Another major obstacle is the lack of predrilling data about water quality in many areas. Although gas companies have tested tens of thousands of water wells above active and potential fracking zones, they haven't widely shared the data. "The lack of baseline information is a really serious issue," says Kate Sinding of the Natural Resources Defense Council in New York City.

Some clarity could come from an unusual situation found along the New York–Pennsylvania border. New York hasn't yet allowed fracking in its part of the Marcellus Shale, so researchers are parachuting into the border zone to quickly document water quality before a single new well is drilled. Laura Lautz of Syracuse University in New York, for example, is analyzing samples from more than 200 homeowner wells chosen at random in southern New York.

A coarser but cheaper approach to assembling predrilling baselines could come from researchers at the U.S. Geological Survey (USGS) and partner institutions. Rather than sample scores of individual wells, they are measuring methane in streams, which collect ground and surface water from a large area. Preliminary work in Utah, North Carolina, and Pennsylvania suggests that the methane persists long enough in some types of streams to provide meaningful measurements, USGS hydrologist Victor Heilweil and colleagues reported in the July/August 2013 issue of *Groundwater*. If perfected, the approach "gives a better chance of seeing the big picture," Heilweil says.

This approach could also allow concerned citizens to monitor the effects of drilling. Local groups, for example, could collect water samples, add chemicals to kill microbes that would otherwise consume any methane, and send the samples to a lab for analysis. Such monitoring methods need to mature, however, and researchers say it's also crucial to have more detailed and complete databases of drilling violations. Until then, the debate over fracking's impact on water quality is likely to endure. And for communities already experiencing drilling, says Penn State's Brantley, the shale gas boom is like "a giant experiment being run in our backyard." ■

mixed with deep water that either today or in the past was filled with microbes that produce methane, known as methanogens.

At about the same time, a team led by Mouser was finding similar hints in a study that screened flowback water from another Marcellus fracking well for microbial DNA. The early flowback contained a variety of salt-tolerant microbes that were not present in the injected water, the team reported online on 6 May in *Environmental Science & Technology*.

Mouser and Sharma suspect microbes are thriving in the brine that fills the shale's pores—and they are hoping their new NSF-funded study will prove it. This year, they plan to work with fracking companies to collect pristine shale samples from new boreholes, before injected surface water contacts the rock. They will get a full sense of what's down there by sequencing the microbial DNA. Then they will try to grow laboratory samples of any deep-living microbes they discover.

The information ultimately could help energy companies improve their methods, the researchers say. Drillers already add biocides to fracking fluids to protect against corrosion caused by bacteria, Mouser notes, but the chemicals might not be effective against deep-dwelling microbes. At the same time, certain fracking additives may actually promote the growth of some microbes, helping gum up wells. And if sulfide-producing microbes establish themselves, their waste products can contaminate the gas, lowering its value. ■

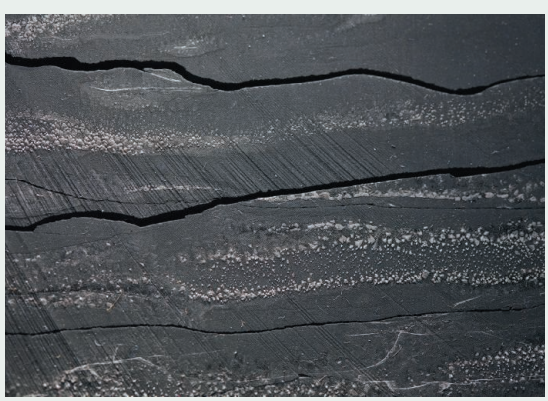

A chunk of Marcellus Shale, where fracking could affect microbes.

PHOTOS: (TOP TO BOTTOM) SCOTT GOLDSMITH; MARK THIESSEN

Published by AAAS

Hunting a climate fugitive

Plugging methane leaks in the urban maze could be key to making shale gas climate-friendly

By **Eli Kintisch,** ***in Boston***

On a windy morning in May, graduate student Kathryn McKain crouches by a ledge near the top of one of Boston's tallest skyscrapers, checking some air sampling equipment. McKain, of Harvard University's engineering department, likes more than just the commanding view: From 215 meters up, the greenhouse gas measurements she's making aren't biased by pollution from individual sources below. "You're really getting measurements representative of the whole city," she says.

Sometimes a falcon lands nearby, presumably using the perch to spot pigeons. The scientists are hunting something else: methane, an invisible but potent heat-trapping gas. They're trying to figure out how much is leaking from the city's vast network of natural gas pipes and tanks.

It's a question that is haunting academics, politicians, and executives who have hailed the boom in shale gas production (see p. 1467) as aiding a critical transition to climate-friendlier energy sources. Burning natural gas releases about half as much carbon dioxide (CO_2) per unit of energy as burning coal and a third less than oil. And as hydraulic fracturing (fracking) methods have helped flood energy markets with relatively cheap natural gas, it has begun to replace coal as the fuel of choice for producing power in the United States. About 28% of the nation's electricity now comes from natural gas, up from 19% in 2005. From 2005 to 2012, U.S. CO_2 emissions dropped by about 11%, and one study said that fuel-switching to gas is responsible for as much as half of that drop. President Barack Obama's proposed new restrictions on carbon pollution from power plants are likely to accelerate the transition.

Many climate policy analysts believe that natural gas can provide a "bridge" to a future energy economy by buying time to develop renewable energy technologies. But that bridge may be more rickety—and less helpful—than envisioned. The reason: Methane, the primary component of natural gas, is itself a potent greenhouse gas, with a warming effect between eight and 72 times stronger than that of CO_2, depending on the time period over which one does the accounting. And recent studies have suggested that large quantities of unburned methane are leaking into the atmosphere—not just from production wells and major pipelines but also from gas lines and tanks that distribute the fuel in cities. The leaks could negate much of the climate benefit of switching to gas.

"Clearly natural gas has potential to help," says Steve Hamburg, chief scientist of the Environmental Defense Fund (EDF) in Boston. "But to meet that potential we have to minimize methane emissions." EDF and other government and private groups have launched a flurry of studies, including McKain's research in Boston, to pin down just how much methane is escaping, and where. At the same time, the concerns are fueling fresh debate over methane's importance as a warming gas—and whether regulators should be doing more to control it.

Infrared imaging of pipes and tanks can reveal methane leaks (dark clouds, lower image).

METHANE PLAYS AN OUTSIZED ROLE in climate. Although it is 200 times less abundant in the atmosphere than CO_2, the way its four carbon-hydrogen bonds jiggle when struck by infrared radiation makes it a highly effective warmer. Overall, methane concentrations are now three times higher than in the preindustrial era, and the molecule may be responsible for as much as one-quarter of current global warming. So climate researchers took notice in 2008, when methane concentrations in Earth's atmosphere began rising after a decade of flat or declining levels.

Some of that atmospheric methane comes from natural sources, such as gas seeps or wetlands. But an estimated one-fifth of the global total—and about 30% of U.S. methane emissions—comes from the natural gas infrastructure, from wells to end users, and the fracking boom is adding thousands of potential new sources of emissions. Getting a handle on well emissions is proving particularly difficult, with recent studies coming to opposite conclusions. Last year, in the biggest study of its kind to date, researchers from the University of Texas, Austin, measured emissions at 190 gas industry sites, including 150 production sites. This bottom-up approach, part of the EDF effort, concluded that existing Environmental Protection Agency (EPA) estimates of industry methane emissions were a little low.

But a top-down study published last year, using more than 10,000 measurements taken from aircraft- and tower-mounted instruments nationwide, concluded that EPA estimates are roughly 1.5 times too low. The study, published in the *Proceedings of the National Academy of Sciences* (*PNAS*) and led by McKain's adviser, geochemist Steven Wofsy of Harvard, used a weather model to track emissions back to their sources.

What might explain the discrepancy? One answer may be so-called superemitters. Just a few components at a drill site—a leaky pipe, valve, or compressor, for example—may be responsible for the lion's share of emissions. Bottom-up studies that miss sites with superemitters may underestimate leaks, while top-down studies might come up with numbers that are dominated by a few major leaks. Overall, some researchers estimate that just 20% of production leaks could account for some 80% of emissions.

To resolve the issue, last October EDF convened 12 research teams using a variety of ground-, air-, and mobile-based measurement methods to conduct a coordinated analysis of emissions at one center of the fracking boom, the Barnett Shale formation in north Texas. The teams are expected to release results soon. But a major role for superemitters would raise hopes that production leaks might be relatively easy to plug. "It raises the possibility of … mitigating them for a big impact," Brandt says.

PLUGGING PIPELINE LEAKS could be a tougher task. A 2005 *Nature* study of Russia's massive pipeline system concluded that 1.4% of the total methane it moves escapes into the atmosphere—three times more than the estimated well losses. Researchers believe

PHOTOS: ENVIRONMENTAL DEFENSE FUND (2)

Downloaded from www.sciencemag.org on June 28, 2014

Published by AAAS

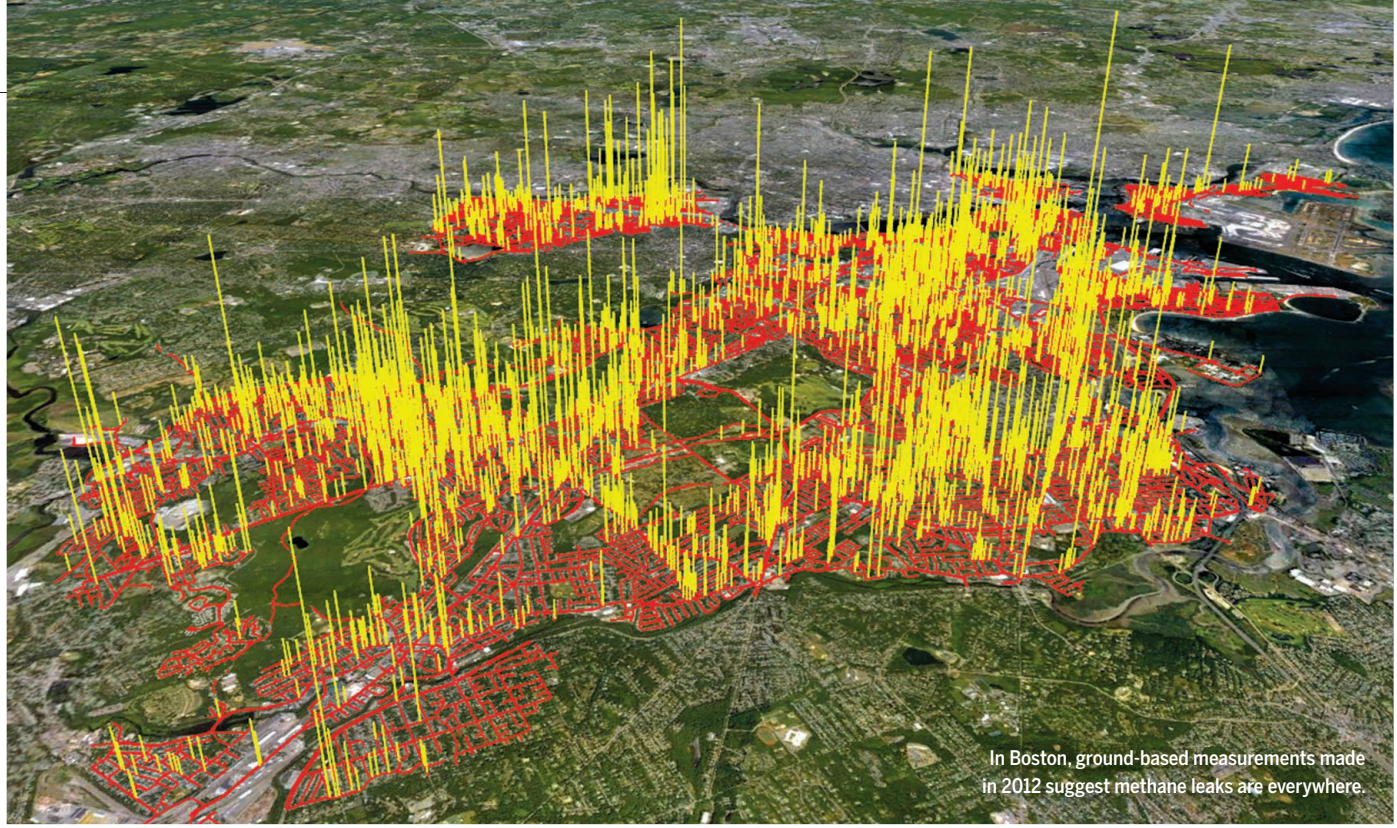

In Boston, ground-based measurements made in 2012 suggest methane leaks are everywhere.

PHOTO: N. G. PHILLIPS *ET AL., ENVIRONMENTAL POLLUTION* **173** (FEBRUARY 2013); WITH PERMISSION FROM ELSEVIER

the loss rate is similar in the U.S. system, which includes nearly 500,000 kilometers of pipe. To confirm that suspicion, researchers at Colorado State University are now working with seven gas firms to use tracer gases to track leaks.

Meanwhile, Harvard's McKain and other researchers are trying to understand how much methane escapes at the far end of the supply chain, including the maze of small pipes and tanks that feed industrial and household consumers in major cities such as Boston, Los Angeles, and Washington, D.C. It's no simple task: It's challenging to differentiate emissions from natural gas systems from those originating in landfills, wetlands, or geologic formations. One solution is to track ethane, which is found alongside methane from natural gas pipelines, but usually not in emissions from other sources. In Los Angeles, however, gas from ubiquitous natural oil and gas seeps has virtually the same ethane signature as pipeline gas, making it very hard to tell the two apart.

As in gas well studies, urban researchers are taking bottom-up and top-down approaches. In Washington, D.C., and Boston, scientists have gotten behind the wheel to conduct street-by-street surveys with car-mounted instruments, uncovering previously undocumented—and occasionally dangerous—methane leaks. The Boston project, co-led by Harvard's Wofsy and biogeochemist Lucy Hutyra of Boston University, is taking a broader view, mounting static instruments on buildings in the city and suburbs to get the big picture. A computer model built by McKain combines weather patterns with methane measurements to infer where the emissions are coming from and how they vary over time.

The team is still crunching the numbers, but it appears that methane emissions in Boston "are really higher than people are expecting them to be," Wofsy says. The total includes leaks and deliberate venting by industry, but it's not clear that there are superemitters that will be easy to target for reductions, Hutyra says. "This is a distributed problem," she says, created by a multitude of relatively small sources.

That pattern could create huge headaches for companies and policymakers aiming to reduce methane emissions. The industry has made a "continued effort" to reduce leakage, says Richard Meyer of the American Gas Association in Washington, D.C. But the financial incentive for chasing down thousands of tiny leaks is essentially nonexistent—especially if gas prices remain relatively low. The irony, notes EDF's Hamburg, is that a 1% or 2% loss rate might do little damage to a company's bottom line—but have a real impact on warming. Still, his group has commissioned a study suggesting that the gas industry could cost-effectively plug about 40% of existing leaks, and it argues that society overall would reap even greater economic benefits if regulators stepped in to require greater reductions. Some states, meanwhile, are already taking steps to require gas companies to do more to identify leaks—sometimes by using infrared cameras that can "see" invisible methane—perhaps with stricter regulation in mind.

JUST HOW MUCH ATTENTION methane should get from regulators is the subject of debate. Many scientists argue for aggressively cutting methane leaks, saying that "could buy us time" to avoid climate tipping points, as atmospheric scientist Drew Shindell of NASA's Goddard Institute for Space Studies in New York City puts it.

Others say CO_2 should remain the key target. Although it is a weaker warmer than methane, it is fiendishly stable, able to survive in the atmosphere—and continue trapping heat—for centuries. Atmospheric methane, in contrast, dies relatively young, typically lasting just a dozen years or so before being dismantled by chemical reactions. What's more, asking policymakers to tackle methane might slow already lagging efforts to cut CO_2, these researchers note. That scenario is "[c]onsistent with limited capital and political will," wrote Harvard researchers Julie Shoemaker and Daniel Schrag last year in *Climatic Change*.

To see how a focus on methane might affect CO_2 mitigation, Shoemaker ran modeling experiments simulating various delays in cutting CO_2 pollution. Each 15-year delay in curbing CO_2, they found, caused the planet to warm by an additional 0.75°C by 2400. (A delay in cutting methane emissions has little long-term effect because methane doesn't accumulate.) Such sobering results suggest "it can't be cutting carbon dioxide or cutting methane," Schrag says. "We've got to develop policies that do both." ■

Published by AAAS

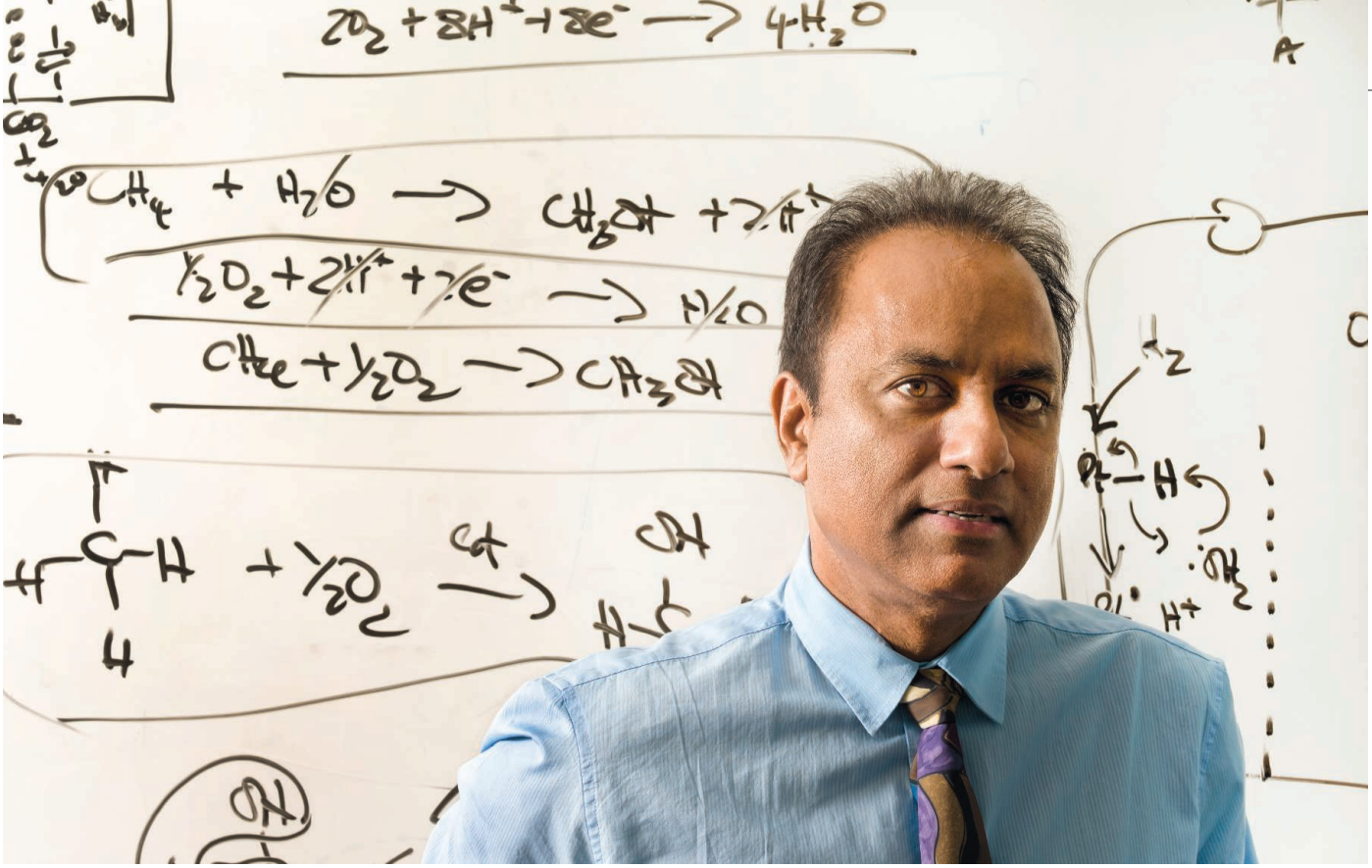

The bond breaker

By transforming methane, chemist Roy Periana aims to turn natural gas into cheap feedstocks for chemical firms

By **Robert Service**

Many chemists strive to be grand architects, building imposing molecular edifices with dozens or even hundreds of atoms, bonds twisting this way and that. Not Roy Periana. He has spent his career focused on just one bond, a link between a carbon and a hydrogen atom in a molecule of methane, the main component of natural gas. "You might say it's kind of sad," Periana says, chuckling. "But if I can control the reactivity of this one bond, I can change the world."

He's getting close. Working with colleagues at the Scripps Research Institute in Jupiter, Florida, Periana has come up with a new way to tweak this bond. If he can perfect his technique, it would give chemists a cheap, efficient way to convert natural gas to methanol and other key starter materials for the petrochemical industry—materials that can then be turned into liquid fuels and commodity chemicals. It's a simple change that could have profound effects—especially as the shale drilling boom provides abundant new supplies of natural gas. It could upend the petrochemical industry, the world's largest economic enterprise, because it would allow the industry to rely on gas rather than oil. It could also profoundly alter global energy security, by providing gas-rich nations with a way to break their dependence on imported oil. The potential financial impact, Periana notes, is enormous: "You're looking at a gazillion dollars."

Given such weighty implications, it's not surprising that chemists have been trying to orchestrate the methane transformation for decades, mostly by using catalysts that can cause the reaction without being consumed themselves. "This has been one of the holy grails of catalysis," says George Huber, a chemist at the University of Wisconsin, Madison. But to date, the methods have been balky or too expensive.

That's where Periana's approach comes in. He's using a different set of would-be catalysts—cheap, abundant metals—plus some extra chemical tricks to convert methane to methanol at low temperatures. But his team still faces major technical obstacles—and some critics suggest Periana is prone to premature hype. Still, many researchers are watching closely. "Roy," says James Mayer, a chemist at the University of Washington, Seattle, "is one of the most imaginative people in the community."

"MY WHOLE VISION was to be a scientist," says Periana, who is 57. But he grew up in the small capital city of Georgetown in what was then British Guiana—now Guyana—in South America. His school had meager science facilities, and Periana spent countless hours in the city's public library, alone with musty, outdated encyclopedias and textbooks. He taught himself how to build a telescope using his grandfather's glasses, constructed his own Bunsen burner, and, of course, synthesized every type of explosive a teenage boy could desire. "The pivotal moment was reading a book that said if you could invent a machine that duplicated photosynthesis, you could feed an entire city," Periana recalls. "I knew then I was going to be an inventor."

Periana's father, a photographer, befriended a U.S. diplomat, who helped secure a U.S. residence permit for Roy. Periana studied at the University of Michigan, Ann Arbor, and ultimately earned his Ph.D. at the University of California (UC), Berkeley, in 1985. There he discovered the problem he's been trying to solve ever since: finding a cheaper, better way to transform gaseous methane—a member of a large class of molecules known as hydrocarbons—into liquid chemical feedstocks.

The conventional way of producing those feedstocks starts with crude oil, a collection of liquid hydrocarbon molecules that are far

PHOTO: MAGGIE STEBER

Downloaded from www.sciencemag.org on June 28, 2014

Published by AAAS

larger than methane. Chemical engineers first distill out midsize hydrocarbons. Then, they use heat and catalytic minerals to break apart the larger "heavy" hydrocarbons, in a process known as cracking.

An alternative approach starts with much smaller hydrocarbons, such as the methane, ethane, and propane in natural gas. Chemists then try to stitch them together to form larger, liquid hydrocarbons. The challenge is the way methane is put together. The molecule consists of one carbon atom surrounded by four hydrogen atoms (CH_4). Each hydrogen shares two electrons with the central carbon, an extremely stable configuration that makes the atoms unwilling to react.

One way to trigger a reaction is to ignite methane. The heat gives methane's carbon atom enough energy to shake free from its hydrogens and react with oxygen. Unfortunately, burning methane obliterates all of its C-H bonds, converting the hydrocarbon to CO_2 and heat. That's nice if you want to heat your house, but not if you want to make liquid fuels.

Nearly a century ago, chemists came up with molecular knitting technologies that leave some of methane's bonds intact. But they are too expensive for most uses because they require relatively high temperatures (between 800°C and 900°C) and costly facilities. (The cost is one reason oil companies each year burn off roughly $40 billion worth of natural gas recovered with oil.)

In the 1970s and 1980s, some researchers thought they'd found a better solution. They discovered that when lithium and a few other metals were paired with oxygen, they would form catalysts that broke those C-H bonds without so much heat, and some even produced small amounts of methanol. But the catalysts were so hungry for C-H bonds that they cannibalized the methanol as fast as it was created. So, after decades of frustration, most researchers gave up. "We ran out of ideas," says George Whitesides, a chemist at Harvard University.

EARLY ON, Periana realized that the failed cannibal catalysts had something in common. They worked by generating other compounds that were "radicals" in chemistry lingo, meaning they have a lone electron in one orbital around the nucleus. That makes the radical eager to either gobble up an additional electron to fill the orbital or cough one out to empty the orbital.

Periana thought a less radical approach might work better. While at UC Berkeley, he helped discover catalysts that didn't use radicals to split C-H bonds in hydrocarbons. But these catalysts, which belong to a part of the periodic table called transition metals, were too fragile and expensive for industrial use. In 1993, while working in California at Catalytica Inc., he and his colleagues developed a potentially practical catalyst that also split the bonds, this time based on mercury 2+ (Hg^{2+}). On the periodic table, Hg^{2+} is next to a cheaper, more abundant class of metals known as main group metals. Again, however, difficulties jacked up the cost; in particular, the team couldn't figure out how to get around a problem involving excess water, which stalled the reaction by quenching the catalyst's thirst for electrons. So he circled back to other transition metals, spending decades on essentially fruitless experiments. "We were stuck," Periana says.

Until last year, when his lab again shifted course to work on thallium (Tl), lead (Pb), and other more abundant main group metals. To their surprise, they found that Tl^{3+} and Pb^{4+} generated methanol—even in the presence of the water that had stalled the earlier mercury catalyst. "Then the eureka moment hit us," Periana says.

The key insight, he says, involved something called the water exchange rate constant. It refers to the fact that atoms don't bond in the static way we typically imagine. Instead, they are more like the shifting partners at a swirling square dance than couples at a formal ball who never separate. And it turns out that different metals "exchange" their water partners at vastly different rates. Thallium's trading rate, for example, is 19 orders of magnitude higher than platinum's.

Such speed dating presents thallium with plenty of opportunities to chassé up to a methane molecule and snag a pair of electrons from a C-H bond. And in the presence of acetic acid and other solvents, the thallium connects what's left of the methane to a molecule in the solvent, creating an alcohol ester. Add water, and you get methanol and more acetic acid.

Periana's team still faces a thorny problem, however: Thallium ions wind up with two extra electrons that must be stripped off to start the cycle anew. To make that process economical, the chemists can't use expensive compounds. Instead, they'll likely need to use just oxygen from air, but have yet to demonstrate that they can do it.

As a result, most chemists are reluctant to call the Periana lab's findings a true breakthrough. "It's still a long way from something that is practical," says John Hartwig, a hydrocarbon chemist at UC Berkeley. Privately, others go further, arguing that Periana routinely overstates his findings, making it sound like they will soon revolutionize the petrochemical business. "With Roy there tends to be more hand waving and less deliverable on the ground" says one U.S.-based chemist.

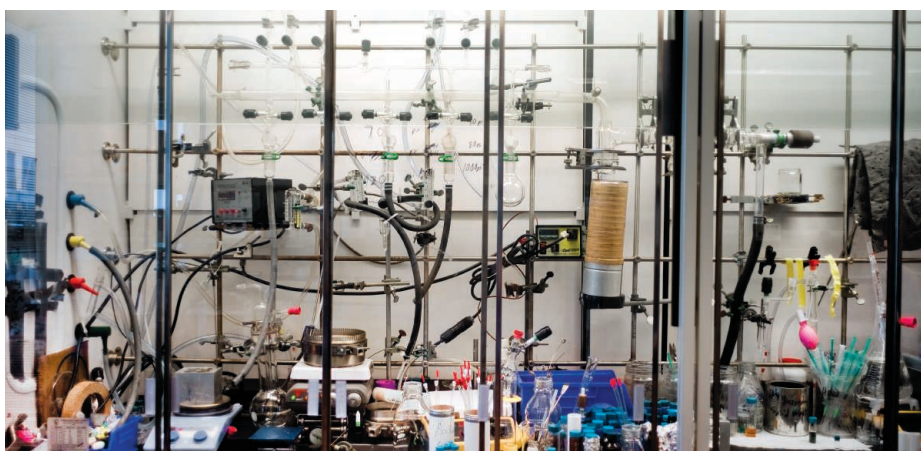

To be successful, Periana's team will need to scale up their laboratory experiments.

PHOTO: MAGGIE STEBER

That said, many outsiders think Periana's scheme just might work. The new insights into metal catalysts are "really important," says Harvard's Whitesides, and "whenever you open the door to a new possible class of reactions, people will take advantage of it."

Periana's team believes it has a solution to the extra electrons. In the 1960s, researchers developed a broad literature on using oxygen in air to snatch electrons from copper, in a process used to make a commodity chemical called acetaldehyde. A similar process will enable them to economically tap air to fuel the metal catalysts, predicts Michael Konnick, a research chemist in Periana's group. "I have no doubt," he says, that "the laws of the universe say it can be done."

It appears that some venture capitalists agree. Periana says he's already seen interest from investment firms and large chemical companies in starting a company to develop the technology. If it works, Periana will finally achieve his goal of cheaply tweaking his favorite chemical bond, and just maybe change the world in the process. ■

Published by AAAS

RESEARCH

Yeast evolves along different paths toward the same goal

Kryazhimskiy et al. *p. 1519*

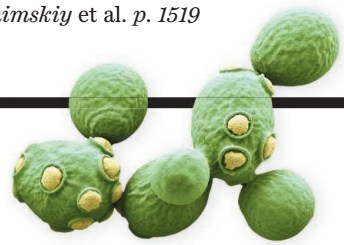

IN *SCIENCE* JOURNALS

Edited by **Stella Hurtley**

NONHUMAN GENETICS

Only one way to make an electric organ?

Electric fish have independently evolved electric organs that help them to communicate, navigate, hunt, and defend themselves. Gallant *et al.* analyzed the genome of the electric eel and the genes expressed in two other distantly related electric fish. The same genes were recruited within the different species to make evolutionarily new structures that function similarly. — LMZ

Science, this issue p. 1522

SENSORY BIOLOGY

How hawkmoths sniff out a flower

Pollinators such as butterflies and bees are the true targets of the flower odors we love so much. Though we might imagine insects "following their noses," the wealth of odors in the real world can drown out the smell of a flower, making it hard to find. Riffel *et al.* found that hawkmoths find angel's trumpets by creating a neuronal picture within their antennal lobe, the part of the moth brain that receives olfactory signals from the antennae (see the Perspective by Szyszka). The picture represents both the flower and the background odors. Finding a flower involves a complex reading of both background and target odors, and changes in the background odors—including human pollutants—can hinder the process. — SNV

Science, this issue p. 1515; see also p. 1454

EARLY ANIMALS

Building coral reefs in ancient times

540 million years ago, in the dawn before the Cambrian explosion, evolution was setting the stage for the global rise of animals. Before they took over the seas, the earliest animals developed strategies to defend themselves against predators. These strategies, which remain common today, include forming skeletons and building reefs. Penny *et al.* discovered a massive fossil reef deposit in Namibia made up of tiny cone-shaped early animals known as *Cloudina*. The reef, which is 20 million years older than other ancient reefs, was probably formed as the *Cloudina* adapted to benefit from reefs, which protect the animals and allow them to feed more efficiently. — NW

Science, this issue p. 1504

QUANTUM METROLOGY

Measuring tiny forces with atomic clouds

For projects such as detecting gravity waves, physicists need to measure tiny forces precisely. Schreppler *et al.* developed an extremely sensitive method for force measurement. They applied a known force on a cloud of ultracold rubidium atoms in an optical cavity. The force caused the atoms to oscillate, and the researchers used optical measurements to monitor the motion. Under optimal conditions, the authors could measure forces with a level of sensitivity only four times

Downloaded from www.sciencemag.org on June 28, 2014

PHOTOS: (TOP TO BOTTOM) EYE OF SCIENCE/SCIENCE SOURCE; NORBERT WU/GETTY IMAGES

Published by AAAS

worse than the fundamental limit imposed by the Heisenberg uncertainty principle. — JS

Science, this issue p. 1486

VIRUS ENTRY

How Lassa virus breaks and enters

Lassa virus, which spreads from rodents to humans, infecting about half a million people every year, can lead to deadly hemorrhagic fever. Like many viruses, Lassa virus binds to cell surface receptors. Jae *et al.* now show that to enter a cell, the virus requires a second receptor, this one inside the infected cell. This requirement sheds light on the "enigmatic resistance" of bird cells to Lassa virus observed three decades ago. Although bird cells have the cell surface receptor, the intracellular receptor cannot bind the virus, stopping it in its tracks. — SMH

Science, this issue p. 1506

HUMAN COGNITION

Selecting the most successful strategy

The brain's prefrontal cortex helps us to make decisions in an uncertain and constantly changing environment. Donoso *et al.* present a model of human reasoning as an algorithm implemented in the prefrontal cortex (see the Perspective by Hare). Brain-imaging experiments supported this model. Depending on the prevailing circumstances, human reasoning can either adapt ongoing behavioral strategies or switch to previously learned strategies. Only when neither approach is appropriate will the brain create new strategies. — PRS

Science, this issue p. 1481, see also p. 1446

CANCER

Old drug learns new anticancer trick

Cancer researchers have been trying to develop drugs that inhibit angiogenesis, the formation of new blood vessels that nourish a tumor and allow it to grow. A few drugs that fight angiogenesis are now used for some cancers, but they are not always effective. Xu *et al.* report a potential addition to the anti-angiogenic armamentarium: nonsteroidal anti-inflammatory agents such as celecoxib, familiar remedies for arthritis. In mice, celecoxib inhibits blood vessel growth by a different mechanism than existing angiogenesis inhibitors. A combination of the two types of drugs was particularly effective in reducing tumor growth and spread. — YN

Sci. Transl. Med. **6**, 242ra84 (2014).

NANOFLUIDICS

Watching lead flow at the nanoscale

Microfluidic devices have recently become useful in commercial chemical synthesis. But what about fluid dynamics at the nanometer scale? Lorenz and Zewail used an electron microscope with nanosecond time resolution to capture images of molten lead flowing through a nanotube. They flash-melted the metal with a laser pulse to begin their flow measurements at a precise time point. The experiments offered insights into viscous friction as well as heat-transfer dynamics in a channel one-thousandth as wide as a strand of hair. — JSY

Science, this issue p. 1496

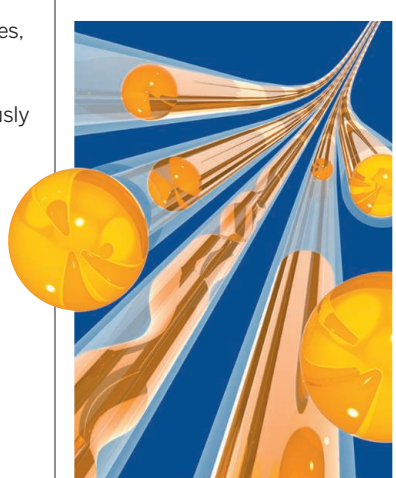

Conceptual view of molten lead flowing through zinc oxide nanotubes.

PHOTOS: (TOP TO BOTTOM) SHANNON KRINGEN/FLICKR; ULRICH J. LORENZ AND AHMED H. ZEWAIL/CALTECH

IN OTHER JOURNALS

Edited by **Kristen Mueller** *and* **Jesse Smith**

A rose petal's textured surface effectively repels water.

MATERIALS SCIENCE

Getting in shape to stay dry longer

Many textured surfaces commonly found in the natural world, such as a rose petal, repel liquids extremely well. Taking a clue from Mother Nature, designers have begun to routinely incorporate surface textures into products ranging from waterproof outdoor clothing to self-cleaning windows. However, under high humidity or pressure, liquid can infiltrate some textured surfaces and reduce their superhydrophobic properties. Checco *et al.* used x-rays to probe the interface region between liquid and a variety of textured silicon surfaces to show that the specific structure of a textured coating affects how the coating fails. This strategy could facilitate the rational design of better water-repellent coatings. — ISO

Phys. Rev. Lett. **112**, 216101 (2014).

CANCER

Long unwinding road to cancer treatment

Cancer chemotherapy is infamous for harming healthy cells. This collateral damage causes the side effects that range from unpleasant (such as hair loss) to life-threatening (such increased susceptibility to infection). They can be particularly devastating for elderly patients. Promising new data may one day lead to a safer treatment for a type of acute myeloid leukemia, which first strikes patients at age 66, on average. Mazurek *et al.* found that when they blocked mouse genes from expressing an enzyme called DDX5, the leukemia cells died, but healthy bone-marrow cells were unharmed. DDX5 made the cancer cells proliferate; inhibiting DDX5 made the cells accumulate toxic molecules called reactive oxygen species, which contributed to cancer cell death. — PAK

Cell Rep. **7**, 10.1016/j.celrep.2014.05.010 (2014).

AGING

Metformin's recipe for a long life

Metformin, a drug commonly prescribed to treat type 2 diabetes, has side effects, but some of these are beneficial, such as fighting certain cancers and increasing longevity. By studying the worm *Caenorhabditis elegans*,

Published by AAAS

The now-extinct woolly mammoth.

EXTINCTION

Miss mammoths? Blame your ancestors

Imagine saber-toothed tigers, giant ground sloths, and car-sized glyptodonts—an armadillo relative—ranging across the entire planet. Only a few tens of thousands of years ago, such charismatic megafauna ruled the earth. What killed them—climate change or human activity? In the first global analysis of extinctions during the Pleistocene geological epoch, Sandom *et al.* found that the expansion of humans out of Africa most likely caused the extinctions over the past 100,000 years. The animals were easy targets: They lacked the fear of humans that comes with years and years of co-evolution. — SNV

Proc. R. Soc. London Ser. B **281**, 20133254 (2014).

a model of aging, De Haes *et al*. discovered the molecular basis for how metformin may prolong lives. In treated worms, metformin promoted mitochondrial respiration, a process that converts nutrients into energy for the cell. Mitochondrial respiration also produces byproducts called reactive oxygen species (ROS), which can react with proteins, harming them. When the worms produced limited amounts of ROS, however, the life span of worms increased. The increase in life span required a protein called peroxiredoxin-2, which is oxidized by ROS and may then activate other enzymes to produce effects that promote longevity. — LBR

Proc. Natl. Acad. Sci. U.S.A. 10.1073/pnas.1321776111 (2014).

CHEMISTRY

Knotty questions in molecular assembly

How would you tie a knot if you couldn't touch either end of the rope? In the past few years, chemists have solved that problem at the molecular scale by precisely designing strand fragments, then luring them into mutually overlapping arrangements around metal ions. Ayme *et al.* now have tested the limits of that approach, exploring how subtle changes to the strands affect the distribution of knots produced in the reaction. Specifically, the authors mixed two types of strands that differed only by the presence or absence of two oxygen atoms. They found that the types sorted themselves remarkably well in combination with iron ions: The longer strands assembled into cross-shaped groups of four, the shorter strands into star-shaped groups of five. — JSY

Angew. Chem. Int. Ed. **53**, 10.1002 anie.201404270 (2014).

COSMOLOGY

Universe inflation or dust emissions?

Doubt enshrouds what was supposedly the biggest discovery in cosmology in a decade. In March, researchers working with BICEP2, a telescope at the South Pole, reported that the pinwheel swirls they saw in the polarization of the cosmic microwave background—the Big Bang's afterglow—came from gravitational waves rippling through the infant universe. That, they said, was the first direct evidence of an exponential growth spurt called inflation in the early universe. But others noted that the signal might emanate instead from dust in our galaxy. Now, in the published paper, Ade *et al*. write that their models of galactic dust "are not sufficiently constrained ... to exclude the possibility of dust emission bright enough to explain the entire excess signal." — AC

Phys. Rev. Lett. **112**, 241101 (2014).

ANIMAL ECOLOGY

The secrets of canopy dwellers revealed

Many mammals in tropical forests spend much of their life in the canopy, which makes their behavior difficult to document. Treetop cameras can help, Gregory *et al*. report. The authors attached motion-triggered cameras high in the branches of a Peruvian tropical forest. In more than 1500 photographs taken over 6 months, they recorded 20 mammal species at crossing points between trees. The animals seemed unfazed by the cameras (though fluttering leaves did tend to trigger the cameras unnecessarily). Like the more familiar camera traps at ground level, arboreal camera traps may become an important tool for recording hitherto hidden behaviors. — AMS

Methods Ecol. Evol. **5**, 443 (2014).

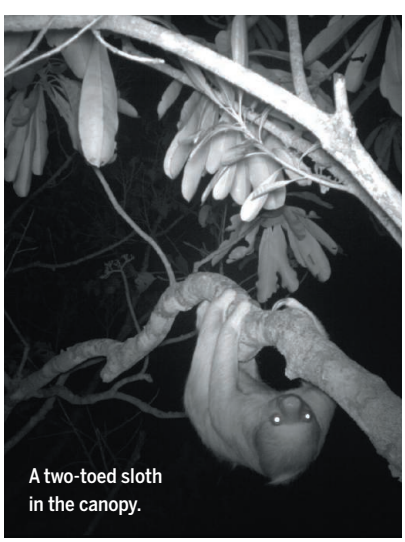

A two-toed sloth in the canopy.

MATERIALS SCIENCE

Tubular friction at the nanoscale

When large-scale objects slide by each other, the amount of friction depends on their surface roughness and the contact area between them. At the nanoscale, though, different factors and forces can affect resistance to motion. Niguès *et al.* examine the response of multiwalled carbon nanotubes (CNTs) and boron nitride nanotubes (BNNTs) as their concentric cylindrical layers are pulled past each other. Whereas the semiconducting CNTs show almost no resistance to sliding motion, the BNNTs show viscous-like dissipation that is proportional to the contact area. The authors attribute this difference to bond character: Boron nitride forms ionic bonds, whereas the bonds in CNTs are purely covalent. Because they slide so much less slickly when they touch, the BNNTs could make highly efficient nanoscale shock absorbers. — MSL

Nat. Mater. 10.1038/nmat3985 (2014).

PHOTOS: (TOP TO BOTTOM) DANIEL ESKRIDGE/STOCKTREK IMAGES/GETTY IMAGES; SMITHSONIAN CONSERVATION BIOLOGY INSTITUTE

Published by AAAS

ALSO IN *SCIENCE*

Edited by **Stella Hurtley**

BATTERIES

Watching battery materials in action

When batteries get rapidly charged and discharged repeatedly, they will often stop working. This is especially true when the cycling changes the crystal structure of the battery components. Liu *et al.* examined the structural changes in components of a type of lithium battery (see the Perspective by Owen and Hector). Their findings explain why $LiFePO_4$ delivers unexpectedly good electrochemical performances, particularly during rapid cycling. — MSL

Science, this issue p. 1480; see also p. 1451

VALLEYTRONICS

Using the valleys in monolayer MoS_2

The electronic structure of the two-dimensional material MoS_2 has two distinct "valleys" of energy that may help to carry information in future electronic devices. Mak *et al.* observed the so-called valley Hall effect in a monolayer of MoS_2. The electrons from different valleys moved in opposite directions across the sample, with one valley being overrepresented with respect to the other. The scientists achieved this by shining circularly polarized light on the material, which created an imbalance in the population of the two valleys. The findings may enable practical applications in the newly formed field of valleytronics. — JS

Science, this issue p. 1489

MACHINE LEARNING

Discerning clusters of data points

Cluster analysis is used in many disciplines to group objects according to a defined measure of distance. Numerous algorithms exist, some based on the analysis of the local density of data points, and others on predefined probability distributions. Rodriguez and Laio devised a method in which the cluster centers are recognized as local density maxima that are far away from any points of higher density. The algorithm depends only on the relative densities rather than their absolute values. The authors tested the method on a series of data sets, and its performance compared favorably to that of established techniques. — JS

Science, this issue p. 1492

GAS FORMATION

Making of methane deep underground

Technologies such as hydraulic fracturing, or "fracking," can now extract natural gas from underground reservoirs. Within the gas, the ratio of certain isotopes holds clues to its origins. Stolper *et al.* analyzed a wide range of natural gas, including samples from some of the most active fracking sites in the United States. Using a "clumped isotope" technique, the authors could estimate the high temperatures at which methane formed deep underground, as well as the lower temperatures at which ancient microbes produced methane. The approach can help to distinguish the degree of mixing of gas from both sources. — NW

Science, this issue p. 1500

MEMBRANE TRAFFICKING

Supplying power: Right time, right place

Cell membranes are very flexible and easily molded to shape; however, to physically pinch off a membrane vesicle from a membrane tube still requires power. A type of molecular machine known as dynamin is involved in this sort of membrane remodeling. Dynamins use guanosine triphosphate (GTP) rather than the more commonly used cellular energy source adenosine triphosphate to work. Boissan *et al.* now show that two separate dynamins found in the cytoplasm or the mitochondria both use the same sort of enzyme—nucleoside diphosphate kinases—to provide GTP at just the right time and the right place to power membrane fission. — SMH

Science, this issue p. 1510

MICROBIAL EVOLUTION

Clouding evolution's crystal ball

Because of a sort of mutation buffering process, different starting mutations can tend to end up with similar overall affects on an organism's fitness. Kryazhimskiy *et al.* evolved lines of yeast, each originating from distinct single genotypes, under the same selective regimen. A subset of clones from these adapted populations was subjected to fitness assays and sequenced. Populations with lower initial fitness, adapted more rapidly than populations with higher initial fitness, so that in the end the fitness levels were similar. — LMZ

Science, this issue p. 1519

Published by AAAS

RESEARCH ARTICLE SUMMARY

BATTERIES

Capturing metastable structures during high-rate cycling of $LiFePO_4$ nanoparticle electrodes

Hao Liu, Fiona C. Strobridge, Olaf J. Borkiewicz, Kamila M. Wiaderek, Karena W. Chapman, Peter J. Chupas, Clare P. Grey*

INTRODUCTION: The ability to achieve high cycling rates in a lithium-ion battery is limited by the Li transport within the electrolyte; the transport of Li ions and electrons within the electrodes; and, when a phase transformation is induced as a result of the Li compositional changes within an electrode, the nucleation and growth of the second phase. The absence of a phase transformation involving substantial structural rearrangements and large volume changes is generally considered to be key for achieving high rates. This assumption has been challenged by the discovery that some nanoparticulate electrode materials, most notably $LiFePO_4$, can be cycled in a battery at very high rates, even though they cycle between two phases during battery operation. This apparent contradiction has been reconciled by the hypothesis that a nonequilibrium solid solution can be formed during reaction to bypass the nucleation step.

RATIONALE: To test this proposal, in situ techniques with high temporal resolution must be used to capture the fast phase transformation processes. We performed in situ synchrotron x-ray diffraction (XRD), which readily detects the structural changes and allows for fast data collection, on a $LiFePO_4$-Li battery at high cycling rates, conditions that are able to drive the system away from equilibrium. We used an electrode comprising ~190-nm $LiFePO_4$ particles, carbon, and binder (30:60:10 weight %), along with an electrochemical cell designed to yield reproducible results over multiple cycles, even at high rates. The high carbon content ensures that the reaction at high rates is not limited by either the electronic conductivity or ionic diffusion within the electrode composite. We compared the experimental results with simulated XRD patterns, in which the effects of strain versus compositional variation were explored. We then adapted a whole-pattern fitting method to quantify the compositional variation in the electrode during cycling.

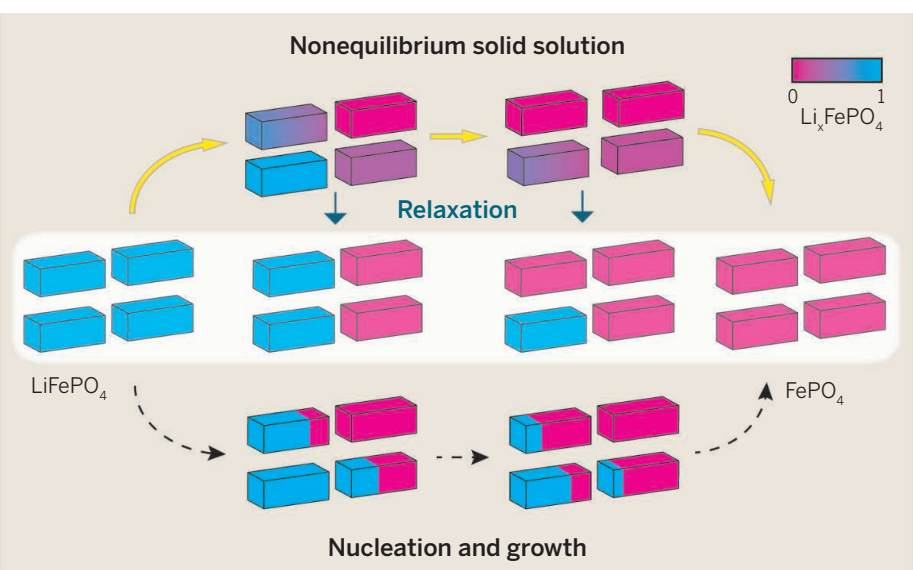

Phase transformation from $LiFePO_4$ (blue) to $FePO_4$ (red). The delithiation (indicated by yellow arrows) proceeds at high rates via the formation of a nonequilibrium solid solution phase Li_xFePO_4 (intermediate purple color), avoiding a classical nucleation process (indicated by dashed arrows). When the reaction is interrupted, the particles relax into the equilibrium configuration (shaded region), where only single-phase particles of $LiFePO_4$ and/or $FePO_4$ are present.

RESULTS: The XRD patterns, collected during high-rate galvanostatic cycling, show the expected disappearance of $LiFePO_4$ Bragg reflections on charge and the simultaneous formation of $FePO_4$ reflections. In addition, the development of positive intensities between the $LiFePO_4$ and $FePO_4$ reflections indicates that particles with lattice parameters that deviate from the equilibrium values of $LiFePO_4$ and $FePO_4$ are formed. The phenomenon is more pronounced at high currents. Detailed simulations of the XRD patterns reveal that this lattice-parameter variation cannot be explained by a $LiFePO_4$-$FePO_4$ interface within the particles, unless the size of the interface is similar to or greater than the size of the entire particle. Instead, the results indicate compositional variation either within or between particles.

ON OUR WEBSITE

Read the full article at http://dx.doi.org/10.1126/science.1252817

CONCLUSION: The results demonstrate the formation of a nonequilibrium solid solution phase, Li_xFePO_4 ($0 < x < 1$), during high-rate cycling, with compositions that span the entire composition between two thermodynamic phases, $LiFePO_4$ and $FePO_4$. This confirms the hypothesis that phase transformations in nanoparticulate $LiFePO_4$ proceed, at least at high rates, via a continuous change in structure rather than a distinct moving phase boundary between $LiFePO_4$ and $FePO_4$. The ability of $LiFePO_4$ to transform via a nonequilibrium single-phase solid solution, which avoids major structural rearrangement across a moving interface, helps to explain its high-rate performance despite a large Li miscibility gap at room temperature. The creation of a low-energy nonequilibrium path by, for example, particle size reduction or cation doping should enable the high-rate capabilities of other phase-transforming electrode materials.

RELATED ITEMS IN *SCIENCE*

J. Owen, A. Hector, Phase-transforming electrodes. *Science* 344, 1451–1452 (2014). DOI: 10.1126/science.1255819

The list of author affiliations is available in the full article online. *Corresponding author. E-mail: cpg27@cam.ac.uk
Cite this article as H. Liu *et al. Science* 344, 1252817 (2014). DOI: 10.1126/science.1252817

Published by AAAS

RESEARCH ARTICLE

BATTERIES

Capturing metastable structures during high-rate cycling of $LiFePO_4$ nanoparticle electrodes

Hao Liu,[1] Fiona C. Strobridge,[1] Olaf J. Borkiewicz,[2] Kamila M. Wiaderek,[2] Karena W. Chapman,[2] Peter J. Chupas,[2] Clare P. Grey[1,3]*

The absence of a phase transformation involving substantial structural rearrangements and large volume changes is generally considered to be a key characteristic underpinning the high-rate capability of any battery electrode material. In apparent contradiction, nanoparticulate $LiFePO_4$, a commercially important cathode material, displays exceptionally high rates, whereas its lithium-composition phase diagram indicates that it should react via a kinetically limited, two-phase nucleation and growth process. Knowledge concerning the equilibrium phases is therefore insufficient, and direct investigation of the dynamic process is required. Using time-resolved in situ x-ray powder diffraction, we reveal the existence of a continuous metastable solid solution phase during rapid lithium extraction and insertion. This nonequilibrium facile phase transformation route provides a mechanism for realizing high-rate capability of electrode materials that operate via two-phase reactions.

Rechargeable lithium-ion batteries are important electrochemical storage devices for portable electronics and increasingly for electrical vehicles. An electrode operates by reversible Li-ion insertion (lithiation) and extraction (delithiation) during charge and discharge. High-rate lithium-ion battery electrode compounds generally form solid solutions with Li over a large composition range so that no phase transformation is induced during (de)lithiation. Phase transformations, if they occur during cycling, are associated with small or negligible volume changes. For example, the Li-excess spinel $Li_{1.06}Mn_2O_{4.10}$ forms a solid solution throughout the delithiation process (*1*), as does the layered compound $LiNi_{1/3}Mn_{1/3}Co_{1/3}O_2$ (*2*, *3*), whereas the high-voltage spinel $Li_x(Ni_{0.5}Mn_{1.5})O_4$ ($0 < x < 1$), shows only a small volume change (3%) for the two-phase region (*4*). Moreover, a clear correlation between cation ordering, reaction mechanism, and rate has yet to be fully established. $LiFePO_4$ (*5*) represents an exception to this rule, because it displays excellent high-rate performance when nanosized (*6*), despite undergoing a first-order phase transformation to $FePO_4$ upon delithiation, a process involving a volume change of 6.8% (*5*). The very limited Li solubility in $LiFePO_4$ and $FePO_4$ suggests that (de)lithiation occurs via a two-phase reaction (*7*–*11*), where the relative $LiFePO_4$:$FePO_4$ phase ratio is changed by a moving phase boundary, and not via a solid solution. Although the Li solubility is found to increase with decreasing particle size (*12*, *13*) as a result of the increased interfacial energy per unit volume, a substantial Li miscibility gap still exists. Taking this interfacial energy into consideration, ex situ diffraction studies of $LiFePO_4$ nanoparticles propose that once an energetically unfavorable $LiFePO_4$-$FePO_4$ interface is formed, this interface will quickly propagate through the particle so as to return to the most stable $LiFePO_4$ or $FePO_4$ state (the "domino-cascade" mechanism) (*14*), explaining why only $LiFePO_4$ and $FePO_4$ particles are observed ex situ (*15*). Thus, at any time during the charge cycling, only a very small subset of particles should be reacting, making it difficult to observe this mechanism in situ.

Because all electrochemical processes operate at an overpotential, the pathways taken during the reaction are not necessarily governed by the thermodynamic properties of the system. As $LiFePO_4$ and $FePO_4$ phases coexist under equilibrium, an overpotential that lowers the Li chemical potential of one phase relative to the other is required to drive the reaction. It has been postulated that this reaction overpotential modifies the phase transformation pathway. Ab initio calculations (*16*) have predicted that instead of forming an interface, the (de)lithiation of a single particle proceeds via nonequilibrium single-phase Li_xFePO_4 ($0 < x < 1$), which bypasses nucleation and proceeds at a much lower overpotential. Once the overpotential is removed, the nonequilibrium Li_xFePO_4 particle relaxes to form the thermodynamic $LiFePO_4$ and $FePO_4$ phases releasing or taking in Li^+ ions from the electrolyte. Making use of this theory, continuum modeling has suggested that a higher fraction of the electrode will react simultaneously via this nonequilibrium solid solution at high rates than at low rates; that is, the fraction of the electrode particles present as Li_xFePO_4 will be higher (*17*). A second continuum modeling study has argued that $LiFePO_4$-$FePO_4$ phase separation (within a single particle) is not seen at high rates due to the dynamic stabilization of the intermediate phases (*18*).

Diffraction methods using neutron or x-ray sources are commonly used for in situ characterization of the structural changes that occur in the crystalline phases within the electrode during electrochemical cycling. Recent in situ x-ray diffraction (XRD) studies of micrometer-sized $LiFePO_4$ at high current rates have shown the appearance of a metastable crystalline phase with an intermediate lithium composition of $Li_{0.6\text{-}0.75}FePO_4$ (*19*). However, investigations of smaller particles have been limited to low (<0.1 C; n C is the current required to either charge or discharge the electrode fully in $1/n$ hours) (*20*) and moderate (1 C) (*21*) current rates, and only small deviations in stoichiometry from $LiFePO_4$ and $FePO_4$ were observed (via changes in lattice parameters) during cycling. Because nanoparticles generally have faster transport kinetics, a higher current rate is required to reach the kinetic limit of a phase transformation.

Our approach involves the use of a dilute electrode in a customized electrochemical cell (*22*), which is capable of achieving high cycling rates, with high reproducibility over multiple cycles, as well as an in situ XRD set-up with high x-ray intensity and a fast read detector to allow the reaction to be probed with high time resolution. The use of the dilute electrode improves both the electronic conductivity and the ion diffusion within the electrode composite (*23*, *24*) and is critical to probe the process intrinsic to the active material, $LiFePO_4$. By studying the nanoparticles under high current rates, we are able to force enough particles to transform simultaneously so that the reacting particles can be detected and the nature of the phase transformations that occur at an overpotential can be determined.

Intermediate Li_xFePO_4 phases induced at high currents

In situ diffraction patterns during the first five cycles of a 10-C galvanostatic charge-discharge of $LiFePO_4$ of average size 186 nm (fig. S1) are shown in Fig. 1A, where the contributions from the cell background and polytetrafluoroethylene (PTFE) peaks are subtracted for clarity. All diffraction peaks can be indexed to either the Li-rich $Li_{1-\alpha}FePO_4$ phase or the Li-poor $Li_\beta FePO_4$ phase in the space group Pnma. As expected, $Li_{1-\alpha}FePO_4$ peaks disappear on charge and are restored on discharge; conversely, $Li_\beta FePO_4$ peaks start to form and grow on charge and disappear on discharge. Unexpectedly, we observed the development of appreciable positive intensities within the 8.15° to 8.4°, 13.95° to 14.1°, and 15.15° to 15.4° 2θ ranges, which indicate the existence of phases with lattice parameters that deviate from those of $LiFePO_4$ and $FePO_4$ under equilibrium. A closer examination of individual diffraction patterns for selected 2θ regions is provided in Fig. 1B. The phenomenon is more pronounced at high current

[1]Department of Chemistry, University of Cambridge, Lensfield Road, Cambridge CB2 1EW, UK. [2]X-ray Science Division, Advanced Photon Source, Argonne National Laboratory, Argonne, IL 60439, USA. [3]Department of Chemistry, Stony Brook University, Stony Brook, NY 11794–3400, USA.
*Corresponding author. E-mail: cpg27@cam.ac.uk

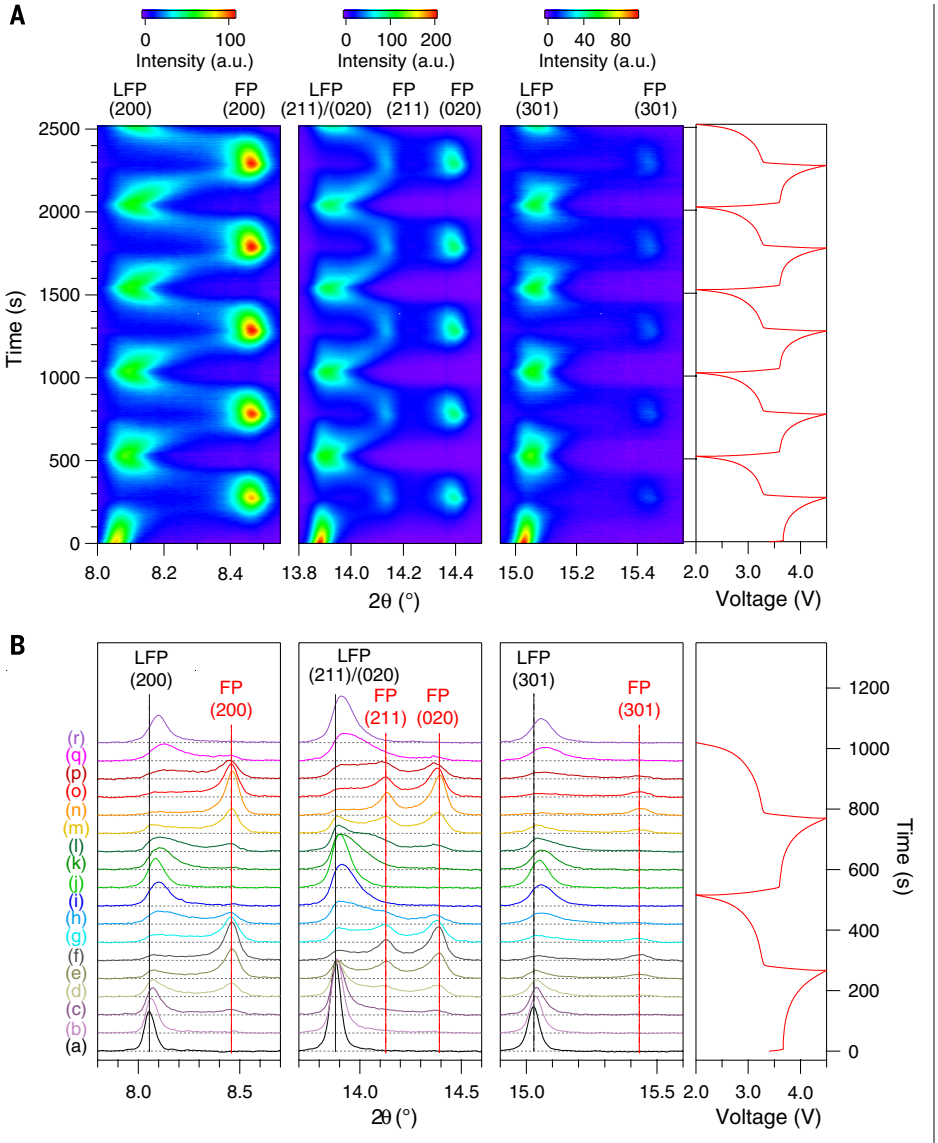

Fig. 1. In situ XRD patterns during galvanostatic charge and discharge at a rate of 10 C. (**A**) The image plot of diffraction patterns for (200), (211), (020), and (301) reflections during the first five charge-discharge cycles. The horizontal axis represents the selected 2θ regions, and time is on the vertical axis. The diffraction intensity is color coded with the scale bar shown on top. The corresponding voltage curve is plotted to the right. LFP, $LiFePO_4$; FP, $FePO_4$; a.u., arbitrary units. (**B**) Selected individual diffraction patterns during the first two cycles stacked against the voltage profile. The baseline is represented by horizontal dashed gray lines. Black vertical lines mark the positions of $LiFePO_4$ peaks at the start of reaction; red vertical lines mark the position of $FePO_4$ peaks formed during the first cycle.

rates, as illustrated by Fig. 2, which compares the results obtained at 5-, 10-, and 20-C rates.

All of the reflections exhibit highly symmetrical profiles at the onset of the first charge [shown in Fig. 1B, pattern (a)], but as charging proceeds, the $LiFePO_4$ (200) and (301) reflections start to broaden asymmetrically toward higher angles [pattern (d)]. The most severe asymmetrical broadening is shown on discharge in patterns (f) and (g), where the (200) reflections from both phases are connected by a positive intensity band. Similar behavior is also found in the second cycle [most notably, patterns (l) and (p)]. Neither the peak position nor the peak shape of $LiFePO_4$ is restored to that of the original state by the end of the second cycle: As shown in pattern (r), all selected peaks shift toward higher angle and broaden. The peak shift indicates a decrease in the unit cell volume, which is attributed to the reduced accessible capacity at high rates. Because the lithium composition is not restored to $LiFePO_4$ at the end of each cycle, a solid solution ($Li_{1-\alpha}FePO_4$) is formed, which has a smaller unit cell volume than stoichiometric $LiFePO_4$. This phase is also more disordered and/or has a shorter coherence length than $LiFePO_4$, resulting in peak broadening.

The unusual evolution of peak shapes comes as a result of the microstructural changes induced during high-rate cycling. In diffraction theory (*25*), the peak shape is a convolution of the instrumental profile, which is symmetrical in this case, and the sample-induced profile due to small crystallite sizes and/or lattice distortions that can originate from strain, composition variations, etc. The size effect produces a symmetrical profile, whereas the lattice distortion effect can give rise to either a symmetrical or asymmetrical profile (*25*), depending on the nature and distribution of the distortion. Thus, the development of an asymmetrical peak profile in this system is solely attributed to lattice distortions and/or compositional distributions. The experimental peak asymmetry exhibits a certain hkl dependence—the (200), (210), (211), (020), and (301) reflections skewing in the opposite direction to the skew observed for the (101) reflection (fig. S2)—that is consistent with that predicted for varying lithium composition between $FePO_4$ and $LiFePO_4$ (i.e., a solid solution). Some anisotropic peak shift and/or asymmetry could also be induced by a mechanical strain built up from the coherent interface between the $LiFePO_4$ and the $FePO_4$ domains during the reaction, which although of different physical origin, will also cause variations in lattice parameters.

Continuous distribution of Li_xFePO_4 phases beyond the thermodynamic miscibility gap

The distribution of lattice parameters can be quantified if its contribution to the peak profile (broadening) can be separated from other sources. One common approach to treat an asymmetrical profile is to deconvolute contributions due to size and lattice-parameter variations by applying a Warren-Averbach Fourier analysis (*25*) to a series of diffraction peaks arising from the same class of reflection. This is difficult to implement in our system because of the low crystal symmetry and severe peak overlap. An alternative approach, adopted here, involves fitting the peak profile by convoluting separate contributions from size and lattice-parameter variations with appropriate analytical functions (see materials and methods). To carry this out, we performed Pawley whole-powder-pattern fitting (*26*) with two phases representing $LiFePO_4$ and $FePO_4$. The effect on the profile from the small crystallite size was modeled by an isotropic size-broadening term, whereas that due to lattice-parameter variations was modeled by convoluting an isotropic microstrain-like broadening term, accounting for the symmetrical distribution of lattice parameters, with spherical harmonics to fit the hkl-dependent asymmetry (*27*) caused by the asymmetrical lattice-parameter distribution. We then used the TOPAS structural refinement package (*28*) to refine the size and lattice-parameter variations in the fitting process, and we achieved satisfactory fits to the observed profile (fig. S3), demonstrating the success of our model in accounting for the asymmetrical peak profiles. Our fittings capture the asymmetry of all the classes of reflections [fig. S3; see, for example, the (200), (211), (020), and (301) reflections], which indicates that the lattice-spacing variation is not limited to only a few crystallographic directions. The scale factor of $LiFePO_4$ + $FePO_4$ remains constant during the reaction (fig. S4), providing evidence that our model is able to capture the bulk of the sample, even during the phase transformation. Instead of a single

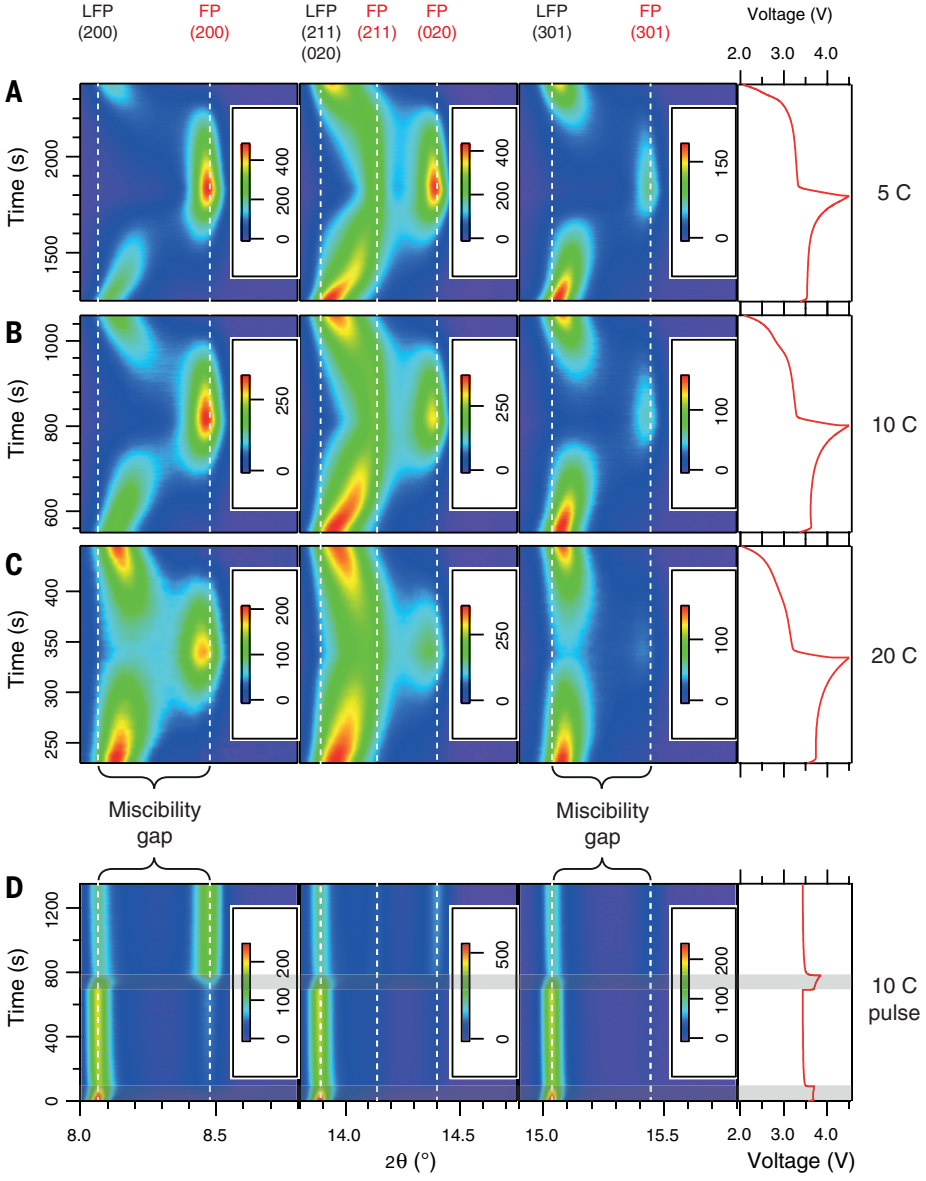

Fig. 2. In situ XRD pattern of $LiFePO_4$ under different electrochemical cycling conditions. (**A** to **C**) Images show the second galvanostatic cycle at 5, 10, and 20 C, respectively. (**D**) Images show the evolution of the charge-relax experiment, where a current equivalent to 10 C is applied for 90 s (highlighted with the horizontal gray bands) followed by an open-circuit relaxation of 10 min. The dashed white lines indicate the peak positions of the $LiFePO_4$ and $FePO_4$ phases at the end of the second relaxation period, which are used to draw the boundaries of the miscibility gap, as determined from the (200) and (301) reflections.

set, we extracted a distribution of all lattice parameters for each diffraction pattern from this analysis.

Contour plots in Fig. 3 show the population density distribution of *a*, *b*, and *c* lattice parameters from both phases during the first two cycles. The $LiFePO_4$ phase initially has a very narrow lattice-parameter distribution, but during the first charge, the lattice parameters from both $LiFePO_4$ and $FePO_4$ become more widely distributed, with an asymmetric tail toward the cell parameters corresponding to the lower and the higher Li compositions, respectively. Although analogous features are found in subsequent discharge and charge cycles, the Li composition range between x = 0.2 and 0.8 (for x in Li_xFePO_4) in the middle of (dis)charge becomes more populated than in the first charge. A similar population density distribution (fig. S5) can be obtained consistently by fitting the (200) and (301) reflections with multiple peaks representing a distribution of lattice parameters.

To identify the dominant cause for the asymmetrical distribution of lattice parameters, we need to separate the effects of compositional variations and strain between two different lattices ($LiFePO_4$ and $FePO_4$). The following observations indicate that the compositional variation mechanism dominates. First, we note that the peak asymmetry of reflections from $LiFePO_4$ persists, even in the absence of any reflections from $FePO_4$, as shown in patterns (i) and (k) of Fig. 1B; this can only be caused by compositional variation because an interface requires the coexistence of both phases. Second, we consider the effect of a possible region affected by the strain introduced by a coherent interface between $LiFePO_4$ and $FePO_4$ on the XRD patterns. Because the interface has been shown to align with the *bc* plane by transmission electron microscopy studies (*7*), it is most relevant to examine the effect of the interface width on the (200) reflections. Figure 4A shows the simulated (200) reflection profiles for a series of widths of the *bc* interface in a particle that is 186 nm long along the *a* axis. We used the strain distribution derived from a coherent twin boundary (*29*), which leads to the *a* lattice-parameter profile at an interface along the *a* axis as

$$a = \frac{a_0 + a_1}{2} + \frac{a_1 - a_0}{2}\tanh\left(\frac{2x}{L}\right) \qquad (1)$$

where a_0 and a_1 are the *a* lattice parameters of $FePO_4$ and $LiFePO_4$, respectively; L is the interfacial width; and x is the distance from the center of the interface. The Li composition profile (and also the structure factor) is discrete and remains constant on either side of the interface, as shown in the right panel of Fig. 4A. We find that for a 10-nm interface, which is approximately the relaxed interface width found in both a micrometer-sized (*7*) and a 172-nm (*8*) particle, the (200) profile remains almost unaffected. Although the simulated profile shows more asymmetry as the interface becomes wider, the asymmetry is mostly associated with the $FePO_4$ reflection, which is opposite to the experimental observation where the asymmetrical broadening is more associated with the $LiFePO_4$ reflection. When the Li composition (and also the structure factor) is allowed to vary continuously across the interface, the *a* lattice-parameter distribution profile follows the exact form described by Eq. 1 if (i) Vegard's law is assumed (i.e., a linear change in the lattice parameters is observed as the lithium composition varies between $FePO_4$ and $LiFePO_4$) and (ii) the regular solution model (*30*) is assumed (Li and vacancy ordering is random). The simulated profile (Fig. 4B) finds much better agreement with the experimentally observed one, but only for interfaces of 100 nm or wider (i.e., of the same order of magnitude as the size of the crystallites). Qualitatively similar trends are expected for interfaces with different orientations (for example, the *ab* and *ac* interfaces). Hence, the experimental profile cannot be explained by an interface maintained solely by mechanical strains, as suggested by the domino-cascade argument (*14*), and must be associated with continuous compositional variations. This is only plausible for a system that can form a solid solution—in this case, only under nonequilibrium conditions.

In a real system, multiple interfaces and/or reaction fronts may exist within a single particle, which can lead to an even more homogenous Li composition distribution within a single particle. Furthermore, increased inhomogeneity may result from the finite one-dimensional (1D) Li^+ transport

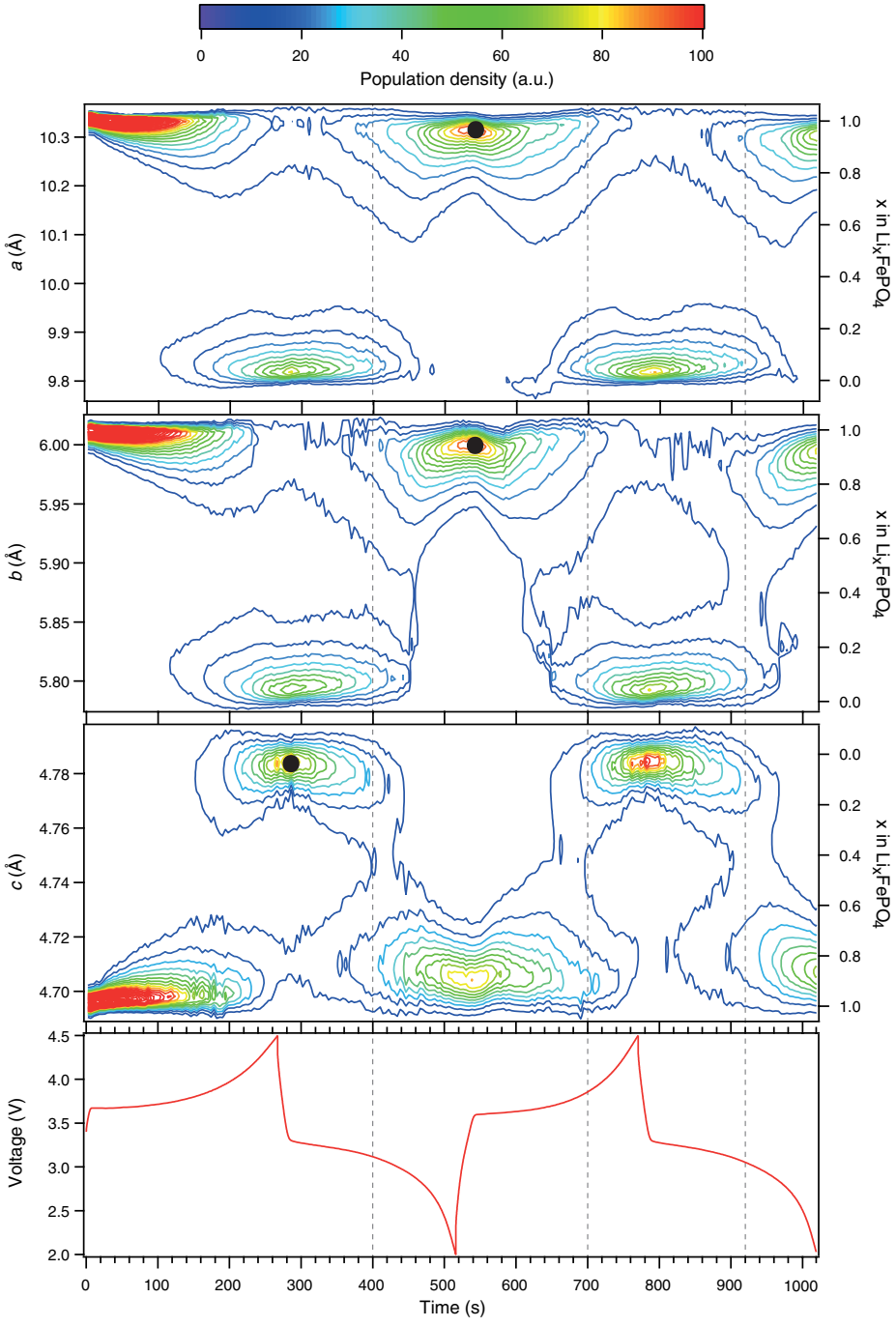

Fig. 3. Lattice-parameter distributions during galvanostatic cycling. The refined $LiFePO_4$ and $FePO_4$ lattice-parameter distributions are shown for the first two charge-discharge cycles at the 10-C rate. The relative population density is color coded, as shown at atop the figure. Given the very narrow distribution and, hence, the very high population density at the beginning of the first charge, the lowest contour is drawn at 7.5% intensity of the maximum intensity (indicated by the solid black circles) in subsequent cycles. The corresponding voltage profile is shown at the bottom. Dashed lines mark the positions where lattice-parameter distributions are most asymmetrical.

in the 1D tunnels of the olivine structure. Li^+ concentration gradients in the electrolyte induced by the high current rate will also give rise to an inhomogeneous state of lithiation across the electrode (*24*); that is, the Li composition varies between particles. Consequently, the asymmetrical broadening of the observed reflection profile cannot be solely attributed to the Li compositional variation within a particle, and at least a substantial part of the broadening is due to compositional variation between particles and across the electrode.

It should be noted that a wide distribution of particle size could potentially lead to asymmetrical peak profiles, due to the particle-size–dependent Li solubility (*12*, *13*, *31*), which could lead to a composition variation based on the particle size. However, the change in the Li solubility is substantial only when the particle size is smaller than 50 nm. Although there are some particles smaller than 50 nm in the sample (fig. S1C), their volumetric fraction is negligible (~6%). Because the phase fraction by x-ray diffraction scales with the total volume of the respective phase, the very small particles (<50 nm) will contribute almost no intensity to the diffraction pattern and will not appreciably affect the peak profile.

Proof of the metastable nature of the Li_xFePO_4 phase

The lithium composition interpolated by Vegard's law is shown on the right axes in Fig. 3. We find that at around 400, 700, and 920 s, where the asymmetrical lattice-parameter distribution is most pronounced, ~20% of the entire electrode probed by the x-ray beam exists with a composition between that of $Li_{0.25}FePO_4$ and $Li_{0.65}FePO_4$. In comparison, the solubilities obtained by Vegard's law in 35- and 140-nm particles with coexisting $LiFePO_4$ and $FePO_4$ domains are $Li_{\sim 0.9}FePO_4$ and $Li_{\sim 0.1}FePO_4$, and $Li_{>0.95}FePO_4$ and $Li_{<0.05}FePO_4$, respectively, even by taking the most generous estimation (*31*). The application of a high current rate thus extends the solid solution into the regime that is thermodynamically prohibited and exists only under nonequilibrium conditions.

To confirm the metastability of the extended solid solution, we carried out an intermittent charging experiment and collected diffraction patterns during both the 10-C charging and the relaxation processes (Fig. 2D). The same whole-powder-pattern fitting method was used to generate the *a*, *b*, and *c* lattice-parameter distribution contour plots (Fig. 5). As expected, asymmetry in the lattice-parameter distribution develops on the $LiFePO_4$ side in the shaded region that highlights the periods during which current is applied, and the distribution gradually becomes more symmetrical once the current is removed and the system is allowed to equilibrate.

Discussion

In contrast to the formation of an intermediate $Li_{0.6\text{-}0.75}FePO_4$ phase under high cycling rates in micrometer-sized particles (*19*), our model reveals the development of a continuous solid solution that extends from the two end-member phases into the thermodynamic miscibility gap. A higher fraction distributed on the $LiFePO_4$ than on the $FePO_4$ side is in good agreement with the nonequilibrium stability phase diagram constructed from the phase-field simulation (*18*), which predicts an asymmetrically vanishing spinodal region with increasing current rate. This asymmetry is also consistent with the thermodynamic phase diagram with greater lithium solubility on the $LiFePO_4$ side at room temperature (*12*, *13*) and a higher solid solution formation temperature on the low Li composition side (*32*, *33*), which indicates a higher energy barrier to form a homogeneous solid solution with low Li composition. Phase transformation via a single-phase solid solution mechanism is generally thought to manifest itself in diffraction studies as a continuous shift in the peak position;

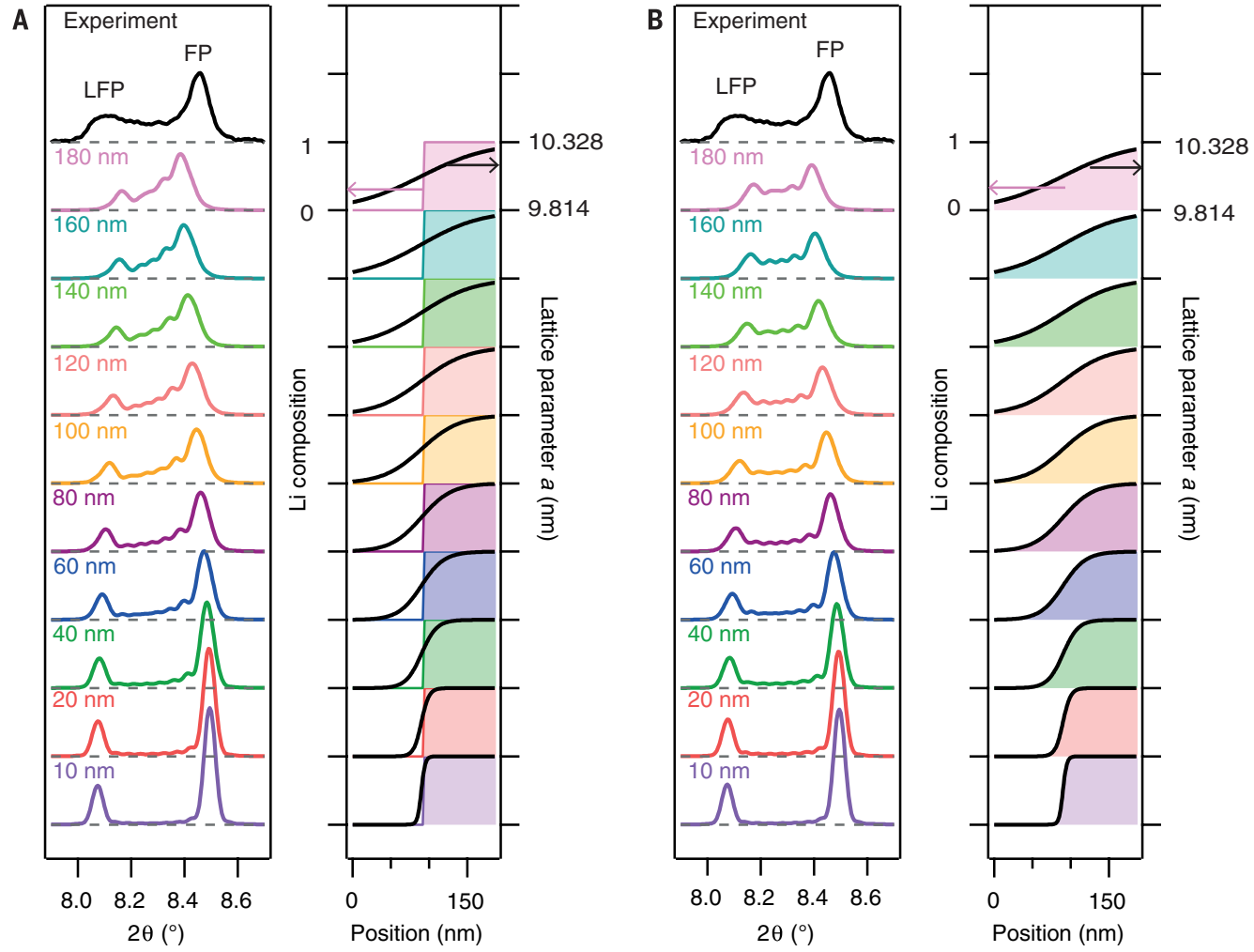

Fig. 4. Simulated reflection profiles. (**A** and **B**) The (200) reflections are simulated for different interface widths between $LiFePO_4$ and $FePO_4$. Left panels compare the simulated profiles with the experimentally measured one (top). Right panels show the corresponding Li composition (shaded areas) and the *a* lattice-parameter profiles (solid black lines) used in the simulation for various interfacial widths. The particle dimension along the *a* axis is 186 nm, and the interface is positioned in the center. The results based on a discrete Li composition profile (mechanical strain only) and a continuous Li compositional variation are shown in (A) and (B), respectively.

that is, all of the particles react at essentially the same time. The distribution of Li compositions seen here is a consequence of the inhomogeneous nature in the reacting nanoparticulate electrode, which has been shown in various studies to react particle by particle (*14*, *15*, *34*, *35*). The high current rate induces more particles to undergo phase transformations at similar times during charge and discharge. The different electronic wiring of the particles and distributions in particle sizes all contribute to the onset of the phase transformation reactions and the variation of the Li compositions between the particles and within the particle (*17*). Detection of the solid solution by powder diffraction is still, however, very difficult due to the small number of reacting particles at any one time. The application of a high current not only induces an overpotential that is large enough to deliver a dynamic phase transformation pathway but also increases the number of reacting particles and, potentially, reaction fronts within a particle, so that the reacting particles can be observed via a bulk measurement technique. However, a large portion of the electrode still remains inactive at any one time, and the diffraction pattern is still dominated by the equilibrium phases $LiFePO_4$ and $FePO_4$.

It is well known that in the mixed olivine system, where the Fe site is occupied by two or more transition metal ions, a thermodynamically stable phase is often observed at intermediate Li composition with extended Li solubility (*36*–*41*). In cases where Fe, Mn, and Co are mixed at the appropriate ratios (*41*, *42*), a single-phase reaction can even be induced. The solid solutions in the mixed olivine phases are distinct from those reported here because they are thermodynamic in origin (occurring for the bulk of the electrode at low current rates; i.e., under equilibrium conditions), resulting primarily from a random distribution of the transition metal ions and, as described in a recent report, from coherency strain between the two end-member phases (*43*).

In summary, the exceptionally high rates observed for $LiFePO_4$ are explained by the existence of a facile nonequilibrium single-phase transformation pathway. Provision of the nonequilibrium solid solution phases may also underpin the high-rate capability of other materials that nominally operate via two-phase reactions.

Materials and methods

Materials synthesis

$LiFePO_4$/C composites were synthesized by a solid-state reaction developed by Kobayashi *et al.* (*13*). 0.556 g lithium carbonate (Li_2CO_3, Aldrich 99.997%), 2.681 g iron(II) oxalate dihydrate [$Fe(II)C_2O_4 \cdot H_2O$, Aldrich 99%], 1.714 g ammonium dihydrogen phosphate ($NH_4H_2PO_4$, Aldrich 99.999%), and 0.261 g Ketjen black (EC-600JD AkzoNobel) were high-energy ball-milled for 40 min to produce homogeneously mixed precursors. The precursors were then pressed into a pellet and sintered at 600°C for 6 hours under flowing Ar gas.

In situ x-ray diffraction measurement

The AMPIX electrochemical cells were used in this experiment; a detailed description of the cell can be found elsewhere (*22*). To ensure optimal high-rate performance, the proportion of active material in the electrode was halved compared

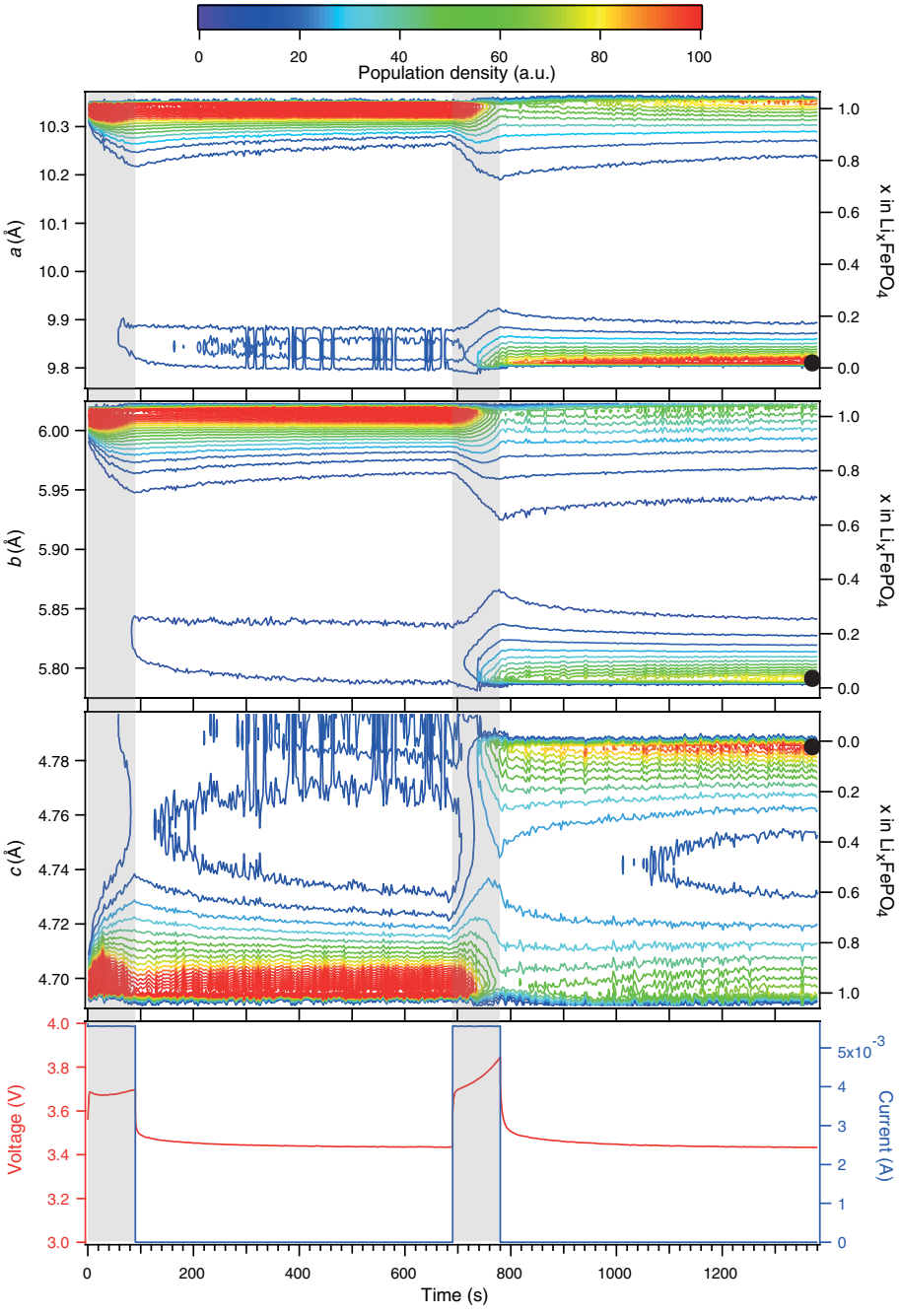

Fig. 5. Lattice-parameter distributions during intermittent charging. The refined $LiFePO_4$ and $FePO_4$ lattice-parameter distributions are shown for the 10-C charging pulse (shaded region) and the subsequent relaxation period. The application of a 10-C current pulse for 90 s (corresponding to the removal of 0.25 Li per $LiFePO_4$ formula unit) is followed by a 10-min relaxation in open-circuit mode. The low $FePO_4$ phase fraction during the first relaxation period is responsible for the greater fluctuation in the lattice parameters. The relative population density is color coded (see top). The lowest contour is drawn at 7.5% intensity of the maximum population density for the $FePO_4$ phase at the end of the second relaxation period (indicated by the solid black circles). In the bottom graph, voltage (red lines) and current (blue lines) are plotted as a function of time.

with typical experiments. $LiFePO_4$ powder (3 mg) was mixed with Super P carbon (Alfa Aesar), carbon black (Vulcan XC-72, Cabot Corporation), and PTFE binder (Sigma-Aldrich) in the mass ratio 3:3:3:1 and was pressed (1.6 to 1.8 ton) into a pellet (13 mm in diameter, ~150 μm in thickness). The electrode pellet was assembled into the AMPIX cell with Li foil as the anode, glass fiber as the separator, and 1 M $LiPF_6$ in 1:1 ethylene carbonate: dimethyl carbonate (Tomiyama Pure Chemical Industries) as the liquid electrolyte. The cells were cycled under conditions described in the text.

In situ synchrotron x-ray powder diffraction measurements were performed in transmission geometry at beamline 17-BM of the Advanced Photon Source at Argonne National Laboratory (wavelength 0.7270 Å, 500-μm-diameter beam). A 2D area detector (Perkin-Elmer), consisting of 2048 pixels by 2048 pixels of 200 μm by 200 μm, in size was used. Measurements were performed at two sample-to-detector distances, the first optimized for improved 2θ resolution. For the 10-C charge-discharge cycling presented in Fig. 1 of the main text, the following was used: 900-mm sample-to-detector distance, with a detector offset of 130 mm from the scattered beam, resulting in a 2θ range of 1° to 25°. The data collection time for each pattern was 4 s, corresponding to a change of 0.011 Li per formula unit of $LiFePO_4$. For a larger 2θ range of 1° to 29°, a sample-to-detector distance of 500 nm, with the detector centered at the scattered beam, was used (data shown for 5-, 10-, 20-C cycling and the intermittent 10-C charge-discharge cycling, all in Fig. 2). The data collection time for each pattern was 3 s, corresponding to a change of 0.004, 0.008, and 0.017 Li per formula unit of $LiFePO_4$ for galvanostatic cycling at 5, 10, and 20 C, respectively.

Whole-powder-pattern fitting of the in situ x-ray diffraction data

The background profile was measured for an assembled AMPIX cell without either electrode and was modeled with seven split pseudo-Voigt functions. These seven peaks were used to describe the background of the in situ patterns, and only the peak intensities were varied to account for the gradual changes in the background intensity. Because the sample thickness is less than the beam size, the instrumental broadening is dominated by the beam size. The instrumental profile was determined from the diffraction pattern of a thin layer of LaB_6 powder (SRM 660a) placed in the same geometry as the $LiFePO_4$ electrode.

The sample profile is a convolution of the size and the strain effects and is modeled separately. A Lorentzian peak profile is used to model the size broadening, and the apparent size is assumed to be isotropic with respect to different (hkl) reflections. The dependence of the full width at half maximum (FWHM), β, on θ is given by

$$\beta = \frac{\lambda}{L \cdot \cos\theta_{hkl}} \quad (2)$$

where λ is the wavelength, and L is the refined apparent size parameter. Because the strain and/or compositional effect induces an asymmetrical profile, it is described by a convolution of a symmetrical and an asymmetrical profile function. A Gaussian profile peak function is chosen to model the symmetrical broadening due to strain, and this strain is also assumed to be isotropic with respect to different (hkl) reflections. The θ dependence of FWHM is given by

$$\beta = E \tan \theta_{hkl} \quad (3)$$

where E is the refined symmetrical strain parameter. The asymmetrical profile is modeled by an exponential function

$$f(\theta) = \exp\left(-\frac{2\theta - 2\theta_{hkl}}{\varepsilon_{hkl}}\right) \quad (4)$$

where ε_{hkl} is the refined parameter, and θ is defined in the range $[\theta_{hkl}, +\infty]$ if $\varepsilon_{hkl} > 0$ and

$[-\infty, \theta_{hkl}]$ if $\varepsilon_{hkl} < 0$. Due to the anisotropic change in the lattice parameters from $LiFePO_4$ to $FePO_4$, where a and b contract and c expands, we have to include an hkl-dependent description of the asymmetrical profile, which is done by including symmetrized spherical harmonics series in ε_{hkl}

$$\varepsilon_{hkl} = \sum_{ij} C_{ij} Y_{ij}(\omega,\varphi)\tan\theta_{hkl} \quad (5)$$

where $Y_{ij}(\omega,\varphi)$ are the symmetrized spherical harmonics that can be found in (*44*, *45*), and C_{ij} are the refined parameters.

The purely strain-induced profile for a certain (hkl) reflection is obtained by convoluting the symmetrical Gaussian function and the exponential function defined at the corresponding θ_{hkl}. This profile is scaled by the scale factor of the respective phase to represent the population density distribution. The whole-powder-pattern fitting of the in situ diffraction patterns within the 2θ range between 7.5° and 22.95° was carried out sequentially in the TOPAS structural refinement package (*28*).

Simulations of XRD reflection profile

Because it has been shown by experiment (*7*) that the $LiFePO_4$-$FePO_4$ phase boundary is in the *bc* plane, we only considered the case of a 1D 186-nm particle along the (h00) direction composed of unit cells that continuously vary in the a lattice parameter, as described by Eq. 1. Each unit along the (h00) direction is assigned with a unique index. We followed the treatment of small coherent domains with continuously varying unit cell parameters by Warren (*25*). For an (h00) reflection, the diffraction power as a function of diffraction angle 2θ can be expressed as

$$P(2\theta) = \frac{K}{\sin^2\theta}\sum_{m'}\sum_{m} f_m f_{m'} e^{(2\pi i/\lambda)(2\sin\theta)(R_{m'}-R_m)} \quad (6)$$

where the subscripts m and m' represent the indices of the unit cells, f_m and $f_{m'}$ are the structure factors of unit cells m and m', R_m and $R_{m'}$ are the position coordinates of unit cells m and m', λ is the x-ray wavelength, and K is a factor independent of θ. The summation is performed over all unit cells in the 1D particle. The structure factor f for the (200) reflection is assumed to vary linearly with the Li composition c (*46*)

$$f(c) = (1-c)\cdot f(0) + c\cdot f(1) \quad (7)$$

where $f(0)$ and $f(1)$ are the structure factors for the (200) reflections of $FePO_4$ and $LiFePO_4$, respectively.

REFERENCES AND NOTES

1. Y. Xia *et al*., Correlating capacity fading and structural changes in $Li_{1+y}Mn_{2-y}O_{4-\delta}$ spinel cathode materials: A systematic study on the effects of Li/Mn ratio and oxygen deficiency. *J. Electrochem. Soc.* **148**, A723–A729 (2001).
2. N. Yabuuchi, T. Ohzuku, Novel lithium insertion material of $LiCo_{1/3}Ni_{1/3}Mn_{1/3}O_2$ for advanced lithium-ion batteries. *J. Power Sources* **119-121**, 171–174 (2003). doi: 10.1016/S0378-7753(03)00173-3
3. D. Zeng, J. Cabana, J. Bréger, W. Yoon, C. P. Grey, Cation ordering in $Li[Ni_xMn_xCo_{(1-2x)}]O_2$-layered cathode materials: A nuclear magnetic resonance (NMR), pair distribution function, x-ray absorption spectroscopy, and electrochemical study. *Chem. Mater.* **19**, 6277–6289 (2007). doi: 10.1021/cm702241a
4. M. Kunduraci, G. G. Amatucci, Synthesis and characterization of nanostructured 4.7 V $Li_xMn_{1.5}Ni_{0.5}O_4$ spinels for high-power lithium-ion batteries. *J. Electrochem. Soc.* **153**, A1345–A1352 (2006). doi: 10.1149/1.2198110
5. A. K. Padhi, K. S. Nanjundaswamy, J. B. Goodenough, Phospho-olivines as positive-electrode materials for rechargeable lithium batteries. *J. Electrochem. Soc.* **144**, 1188–1194 (1997). doi: 10.1149/1.1837571
6. B. Kang, G. Ceder, Battery materials for ultrafast charging and discharging. *Nature* **458**, 190–193 (2009). doi: 10.1038/nature07853; pmid: 19279634
7. G. Chen, X. Song, T. J. Richardson, Electron microscopy study of the $LiFePO_4$ to $FePO_4$ phase transition. *Electrochem. Solid-State Lett.* **9**, A295–A298 (2006). doi: 10.1149/1.2192695
8. L. Laffont *et al*., Study of the $LiFePO_4$/$FePO_4$ two-phase system by high-resolution electron energy loss spectroscopy. *Chem. Mater.* **18**, 5520–5529 (2006). doi: 10.1021/cm0617182
9. J. L. Allen, T. R. Jow, J. Wolfenstine, Analysis of the $FePO_4$ to $LiFePO_4$ phase transition. *J. Solid State Electrochem.* **12**, 1031–1033 (2008). doi: 10.1007/s10008-007-0459-1
10. C. V. Ramana, A. Mauger, F. Gendron, C. M. Julien, K. Zaghib, Study of the Li-insertion/extraction process in $LiFePO_4$/$FePO_4$. *J. Power Sources* **187**, 555–564 (2009). doi: 10.1016/j.jpowsour.2008.11.042
11. Y. Zhu *et al*., In situ atomic-scale imaging of phase boundary migration in $FePO_4$ microparticles during electrochemical lithiation. *Adv. Mater.* **25**, 5461–5466 (2013). doi: 10.1002/adma.201301374; pmid: 23873760
12. N. Meethong, H.-Y. S. Huang, W. C. Carter, Y.-M. Chiang, Size-dependent lithium miscibility gap in nanoscale $Li_{1-x}FePO_4$. *Electrochem. Solid-State Lett.* **10**, A134–A138 (2007). doi: 10.1149/1.2710960
13. G. Kobayashi *et al*., Isolation of solid solution phases in size-controlled Li_xFePO_4 at room temperature. *Adv. Funct. Mater.* **19**, 395–403 (2009). doi: 10.1002/adfm.200801522
14. C. Delmas, M. Maccario, L. Croguennec, F. Le Cras, F. Weill, Lithium deintercalation in $LiFePO_4$ nanoparticles via a domino-cascade model. *Nat. Mater.* **7**, 665–671 (2008). doi: 10.1038/nmat2230; pmid: 18641656
15. G. Brunetti *et al*., Confirmation of the domino-cascade model by $LiFePO_4$/$FePO_4$ precession electron diffraction. *Chem. Mater.* **23**, 4515–4524 (2011). doi: 10.1021/cm201783z
16. R. Malik, F. Zhou, G. Ceder, Kinetics of non-equilibrium lithium incorporation in $LiFePO_4$. *Nat. Mater.* **10**, 587–590 (2011). doi: 10.1038/nmat3065; pmid: 21765400
17. B. Orvananos *et al*., Architecture dependence on the dynamics of nano-$LiFePO_4$ electrodes. *Electrochim. Acta* doi: 10.1016/j.electacta.2014.06.029 (2014).
18. P. Bai, D. A. Cogswell, M. Z. Bazant, Suppression of phase separation in $LiFePO_4$ nanoparticles during battery discharge. *Nano Lett.* **11**, 4890–4896 (2011). doi: 10.1021/nl202764f; pmid: 21985573
19. Y. Orikasa *et al*., Direct observation of a metastable crystal phase of Li_xFePO_4 under electrochemical phase transition. *J. Am. Chem. Soc.* **135**, 5497–5500 (2013). doi: 10.1021/ja312527x; pmid: 23544671
20. N. Sharma *et al*., Direct evidence of concurrent solid-solution and two-phase reactions and the nonequilibrium structural evolution of $LiFePO_4$. *J. Am. Chem. Soc.* **134**, 7867–7873 (2012). doi: 10.1021/ja301187u; pmid: 22482702
21. Y. Orikasa *et al*., Transient phase change in two phase reaction between $LiFePO_4$ and $FePO_4$ under battery operation. *Chem. Mater.* **25**, 1032–1039 (2013). doi: 10.1021/cm303411t
22. O. J. Borkiewicz *et al*., The AMPIX electrochemical cell: A versatile apparatus for in situ x-ray scattering and spectroscopic measurements. *J. Appl. Cryst.* **45**, 1261–1269 (2012). doi: 10.1107/S0021889812042720
23. C. Fongy, A.-C. Gaillot, S. Jouanneau, D. Guyomard, B. Lestriez, Ionic vs electronic power limitations and analysis of the fraction of wired grains in $LiFePO_4$ composite electrodes. *J. Electrochem. Soc.* **157**, A885–A891 (2010). doi: 10.1149/1.3432559
24. G. Ouvrard *et al*., Heterogeneous behaviour of the lithium battery composite electrode $LiFePO_4$. *J. Power Sources* **229**, 16–21 (2013). doi: 10.1016/j.jpowsour.2012.11.057
25. B. E. Warren, in *X-ray Diffraction* (Addison-Wesley, Reading, MA, 1969), chap. 13.
26. G. Pawley, Unit-cell refinement from powder diffraction scans. *J. Appl. Cryst.* **14**, 357–361 (1981). doi: 10.1107/S0021889881009618
27. A. L. Goodwin *et al*., Colossal positive and negative thermal expansion in the framework material $Ag_3[Co(CN)_6]$. *Science* **319**, 794–797 (2008). doi: 10.1126/science.1151442; pmid: 18258911
28. A. A. Coelho, TOPAS-Academic, version 4.1 (computer software) (Coelho Software, Brisbane, 2007).
29. G. Barsch, J. Krumhansl, Twin boundaries in ferroelastic media without interface dislocations. *Phys. Rev. Lett.* **53**, 1069–1072 (1984). doi: 10.1103/PhysRevLett.53.1069
30. J. W. Cahn, J. E. Hilliard, Free energy of a nonuniform system. I. Interfacial free energy. *J. Chem. Phys.* **28**, 258–267 (1958). doi: 10.1063/1.1744102
31. M. Wagemaker *et al*., Dynamic solubility limits in nanosized olivine $LiFePO_4$. *J. Am. Chem. Soc.* **133**, 10222–10228 (2011). doi: 10.1021/ja2026213; pmid: 21598941
32. J. L. Dodd, R. Yazami, B. Fultz, Phase diagram of Li_xFePO_4. *Electrochem. Solid-State Lett.* **9**, A151–A155 (2006). doi: 10.1149/1.2164548
33. C. Delacourt, P. Poizot, J.-M. Tarascon, C. Masquelier, The existence of a temperature-driven solid solution in Li_xFePO_4 for $0 \le x \le 1$. *Nat. Mater.* **4**, 254–260 (2005). doi: 10.1038/nmat1335
34. W. C. Chueh *et al*., Intercalation pathway in many-particle $LiFePO_4$ electrode revealed by nanoscale state-of-charge mapping. *Nano Lett.* **13**, 866–872 (2013). doi: 10.1021/nl3031899; pmid: 23362838
35. J. D. Sugar *et al*., High-resolution chemical analysis on cycled $LiFePO_4$ battery electrodes using energy-filtered transmission electron microscopy. *J. Power Sources* **246**, 512–521 (2014). doi: 10.1016/j.jpowsour.2013.08.003
36. A. Yamada, Y. Kudo, K.-Y. Liu, Phase Diagram of $Li_xMn_yFe_{1-y}PO_4$ ($0 \le x, y \le 1$). *J. Electrochem. Soc.* **148**, A1153–A1158 (2001). doi: 10.1149/1.1401083
37. J. Molenda, W. Ojczyk, J. Marzec, Electrical conductivity and reaction with lithium of $LiFe_{1-y}Mn_yPO_4$ olivine-type cathode materials. *J. Power Sources* **174**, 689–694 (2007). doi: 10.1016/j.jpowsour.2007.06.238
38. K.-W. Nam *et al*., In situ x-ray absorption and diffraction studies of carbon coated $LiFe_{1/4}Mn_{1/4}Co_{1/4}Ni_{1/4}PO_4$ cathode during first charge. *Electrochem. Commun.* **11**, 913–916 (2009). doi: 10.1016/j.elecom.2009.02.031
39. K.-W. Nam, W.-S. Yoon, K. Zaghib, K. Yoon Chung, X.-Q. Yang, The phase transition behaviors of $Li_{1-x}Mn_{0.5}Fe_{0.5}PO_4$ during lithium extraction studied by in situ x-ray absorption and diffraction techniques. *Electrochem. Commun.* **11**, 2023–2026 (2009). doi: 10.1016/j.elecom.2009.08.044
40. A. Perea *et al*., Operando ^{57}Fe Mössbauer and XRD investigation of $Li_xMn_yFe_{1-y}PO_4$/C composites ($y = 0$; 0.25). *RSC Adv.* **2**, 2080–2086 (2012). doi: 10.1039/c1ra00256b
41. H. Gwon, D.-H. Seo, S.-W. Kim, J. Kim, K. Kang, Combined first-principle calculations and experimental study on multi-component olivine cathode for lithium rechargeable batteries. *Adv. Funct. Mater.* **19**, 3285–3292 (2009). doi: 10.1002/adfm.200900414
42. K.-Y. Park *et al*., Factors that affect the phase behavior of multi-component olivine ($LiFe_xMn_yCo_{1-x-y}PO_4$; $0 < x, y < 1$) in lithium rechargeable batteries: One-phase reaction vs. two-phase reaction. *J. Electrochem. Soc.* **160**, A444–A448 (2013). doi: 10.1149/2.036303jes
43. D. B. Ravnsbæk *et al*., Extended solid solutions and coherent transformations in nanoscale olivine cathodes. *Nano Lett.* **14**, 1484–1491 (2014). doi: 10.1021/nl404679t; pmid: 24548146
44. N. C. Popa, Texture in Rietveld refinement. *J. Appl. Cryst.* **25**, 611–616 (1992). doi: 10.1107/S0021889892004795
45. M. Järvinen, Application of symmetrized harmonics expansion to correction of the preferred orientation effect. *J. Appl. Cryst.* **26**, 525–531 (1993). doi: 10.1107/S0021889893001219
46. P. S. Rudman, An x-ray diffraction method for the determination of composition distribution in inhomogeneous binary solid solutions. *Acta Crystallogr.* **13**, 905–909 (1960). doi: 10.1107/S0365110X60002211

ACKNOWLEDGMENTS

This work was supported as part of the Northeastern Center for Chemical Energy Storage, an Energy Frontier Research Center funded by the U.S. Department of Energy (DOE), Office of Science, Office of Basic Energy Sciences under award no. DE-SC0001294. Work performed at Argonne National Laboratory and use of the Advanced Photon Source, an Office of Science User Facility operated for the DOE Office of Science by Argonne National Laboratory, were supported by DOE under contract no. DE-AC02-06CH11357. H.L. acknowledges the funding from European Union FP7-265368 via the Eurolion Project and the Cambridge Overseas Trust. F.C.S. acknowledges the funding from the Engineering Physical Science Research Council via a Doctoral Training Partnership Award. We thank B. Orvananos, H. C. Yu, K. Thornton, R. Malik, A. Abdellahi, G. Ceder, and M. S. Whittingham for helpful discussions and comments. H.L., F.C.S., O.J.B. and K.M.W. carried out the experiments; H.L., K.W.C., P.J.C. and C.P.G. performed the analysis; and C.P.G. and H.L. wrote the manuscript with help from all coauthors.

SUPPLEMENTARY MATERIALS

www.sciencemag.org/content/344/6191/1252817/suppl/DC1
Supplementary Text
Figs. S1 to S5
References

3 March 2014; accepted 22 May 2014
10.1126/science.1252817

RESEARCH ARTICLE

HUMAN COGNITION

Foundations of human reasoning in the prefrontal cortex

Maël Donoso,[1,2,3] Anne G. E. Collins,[2,4] Etienne Koechlin[1,2,3]*

The prefrontal cortex (PFC) subserves reasoning in the service of adaptive behavior. Little is known, however, about the architecture of reasoning processes in the PFC. Using computational modeling and neuroimaging, we show here that the human PFC has two concurrent inferential tracks: (i) one from ventromedial to dorsomedial PFC regions that makes probabilistic inferences about the reliability of the ongoing behavioral strategy and arbitrates between adjusting this strategy versus exploring new ones from long-term memory, and (ii) another from polar to lateral PFC regions that makes probabilistic inferences about the reliability of two or three alternative strategies and arbitrates between exploring new strategies versus exploiting these alternative ones. The two tracks interact and, along with the striatum, realize hypothesis testing for accepting versus rejecting newly created strategies.

Human reasoning subserves adaptive behavior and has evolved facing the uncertainty of everyday environments. In such situations, probabilistic inferential processes (i.e., Bayesian inferences) make optimal use of available information for making decisions. Human reasoning involves Bayesian inferences accounting for human responses that often deviate from formal logic (*1*). Bayesian inferences also operate in the prefrontal cortex (PFC) and guide behavioral choices (*2*, *3*). Everyday environments, however, are changing and open-ended, so that the range of uncertain situations and associated behavioral strategies (i.e., internal maps linking stimuli, actions, and expected outcomes) becomes potentially infinite. In such environments, probabilistic inferences involve Dirichlet process mixtures (*4*–*7*) and rapidly yield intractable computations. This computational complexity problem constitutes a fundamental constraint on the evolution of higher cognitive functions and raises the issue of the actual nature of inferential processes implemented in the PFC.

A model of reasoning processes in the human PFC

To address this issue, we proposed a model (*8*) that describes human reasoning, as it guides behavior, as a computationally tractable, online algorithm approximating Dirichlet process mixtures (*9*). The algorithm combines forward Bayesian inferences operating over a few concurrent behavioral strategies stored in long-term memory with hypothesis testing for possibly updating this inferential buffer with new strategies formed from long-term memory. The algorithm notably serves to arbitrate between (i) staying with the ongoing behavioral strategy and possibly learning external contingencies, (ii) switching to other learned strategies, and (iii) forming new behavioral strategies.

For integrating online Bayesian inferences and hypothesis testing, the algorithm's key feature is inferring the absolute reliability of every monitored strategy: namely, the posterior probability that the current situation matches the situation the strategy has learned, given both action outcomes (and possibly contextual cues), and the possibility that no match occurs with any monitored strategies. To estimate these probabilities, the model assumes that, in the latter case, action outcomes expected from the monitored strategies are equiprobable (*9*). Thus, every monitored strategy may appear as being either reliable (i.e., more likely matching than not matching the current situation) or unreliable (the converse). When a strategy is reliable, the others are necessarily unreliable, so that the algorithm is an exploitation state (Fig. 1): The reliable strategy is the actor, namely, the unique strategy for selecting and learning the actions that maximize rewards (typically through reinforcement learning), whereas the other monitored strategies are treated as counterfactual. When all monitored strategies become unreliable, the algorithm then switches into an exploration state corresponding to hypothesis testing: A new strategy is formed as a weighted mixture of strategies stored in long-term memory, then probed and monitored as actor (*9*). If the strategy is a priori unreliable, this probe actor learns, so that the algorithm may subsequently return to the exploitation state in two ways. Either one counterfactual strategy becomes reliable, while the probe actor remains unreliable: The former is then retrieved as actor, and the latter is rejected (disbanded). Or the probe actor becomes reliable, while counterfactual strategies remain unreliable. The probe actor is then confirmed: It remains the actor, the new strategy is simply consolidated into long-term memory, and the repertoire

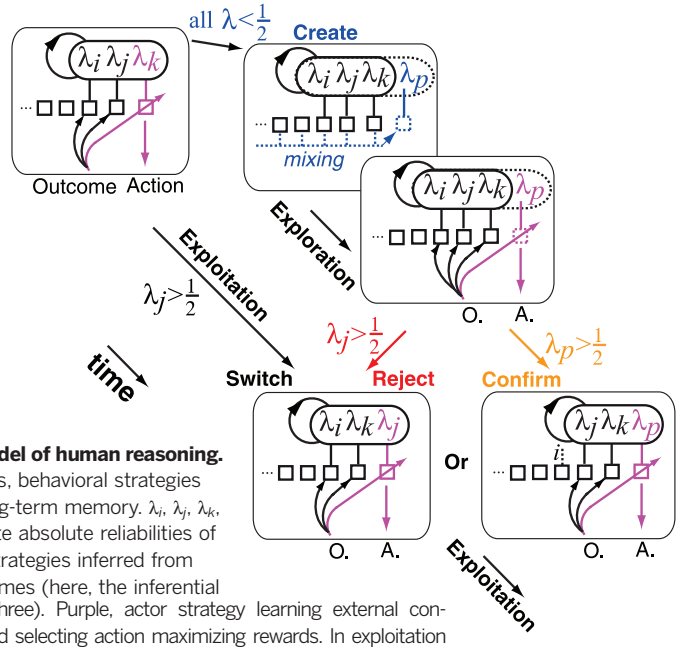

Fig. 1. A model of human reasoning. Solid squares, behavioral strategies stored in long-term memory. λ_i, λ_j, λ_k, and λ_p denote absolute reliabilities of monitored strategies inferred from action outcomes (here, the inferential capacity is three). Purple, actor strategy learning external contingencies and selecting action maximizing rewards. In exploitation periods, the actor is reliable (i.e., $\lambda_{actor} > 1 - \lambda_{actor}$ or $\lambda_{actor} > ½$) and the others are necessarily unreliable (because $\sum\lambda \leq 1$). Otherwise, the system switches into exploration (all $\lambda < ½$) and creates a probe actor (p) from mixing strategies stored in long-term memory (blue). Exploration periods terminate when either one counterfactual strategy (j) or probe actor (p) becomes reliable: The probe actor is then rejected (red) or confirmed (orange). See text for details.

[1]INSERM, Laboratoire de Neurosciences Cognitives (U960), 29 rue d'Ulm, 75005 Paris, France. [2]Département d'Etudes Cognitives (DEC), Ecole Normale Supérieure, 29 rue d'Ulm, 75005 Paris, France. [3]Centre de Neuro-imagerie de Recherche (CENIR), Université Pierre et Marie Curie, 4 place Jussieu, 75005 Paris, France. [4]Brown University, Providence, RI 02912, USA.
*Corresponding author. E-mail: etienne.koechlin@upmc.fr

of stored strategies is expanded. In case the inferential buffer has further reached its capacity limit, the counterfactual strategy used the least recently as actor is then discarded from the buffer (but remains stored in long-term memory).

Consistent with the capacity limit of human working memory (*10*), human decisions are best predicted when the inferential buffer is limited to two or three concurrent counterfactual strategies (*8*). We then hypothesized that the human PFC implements this algorithm. We expected anterior PFC regions to form the inferential buffer (*3*, *11*–*13*) and more posterior PFC regions in association with basal ganglia to drive actor learning, selection, and creation on the basis of hypothesis testing (*14*–*18*). The model predicts that anterior PFC regions concurrently infer the absolute reliability of actor and counterfactual strategies that the algorithm builds online. More posterior PFC regions then detect when, in the inferential buffer, actor strategies become unreliable for creating probe actors, as well as when counterfactual strategies become reliable for retrieving them as actor (and possibly rejecting probe actors). In basal ganglia, the ventral striatum subserves reinforcement learning (*16*, *19*, *20*) and is predicted to detect when, in the inferential buffer, probe actors become reliable for confirming them in long-term memory (*21*).

Behavioral paradigm

To test these predictions, we used functional magnetic resonance imaging (fMRI) and scanned 40 healthy participants, while they were responding to successively presented digits and searching for three-digit combinations by trial and error (fig. S1) (*9*). Feedbacks were noisy, and combinations changed episodically. Unbeknownst to them, participants performed two distinct sessions. In the open session, every episode corresponded to new combinations, whereas in the recurrent session, only three combinations reoccurred unpredictably across episodes. The protocol thus induced participants to reason from feedbacks whether they had to perseverate with the same combination and possibly adjust it, reuse previously learned ones, or learn by searching for new combinations.

In every trial, participants' responses were either correct, perseverative (incorrect in the current episode but correct in the preceding episode), or exploratory (neither correct nor perseverative). Overall, participants performed much below the statistical optimum (*8*). In both conditions, correct response rates increased from ~5% at episode onsets to a plateau at ~85% about 25 trials later (chance level: 25%) (Fig. 2, left). Exploratory response rates increased from ~10% at episode onsets, peaked at ~40% five trials later, and then returned to ~10% (chance level: 50%). Correct responses increased and exploratory responses vanished faster in the recurrent episodes than in the open episodes (both F values > 21.8, P values < 0.0001). In the first trials of recurrent episodes, furthermore, a positive feedback caused the production of correct responses in the next trial, even when the two successively presented digits differed: The statistical dependence between two successive correct responses increased in the first trials of recurrent compared with open episodes (trials 1 and 2: T values > 2.25, P < 0.03) (Fig. 2, bottom), while remaining similar in both conditions on the following trials. In these first recurrent trials, accordingly, participants used feedbacks to retrieve previously learned combinations rather than recollecting each digit-response association separately. Participants consequently built and stored multiple combinations and monitored feedbacks for either retrieving these combinations or learning new ones. Combinations thus defined behavioral strategies associating digits, responses, and expected feedbacks.

We fit the model free parameters (buffer-capacity, prior reliability, recollection entropy of probe actors, and reinforcement learning parameters) to each participant's series of responses (table S1) (*9*). In both recurrent and open episodes, the fitted model predicted participants' responses and their statistical dependencies across successive trials (Fig. 2, right). The model fit significantly better than alternative models, independently of model complexity and fitting criteria (fig. S2) (*9*). Moreover, fitted parameters were independent of which session was fitted (T < 1) and, consequently, unrelated to the number of combinations used in recurrent sessions. The best-fitting capacity—whether fixed or averaged across subjects—included two counterfactual strategies (mean = 2.6, SEM = 0.24, median = 2) (table S1).

The model critically reveals that the gradual variations of responses reported above are actually artifacts from aligning performances from episode onsets and averaging across episodes (Fig. 3). After most episode changes (93.9% and 94.2% of recurrent and open episodes, respectively), indeed, the algorithm switched from exploitation to exploration and created probe actors from long-term memory at variable time points across episodes [on average 3.3 (SD = 0.9) and 4.2 (SD = 1.3) trials after recurrent and open episode onsets, respectively]. We refer to these algorithmic transitions as switch-in events. Realigning model and participants' performances on these switch-in events rather than episode onsets (Fig. 3, left) shows that, in exploitation trials preceding switch-in events, both model and participants' responses were virtually unaffected by episode changes and remained mostly perseverative (~85 to 90%), whereas residual responses remained randomly distributed across exploratory and correct responses (~8% and ~4% of residual responses, respectively). In switch-in trials, by contrast,

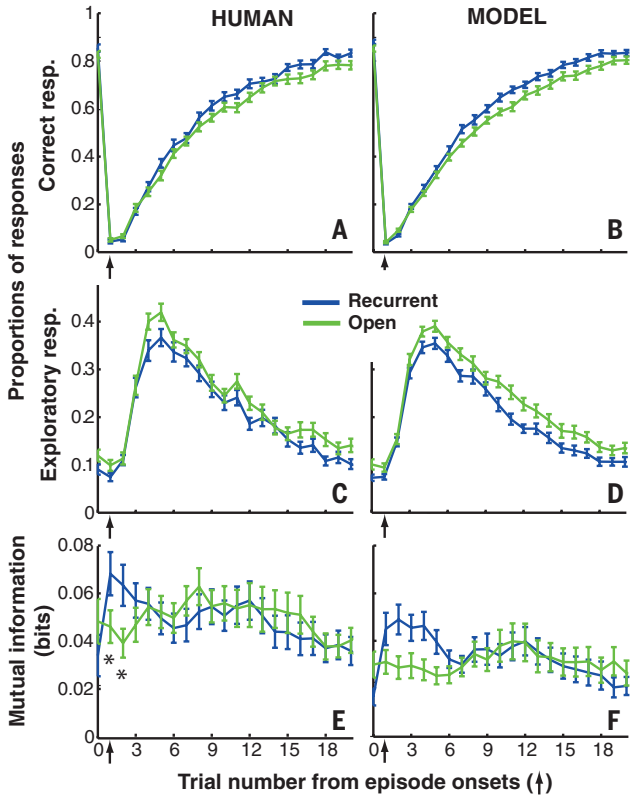

Fig. 2. Behavioral performances following episode changes. Proportion of correct (top) and exploratory (middle) responses from episode onsets (arrows). (**A**, **C**, and **E**) participants' performances. (**B**, **D**, and **F**) Fitted model predictions in every trial given participants' responses in previous trials. (E and F) Statistical dependences between two successive correct responses produced by participants (E) and fitted model simulations (F) (mutual information computed over five-trials sliding windows). Green: open episodes; blue: recurrent episodes. Error bars are SEM across participants. See table S1 for model parameters. *P < 0.05.

perseverative responses abruptly dropped off (~40%), and exploratory responses abruptly increased to a plateau (~35 to 40%). In exploration trials following switch-in events, both model and participants' exploratory responses remain on the plateau, whereas perseverative responses slowly decreased (correct responses consequently increased slowly).

In 43% of recurrent episodes, the algorithm terminated these exploration periods by retrieving counterfactual strategies and rejecting probe actors [on average 10.1 (SD = 3.2) after episode onsets]. In the remaining recurrent episodes (57%) and most open episodes (84%), the algorithm terminated exploration by confirming probe actors in long-term memory [on average 6.7 (SD = 3.3) and 8.1 (SD = 3.9) trials after recurrent and open episode onsets, respectively]. We refer to these algorithmic transitions as rejection and confirmation events, respectively. Realigning again model and participants' performances on these rejection and confirmation events reveals that (Fig. 3, right), when rejection events occurred, both model and participants' correct responses abruptly increased and exploratory responses abruptly dropped off; when confirmation events occurred, by contrast, correct and exploratory responses exhibited no abrupt changes and, as expected, gradually increased and decreased, respectively (more results in supplementary text).

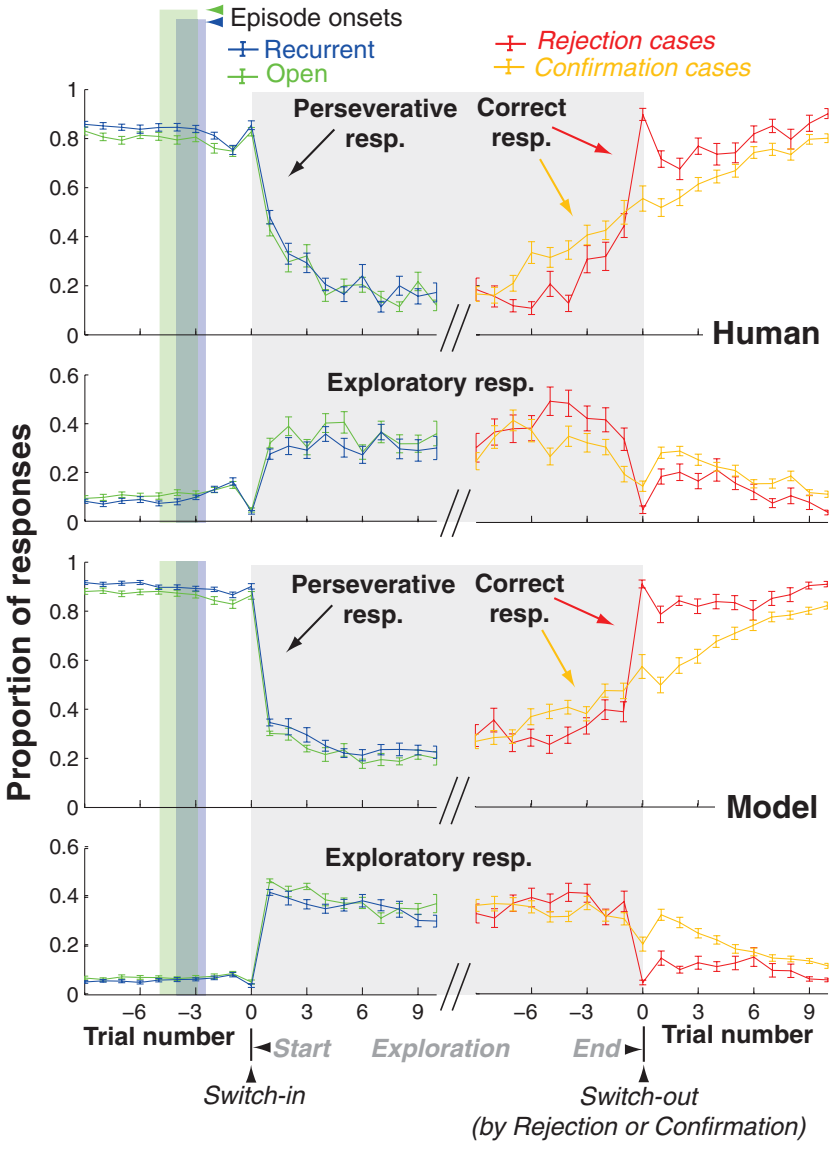

Fig. 3. Behavioral performances according to predicted algorithmic transitions. Model predictions (bottom) and participants' performances (top) realigned on switch-in (left), rejection (right, red) and confirmation (right, orange) events occurring in the algorithm. Data points following switch-in events and preceding rejection and confirmation events included only exploration trials. Model predictions are computed in every trial given participants' responses in previous trials. Green, open episodes; blue, recurrent episodes. Green and blue shaded areas are centered on the average of episode onsets preceding switch-in events (width: standard deviations). Perseverative responses correspond to correct responses in preceding episodes. Error bars are SEM across participants.

Brain activations associated with reasoning computations

We then investigated whether fMRI activations confirm the implementation of the proposed algorithm in the PFC. To identify activations associated with inferring strategies' absolute reliability, we considered three reliability variables derived from the best-fitting model: actor and first- and second-alternative reliability. We entered these variables orthogonalized in that order in a unique regression analysis, which also included algorithmic events switch-in, rejection, and confirmation as regressors, along with those modeling exploration and exploitation trials (*9*). The regression factored out possible confounding variables including reward expectations, outcome predictions, and feedback values. We identified activations using significance thresholds set to $P = 0.05$ (familywise error corrected for multiple comparisons over the frontal lobes), and post hoc analyzes removed selection biases (*22*).

Strategies' reliability correlated with anterior PFC activations. Actor reliability correlated with ventromedial PFC (vmPFC) and perigenual anterior cingulate (pgACC) cortex activations, whereas right frontopolar cortex (FPC) activations correlated concurrently with both first- and second-alternative reliability (Fig. 4). No other regions exhibited such correlations ($P > 0.01$, uncorrected). vmPFC and pgACC activations that increased with actor reliability further decreased with first- and, more strongly, with second-alternative reliability, whereas right FPC activations decreased with actor reliability while increasing with first- and, more strongly, with second-alternative reliability (Fig. 4). The symmetrical, left FPC region marginally exhibited the same activation pattern as the right FPC (actor and first- and second-alternative reliability: all $T > 1.99$, $P < 0.053$). Accordingly, the less a strategy was eligible as actor, the more its reliability elicited FPC detrimentally to vmPFC and/or pgACC activations. vmPFC-pgACC and left FPC activations were also associated with feedback values ($T > 2.43$, $P < 0.0195$), from which strategies' reliability is inferred.

Using the same regression analysis, we next examined activations in switch-in, rejection, and confirmation events associated with hypothesis testing. These algorithmic events elicited more posterior PFC activations. Medially, the dorsal ACC (dACC) responded selectively to switch-in events (Fig. 5A). Switch-in events elicited larger dACC responses than exploitation and exploration trials (both $T > 3.59$, $P < 0.001$) and than rejection and confirmation events (both $T = 2.02$, $P = 0.05$). The latter events elicited no significant dACC responses compared with exploitation and exploration trials ($T < 2.02$, $P > 0.05$). Confirmation events elicited only marginal dACC responses ($T = 2.32$, $P = 0.03$). Laterally, the left PFC [Brodmann's area (BA) 45, middle lateral prefrontal cortex (mid-LPC)] responded selectively to rejection events (Fig. 5B). Rejection events

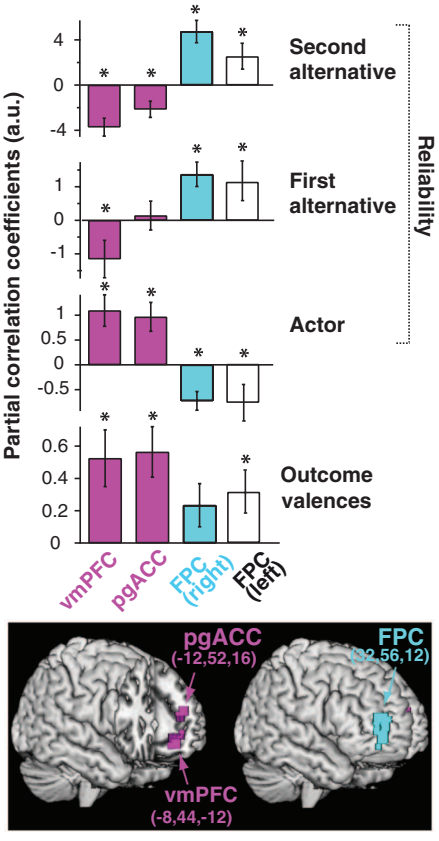

Fig. 4. Brain activations associated with reliability inferences. (**Bottom**) 3D rendering of all brain activations correlating with actor reliability (magenta) and with first- and second-alternative reliability (cyan) (thresholded at $P < 0.005$ (voxel-wise, uncorrected) and $P < 0.05$ (cluster-wise) for display purpose). Montreal Neurological Institute (MNI) coordinates of activation peaks are showed in brackets. (**Top**) Partial correlation coefficients for feedback valence, actor, and first- and second-alternative reliability averaged over activation clusters; a.u., arbitrary units. White bars are for the region symmetrical to right FPC activations (left FPC). Error bars are SEM across participants. *$P < 0.05$.

elicited larger mid-LPC activations than exploitation and exploration trials (both $T > 4.53$, $P < 0.00006$) and than switch-in and confirmation events (joint effect: $T = 2.38$, $P = 0.022$). The latter events elicited no significant mid-LPC responses (both $T < 1.69$, $P > 0.10$). Both the dACC and mid-LPC exhibited no differential responses between exploitation and exploration trials (Ts < 1) (Fig. 5, A and B) and no responses in the trials immediately preceding and following switch-in and rejection events (Fig. 6). Thus, dACC and mid-LPC responses to switch-in and rejection events, respectively, reflected the algorithmic transitions rather than the differential production of perseverative, exploratory versus correct responses and associated cognitive states around these events. Furthermore, as both switch-in and rejection events involve actor switching based on the same reliability threshold (= ½), these differential activations could not simply reflect choice uncertainty and general inhibition or selection mechanisms across monitored strategies. Instead, these results indicate that the dACC detects when actors monitored in the pgACC-vmPFC become unreliable for triggering the creation of probe actors, whereas the mid-LPC detects when counterfactual strategies monitored in the FPC become reliable for retrieving them as actor.

Only the ventral striatum responded selectively to confirmation events (Fig. 5C). Confirmation events elicited larger ventral-striatal activations than exploitation and exploration trials (both $T > 3.59$, $P < 0.0009$) and than switch-in and rejection events (both $T > 2.99$, $P < 0.005$). There were no significant ventral-striatal responses to switch-in and rejection events compared with exploitation and exploration trials (all $T < 1.99$, $P > 0.06$) nor differential ventral-striatal responses between exploitation and exploration trials ($T = 1.11$, $P = 0.27$), nor significant ventral-striatal responses in the trials immediately preceding and following confirmation events (Fig. 6). The region concurrently responded to reward predictions errors: Ventral striatal activations correlated both positively with feedback rewarding values ($T = 5.04$, $P = 0.00002$) and negatively with reward expectations ($T = 4.25$, $P = 0.00013$). Thus, beyond its involvement in actor reinforcement learning over trials (*16*), the ventral striatum exhibited additional responses in confirmation events. Because the vmPFC-pgACC projects to the ventral striatum (*23*) and encoded actor reliability, the evidence is that the ventral striatum detects when newly created strategies driving behavior become reliable, presumably for confirming their storage in long-term memory.

The dorsal striatum responded selectively to switch-in events (fig. S3), whereas bilateral posterior PFC (BA 44, post-LPC) and left premotor regions responded to both switch-in and confirmation events (fig. S4). These activations accord with the involvement of posterior frontal-striatal circuits in forming and storing action sets (*18*): Dorsal- and ventral-striatal responses correlated with premotor and post-LPC responses in switch-in and confirmation events, respectively, when the algorithm created and confirmed probe actors in long-term memory (fig. S5). We found no other frontal and basal responses ($P > 0.05$, uncorrected) except bilateral responses to switch-in events in FPC regions reported above (fig. S3), which likely reflected that, concomitant to probe actor creation, the former actor registers as an additional counterfactual strategy in the inferential buffer (more results in supplementary text).

Prefrontal foundations of human reasoning

The predicted algorithmic transitions associated with hypothesis testing and accounting for participants' behavior occurred within the frontal lobes in the expected PFC and striatal regions. Moreover, the anterior PFC encoded the predicted absolute reliability signals associated with the concurrent behavioral strategies the algorithm creates, learns, tests, and retrieves for driving action. These results support the hypothesis that the proposed algorithm describes reasoning PFC processes guiding adaptive behavior (supplementary text). Accordingly, the frontal lobes implement two concurrent inferential tracks. First, a medial track comprising the vmPFC-pgACC, dACC, and ventral striatum makes inferences about the actor strategy that, through reinforcement learning, selects and learns the actions maximizing reward. Whereas the vmPFC-pgACC infers the actor's absolute reliability, the dACC detects when it becomes unreliable for triggering exploration—i.e., the formation of a new strategy from long-term memory to serve as actor. The ventral striatum then detects when this new actor strategy becomes reliable, which terminates exploration and confirms it in long-term memory. Second, a lateral track comprising the FPC and mid-LPC makes inferences about two or three alternative strategies stored in long-term memory. Whereas the FPC concurrently infers the absolute reliability of these counterfactual strategies from action outcomes, the mid-LPC detects when one becomes reliable for retrieving it as actor.

This medial-lateral segregation stems from the model core notion of absolute reliability, which yields to distinguishing between switching away from ongoing behavior (the actor becomes unreliable) versus switching to another behavioral strategy stored in long-term memory (one counterfactual strategy becomes reliable). In this protocol, the two events never coincided, which would have required alternating between only two recurrent situations associated with two distinct strategies (the actor unreliability then implies the reliability of the alternative strategy) (*24*). The dACC thus triggers switching away from ongoing behavior with the formation of new behavioral strategies, whereas the mid-LPC enables the switch to counterfactual strategies. The model may thus explain dACC activations observed in detecting unexpected action outcomes (*25*), switching to exploratory behaviors (*26*) and starting new behavioral tasks (*27*), and LPC activations in retrieving task sets (*15*, *28*). Consistent with the model prediction, moreover, the dACC and mid-LPC coactivate when participants switch back and forth between only two alternative behaviors (*11*).

The model further indicates that the coupling between the medial and lateral track realizes hypothesis testing bearing upon new behavioral strategies created from long-term memory. Serving as a probe actor initially set as being unreliable, newly created strategies are disbanded when the mid-LPC detects that one counterfactual strategy has become reliable for retrieving it as actor. However, the ventral striatum adjusts probe actors to external contingencies through reinforcement learning (*16*, *19*, *20*) and detects when probe actors eventually become reliable. In that event, the ventral striatum confirms probe actors in long-term memory as additional, subsequently recoverable, strategies. The interplay between the dACC, mid-LPC, and ventral striatum thus controls switches in and out of exploration periods corresponding to hypothesis testing of newly created strategies. Accordingly, every decision to create new strategies may be subsequently revised according to new

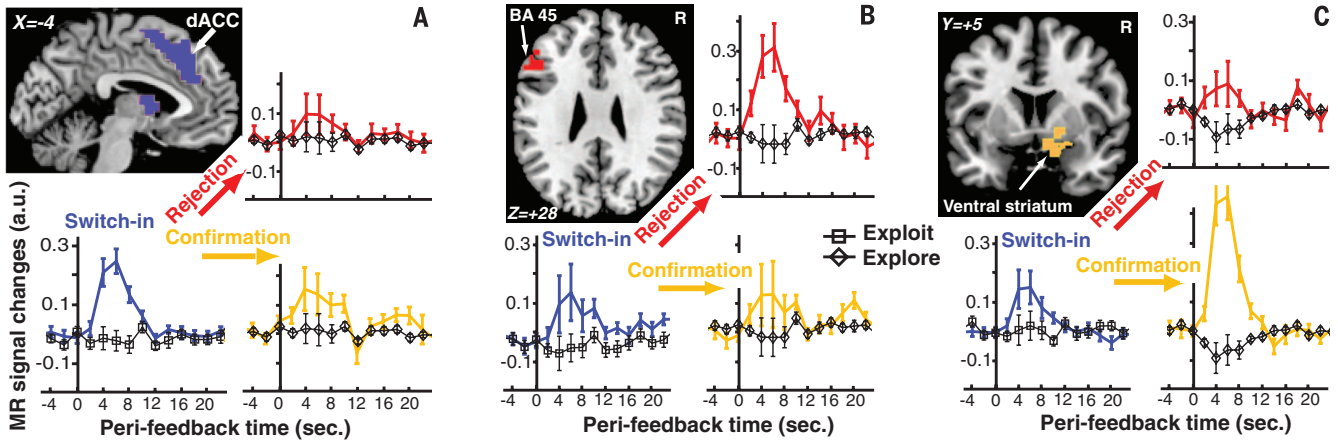

Fig. 5. Prefrontal and basal responses to predicted algorithmic transitions. On the brain slices, activations in switch-in (blue), rejection (red), and confirmation (orange) events superimposed on anatomical templates [thresholded at $P < 0.005$ (voxel-wise, uncorrected) and $P < 0.05$ (cluster-wise) for display purposes]. (**A** to **C**) *X*, *Y*, and *Z* are slice MNI coordinates corresponding to activation peaks (table S2). Graphs show perifeedback magnetic resonance responses to switch-in, rejection, and confirmation events averaged over activation clusters and factoring out all other effects. Black lines are perifeedback MR responses in exploitation (square) and exploration (diamond) trials. Error bars are SEM across participants.

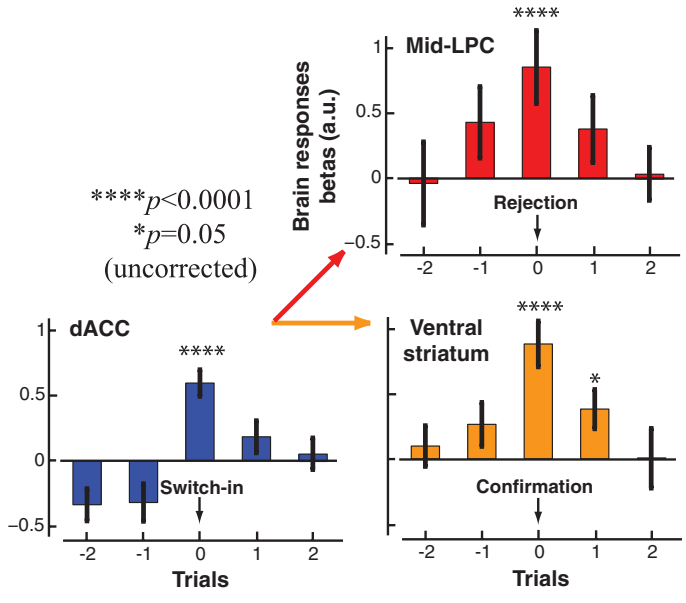

Fig. 6. Prefrontal and striatal responses around algorithmic transitions. Magnetic resonance responses to feedbacks in dACC, mid-LPC, and ventral striatum on trials preceding and following switch-in, rejection, and confirmation events. Bars are partial correlation coefficients (betas) from the regression analysis (a.u., arbitrary units) described in the text and corresponding to event-related regressors modeling switch-in, rejection, and confirmation events shifted 0, 1, or 2 trials preceding and following actual occurrences of these events. Error bars are SEM across subjects. Maximal and significant responses (when corrected for multiple comparisons around algorithmic events) were elicited only when the events occurred in the algorithm.

information, which is critical in optimal adaptive processes operating in open-ended environments for dealing with the intrinsic nonparametric nature of strategy creation (*4*).

Hypothesis testing derives from inferences about the absolute reliability of actor and two or three counterfactual strategies, which involved the vmPFC-pgACC and FPC, respectively. The dissociation supports the distinction between the notion of actor and a counterfactual strategy and accords with the vmPFC-pgACC and FPC involvement in monitoring ongoing and unchosen courses of action, respectively (*3*, *11*, *12*, *29*, *30*). Strategy absolute reliability measures to which extent the strategy is applicable to the current situation—i.e., current external contingencies and those learned by the strategy result from the same latent cause. The vmPFC-pgACC thus infers to which extent the latent cause determining current action outcomes remains unchanged. The FPC infers to which extent the latter result from two or three previously identified latent causes. Latent causes are abstract constructs resulting from hypothesis testing implemented through the interplay between the dACC, mid-LPC, and ventral striatum. Latent causes organize long-term memory as a repertoire of behavioral strategies treated as separable entities. By detecting the reliability or unreliability of monitored strategies, the dACC, mid-LPC, and ventral striatum then appear to implement true or false exclusive judgments about possible causes of observed contingencies for selecting appropriate behavioral strategies. The model thus describes how the PFC forms a unified inferential system subserving reasoning in the service of adaptive behavior. Among the prefrontal regions, the FPC is likely specific to humans (*31*, *32*), which suggests that the ability to jointly infer multiple possible causes of observed contingencies and, consequently, to test new causal hypotheses emerging from long-term memory is unique to humans.

REFERENCES AND NOTES

1. M. Oaksford, N. Chater, *Behav. Brain Sci.* **32**, 69–84; discussion 85–120 (2009).
2. T. E. Behrens, M. W. Woolrich, M. E. Walton, M. F. Rushworth, *Nat. Neurosci.* **10**, 1214–1221 (2007).
3. E. D. Boorman, T. E. Behrens, M. W. Woolrich, M. F. Rushworth, *Neuron* **62**, 733–743 (2009).
4. Y. W. Teh, M. I. Jordan, M. J. Beal, D. M. Blei, *J. Am. Stat. Assoc.* **101**, 1566–1581 (2006).
5. F. Doshi-Velez, *Adv. Neural Inf. Process. Syst.* **21**, 477–485 (2009).
6. N. D. Daw, A. Courville, *Adv. Neural Inf. Process. Syst.* **20**, 369–376 (2007).
7. S. J. Gershman, D. M. Blei, Y. Niv, *Psychol. Rev.* **117**, 197–209 (2010).
8. A. Collins, E. Koechlin, *PLOS Biol.* **10**, e1001293 (2012).
9. Materials and methods are available online as supplementary material on *Science* Online.
10. N. Cowan, in *Human Learning and Memory*, C. Izawa, N. Ohta, Eds. (Erlbaum, Mahwah, NJ, 2005), pp. 155–175.
11. A. N. Hampton, P. Bossaerts, J. P. O'Doherty, *J. Neurosci.* **26**, 8360–8367 (2006).
12. E. Koechlin, A. Hyafil, *Science* **318**, 594–598 (2007).
13. E. D. Boorman, T. E. Behrens, M. F. Rushworth, *PLOS Biol.* **9**, e1001093 (2011).
14. E. Koechlin, C. Ody, F. Kouneiher, *Science* **302**, 1181–1185 (2003).
15. K. Sakai, R. E. Passingham, *Nat. Neurosci.* **6**, 75–81 (2003).
16. J. O'Doherty *et al.*, *Science* **304**, 452–454 (2004).
17. E. Koechlin, C. Summerfield, *Trends Cogn. Sci.* **11**, 229–235 (2007).
18. D. Badre, A. S. Kayser, M. D'Esposito, *Neuron* **66**, 315–326 (2010).
19. W. Schultz, P. Dayan, P. R. Montague, *Science* **275**, 1593–1599 (1997).
20. K. Doya, *HFSP J.* **1**, 30–40 (2007).
21. J. J. Ribas-Fernandes *et al.*, *Neuron* **71**, 370–379 (2011).
22. M. Esterman, B. J. Tamber-Rosenau, Y. C. Chiu, S. Yantis, *Neuroimage* **50**, 572–576 (2010).

23. G. E. Alexander, M. R. DeLong, P. L. Strick, *Annu. Rev. Neurosci.* **9**, 357–381 (1986).
24. S. Charron, E. Koechlin, *Science* **328**, 360–363 (2010).
25. W. H. Alexander, J. W. Brown, *Nat. Neurosci.* **14**, 1338–1344 (2011).
26. N. Kolling, T. E. Behrens, R. B. Mars, M. F. Rushworth, *Science* **336**, 95–98 (2012).
27. N. U. Dosenbach *et al.*, *Neuron* **50**, 799–812 (2006).
28. K. Sakai, *Annu. Rev. Neurosci.* **31**, 219–245 (2008).
29. B. De Martino, S. M. Fleming, N. Garrett, R. J. Dolan, *Nat. Neurosci.* **16**, 105–110 (2013).
30. E. Koechlin, G. Basso, P. Pietrini, S. Panzer, J. Grafman, *Nature* **399**, 148–151 (1999).
31. K. Teffer, K. Semendeferi, *Prog. Brain Res.* **195**, 191–218 (2012).
32. F. X. Neubert, R. B. Mars, A. G. Thomas, J. Sallet, M. F. Rushworth, *Neuron* **81**, 700–713 (2014).

ACKNOWLEDGMENTS

We thank C. Summerfield and S. Palminteri for their helpful comments. Funded by a European Research Council Grant (ERC-2009-AdG#250106) to E.K. MRI data are available at http://central.xnat.org, project ID: PROBE.

SUPPLEMENTARY MATERIALS

www.sciencemag.org/content/344/6191/1481/suppl/DC1
Materials and Methods
Supplementary Text
Figs. S1 to S5
Tables S1 and S2
References (*33*–*36*)

14 February 2014; accepted 15 May 2014
Published online 29 May 2014;
10.1126/science.1252254

REPORTS

QUANTUM METROLOGY

Optically measuring force near the standard quantum limit

Sydney Schreppler,[1]* Nicolas Spethmann,[1] Nathan Brahms,[1]† Thierry Botter,[1]‡ Maryrose Barrios,[1]§ Dan M. Stamper-Kurn[1,2]

The Heisenberg uncertainty principle sets a lower bound on the noise in a force measurement based on continuously detecting a mechanical oscillator's position. This bound, the standard quantum limit, can be reached when the oscillator subjected to the force is unperturbed by its environment and when measurement imprecision from photon shot noise is balanced against disturbance from measurement back-action. We applied an external force to the center-of-mass motion of an ultracold atom cloud in a high-finesse optical cavity and measured the resulting motion optically. When the driving force is resonant with the cloud's oscillation frequency, we achieve a sensitivity that is a factor of 4 above the standard quantum limit and consistent with theoretical predictions given the atoms' residual thermal disturbance and the photodetection quantum efficiency.

Several decades ago, mounting efforts to detect directly the gravitational radiation produced by distant astrophysical sources prompted investigation of the detection limits imposed by the quantum-mechanical properties of the sensors (*1*–*3*). Early gravitational wave detectors (*4*) and subsequent table-top force-measurement systems (*5*, *6*) were dominated by thermal noise that masked the contributions of detection uncertainty from the measurements themselves. Additionally, technical sources of optical noise emerging at high measurement strength obscured the effect of measurement back-action in macroscopic systems subject to strong optical probing (*6*), delaying until recently the observation of such back-action noise (*7*, *8*). A purely quantum limit to force-measurement sensitivity for a continuously probed mechanical oscillator occurs when thermal noise has been reduced to the level of zero-point fluctuations. This standard quantum limit (SQL) is reached when noise introduced by the measurement, which uses a coherent state of probe light, is carefully balanced with the statistical fluctuations of the measurement outcome. A wide array of platforms, having sizes spanning many orders of magnitude, have pushed ever closer to the SQL (*9*–*12*). Sensitivity to forces as small as $(390\ \mathrm{yN})^2/\mathrm{Hz}$ has been reported (*13*); however, measured noise levels are still six to eight orders of magnitude larger (that is, much less sensitive) than the SQL (*14*, *15*).

One way to measure a small force is to apply it to a mechanical harmonic oscillator and then to detect the resulting motion by illuminating the oscillator with light and measuring the phase shift of the reflected beam. Measurement strength is enhanced by placing the oscillator within a resonant optical cavity (*16*). In such an optomechanical system, measurement strength can be characterized by the optomechanical cooperativity $C_{\mathrm{om}} = 4ng_{\mathrm{om}}^2/(\kappa\Gamma)$, where n is the number of probe photons within the cavity, g_{om} is the single-photon optomechanical coupling rate, Γ is the mechanical oscillator full-linewidth, and κ is the optical cavity half-linewidth. C_{om} can be understood as the rate at which one gathers information about the oscillator's motion relative to optical and mechanical decay rates. Quantization of the optical cavity's electromagnetic field (shot noise) sets a lower bound on the imprecision of an optical phase measurement, which varies inversely with C_{om}. In the regime

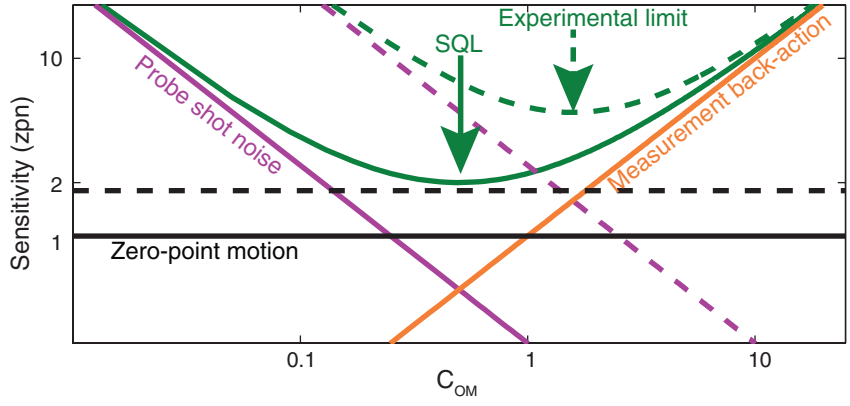

Fig. 1. Contributions to the SQL of force detection. Theoretical shot noise imprecision from probe light (purple lines) decreases and measurement back-action noise (orange line) increases as C_{om} rises. Together with the zero-point fluctuations (black lines), these sum to the total measurement sensitivity (green curves). Dashed lines show noise bounds corrected for imperfect detection efficiency and small nonzero phonon occupation. Sensitivity plotted in units of zero-point force noise ($\mathrm{zpn} = 2\Gamma p_{\mathrm{HO}}^2$, as in Eq. 1).

[1]Department of Physics, University of California, Berkeley, CA 94720, USA. [2]Materials Sciences Division, Lawrence Berkeley National Laboratory, Berkeley, CA 94720, USA.
*Corresponding author. E-mail: sschreppler@berkeley.edu
†Present address: Cisco Systems, Incorporated, San Francisco, CA 94158, USA. ‡Present address: Jet Propulsion Laboratory, Pasadena, CA 91109, USA. §Present address: Department of Physics, Harvard University, Cambridge, MA 02138, USA.

of low C_{om}, force measurement sensitivity is mostly limited by optical shot noise, whereas at high C_{om} the influence of measurement back-action becomes dominant (Fig. 1). The SQL occurs where these two noise contributions are equivalent.

More quantitatively, the total force measurement sensitivity (i.e., the minimum detectable force variation) at a given (angular) frequency $\omega = 2\pi \times f$, and when measuring phase modulation of the cavity probe light, is

$$S_{FF}(\omega) = 2\Gamma p_{HO}^2 \left[\frac{1}{4\varepsilon C_{om}} \frac{(\omega - \omega_m)^2 + (\Gamma/2)^2}{(\Gamma/2)^2} + (2\nu + 1) + C_{om} \right] \quad (1)$$

where p_{HO} is the root mean square (rms) momentum of the harmonic oscillator ground state, ε is the optical detection efficiency, ω_m is the mechanical resonance frequency, and ν is the thermal phonon occupation of the oscillator. The first term in Eq. 1 contains the imprecision in force measurement from photon shot noise, given as the imprecision in position measurement $S_{zz}^{imp} = z_{HO}^2/(2\Gamma\varepsilon C_{om})$ divided by the square magnitude of the mechanical susceptibility $\chi(\omega) = \{2m\omega_m[-(\omega - \omega_m) - i\Gamma/2]\}^{-1}$ for a single mechanical oscillator with mass m, harmonic oscillator length z_{HO}, and in the limit that $\Gamma \ll \omega_m$. The second term in Eq. 1 describes the thermal and quantum oscillator fluctuations, and the third the force noise from measurement back-action; both represent incoherent force noise that obscures the force signal one wishes to measure. Reduced detection efficiency increases the contribution of shot noise for all levels of C_{om}, raising the force-noise minimum and moving it to higher C_{om}.

Previous works (*14, 15, 17, 18*) have demonstrated position-detection imprecision S_{zz}^{imp} below the SQL for such a measurement, $S_{zz}^{SQL} = 4z_{HO}^2/\Gamma$. However, in those works, the total position-measurement sensitivity $S_{zz}(\omega) = |\chi(\omega)|^2 S_{FF}(\omega)$ was only below S_{zz}^{SQL} far from mechanical resonance, where $|\chi(\omega)|$ is low. On resonance, where force sensitivity is finest, these experiments measured a position sensitivity far above that predicted for a back-action driven oscillator connected to a zero-temperature bath. In contrast, we characterized the total sensitivity (including all terms in Eq. 1, not just the imprecision) to forces applied both at and away from ω_m by using an oscillator prepared near its motional ground state and subject to quantum-mechanical radiation pressure fluctuations.

In our experiments, we applied a calibrated optical-dipole force to a gas of ultracold rubidium atoms, inducing center-of-mass motion of the gas. We measured this force-induced motion first by placing the gas (our forced mechanical oscillator) within a high-finesse Fabry-Pérot optical cavity and then by using a weak probe beam to detect variations in the cavity resonance frequency (*19–21*). Before being forced and probed, the mechanical mode of the gas was near its motional ground state, with thermal occupation of $\nu = 1.2$ phonons (*22*), allowing for observation near the lower bounds of sensitivity imposed by shot noise.

We relied on the decoupling of our cold atomic system from its environment to approach the SQL of force sensitivity. Initially, atoms were loaded predominantly into a single site of a trichromatic optical lattice (Fig. 2) composed of two far-off-resonant trapping beams (840 and 860 nm) and one probe beam (780 nm) detuned 24 GHz from atomic resonance. The lattice potential was produced by standing waves of these three light fields, each resonant with a different TEM_{00} (transverse electromagnetic) mode of the optical cavity. The atoms were localized well within the Lamb-Dicke regime, such that the cavity optical mode interacted primarily with their collective center-of-mass mechanical mode (*21*). An optical superlattice allowed us to separate spectrally the collective mechanical modes of atoms in neighboring lattice sites, identifying the mode within a single site having resonance frequency $\omega_m = 2\pi \times 110$ kHz as our oscillator of interest (*23*). Additionally, we could apply a driving force at and around the mechanical resonance frequency of this oscillator by modulating the intensity of one trapping beam (Fig. 2 inset) while keeping the others fixed, the dominant effect of which was to displace the center of mass of the atoms without exciting them parametrically. Calculating this applied force requires calibrating both the static dipole force applied by the 840-nm beam at its full power and the modulation index of the drive intensity (*22*).

The atoms were positioned at a location where the probe beam's intensity varied linearly with position (Fig. 2). The probe light was tuned to be resonant with the cavity mode when the atoms were at their equilibrium position. Thus, position fluctuations of the atoms led to phase fluctuations of the light exiting the cavity, which

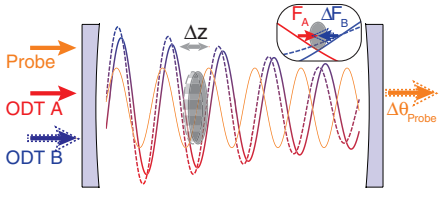

Fig. 2. Trichromatic lattice potential landscape. Atoms (gray oval) are trapped in a conservative optical-dipole potential (red-blue gradient curve) created dominantly by two standing-wave light fields with wavelengths of 860 and 840 nm. At the trapping location, the cavity probe light (wavelength of 780 nm, orange curve) has a strong intensity gradient, maximizing the position-measurement strength. The 840-nm (ODT B) trap amplitude is varied (dashed lines) to produce a modulated force on the atoms that is optomechanically transduced onto the phase of the probe light. (**Inset**) The two trapping light fields produce equal and opposite axial forces on the atoms. Amplitude modulation of ODT B results in a force that shifts the potential minimum. Schematic is not to scale.

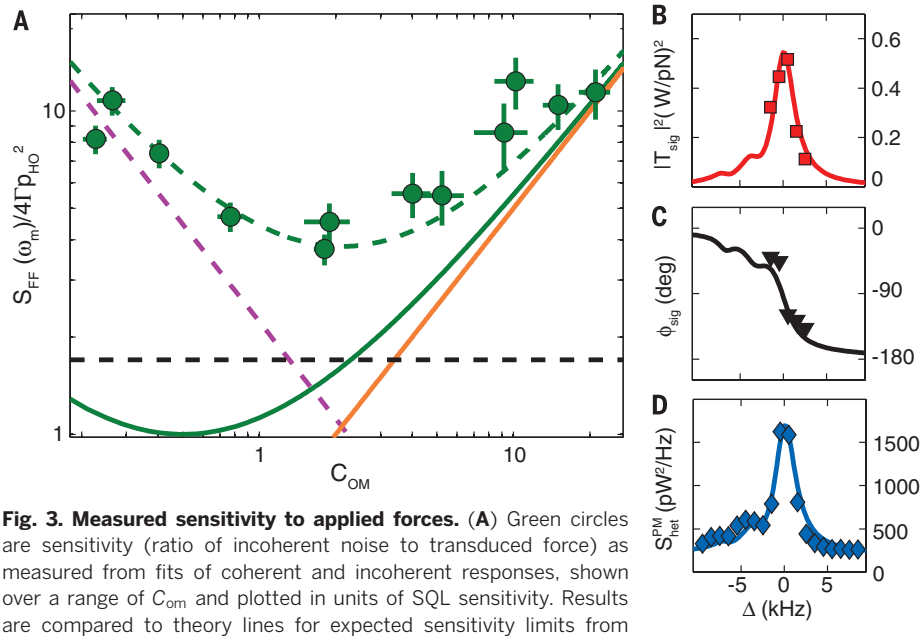

Fig. 3. Measured sensitivity to applied forces. (**A**) Green circles are sensitivity (ratio of incoherent noise to transduced force) as measured from fits of coherent and incoherent responses, shown over a range of C_{om} and plotted in units of SQL sensitivity. Results are compared to theory lines for expected sensitivity limits from probe shot noise (purple line), measurement back action (orange line), thermal and zero-point fluctuations (black dashed line), and total noise (green curve). Theory lines are shown for perfect (solid) and calibrated (dashed) detection efficiency and phonon occupation. Error bars include contributions from uncertainty of the atom number calibration and of the fits. An example of the simultaneous fits for (**B**) the squared amplitude $|T_{sig}|^2$ (data, red squares; fit, red curve) and (**C**) phase ϕ_{sig} (data, black triangles; fit, black curve) of the coherent response, and (**D**) the incoherent noise spectrum S_{het}^{PM} (data, blue diamonds; fit, blue curve), for data at $C_{om} = 4$. See (*22*) for definitions of terms.

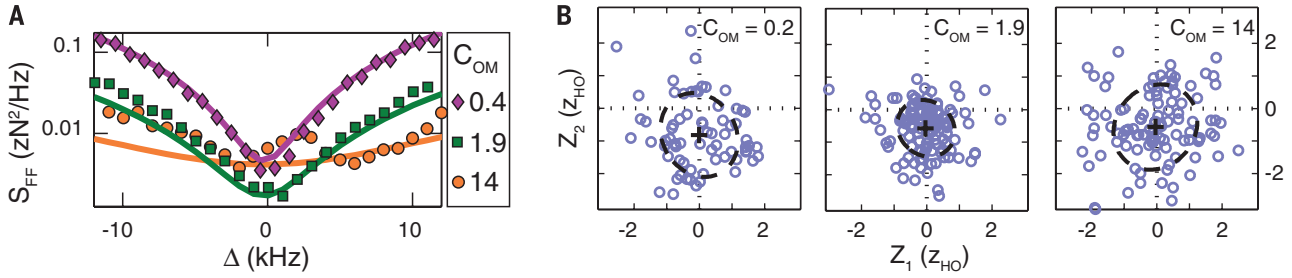

Fig. 4. Sensitivity spectra and phase space representations. (**A**) Force spectral density measured at C_{om} = 0.4 (purple diamonds), 1.9 (green squares), and 14 (orange circles), accompanied by theory lines given by Eq. 1. Deviation of orange data from theory is a second-order effect of slight asymmetries in the mechanical response that arise at high C_{om} and are not captured by the Lorentzian fits, with the effect compounded by taking the ratio of the data to the fit. (**B**) Phase space representations of displacements in units of z_{HO} (blue circles) with one-sigma error ellipse (dashed black curves) and average values (black crosses) plotted for C_{om} = 0.2, 1.9, and 14 (left to right). Deviations from circularity of around 10% are consistent with expected uncertainty given the finite sample size. Positions of black crosses correspond to average forced displacements.

we detected with a heterodyne receiver. When a force was applied, the driven oscillator response was optomechanically transduced into coherent phase fluctuations of the probe light, whereas the measurement noise produced incoherent fluctuations.

During separate repetitions of the experiment, we applied the calibrated force at 1-kHz intervals at and around mechanical resonance, scanning the spectral line shape of the coherent response. The ratio of the complex spectral response to the applied force is the measured susceptibility (Fig. 3, B and C), which we expected to be proportional to $\chi(\omega)$.

We tuned C_{om} over two orders of magnitude by varying the probe intensity. C_{om} was measured from the optomechanical response to the probe. For each force modulation frequency and at each C_{om}, we prepared a new atomic oscillator, addressed it with a modulated force of constant amplitude, and optically probed its response. We repeated this process 100 to 200 times per set of measurement parameters and averaged the results. The heterodyne power spectrum absent the coherent driven response determined the imprecision noise of our measurement (*22*). This incoherent shot noise–driven response gave our total noise spectrum at a given C_{om} (Fig. 3D).

We simultaneously fitted the coherent driven response and the incoherent noise spectral response of our oscillator at each C_{om} to a Lorentzian resonance condition (*22*) that included a primary peak at ω_m and two secondary peaks slightly red-detuned (Fig. 3, B to D). These secondary peaks arose from the anharmonicity of single-atom motion in our optical superlattice, where atoms excited to higher bands of the trap encountered decreasing level spacing with increasing energy. Because the force we applied displaced the atoms by a fraction of their harmonic oscillator length, we approximated the primary peak as harmonic. From each fit, we extracted the incoherent and coherent response amplitudes as well as Γ and ω_m. These parameters, together with the calibrated value of the applied force, determined our force sensitivity on resonance (Fig. 3A).

The ratio of the total noise spectrum to the transduced force spectrum gives the sensitivity of Eq. 1, which is minimized when the oscillator is driven resonantly and probed with $C_{om} = \varepsilon^{-1/2}/2$, such that $S_{FF}(\omega_m) = 2\Gamma p_{HO}^2[(2\nu+1) + 1/\sqrt{\varepsilon}]$. With perfect detection efficiency and oscillator motion limited to zero-point fluctuations, the SQL sensitivity for our oscillator (with $\Gamma = 2\pi \times 3$ kHz and $m = 1.8 \times 10^{-22}$ kg for 1200 ^{87}Rb atoms) is $4\Gamma p_{HO}^2 = (21 \pm 1\ \mathrm{yN})^2/\mathrm{Hz}$. However, given our system's calibrated photodetection efficiency of 11%, use of heterodyne rather than homodyne detection (giving $\varepsilon = 0.056$), and average thermal occupation of 1.2 phonons, our predicted limit is $(41 \pm 1\ \mathrm{yN})^2/\mathrm{Hz}$ and is expected to occur at C_{om} = 2. Our measured force sensitivity is $(42 \pm 13\ \mathrm{yN})^2/\mathrm{Hz}$, in agreement with theoretical prediction and 4 times higher than the SQL. This corresponds to a measured acceleration sensitivity of $(0.02g)^2/\mathrm{Hz}$, where g is the gravitational acceleration. Both technical limitations of our measurement can be ameliorated straightforwardly: Near-infrared photons can be detected with efficiencies exceeding ε = 0.9 (*24*), and colder atomic gases can be produced with improved evaporative cooling. For off-resonant detection (Fig. 4A), the minimum force sensitivity is achieved at $C_{om} > 2$ and is necessarily greater than the noise limits for forces applied at ω_m.

Another interpretation of the quantum limit of force sensitivity states that, at the SQL, the total force noise introduced by performing a measurement over the course of one mechanical damping period equals the zero-point fluctuations of the coherent system (*25*, *26*). This can be seen in Fig. 1, where at the SQL the contributions of shot noise and measurement back-action sum to one unit of zero-point motion. Therefore, the total noise in the detection of forces is at best limited to twice the zero-point noise. Our phase-sensitive optical measurement records the forced displacement of our coherent mechanical state and the quantum-limited noise associated with its measurement. Figure 4B shows these complex responses measured over 1 ms, that is, averaged over about 18 mechanical damping periods. These phase-space plots highlight the difference between the measurement of force and of position: Whereas our position measurement noise S_{zz} is given by the width of the measurement distribution, our force measurement noise S_{FF} is the ratio of this to the distribution's average displacement from the origin.

Uncertainty in the scaled position measurement is related to the position sensitivity by $\Delta Z_1 \Delta Z_2 = S_{zz}/(z_{HO}^2 \tau)$, where τ is the measurement time and Z_1 and Z_2 are the real and imaginary displacement quadratures, respectively, in units of z_{HO}. Substitution of the minimum S_{zz} produces an uncertainty relation for the sensitivity of the state measurement:

$$\langle \Delta Z_1 \rangle \langle \Delta Z_2 \rangle \geq \frac{2}{\tau\Gamma}[(2\nu+1) + 1/\sqrt{\varepsilon}] \quad (2)$$

The minimum uncertainty condition for this inequality is the quantum limit, consistent with twice the zero-point fluctuations. A covariance matrix of the experimental results gives an error ellipse whose radii quantify the rms noise of measurement in the respective quadratures. Near the quantum limit, we observe a spread of points with $\langle \Delta Z_1 \rangle \langle \Delta Z_2 \rangle = 0.8$. As with the measure of force-noise sensitivity, this value matches our prediction well and is about four times the standard minimum sensitivity value.

The achievement of force measurement near the SQL encourages investigations of sensitivity beyond this level. Several proposed methods that could allow optomechanical systems to overcome this limit rely on noise correlations introduced into the system. Measurement techniques that evade back-action (*3*) have already been demonstrated to reduce classical noise in force detection (*27*, *28*), whereas other proposals call for the coupling of two optical cavity modes (*29*–*31*) or the measurement of a single quadrature using phase-sensitive quantum nondemolition detection (*3*, *25*, *32*). Enhanced force sensitivity and the understanding of its fundamental limits may allow for improved atomic force microscopy, the direct detection of gravitational waves (*11*), and measurements of corrections to Newtonian gravity (*33*).

δ_i is measured by computing the minimum distance between the point i and any other point with higher density:

$$\delta_i = \min_{j:\rho_j > \rho_i} (d_{ij}) \quad (2)$$

For the point with highest density, we conventionally take $\delta_i = \max_j(d_{ij})$. Note that δ_i is much larger than the typical nearest neighbor distance only for points that are local or global maxima in the density. Thus, cluster centers are recognized as points for which the value of δ_i is anomalously large.

This observation, which is the core of the algorithm, is illustrated by the simple example in Fig. 1. Figure 1A shows 28 points embedded

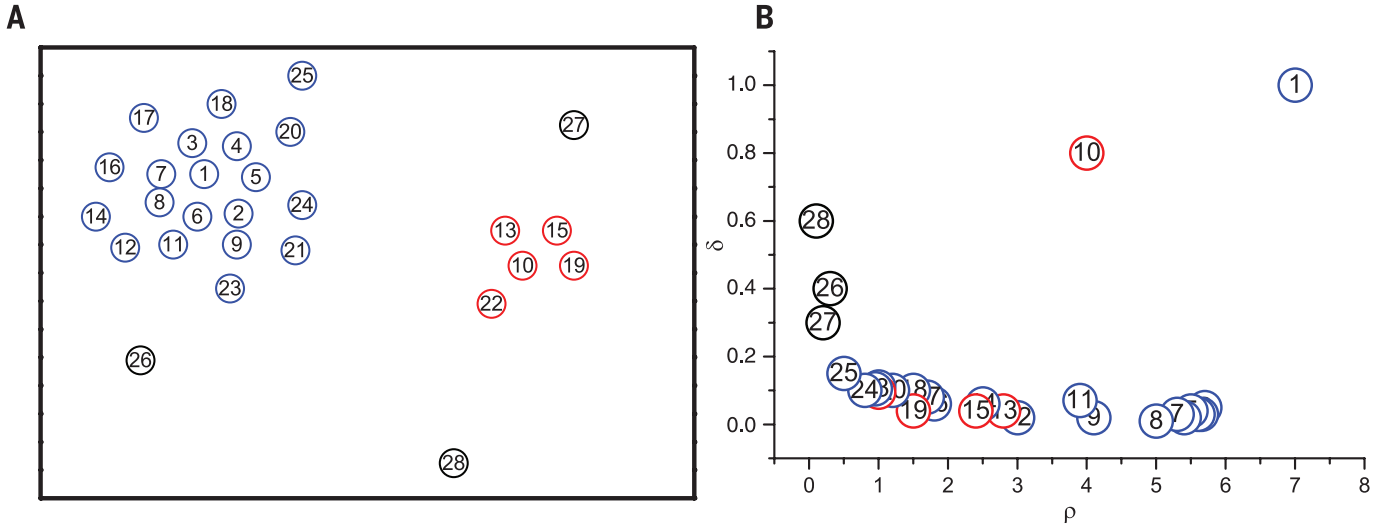

Fig. 1. The algorithm in two dimensions. (**A**) Point distribution. Data points are ranked in order of decreasing density. (**B**) Decision graph for the data in (A). Different colors correspond to different clusters.

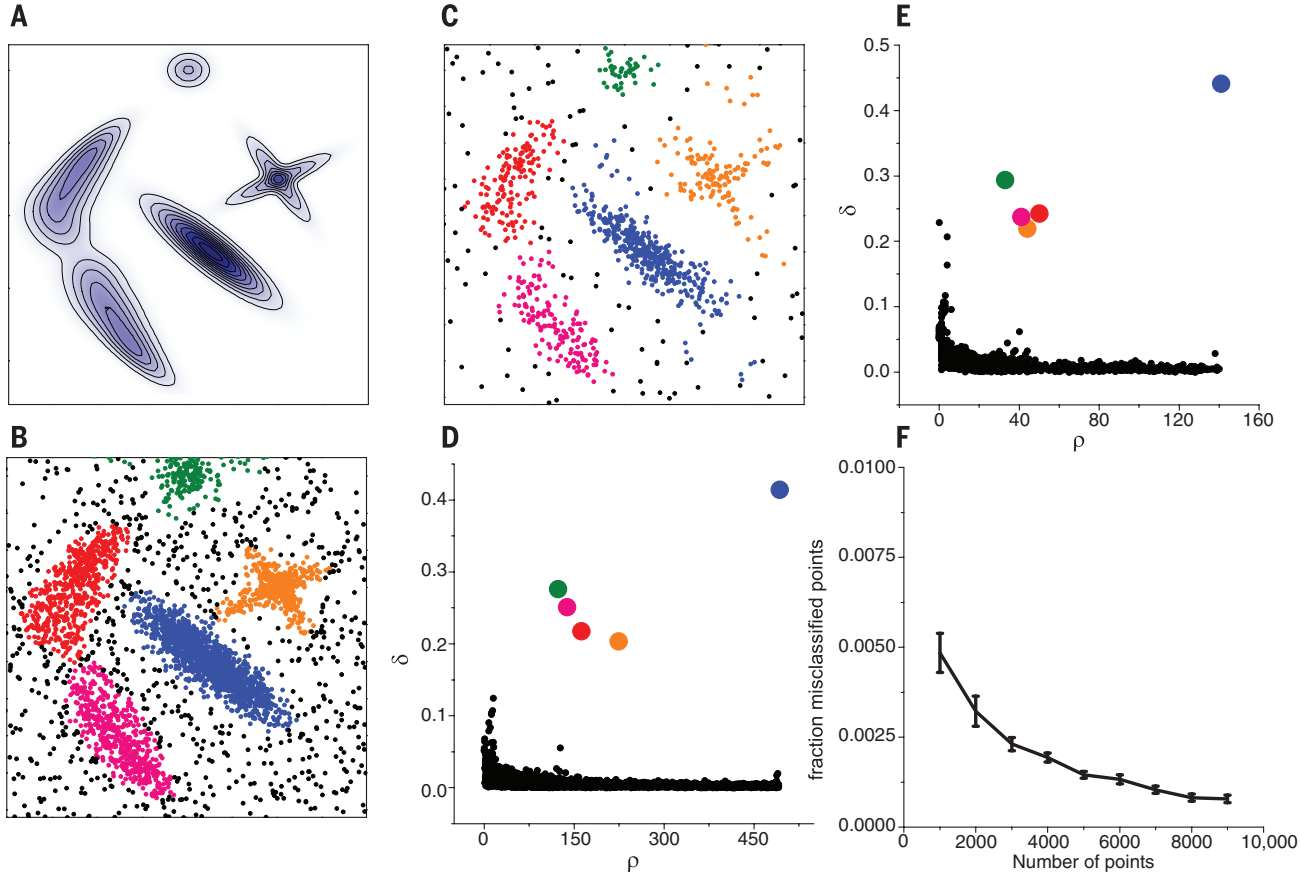

Fig. 2. Results for synthetic point distributions. (**A**) The probability distribution from which point distributions are drawn. The regions with lowest intensity correspond to a background uniform probability of 20%. (**B** and **C**) Point distributions for samples of 4000 and 1000 points, respectively. Points are colored according to the cluster to which they are assigned. Black points belong to the cluster halos. (**D** and **E**) The corresponding decision graphs, with the centers colored by cluster. (**F**) The fraction of points assigned to the incorrect cluster as a function of the sample dimension. Error bars indicate the standard error of the mean.

in a two-dimensional space. We find that the density maxima are at points 1 and 10, which we identify as cluster centers. Figure 1B shows the plot of δ_i as a function of ρ_i for each point; we will call this representation the decision graph. The value of δ for points 9 and 10, with similar values of ρ, is very different: Point 9 belongs to the cluster of point 1, and several other points with a higher ρ are very close to it, whereas the nearest neighbor of higher density of point 10 belongs to another cluster. Hence, as anticipated, the only points of high δ and relatively high ρ are the cluster centers. Points 26, 27, and 28 have a relatively high δ and a low ρ because they are isolated; they can be considered as clusters composed of a single point, namely, outliers.

After the cluster centers have been found, each remaining point is assigned to the same cluster as its nearest neighbor of higher density. The cluster assignment is performed in a single step, in contrast with other clustering algorithms where an objective function is optimized iteratively (*2*, *8*).

In cluster analysis, it is often useful to measure quantitatively the reliability of an assignment. In approaches based on the optimization of a function (*2*, *8*), its value at convergence is also a natural quality measure. In methods like DBSCAN (*9*), one considers reliable points with density values above a threshold, which can lead to low-density clusters, such as those in Fig. 2E, being classified as noise. In our algorithm, we do not introduce a noise-signal cutoff. Instead, we first find for each cluster a border region, defined as the set of points assigned to that cluster but being within a distance d_c from data points belonging to other clusters. We then find, for each cluster, the point of highest density within its border region. We denote its density by ρ_b. The points of the cluster whose density is higher than ρ_b are considered part of the cluster core (robust assignation). The others are considered part of the cluster halo (suitable to be considered as noise).

In order to benchmark our procedure, let us first consider the test case in Fig. 2. The data points are drawn from a probability distribution with nonspherical and strongly overlapping peaks (Fig. 2A); the probability values corresponding to the maxima differ by almost an order of magnitude. In Fig. 2, B and C, 4000 and 1000 points, respectively, are drawn from the distribution in Fig. 2A. In the corresponding decision graphs (Fig. 2, D and E), we observe only five points with a large value of δ and a sizeable density. These points are represented in the graphs as large solid circles and correspond to cluster centers. After the centers have been selected, each point is assigned either to a cluster or to the halo. The algorithm captures the position and shape of the probability peaks, even those corresponding to very different densities (blue and light green points in Fig. 2C) and nonspherical peaks. Moreover, points assigned to the halo correspond to regions that by visual inspection of the probability distribution in Fig. 2A would not be assigned to any peak.

To demonstrate the robustness of the procedure more quantitatively, we performed the analysis by drawing 10,000 points from the distribution in Fig. 2A, considering as a reference the cluster assignment obtained on that sample. We then obtained reduced samples by retaining only a fraction of points and performed cluster assignment for each reduced sample independently. Figure 2F shows, as a function of the size of the reduced sample, the fraction of points assigned to a cluster different than the one they were assigned to in the reference case. The fraction of misclassified points remains well below 1% even for small samples containing 1000 points.

Varying d_c for the data in Fig. 2B produced mutually consistent results (fig. S1). As a rule of thumb, one can choose d_c so that the average number of neighbors is around 1 to 2% of the total number of points in the data set. For data

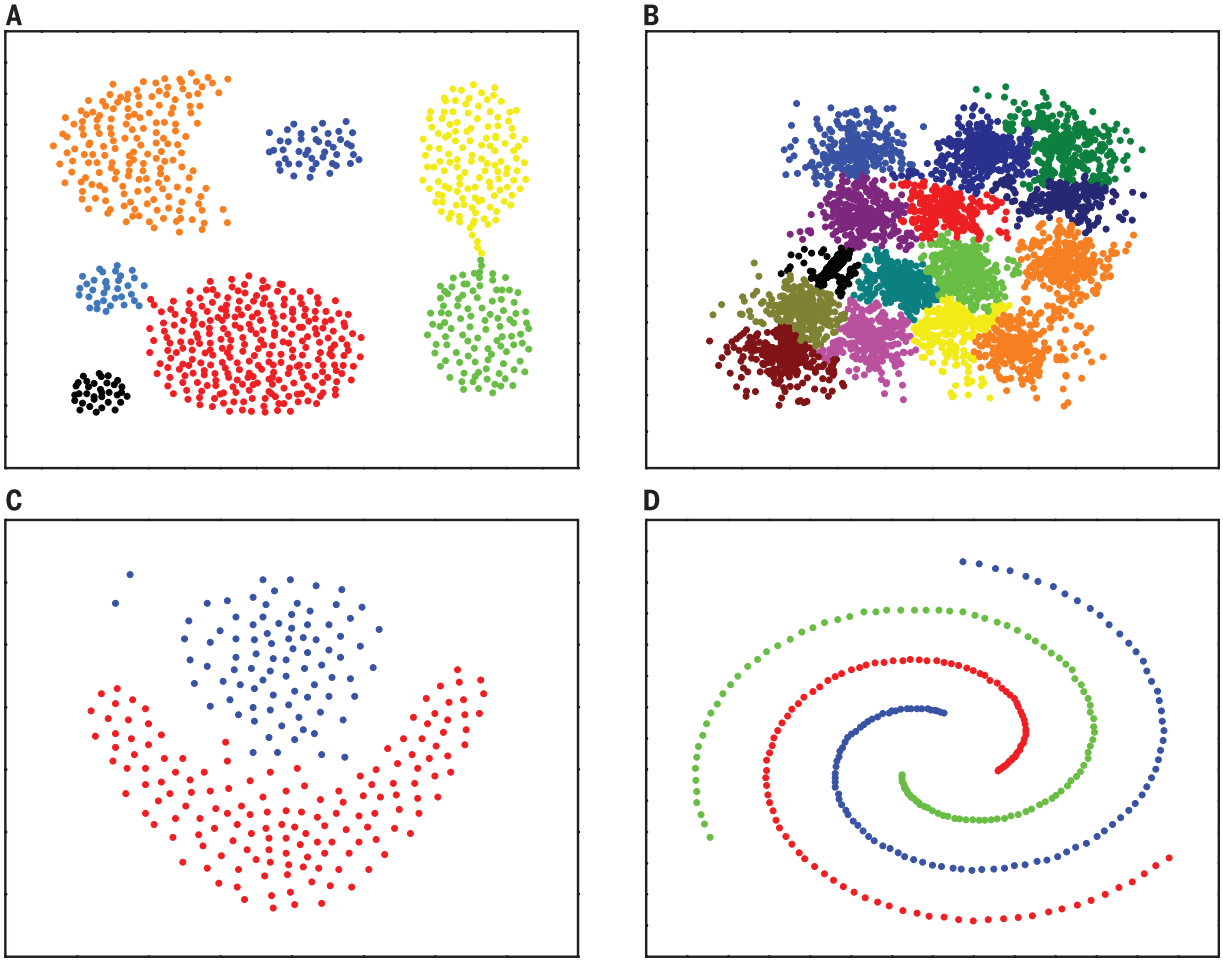

Fig. 3. Results for test cases in the literature. Synthetic point distributions from (*12*) (**A**), (*13*) (**B**), (*14*) (**C**), and (*15*) (**D**).

sets composed by a small number of points, ρ_i might be affected by large statistical errors. In these cases, it might be useful to estimate the density by more accurate measures (*10*, *11*).

Next, we benchmarked the algorithm on the test cases presented in Fig. 3. For computing the density for cases with few points, we adopted the exponential kernel described in (*11*). In Fig. 3A, we consider a data set from (*12*), obtaining results comparable to those of the original article, where it was shown that other commonly used methods fail. In Fig. 3B, we consider an example with 15 clusters with high overlap in data distribution taken from (*13*); our algorithm successfully determines the cluster structure of the data set. In Fig. 3C, we consider the test case for the FLAME (fuzzy clustering by local approximation of membership) approach (*14*), with results comparable to the original method. In the data set originally introduced to illustrate the performance of path-based spectral clustering (*15*) shown in Fig. 4D, our algorithm correctly finds the three clusters without the need of generating a connectivity graph. As comparison, in figs. S3 and S4 we show the cluster assignations obtained by K-means (*2*) for these four test cases and for the example in Fig. 2. Even if the K-means optimization is performed with use of the correct value of K, the assignations are, in most of the cases, not compliant with visual intuition.

The method is robust with respect to changes in the metric that do not significantly affect the distances below d_c, that is, that keep the density estimator in Eq. 1 unchanged. Clearly, the distance in Eq. 2 will be affected by such a change of metric, but it is easy to realize that the structure of the decision graph (in particular, the number of data points with a large value of δ) is a consequence of the ranking of the density values, not of the actual distance between far away points. Examples demonstrating this statement are shown in fig. S5.

Our approach only requires measuring (or computing) the distance between all the pairs of data points and does not require parameterizing a probability distribution (*8*) or a multidimensional density function (*10*). Therefore, its performance is not affected by the intrinsic dimensionality of the space in which the data points are embedded. We verified that, in a test case with 16 clusters in 256 dimensions (*16*), the algorithm finds the number of clusters and assigns the points correctly (fig. S6). For a data set with 210 measurements of seven x-ray features for three types of wheat seeds from (*17*), the algorithm correctly predicts the existence of three clusters and classifies correctly 97% of the points assigned to the cluster cores (figs. S7 and S8).

We also applied the approach to the Olivetti Face Database (*18*), a widespread benchmark for machine learning algorithms, with the aim of identifying, without any previous training, the number of subjects in the database. This data set poses a serious challenge to our approach because the "ideal" number of clusters (namely of distinct subjects) is comparable with the number of elements in the data set (namely of different images, 10 for each subject). This makes a reliable estimate of the densities difficult. The similarity between two images was computed by following (*19*). The density is estimated by a Gaussian kernel (*11*) with variance $d_c = 0.07$. For such a small set, the density estimator is unavoidably affected by large statistical errors; thus, we assign images to a cluster following a slightly more restrictive criterion than in the preceding examples. An image is assigned to the same cluster of its nearest image with higher density only if their distance is smaller than d_c. As a consequence, the images further than d_c from any other image of higher density remain unassigned. In Fig. 4, we show the results of an analysis performed for the first 100 images in the data set. The decision graph (Fig. 4A) shows the presence of several distinct density maxima. Unlike in other examples, their exact number is not clear, a consequence of the sparsity of the data points. A hint for choosing the number of centers is provided by the plot of $\gamma_i = \rho_i \delta_i$ sorted in decreasing order (Fig. 4B). This graph shows that this quantity, that is by definition large for cluster centers, starts growing

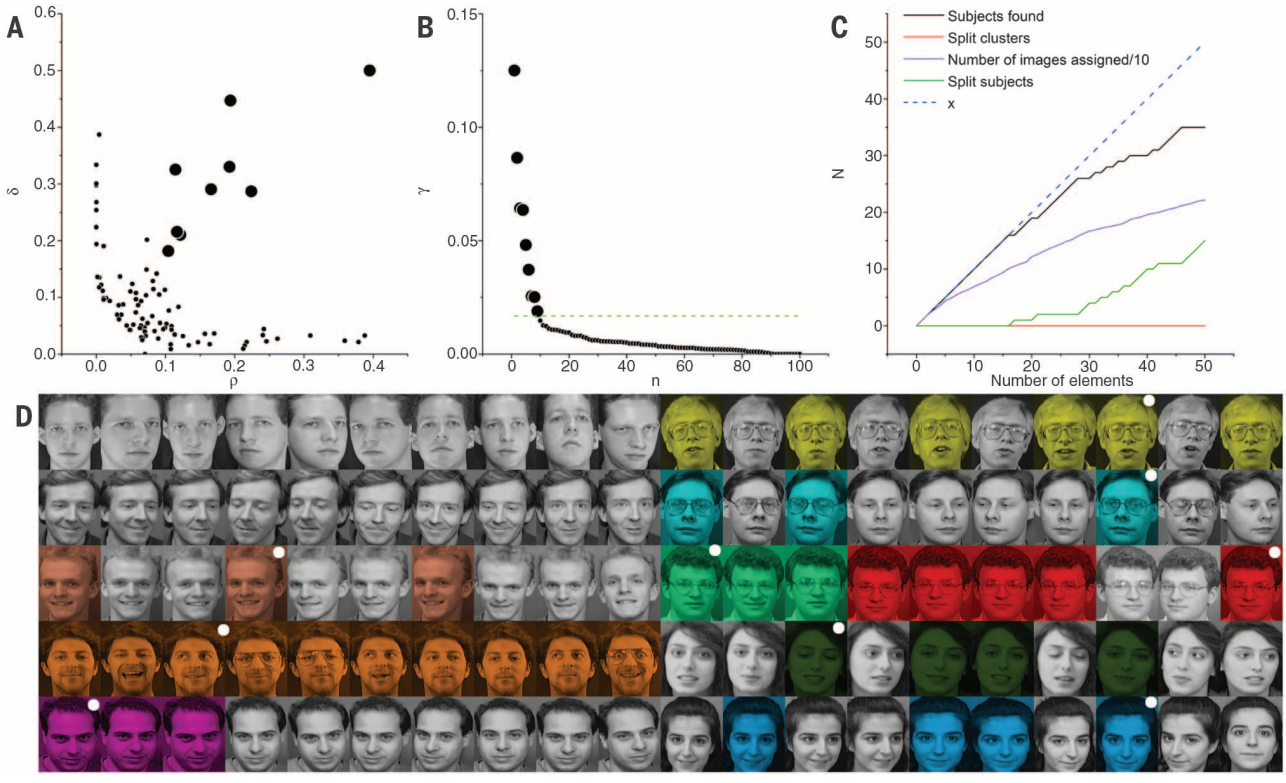

Fig. 4. Cluster analysis of the Olivetti Face Database. (**A**) The decision graph for the first hundred images in the database (*18*). (**B**) The value of $\gamma_i = \rho_i \delta_i$ in decreasing order for the data in (A). (**C**) The performance of the algorithm in recognizing subjects in the full database as a function of the number of clusters: number of subjects recognized as individuals (black line), number of clusters that include more than one subject (red line), number of subjects split in more than one cluster (green), and number of images assigned to a cluster divided by 10 (purple). (**D**) Pictorial representation of the cluster assignations for the first 100 images. Faces with the same color belong to the same cluster, whereas gray images are not assigned to any cluster. Cluster centers are labeled with white circles.

anomalously below a rank order 9. Therefore, we performed the analysis by using nine centers. In Fig. 4D, we show with different colors the clusters corresponding to these centers. Seven clusters correspond to different subjects, showing that the algorithm is able to "recognize" 7 subjects out of 10. An eighth subject appears split in two different clusters. When the analysis is performed on all 400 images of the database, the decision graph again does not allow recognizing clearly the number of clusters (fig. S9). However, in Fig. 4C we show that by adding more and more putative centers, about 30 subjects can be recognized unambiguously (fig. S9). When more centers are included, the images of some of the subjects are split in two clusters, but still all the clusters remain pure, namely include only images of the same subject. Following (*20*) we also computed the fraction of pairs of images of the same subject correctly associated with the same cluster (r_{true}) and the fraction of pairs of images of different subjects erroneously assigned to the same cluster (r_{false}). If one does not apply the cutoff at d_c in the assignation (namely if one applies our algorithm in its general formulation), one obtains $r_{true} \sim 68\%$ and $r_{false} \sim 1.2\%$ with ~42 to ~50 centers, a performance comparable to a state-of-the-art approach for unsupervised image categorization (*20*).

Last, we benchmarked the clustering algorithm on the analysis of a molecular dynamics trajectory of trialanine in water at 300 K (*21*). In this case, clusters will approximately correspond to kinetic basins, namely independent conformations of the system that are stable for a substantial time and separated by free energy barriers, that are crossed only rarely on a microscopic time scale. We first analyzed the trajectory by a standard approach (*22*) based on a spectral analysis of the kinetic matrix, whose eigenvalues are associated with the relaxation times of the system. A gap is present after the seventh eigenvalue (fig. S10), indicating that the system has eight basins; in agreement with that, our cluster analysis (fig. S10) gives rise to eight clusters, including conformations in a one-to-one correspondence with those defining the kinetic basins (*22*).

Identifying clusters with density maxima, as is done here and in other density-based clustering algorithms (*9*, *10*), is a simple and intuitive choice but has an important drawback. If one generates data points at random, the density estimated for a finite sample size is far from uniform and is instead characterized by several maxima. However, the decision graph allows us to distinguish genuine clusters from the density ripples generated by noise. Qualitatively, only in the former case are the points corresponding to cluster centers separated by a sizeable gap in ρ and δ from the other points. For a random distribution, one instead observes a continuous distribution in the values of ρ and δ. Indeed, we performed the analysis for sets of points generated at random from a uniform distribution in a hypercube. The distances between data points entering in Eqs. 1 and 2 are computed with periodic boundary conditions on the hypercube. This analysis shows that, for randomly distributed data points, the quantity $\gamma_i = \rho_i \delta_i$ is distributed according to a power law, with an exponent that depends on the dimensionality of the space in which the points are embedded. The distributions of γ for data sets with genuine clusters, like those in Figs. 2 to 4, are strikingly different from power laws, especially in the region of high γ (fig. S11). This observation may provide the basis for a criterion for the automatic choice of the cluster centers as well as for statistically validating the reliability of an analysis performed with our approach.

REFERENCES AND NOTES

1. R. Xu, D. Wunsch 2nd, *IEEE Trans. Neural Netw.* **16**, 645–678 (2005).
2. J. MacQueen, in *Proceedings of the Fifth Berkeley Symposium on Mathematical Statistics and Probability*, L. M. Le Cam, J. Neyman, Eds. (Univ. California Press, Berkeley, CA, 1967), vol. 1, pp. 281–297.
3. L. Kaufman, P. J. Rousseeuw, *Finding Groups in Data: An Introduction to Cluster Analysis*, vol. 344 (Wiley-Interscience, New York, 2009).
4. B. J. Frey, D. Dueck, *Science* **315**, 972–976 (2007).
5. J. H. Ward Jr., *J. Am. Stat. Assoc.* **58**, 236–244 (1963).
6. F. Höppner, F. Klawonn, R. Kruse, T. Runkler, *Fuzzy Cluster Analysis: Methods for Classification, Data Analysis and Image Recognition* (Wiley, New York, 1999).
7. A. K. Jain, *Pattern Recognit. Lett.* **31**, 651–666 (2010).
8. G. J. McLachlan, T. Krishnan, *The EM Algorithm and Extensions* (Wiley Series in Probability and Statistics vol. 382, Wiley-Interscience, New York, 2007).
9. M. Ester, H.-P. Kriegel, J. Sander, X. Xu, in *Proceedings of the 2nd International Conference on Knowledge Discovery and Data Mining*, E. Simoudis, J. Han, U. Fayyad, Eds. (AAAI Press, Menlo Park, CA, 1996), pp. 226–231.
10. K. Fukunaga, L. Hostetler, *IEEE Trans. Inf. Theory* **21**, 32–40 (1975).
11. Y. Cheng, *IEEE Trans. Pattern Anal. Mach. Intell.* **17**, 790 (1995).
12. A. Gionis, H. Mannila, P. Tsaparas, *ACM Trans. Knowl. Discovery Data* **1**, 4, es (2007).
13. P. Fränti, O. Virmajoki, *Pattern Recognit.* **39**, 761–775 (2006).
14. L. Fu, E. Medico, *BMC Bioinformatics* **8**, 3 (2007).
15. H. Chang, D.-Y. Yeung, *Pattern Recognit.* **41**, 191–203 (2008).
16. P. Fränti, O. Virmajoki, V. Hautamäki, *IEEE Trans. Pattern Anal. Mach. Intell.* **28**, 1875–1881 (2006).
17. M. Charytanowicz *et al.*, *Information Technologies in Biomedicine* (Springer, Berlin, 2010), pp. 15–24.
18. F. S. Samaria, A. C. Harter, in *Proceedings of 1994 IEEE Workshop on Applications of Computer Vision* (IEEE, New York, 1994), pp. 138–142.
19. M. P. Sampat, Z. Wang, S. Gupta, A. C. Bovik, M. K. Markey, *IEEE Trans. Image Process.* **18**, 2385–2401 (2009).
20. D. Dueck, B. Frey, *ICCV 2007. IEEE 11th International Conference on Computer Vision* (IEEE, New York, 2007), pp. 1–8.
21. F. Marinelli, F. Pietrucci, A. Laio, S. Piana, *PLOS Comput. Biol.* **5**, e1000452 (2009).
22. I. Horenko, E. Dittmer, A. Fischer, C. Schütte, *Multiscale Model. Simulation* **5**, 802–827 (2006).

ACKNOWLEDGMENTS

We thank E. Tosatti, D. Amati, F. Laio, F. Marinelli, A. Maritan, R. Allen, J. Nasica, and M. d'Errico for stimulating discussion. We acknowledge financial support from the grant Associazione Italiana per la Ricerca sul Cancro 5 per mille, Rif. 12214, and Fondo per gli Investimenti della Ricerca di Base–Accordo di programma, Rif. RBAP11ETKA.

SUPPLEMENTARY MATERIALS

www.sciencemag.org/content/344/6191/1492/suppl/DC1
Figs. S1 to S11
Data S1

18 June 2013; accepted 23 May 2014
10.1126/science.1242072

NANOFLUIDICS

Observing liquid flow in nanotubes by 4D electron microscopy

Ulrich J. Lorenz and Ahmed H. Zewail*

Nanofluidics involves the study of fluid transport in nanometer-scale structures. We report the direct observation of fluid dynamics in a single zinc oxide nanotube with the high spatial and temporal resolution of four-dimensional (4D) electron microscopy. The nanotube is filled with metallic lead, which we melt in situ with a temperature jump induced by a heating laser pulse. We then use a short electron pulse to create an image of the ensuing dynamics of the hot liquid. Single-shot images elucidate the mechanism of irreversible processes, whereas stroboscopic diffraction patterns provide the heating and cooling rates of single nanotubes. The temporal changes of the images enable studies of the viscous friction involved in the flow of liquid within the nanotube, as well as studies of mechanical processes such as those that result in the formation of extrusions.

Advances in nanofabrication have made it possible to reduce the size of microfluidic devices and to study fluid flow at the nanometer scale (*1*, *2*). Nanoscale fluid dynamics and transport properties are dominated by surface effects and may substantially differ from those occurring at larger scales. For water in carbon nanotubes, for example, flow rates have been reported to exceed the predictions of classical continuum theory by several orders of magnitude (*3*–*5*). However, the degree of the enhancement remains a point of discussion (*6*). The study of a single nanochannel, rather than a large ensemble, should reduce the experimental uncertainty and provide an opportunity to visualize mechanical and fluid dynamics at the nanoscale. Such experiments not only incur the challenge of preparing

Physical Biology Center for Ultrafast Science and Technology, Arthur Amos Noyes Laboratory of Chemical Physics, California Institute of Technology, Pasadena, CA 91125, USA.
*Corresponding author. E-mail: zewail@caltech.edu

suitable structures, but also require appropriate tools to initiate and probe liquid flow in situ.

Electron microscopy affords the necessary spatial resolution to study liquids confined in carbon nanotubes and between graphene sheets (*7*, *8*). Static high-resolution transmission electron micrographs have revealed water networks in single nanotubes with diameters of 2 to 5 nm (*9*). Moreover, the filling of single-walled nanotubes with mercury through electrocapillarity has been demonstrated (*10*). Slow fluid phenomena have been imaged with a time resolution of seconds, such as the deformation of water droplets encapsulated in tubes with diameters of about 100 nm under electron beam heating (*11*) or the condensation of water vapor in larger nanotubes, as observed with an environmental scanning electron microscope (*12*). Recently, in situ nanomanipulation in a scanning electron microscope was used to manufacture nanofluidic devices consisting of a single boron nitride nanotube (diameter 30 to 80 nm) bridging two sides of a thin membrane; large osmotically induced electric currents generated by a salinity gradient across the tube were demonstrated (*13*). Imaging liquid flow directly and with a time resolution sufficient to capture the fast processes occurring far from equilibrium would provide further insight into fluid dynamics in a single nanotube.

Here, we used 4D electron microscopy to visualize nanofluidic phenomena in real time, combining the spatial resolution of a transmission electron microscope with the (ultra)fast time resolution of optical techniques (*14*, *15*). We initiate the dynamics by melting the lead core of a ZnO nanotube in situ with a temperature jump induced by a single laser pulse. The core reaches a temperature of several hundred degrees above the melting point, then recools on a time scale of 200 ns. The dynamics that ensue when the pressurized liquid expands in the nanochannel are imaged using an electron pulse accelerated to 120 keV, corresponding to a de Broglie wavelength of 3.3 pm. This approach permits us to study a wide range of nanofluidic phenomena in individual nanotubes. Short lead columns appear to move randomly in the nanotubes, splitting into shorter sections and fusing again. Droplets form on the outside of the tube on a time scale of nanoseconds when the pressurized liquid forces its way through microscopic leaks or shoots out of an open end. The laser-induced pressure jump induces the fission of a small lead column, the explosion of a droplet, or even the rupture of the tube wall. Lastly, the nature of the flow itself and the role of viscous friction at the nanoscale were elucidated by recording the expansion dynamics of the lead column. For such length scales, we developed a simplified model that allows for the extraction of the slip length, which is determined here to be on the order of 100 nm.

Experiments were performed using the UEM-1 instrument (*16*). Lead-filled ZnO nanotubes (*17*) were placed on a graphite film (1 to 6 monolayers on 2000 mesh copper) and studied at 363 K, well below the melting point of lead (T_m = 600.64 K) (*18*). Figure 1A shows a micrograph

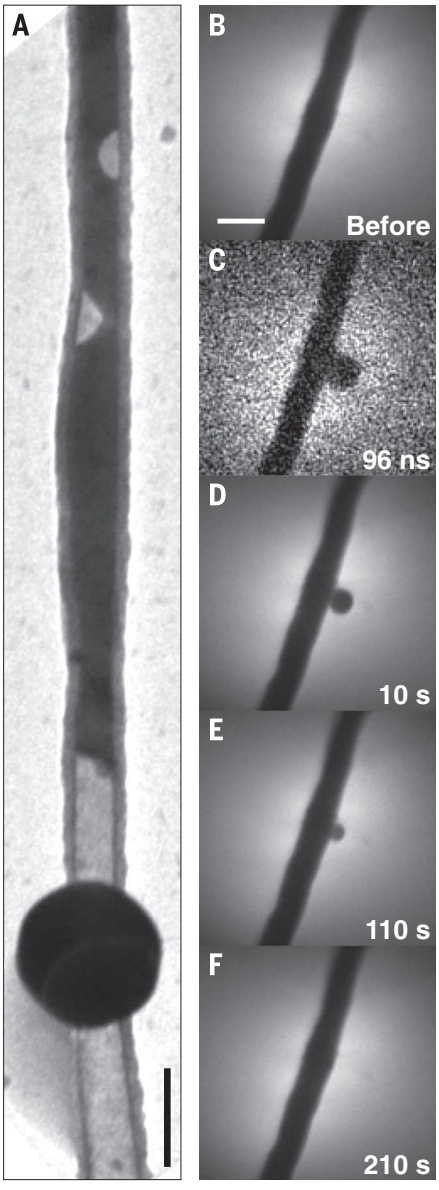

Fig. 1. Imaging of a single nanotube and temporal evolution of an extrusion. (**A**) Micrograph of a lead-filled ZnO nanotube under irradiation with the picosecond laser. At the bottom, molten lead has leaked out of the tube, and voids have formed in the remaining lead core at the top. Scale bar, 100 nm. (**B** to **F**) Fate of an extrusion formed by a single laser pulse. When the filled nanotube in (B) is laser-heated, part of the molten core is forced out of the tube through a leak, as visible in (C), which was recorded after 96 ns. After the tube has cooled, the extrusion is slowly reabsorbed on a time scale of several minutes [(D) to (F)]. Scale bar, 200 nm.

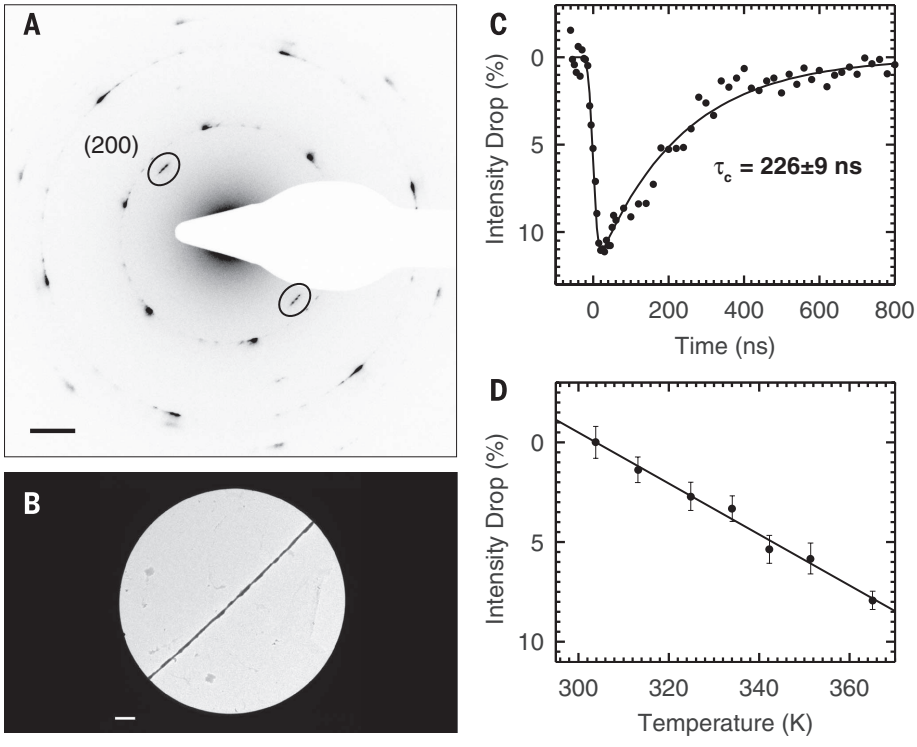

Fig. 2. Diffraction pattern of a nanotube, temporal evolution of the diffraction intensity, and temperature dependence. (**A**) Selected-area diffraction pattern of the nanotube shown in (**B**). Scale bars, 2 nm^{-1} and 500 nm, respectively. The lead core gives rise to the circled groups of (200) reflections. (**C**) The integrated diffraction intensity is shown as a function of time after laser excitation. From a fit with an exponential function, broadened to account for temporal jitter and the finite width of the electron probe pulse, a cooling time τ_c = 226 ± 9 ns is obtained. (**D**) Plot of the diffraction intensity as a function of the sample temperature without pump laser. Error bars indicate SEM of 20 measurements for every data point.

of a typical nanotube under irradiation with a train of picosecond laser pulses (532 nm; repetition rate 0.5 Hz, fluence 33 mJ/cm^2). The tube has an irregular shape with a wall thickness between 10 and 15 nm and an inner diameter that varies between 30 and 50 nm. At the bottom of the image, a lead particle 150 nm in diameter is visible, which formed when molten lead leaked through an imperfection in the wall, draining the tube in its vicinity. At the top, voids have formed in the remaining lead core. Movie S1 shows how the column repeatedly splits into shorter sections that appear to perform random jumps and merge again later, their movement being the result of both their initial rapid expansion and their slower contraction upon cooling. As it resolidifies, the lead column is trapped in non-equilibrium configurations, such as the one containing voids; changes in diffraction contrast indicate that ordered domains are formed with random orientations.

The laser pulse directly heats the solid lead core and transforms it into a hot, pressurized liquid, thus triggering its rapid expansion and initiating the dynamics we observe; at the wavelength used, ZnO absorbs only weakly. Metal nanoparticles are known to melt in less than 100 ps (*19*, *20*), which is fast on the time scale of the nanofluidic processes studied here (nanoseconds). Melting is therefore complete before flow dynamics occur. We performed time-resolved diffraction experiments to study the temperature jump and cooling rates (*16*). Figure 2A displays the selected-area diffraction pattern of the nanotube shown in Fig. 2B. Besides the reflections of the graphite substrate, groups of spots are visible, which arise from domains of the lead core fulfilling the Bragg condition (circles). Their intensity as a function of time after laser excitation was measured by recording stroboscopic diffraction patterns with the electron pulses of the microscope (Fig. 2C). For these studies of the temperature jump and cooling dynamics, the laser fluence was reduced to one-tenth of the initial value to avoid melting of the sample and altering the lead core irreversibly with every laser shot.

As a result of the temperature jump, the diffraction intensity initially drops sharply and then recovers exponentially with a time constant of 226 ns (solid line in Fig. 2C). We find this to be a typical cooling time, which leaves only a short time window during which the liquid behavior can be observed. From a calibration measurement of the diffraction intensity as a function of the sample temperature (Fig. 2D), we determined the initial temperature jump of the tube to be 106 K. By extrapolating to high laser fluence and taking the different tube dimensions into account (*16*), we estimate that the nanotube in Fig. 1A reaches an initial temperature greater than 1000 K, well above the melting point of lead.

Although it is certain that in situ melting of the lead core and fluid motion have taken place (movie S1), the elucidation of the nature of these processes obviously requires a time resolution that matches their inherent time scale. This is achieved here by recording micrographs with a

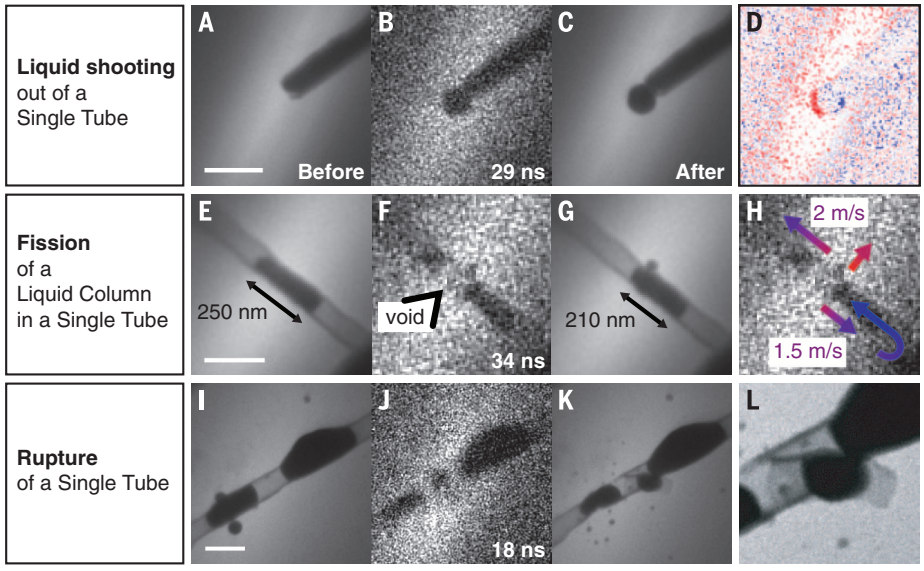

Fig. 3. Dynamics of different phenomena observed in single-shot experiments. Micrographs of the nanotubes were recorded before and after exposure to a single laser pulse. (**A** to **D**) Lead shooting out of the open end of a nanotube. The difference image (D) is obtained by subtracting (B) from (C); red and blue denote positive and negative intensity, respectively. (**E** to **H**) A short lead column fissioning. In (H), the movements of the fragments are indicated by arrows. (**I** to **L**) A nanotube rupturing at high laser fluence. Shown in (K) [and in (L) at higher magnification] is a fragment of the shattered tube wall with a lump of lead attached to it. Scale bars, 200 nm.

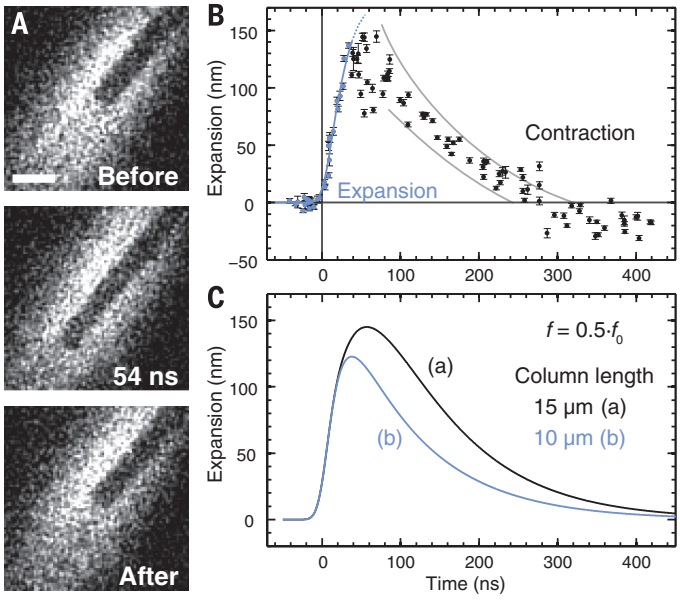

Fig. 4. Expansion dynamics of the liquid in a single nanotube. (**A**) Single-shot images showing the partially filled tube with inner diameter of 55 nm (see also fig. S3); scale bar, 100 nm. When heated with a single laser pulse, the lead column expands (140 nm at 54 ns, dark contrast) before returning to its original length at long times. (**B**) The complete dynamics obtained from a series of such experiments. The gray lines have been inserted to guide the eye. The friction coefficient f is estimated from a fit of the initial expansion (blue line and dots), where the fit function has been convoluted with a Gaussian of 10 ns full width at half maximum to account for the finite duration of the probe electron pulse. Error bars indicate SE of the fit used to extract the displacement of the meniscus. (**C**) Numerical simulations for two different column lengths l, where the parameters of the simulation have been adjusted to match the experiment (*16*). In particular, we obtained good agreement with a cooling time of 100 ns. Here, a friction coefficient $f = 0.5 \cdot f_0 = 0.5 \cdot 8\pi\eta$ was used, where η is the viscosity of lead at 1700 K (*33*).

single electron burst, fired at a short delay after the laser pulse, analogous to the method used for flash photography of fast-moving objects. Figure 1B depicts the image of a nanotube (outer diameter 130 nm) with a continuous lead column. The pressure jump induced by a single laser pulse forces part of the molten core to leak through the tube wall. At a delay time of 96 ns, a nearly spherical lead droplet (diameter 150 nm) has erupted on the outside of the tube (Fig. 1C). Such extrusions (see also Fig. 3) probably form when the liquid forces its way through microscopic channels in the amorphous ZnO walls of the tube. The diameter of these channels must be considerably smaller than the size of the extrusions, on the order of several nanometers.

The extrusion has shrunk to a diameter of 110 nm after 10 s (Fig. 1D) and is slowly being reabsorbed by the tube, long after the heat provided by the laser pulse has been dissipated (Fig. 1, E and F, and movie S2). On a time scale of 3 min, it contracts further to a diameter of 50 nm before it finally disappears from view; its volume decreases linearly with time (fig. S4). The extrusion fills a void in the tube formed upon cooling of the lead column, which is energetically favorable because it reduces the total surface area of the column and extrusion. This process is likely attributable to the suppression of the melting point of the material confined in the small channel connecting the extrusion to the interior of the tube (*21*). Moreover, surface melting of lead nanoparticles occurs well below the bulk melting point (*21*), so that a continuous path exists along which lead atoms can migrate back into the tube.

In Fig. 3, we display images of various irreversible flow phenomena. Figure 3A shows the open tip of a nanotube with an inner diameter of 60 nm. After the laser pulse (Fig. 3C), a lead particle 110 nm in diameter is seen to adhere to the tip; a single-shot image (Fig. 3B) reveals that at 29 ns, the droplet has already formed. The difference of these two images is displayed in Fig. 3D, where red and blue encode positive and negative intensity, respectively. The image reveals that the droplet shrinks as the lead column cools and contracts. When we exposed the tube to further laser pulses, the lead sphere successively grew and expanded strongly at short delays, before it shrank again upon cooling (fig. S5).

Figure 3E depicts a nanotube with an inner diameter of 55 nm that has been almost completely drained in situ, except for a lead column 250 nm in length. When heated with the laser pulse, the column splits into two segments (Fig. 3F, recorded at 34 ns). For this to happen, the energy deposited by the laser must be sufficient to overcome the barrier for fission. In Fig. 3G, taken at a long delay time after the laser pulse, only the larger of the two segments is still visible, while the shorter one has been accelerated out of the frame. A small spherical extrusion 40 nm in diameter is visible on top of the tube, which can already be discerned in Fig. 3F. Its formation must have preceded the separation of the segments, which have already moved away from the site of the leak. Figure 3H summarizes the sequence of events. After the laser pulse, the extrusion rapidly erupts on the side of the tube and the column fissions. The smaller and larger segments move apart with speeds of about 1.5 and 2 m/s, respectively, as estimated from the distance they have traveled in Fig. 3F. The smaller segment leaves the image frame, whereas the larger segment flows back upon cooling and settles near the extrusion.

At higher fluences and with multiple pulses, the laser-induced pressure jump can easily rupture the tube wall at defect sites. Figure 3I shows a tube that has already been exposed to several laser pulses. Two segments of the previously continuous lead column remain, one featuring an extrusion on either side and the other located at a breach of the tube wall, where lead has accumulated into an oblong mass. Upon irradiation with a further laser pulse, in this case doubling the pulse energy, the tube visibly deforms and the extrusions explode into an array of smaller particles (Fig. 3K). Most notably, as can be seen at higher magnification (Fig. 3L), part of the wall ruptures under the laser-induced pressure jump and detaches with a lead particle clinging to it. The resolution of Fig. 3J, taken at 18 ns, is somewhat reduced at this high laser fluence. Nonetheless, we clearly observe the lead particle in flight, appearing between the two lead column segments. By comparing the single-shot image with the images taken before and after, we can infer that it detached from the left segment and was propelled to the right while adhering to the wall fragment, which remained attached on its right side and moved as if on a hinge.

In the absence of the above irreversible phenomena, it is possible to study viscous friction at the nanoscale. To this end, we focused on nanotubes that are robust enough to withstand laser pulses of high fluence. When the tube in Fig. 4A (inner diameter 55 nm; fig. S6) is heated with a single laser pulse, its lead core rapidly expands (140 nm at a delay of 54 ns). Figure 4B displays the entire dynamics obtained from more than 100 single-shot experiments. During the first 30 ns, the meniscus advances with a nearly constant speed of 3.9 m/s. The column subsequently contracts more slowly, shrinking to its initial length in 300 ns. The scatter of the data points reflects changes in the initial conditions of every experiment, leading to slightly different dynamics. Apart from variations of the shape of the meniscus, we also observe that the column recedes after every laser pulse by several nanometers, likely because lead leaks out of the other end of the tube, which results in negative expansion at delays longer than 300 ns.

To model the expansion dynamics, we developed an analog of Washburn's law (*22*), which successfully describes the dynamics of capillary filling for incompressible liquids. However, we assume that the expansion of the liquid column, not the capillary force, drives the fluid motion (*16*). Assuming laminar flow and neglecting the energy cost of displacing and deforming the meniscus, we treat the liquid as a cylinder whose longitudinal expansion is slowed by viscous friction. By solving the resulting differential equation numerically, we obtain the displacement of the meniscus as a function of time, as shown in Fig. 4C for typical column lengths of l = 15 μm and 10 μm (black and blue curves, respectively); the free parameters have been adjusted to match the experiment (*16*). The qualitative agreement with the observed dynamics suggests that the model captures the underlying physics.

The displacement x of the advancing meniscus at early times t after the laser pulse was derived as

$$x = x_e + \exp\left[-\frac{f}{2m}(t - t_0)\right] \cdot [-x_e + v_0(t - t_0)] \quad (1)$$

where f is the friction coefficient, x_e is the equilibrium displacement of the meniscus after the temperature jump, v_0 is its initial velocity, and m is the mass per unit length of the lead column. Here, t_0 is included to allow for a delayed onset of the expansion. Equation 1 expresses the intuitive result that in the absence of friction (f = 0), the meniscus moves freely with constant velocity v_0; when f is small, Eq. 1 reduces to

$$x \approx \left[\left(\frac{x_e f}{2m} + v_0\right) \cdot (t - t_0)\right] - \left[\frac{f v_0}{2m} \cdot (t - t_0)^2\right] \quad (2)$$

Thus, friction manifests itself in the deviation of the expansion curve from linearity. In Washburn's law, the friction coefficient is assumed to be the same as for Poiseuille flow, $f_0 = 8\pi\eta$, where η is the dynamic viscosity of bulk liquid lead (*22*).

In contrast to the simulation in Fig. 4C, where we have chosen $f = 0.5 \cdot f_0$, the experimental expansion curve was found not to deviate strongly from a straight line, indicating that f must be relatively small. Using Eq. 1, f was determined from a fit of the blue dots in Fig. 4B; the mass per unit length $m = 2.69 \times 10^{-11}$ kg/m is known, the velocity v_0 = 3.9 m/s is obtained from a linear fit of the early expansion curve, and x_e = 150 nm is estimated from the maximum displacement of the meniscus in the image. The friction coefficient f was obtained to be $0.06 \cdot f_0$ (i.e., 6% of the value of macroscopic continuum dynamics). Within the experimental errors, we conclude that f is reduced by at least one order of magnitude relative to the bulk value (*23*).

Whereas Poiseuille's law, from which f_0 is derived, assumes that the liquid is stationary at the interface, the substantial reduction of the friction coefficient indicates a finite slip velocity of the lead column at the tube wall. Slippage is described in terms of the slip length δ, the distance from the interface at which the velocity profile of the flowing liquid extrapolates to zero (*2*, *24*, *25*). A modified Poiseuille law incorporating slip (*4*) gives

$$\delta = \frac{R}{4} \cdot \left(\frac{f_0}{f} - 1\right) \quad (3)$$

where R = 27.5 nm is the radius of the tube. From the dynamics in Fig. 4B, we obtained a

slip length of 112 nm, implying that the velocity profile of the moving column is almost flat. Such a large slip length is supported by the strength of the interaction between liquid lead and the ZnO tube as well as by the nature of the experiment, which is carried out under far-from-equilibrium conditions.

The contact angles of liquid metals on metal oxide surfaces are usually larger than 90° (*26*, *27*); that is, the surface repels the liquid. For rough surfaces, such as the irregular inner walls of the ZnO tubes, this effect is even more pronounced. Under such nonwetting conditions, large slip lengths have been measured, up to tens of micrometers in the extreme case of superhydrophobic surfaces (*25*). We also note that the lead column may have an oxide skin (*28*), which increases the apparent viscosity of liquid metals at low shear rates (*27*). However, it is difficult to predict how this would affect the nanofluidic behavior at the high shear rates in our experiment (~10^7 s^{-1}, as estimated from the flow velocity and the tube dimensions). Under such conditions, the slip length may also increase with shear rate. Simulations for smooth surfaces have found the slip length to diverge at shear rates of ~10^8 s^{-1} (*25*, *29*). Moreover, on rough surfaces, large shear rate–dependent slip lengths have been demonstrated experimentally (*30*); however, nano-sized vapor bubbles on the surface may play a role in such experiments (*30*).

We believe that the approach presented here should find applications in the study of nanoscale phenomena that have previously been inaccessible, including the investigation of nanofluidic structures or biological channels (*31*) with high spatial and temporal resolutions. The study of phase transitions in nanoconfined environments constitutes another area that will benefit from the capability to manipulate and visualize single nanotubes in situ.

REFERENCES AND NOTES

1. J. C. T. Eijkel, A. van den Berg, *Microfluid. Nanofluid.* **1**, 249–267 (2005).
2. L. Bocquet, E. Charlaix, *Chem. Soc. Rev.* **39**, 1073–1095 (2010).
3. M. Majumder, N. Chopra, R. Andrews, B. J. Hinds, *Nature* **438**, 44 (2005).
4. J. K. Holt *et al.*, *Science* **312**, 1034–1037 (2006).
5. M. Whitby, L. Cagnon, M. Thanou, N. Quirke, *Nano Lett.* **8**, 2632–2637 (2008).
6. M. Whitby, N. Quirke, in *Handbook of Nanophysics: Nanotubes and Nanowires*, K. D. Sattler, Ed. (CRC Press, Boca Raton, FL, 2011), chap. 11.
7. J. M. Yuk *et al.*, *Science* **336**, 61–64 (2012).
8. Q. Chen *et al.*, *Nano Lett.* **13**, 4556–4561 (2013).
9. N. Naguib *et al.*, *Nano Lett.* **4**, 2237–2243 (2004).
10. J. Y. Chen, A. Kutana, C. P. Collier, K. P. Giapis, *Science* **310**, 1480–1483 (2005).
11. Y. Gogotsi, J. A. Libera, A. Guvenc-Yazicioglu, C. M. Megaridis, *Appl. Phys. Lett.* **79**, 1021–1023 (2001).
12. M. P. Rossi *et al.*, *Nano Lett.* **4**, 989–993 (2004).
13. A. Siria *et al.*, *Nature* **494**, 455–458 (2013).
14. A. H. Zewail, *Science* **328**, 187–193 (2010).
15. A. H. Zewail, J. M. Thomas, *4D Electron Microscopy: Imaging in Space and Time* (Imperial College Press, London, 2010).
16. See supplementary materials on *Science* Online.
17. C.-Y. Wang, N.-W. Gong, L.-J. Chen, *Adv. Mater.* **20**, 4789–4792 (2008).
18. P. J. Linstrom, W. G. Mallard, Eds., *Thermodynamics Source Database* (NIST Chemistry WebBook, NIST Standard Reference Database No. 69; National Institute of Standards and Technology, Gaithersburg, MD, 2014).
19. S. Link, C. Burda, B. Nikoobakht, M. A. El-Sayed, . *Chem. Phys. Lett.* **315**, 12–18 (1999).
20. C. Y. Ruan, Y. Murooka, R. K. Raman, R. A. Murdick, *Nano Lett.* **7**, 1290–1296 (2007).
21. H. Sakai, *Surf. Sci.* **351**, 285–291 (1996).
22. P.-G. de Gennes, F. Brochard-Wyart, D. Quere, *Capillarity and Wetting Phenomena: Drops, Bubbles, Pearls, Waves* (Springer, New York, 2004).
23. Similar values for f were obtained when x_e was varied. We determined f_0 to be 2.14×10^{-2} Pa·s using the viscosity of bulk lead at 1700 K, the estimated temperature of the tube after the laser pulse (*16*); shear thinning is expected to be insignificant despite the high shear rate in our experiment (*32*). For other nanotubes of larger diameter, on the order of 100 nm, similar friction coefficients were obtained.
24. M. Whitby, N. Quirke, *Nat. Nanotechnol.* **2**, 87–94 (2007).
25. L. Bocquet, J. L. Barrat, *Soft Matter* **3**, 685–693 (2007).
26. D. Chatain, *Annu. Rev. Mater. Res.* **38**, 45–70 (2008).
27. Q. Xu, N. Oudalov, Q. T. Guo, H. M. Jaeger, E. Brown, *Phys. Fluids* **24**, 063101 (2012).
28. G. Yi, W. Schwarzacher, *Appl. Phys. Lett.* **74**, 1746–1748 (1999).
29. P. A. Thompson, S. M. Troian, *Nature* **389**, 360–362 (1997).
30. C. Cottin-Bizonne, B. Cross, A. Steinberger, E. Charlaix, *Phys. Rev. Lett.* **94**, 056102 (2005).
31. E. Tajkhorshid *et al.*, *Science* **296**, 525–530 (2002).
32. C. Desgranges, J. Delhommelle, *Phys. Rev. B* **78**, 184202 (2008).
33. *Handbook on Lead-Bismuth Eutectic Alloy and Lead Properties, Materials Compatibility, Thermal-Hydraulics and Technologies* (Nuclear Energy Agency, Organisation for Economic Co-operation and Development, 2007).

ACKNOWLEDGMENTS

Supported by NSF grant DMR-0964886 and Air Force Office of Scientific Research grant FA9550-11-1-0055 in the Physical Biology Center for Ultrafast Science and Technology at Caltech, which is supported by the Gordon and Betty Moore Foundation. U.J.L. was partly supported by a postdoctoral fellowship from the Swiss National Science Foundation.

SUPPLEMENTARY MATERIALS

www.sciencemag.org/content/344/6191/1496/suppl/DC1
Materials and Methods
Supplementary Text
Figs. S1 to S6
Movies S1 and S2
References (*34*–*40*)

19 March 2014; accepted 27 May 2014
10.1126/science.1253618

GAS FORMATION

Formation temperatures of thermogenic and biogenic methane

D. A. Stolper,[1]* M. Lawson,[2] C. L. Davis,[2] A. A. Ferreira,[3] E. V. Santos Neto,[3] G. S. Ellis,[4] M. D. Lewan,[4] A. M. Martini,[5] Y. Tang,[6] M. Schoell,[7] A. L. Sessions,[1] J. M. Eiler[1]

Methane is an important greenhouse gas and energy resource generated dominantly by methanogens at low temperatures and through the breakdown of organic molecules at high temperatures. However, methane-formation temperatures in nature are often poorly constrained. We measured formation temperatures of thermogenic and biogenic methane using a "clumped isotope" technique. Thermogenic gases yield formation temperatures between 157° and 221°C, within the nominal gas window, and biogenic gases yield formation temperatures consistent with their comparatively lower-temperature formational environments (<50°C). In systems where gases have migrated and other proxies for gas-generation temperature yield ambiguous results, methane clumped-isotope temperatures distinguish among and allow for independent tests of possible gas-formation models.

The environmental conditions, rates, and mechanisms of methane formation are critical to understanding the carbon cycle and for predicting where economically substantial amounts of methane form. Conventional models of thermogenic methane formation predict that (i) gas formation is kinetically controlled by time, temperature, and organic matter composition (*1*); (ii) gases cogenerated with oil form below ~150° to 160°C (*2*–*4*); and (iii) gases created from the breakdown (cracking) of oil or refractory kerogen form above ~150° to 160°C (*2*–*4*). Microbially produced (biogenic) methane in nature is thought to form mostly below ~80°C (*5*, *6*).

Our understanding of the kinetics of thermogenic methane formation is dominantly constrained by extrapolating kinetic parameters from high-temperature (~>300°C) laboratory experiments to lower-temperature (~100° to 200°C), geologically relevant conditions (*7*). These experiments are sensitive to heating rates (*7*) and the activity of water (*1*, *7*–*10*), minerals (*1*), and transition metals (*11*); the observed range of derived kinetic parameters can result in divergent predictions for natural methane-formation temperatures (*1*, *10*). Additionally, many thermogenic gases have migrated from their source to a reservoir (*3*, *12*–*14*). Although these migrated gases dominate the data sets used to calibrate empirical models of thermogenic methane formation

[1]Division of Geological and Planetary Sciences, California Institute of Technology, 1200 East California Boulevard, Pasadena, CA 91125, USA. [2]ExxonMobil Upstream Research Company, Houston, TX, USA. [3]Division of Geochemistry, Petrobras Research and Development Center (CENPES), Rio de Janeiro, RJ, Brazil. [4]U.S. Geological Survey, Denver Federal Center, Denver, CO, USA. [5]Department of Geology, Amherst College, Amherst, MA, USA. [6]Power, Environmental, and Energy Research Institute, Covina, CA, USA. [7]GasConsult International Inc, Berkeley, CA, USA.
***Corresponding author. E-mail: dstolper@caltech.edu**

(*3*, *13*–*15*), the ability to understand their thermal histories, and thus accurately calibrate models, is hampered by (i) a lack of independent constraints on the thermal histories of the source and reservoir rocks and the timing of gas migration, and (ii) the possibility that a reservoir contains a mixture of gases from different sources. Finally, biogenic gases are produced ubiquitously in near-surface sedimentary environments (*6*, *16*) and can comingle with thermogenic gases (*17*). Despite the many empirical tools used to distinguish biogenic from thermogenic gases (*18*), identifying the sources and quantifying relative contributions of biogenic and thermogenic gases in nature remains challenging (*17*).

We measured multiply substituted ("clumped") isotope temperatures of methane (*19*) generated via the experimental pyrolysis of larger organic molecules and sampled from natural thermogenic deposits of the Haynesville Shale (USA), Marcellus Shale (USA), and Potiguar Basin (Brazil) (*20*) and from natural systems with methanogens from the Gulf of Mexico and Antrim Shale (USA). We quantified the abundance of both $^{13}CH_3D$ and $^{12}CH_2D_2$, two clumped isotopologues of methane, relative to a random isotopic distribution via the parameter Δ_{18} (*20*). For isotopically equilibrated systems, Δ_{18} values are a function of temperature, dependent only on the isotopic composition of methane, and thus can be used to calculate methane-formation temperatures (Fig. 1A) (*19*, *20*, *21*). It was not obvious before this work what Δ_{18}-based temperatures of natural samples would mean, in part because conventional models assume that methane forms via kinetically (as opposed to equilibrium) controlled reactions (*1*–*3*, *8*, *22*–*24*).

We generated methane from larger hydrocarbon molecules at constant temperatures in two experiments: pyrolysis of propane at 600°C (*20*) and closed-system hydrous pyrolysis (*7*, *9*) of organic matter at 360°C (*20*). For both, Δ_{18} temperatures are within 2 standard deviations (σ) of experimental temperatures (Fig. 1A and table S1). This supports the suggestion in (*19*) that measured Δ_{18}-based temperatures of thermogenic methane could record formation temperatures.

We next examined thermogenic shale gases from the Haynesville Shale (*25*). In shale-gas systems, the shale is both the source and reservoir for generated hydrocarbons (*26*), thus minimizing complications associated with gas migration for our interpretations. Geological constraints indicate that the Haynesville Shale has undergone minimal uplift (~<0.5 km) (20) since reaching maximum burial temperatures (modeled to currently be within 5° to 17°C of maximum burial temperatures; tables S2 and S3) (20). Measured Δ_{18} temperatures range from 169° to 207°C, overlapping, within uncertainty, current reservoir temperatures (163° to 190°C; Fig. 1, A and B, and table S2). We also compared the Δ_{18} temperatures to independently calculated gas-formation temperatures using the generation kinetics of Burnham (*20*, *27*). Modeled average gas-formation temperatures from secondary oil breakdown range from 168° to 175°C (table S3) (20). The modeled temperatures are lower than, but within uncertainty of, measured Δ_{18} temperatures (table S2). This difference likely reflects the fact that the model calculates an average formation temperature that includes all hydrocarbon gases (i.e., $C_{1\text{-}5}$ alkanes), but the types of experiments used to calibrate the model generate methane at a higher average temperature than other hydrocarbon gases (*28*). Thus, average methane-formation temperatures should be higher than those modeled for average hydrocarbon gas-formation temperatures. Consequently, Δ_{18} temperatures are consistent with expected methane-formation temperatures. However, in this case, it is also possible that methane reequilibrated from some other, initial Δ_{18} value to one consistent with its subsequent storage temperatures.

Next, we considered shale gases from uplifted rocks (>3 km of uplift after maximum burial) (20) in the Marcellus Shale (*29*), which reached modeled maximum burial temperatures of 183° to 219°C, but today are 60° to 70°C (tables S2 and S3) (20). This system allows us to examine the effects of gradual cooling and long-term storage at temperatures colder than methane-formation temperatures on Δ_{18} values. Samples yield Δ_{18} temperatures from 179° to 207°C, overlapping those for the Haynesville Shale and hotter than current reservoir temperatures (Fig. 1B). Modeled formation temperatures (using the Burnham kinetics as above) (27) are 171° to 173°C (table S3)—the modeled temperatures are again slightly lower than the measured Δ_{18} temperatures (for reasons discussed above), but the two are within analytical uncertainty (table S2). We conclude that Δ_{18} temperatures of Marcellus Shale methane are indistinguishable from independent expectations regarding methane-formation temperatures and were not noticeably influenced by later cooling.

We also examined thermogenic gases from the southwestern sector of the Potiguar Basin (*30*) that migrated from deeper sources to shallower reservoirs (*31*). Here, measured Δ_{18} temperatures range from 157° to 221°C and exceed current reservoir temperatures (66° to 106°C; table S2). This is consistent with vertical migration of gases from hotter sources to cooler reservoirs (*3*). We note that some source rocks in the Potiguar Basin near where samples were collected have experienced sufficient burial temperatures to reach a vitrinite reflectance of 2.7%, within the range observed for the Haynes ville and Marcellus Shale gas source rocks (1.7 to 3.1%; table S3) and consistent with the high-temperature (>150° to 160°C) (2–4)

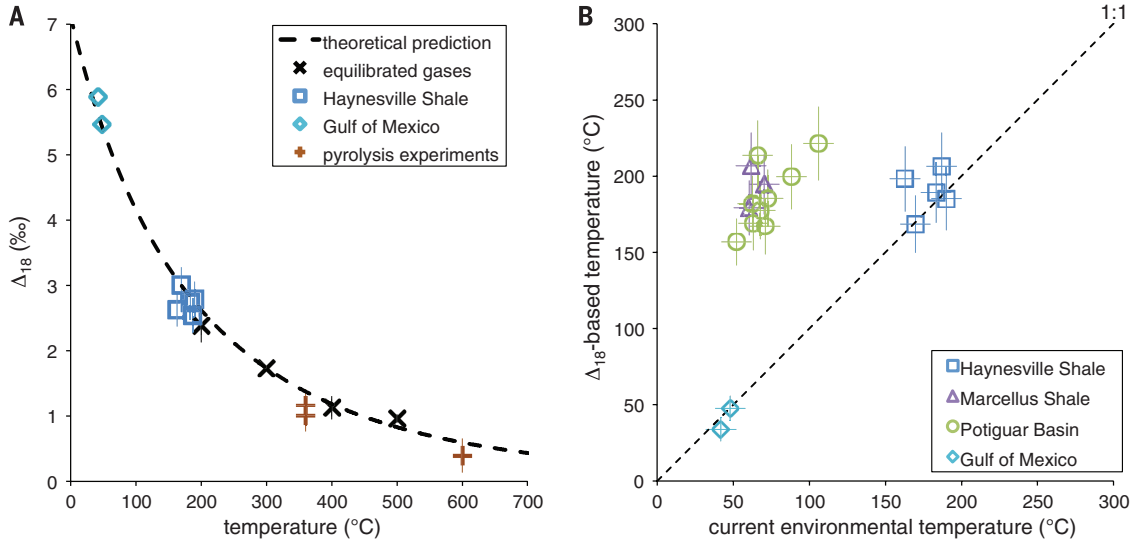

Fig. 1. Comparisons of Δ_{18} temperatures to environmental/formation temperatures. (**A**) Formation/reservoir temperatures versus Δ_{18} values. The dashed line is the theoretical dependence of Δ_{18} on temperature (*19*). Equilibrated gas data are from (*19*). Temperatures are formation/equilibration temperatures for the pyrolysis and equilibrated samples and current reservoir temperatures for the Haynesville Shale and Gulf of Mexico samples. (**B**) Current reservoir temperatures versus Δ_{18} temperatures for all natural samples investigated except the Antrim Shale samples, which are excluded because they are a mixture of thermogenic and biogenic gases. The dotted line is a 1:1 line. Uncertainty for well temperatures is estimated to be ~±10°C. Error bars are 1σ.

"dry gas zone" in which oil is hypothesized to crack to gas (*3*). Thus, the Δ_{18} temperatures from Potiguar Basin methane (157° to 221°C) are compatible with the thermal history of some source rocks in the region. Additionally, a positive correlation exists between the Δ_{18} temperatures and $\delta^{13}C$ values (*32*) of Potiguar Basin gases (Fig. 2; $P = 0.008$) with a slope, 5.3°C/per mil (‰) (±2.2; 1σ), within error of some theoretical estimates, 8.8°C/‰ (*20*, *22*) and 9.4°C/‰ (*20*, *23*). This relationship is expected because earlier-generated methane is thought to form at lower temperatures with lower $\delta^{13}C$ values than methane formed later at higher temperatures (*2*, *3*, *15*, *23*). The Potiguar Basin samples raise the issue that mixing of gases with differing $\delta^{13}C$ and δD values can result in Δ_{18} values that are not simply weighted averages of the endmembers (*19*, *20*). However, in this specific case (and for the shale gases), $\delta^{13}C$ and δD values do not span a sufficiently large range for mixing between samples to result in Δ_{18}-based temperatures different (within analytical uncertainty) from the actual average formation temperatures of the mixtures (fig. S2) (20).

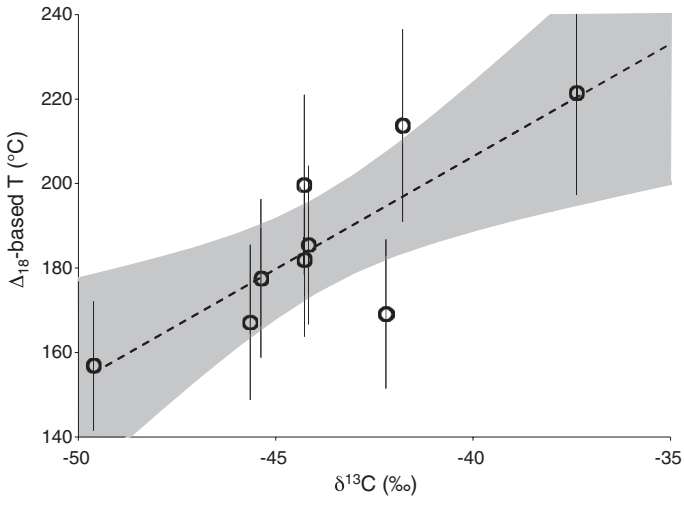

Fig. 2. $\delta^{13}C$ values versus Δ_{18} temperatures for methane from the Potiguar Basin. A positive correlation ($P = 0.008$) between $\delta^{13}C$ values and Δ_{18}-based temperatures of methane is observed. The gray band is the 95% confidence interval for the linear regression through the data. Error bars are 1σ.

The data discussed above are consistent with the interpretation that Δ_{18} values of thermogenic methane reflect isotopic equilibrium at the temperature of methane formation and that the "closure temperature" above which Δ_{18} values can freely re-equilibrate is ~>200°C in geological environments because (i) experimentally generated methane yields Δ_{18} values within error of formation temperatures (Fig. 1A). (ii) All Δ_{18} temperatures from natural samples are geologically reasonable formation temperatures (*1*–*4*, *10*). (iii) Haynesville Shale Δ_{18} temperatures are within uncertainty of current and modeled maximum burial temperatures (Fig. 1, A and B). (iv) Haynesville and Marcellus Shale Δ_{18} temperatures are within error of independently modeled gas-formation temperatures. (v) Haynesville and Marcellus Shale Δ_{18} temperatures overlap despite the differing thermal histories of each system (the Marcellus Shale cooled by >100°C after gas generation). This would not be expected if Δ_{18} temperatures represent closure temperatures and thus reset during cooling of the host rocks. And (vi) Potiguar Basin Δ_{18} temperatures and $\delta^{13}C$ values are positively correlated (Fig. 2), with a slope within error of theoretical predictions.

The agreement between the Haynesville and Marcellus Shale methane Δ_{18} temperatures and

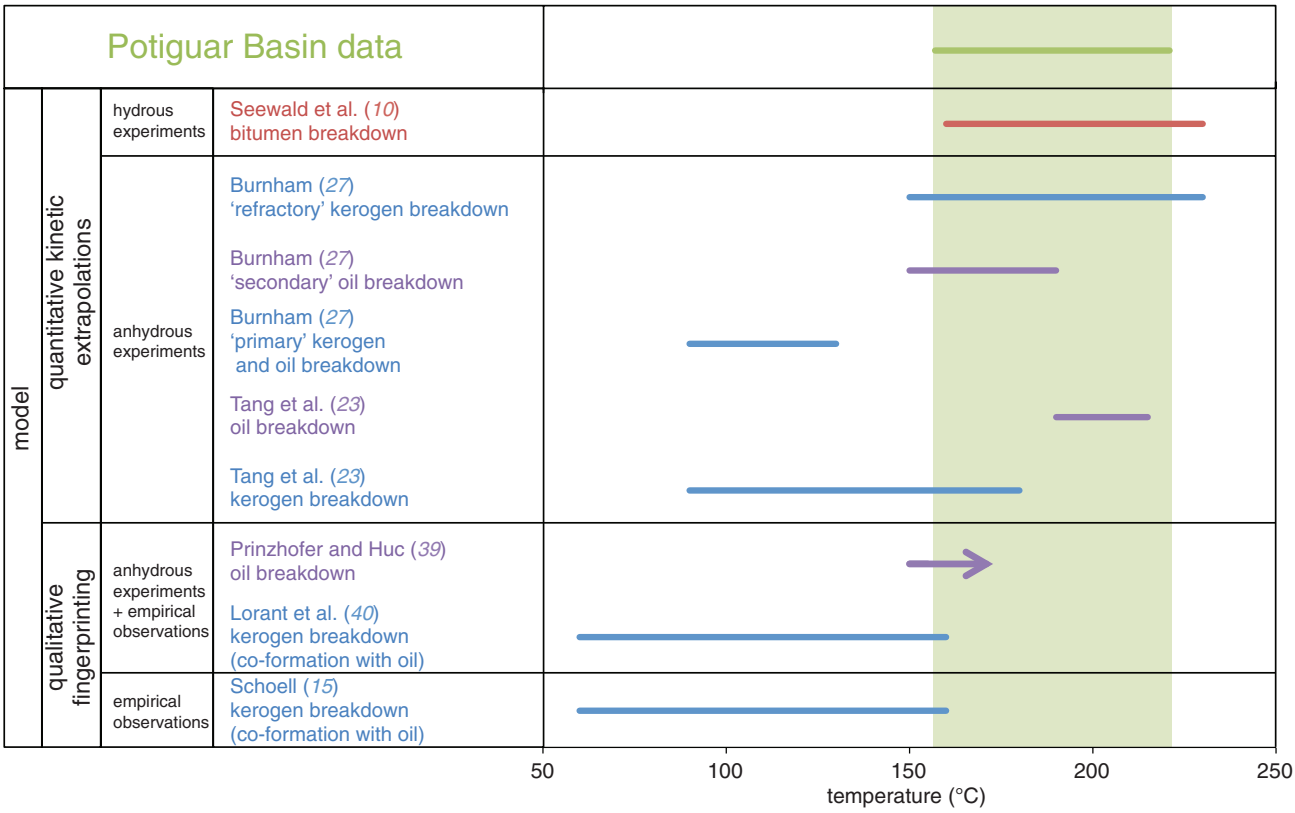

Fig. 3. Comparison of modeled methane-formation temperatures to Δ_{18} temperatures. Blue lines indicate gases generated from kerogen breakdown; purple lines, gases generated from oil breakdown; and red line, gases generated from bitumen breakdown. The green line indicates the measured range of Δ_{18} temperatures from the Potiguar Basin. Models are from (*10*, *15*, *23*, *27*, *39*, *40*) and described in (*20*).

modeled formation temperatures demonstrates that relatively simple gas-generation models are accurate when the thermal histories of the source rocks are constrained. The formation temperatures of the Potiguar Basin gases are challenging to constrain with such models due to gas migration, which obscures the location and timing of gas formation. Previously, these gases were interpreted to have been cogenerated with oils (*30*) and thus below ~160°C (*2*–*4*). This disagreement between our data and published interpretations inspired us to examine a range of gas-formation models (*20*) for the Potiguar Basin samples (Fig. 3). All models presented are in common use and constrained by similar gas chemistry data (*20*); however, many disagree with each other and together predict a range of >170°C for gas formation (Fig. 3). The Δ_{18} temperatures allow these models to be independently evaluated, rejecting some (e.g., low-temperature gas generation solely from kerogen) and narrowing the permitted interpretations. Specifically, methane in the Potiguar Basin could have formed via the mixing of gases produced by low-temperature (~<150° to 180°C) kerogen breakdown with gases generated from higher-temperature (~>150° to 160°C) oil breakdown, consistent with the models of Tang *et al*. (*23*) and Burnham (*27*). This scenario requires a specific set of mixing components to generate the observed formation temperatures, $C_1/\Sigma C_{1\text{-}5}$ values (table S2), and correlation between Δ_{18} temperatures and methane $\delta^{13}C$ values. Alternatively, the model of Seewald *et al*. (*10*), which is the only model presented to incorporate the importance of water in gas formation, is consistent with the Δ_{18} temperatures and $C_1/\Sigma C_{1\text{-}5}$ values (<85%; table S2) for the Potiguar Basin gases. This may indicate that water should be considered in models of methane formation. Although the gas-generation temperatures derived from the breakdown of refractory kerogen, as in the model of Burnham (*27*), appear compatible with the Δ_{18} temperatures (Fig. 3), this organic source dominantly generates methane (*27*) and thus cannot be the sole source of gas to the system due to the high concentration of $C_{2\text{-}5}$ alkanes in the gases (<85% $C_1/\Sigma C_{1\text{-}5}$; table S2).

Thus, while the addition of Δ_{18} temperatures does not provide a unique interpretation of the origin of the Potiguar Basin gases, it rules out several otherwise plausible interpretations and places specific constraints on the remaining models. Notably, our results for the Potiguar Basin indicate that the formation environments for methane extend to higher temperatures (and presumably depths) in this system than many models of petroleum genesis predicted (Fig. 3) and supports experimental evidence that substantial quantities of methane can be generated at higher temperatures than is sometimes appreciated (*33*). This observation requires that this basin possesses a previously unsuspected "root" that reached high temperatures at some point in its history, generating high-temperature methane that ascended into shallower reservoirs. Thus, Δ_{18} temperatures not only constrain the conditions and mechanisms of methane formation, but also provide a window into the geological and thermal histories of basins in which methane forms.

To examine Δ_{18}-based temperatures from known low-temperature sources of methane, we measured Δ_{18} values from two sources of biogenic gases produced from the biodegradation of oil (Gulf of Mexico). They return Δ_{18} temperatures (34° ± 8°C and 48° ± 8°C) within error of their current reservoir temperatures (42° and 48°C, respectively; Fig. 1, A and B, and table S2). We further measured two gases from the Antrim Shale, which has been interpreted as containing a mixture of biogenic gases higher in $C_1/\Sigma C_{1\text{-}5}$ and thermogenic gases lower in $C_1/\Sigma C_{1\text{-}5}$ (*17*). The sample closer to the biogenic endmember (99.99% $C_1/\Sigma C_{1\text{-}5}$) returns a Δ_{18} temperature of 40°C (±10; 1σ), whereas the sample interpreted here to be closer to a thermogenic endmember (88.9% $C_1/\Sigma C_{1\text{-}5}$) returns a higher temperature of 115°C (±12°C; 1σ). Thus, the natural biogenic gases have Δ_{18} temperatures consistent with their expected formation temperatures, both as pure endmembers and as dominant components of mixtures. We note that preliminary results for methanogens grown in pure culture (*34*) indicate that they can produce methane out of internal isotopic equilibrium. Nevertheless, our measurements of natural biogenic methane indicate that natural environments (at least those investigated to date) permit the attainment of local internal isotopic equilibrium in methane.

These results indicate that Δ_{18} values can be used to calculate formation temperatures of methane from both pure and mixed thermogenic and biogenic gas deposits and interrogate models of gas formation and geological histories of basins. Additionally, if the interpretation of Δ_{18}-based temperatures as formation temperatures is correct, it has implications for our understanding of the chemistry of thermogenic and biogenic methane formation. Specifically, it requires a previously unrecognized step for both processes that allows C-H bonds to equilibrate during methane formation. This interpretation is unexpected because $\delta^{13}C$ values of thermogenic and biogenic methane are almost universally considered to be controlled by kinetic-isotope effects rather than equilibrium-thermodynamic effects (*2*, *16*, *22*–*24*, *35*). This apparent contradiction can be reconciled if reacting methane precursors (e.g., methyl groups) undergo local hydrogen exchange faster than the rate of net methane generation. For thermogenic gases, this could occur via exchange reactions with water (*36*) or catalytic hydrogen exchange on organic macromolecules, mineral surfaces, or transition metals (*11*, *37*). For biogenic methane, reversible hydrogen exchange could occur on methane or methane precursors if the pathway for methane formation is partially reversible (*35*, *38*). Thus, Δ_{18} measurements may also elucidate chemical and biochemical mechanisms of methane formation.

REFERENCES AND NOTES

1. J. S. Seewald, *Nature* **426**, 327–333 (2003).
2. C. Clayton, *Mar. Pet. Geol.* **8**, 232–240 (1991).
3. J. M. Hunt, *Petroleum Geochemistry and Geology* (Freeman, New York, 1996).
4. T. Quigley, A. Mackenzie, *Nature* **333**, 549–552 (1988).
5. A. Wilhelms *et al*., *Nature* **411**, 1034–1037 (2001).
6. D. L. Valentine, *Annu. Rev. Mar. Sci.* **3**, 147–171 (2011).
7. M. Lewan, T. Ruble, *Org. Geochem.* **33**, 1457–1475 (2002).
8. J. Espitalié, P. Ungerer, I. Irwin, F. Marquis, *Org. Geochem.* **13**, 893–899 (1988).
9. M. Lewan, *Geochim. Cosmochim. Acta* **61**, 3691–3723 (1997).
10. J. S. Seewald, B. C. Benitez-Nelson, J. K. Whelan, *Geochim. Cosmochim. Acta* **62**, 1599–1617 (1998).
11. F. D. Mango, J. Hightower, *Geochim. Cosmochim. Acta* **61**, 5347–5350 (1997).
12. W. England, A. Mackenzie, D. Mann, T. Quigley, *J. Geol. Soc. London* **144**, 327–347 (1987).
13. L. C. Price, M. Schoell, *Nature* **378**, 368–371 (1995).
14. B. P. Tissot, D. H. Welte, *Petroleum Formation and Occurrence: A New Approach to Oil and Gas Exploration* (Springer-Verlag, Berlin, 1978).
15. M. Schoell, *AAPG Bull.* **67**, 2225 (1983).
16. M. J. Whiticar, E. Faber, M. Schoell, *Geochim. Cosmochim. Acta* **50**, 693–709 (1986).
17. A. M. Martini, J. M. Budai, L. M. Walter, M. Schoell, *Nature* **383**, 155–158 (1996).
18. M. J. Whiticar, *Chem. Geol.* **161**, 291–314 (1999).
19. D. A. Stolper *et al*., *Geochim. Cosmochim. Acta* **126**, 169–191 (2014).
20. Materials and methods are available as supplementary materials on *Science* Online.
21. J. M. Eiler, *Earth Planet. Sci. Lett.* **262**, 309–327 (2007).
22. Y. Ni *et al*., *Geochim. Cosmochim. Acta* **75**, 2696–2707 (2011).
23. Y. Tang, J. Perry, P. Jenden, M. Schoell, *Geochim. Cosmochim. Acta* **64**, 2673–2687 (2000).
24. Y. Xiao, *Rev. Mineral. Geochem.* **42**, 383–436 (2001).
25. U. Hammes, H. S. Hamlin, T. E. Ewing, *AAPG Bull.* **95**, 1643–1666 (2011).
26. J. B. Curtis, *AAPG Bull.* **86**, 1921 (2002).
27. A. Burnham, "A simple kinetic model of petroleum formation and cracking" (Lawrence Livermore National Lab, report UCID 21665, 1989).
28. P. Ungerer, *Org. Geochem.* **16**, 1–25 (1990).
29. G. G. Lash, T. Engelder, *AAPG Bull.* **95**, 61–103 (2011).
30. A. Prinzhofer, E. V. Dos Santos Neto, A. Battani, *Mar. Pet. Geol.* **27**, 1273–1284 (2010).
31. L. Trindade, S. C. Brassell, E. V. Santos Neto, *AAPG Bull.* **76**, 1903 (1992).
32. $\delta = (R/R_{std} - 1) \times 1000$ where $^{13}R = [^{13}C]/[^{12}C]$, $^{D}R = [D]/[H]$, and "std" denotes the standard to which all measurements are referenced (Vienna Pee Dee belemnite for carbon and Vienna standard mean ocean water for hydrogen isotopes).
33. N. Mahlstedt, B. Horsfield, *Mar. Pet. Geol.* **31**, 27–42 (2012).
34. D. A. Stolper *et al*., *Mineral. Mag.* **78**, 2393 (2014).
35. D. L. Valentine, A. Chidthaisong, A. Rice, W. S. Reeburgh, S. C. Tyler, *Geochim. Cosmochim. Acta* **68**, 1571–1590 (2004).
36. T. Hoering, *Org. Geochem.* **5**, 267–278 (1984).
37. F. D. Mango, J. Hightower, A. T. James, *Nature* **368**, 536–538 (1994).
38. S. Scheller, M. Goenrich, R. Boecher, R. K. Thauer, B. Jaun, *Nature* **465**, 606–608 (2010).
39. A. A. Prinzhofer, A. Y. Huc, *Chem. Geol.* **126**, 281–290 (1995).
40. F. Lorant, A. Prinzhofer, F. Behar, A.-Y. Huc, *Chem. Geol.* **147**, 249–264 (1998).

ACKNOWLEDGMENTS

This work was supported by the NSF, Petrobras, ExxonMobil, and Caltech. We thank Petrobras and ExxonMobil for providing samples and permission to publish, C. Araújo and B. Peterson for helpful discussions, and R. Burruss and three anonymous reviewers for helpful comments on the manuscript. Any use of trade, firm, or product names is for descriptive purposes only and does not imply endorsement by the U.S. Government. All data used to support the conclusions in this manuscript are provided in the supplementary materials.

SUPPLEMENTARY MATERIALS

www.sciencemag.org/content/344/6191/1500/suppl/DC1
Materials and Methods
Supplementary Text
Figs. S1 to S5
Tables S1 to S6
References (*41*–*63*)

8 April 2014; accepted 2 June 2014
10.1126/science.1254509

EARLY ANIMALS

Ediacaran metazoan reefs from the Nama Group, Namibia

A. M. Penny,[1]* R. Wood,[1] A. Curtis,[1] F. Bowyer,[1] R. Tostevin,[2] K.-H. Hoffman[3]

Reef-building in metazoans represents an important ecological innovation whereby individuals collectively enhance feeding efficiency and gain protection from competitors and predation. The appearance of metazoan reefs in the fossil record therefore indicates an adaptive response to complex ecological pressures. In the Nama Group, Namibia, we found evidence of reef-building by the earliest known skeletal metazoan, the globally distributed *Cloudina*, ~548 million years ago. These *Cloudina* reefs formed open frameworks without a microbial component but with mutual attachment and cementation between individuals. Orientated growth implies a passive suspension-feeding habit into nutrient-rich currents. The characteristics of *Cloudina* support the view that metazoan reef-building was promoted by the rise of substrate competitors and predators.

The appearance and rapid diversification of metazoans with fossilizable hard parts around the Precambrian-Cambrian boundary [541 million years ago (Ma)] is one of the most dramatic events of evolution (*1*, *2*). Biomineralization, which first occurred in metazoans in the Ediacaran, went on to mark a step change in biodiversity, in the complexity of marine ecosystems, and in the workings of the global carbon cycle. Metazoan hard parts from late Ediacaran (terminal Proterozoic) strata (~552 to 541 Ma) are represented by mineralized and nonmineralized tubes (*3*), possible siliceous microfossils (*4*, *5*), and supportive calcareous skeletons (*3*, *6*, *7*).

These calcified taxa were sessile benthos and grew in equatorial, shallow marine carbonate settings, raising the possibility that they formed reefs. The evolution of the reef-building habit represents an important ecological innovation, involving close aggregating growth, permanent fixture to a hard substrate, and creation of topographic relief on the sea floor. Reefs are an important focus of biodiversity in modern ecosystems and have been since their inception. Previously, the oldest known metazoan reefs were the archaeocyath sponge reefs of the Lower Cambrian (Tommotian), around 530 million years (*8*).

With the exception of *Namapoikia*, which is found within fissures in microbialite reefs (*7*), Ediacaran skeletal forms have only generally constrained ecological preferences (*3*, *6*, *9*). The oldest and most widely described of these is *Cloudina*, a genus characterized by stacked funnel-shaped elements that form a distinctive cone-in-cone exoskeleton. *Cloudina* was first described from the Nama Group of southern Namibia (*10*) and has subsequently been reported globally from late Ediacaran carbonates (*3*, *11*, *12*). *Cloudina* has been interpreted previously as a sessile and gregarious filter feeder of possible Cnidarian affinity (*11*) with an epibenthic mode of life associated with, or attached to, microbial mats or thrombolitic reefs (*3*, *11*–*17*). Various growth habits have been reported: *Cloudina* may have grown either vertically from or within microbial surfaces (*11*, *12*), where the apical part of the tube (or cone) may have served as an attachment site (*16*); embedded either vertically or subhorizontally within thrombolites (*17*); or recumbently attached to the upper surfaces of thrombolitic heads (*17*).

We present evidence for in situ reef-building growth in *Cloudina* (Fig. 1). We found reef-building *Cloudina* in the Omkyk Member of the Nama Group, Namibia (fig. S1A). The Nama Group is a series of interbedded shallow marine carbonates and siliciclastics deposited in a storm-dominated ramp setting (*18*–*20*) (fig. S2). The Omkyk Member, at the base of the succession, is a carbonate unit containing a series of microbial reefs as well as the fossils of the earliest skeletal metazoans. An ash bed that immediately overlies the Omkyk Member has been dated recently as 547.32 ± 0.31 Ma (*21*). The dominant reef-building *Cloudina* species is the larger *C. hartmannae*, but the smaller *C. riemkeae* is also noted in reef settings, where it may play an accessory role.

Cloudina reefs grew associated with larger thrombolitic and stromatolitic reefs within the Driedoornvlagte pinnacle reef complex, near Rietoog (23°S, 51.50′; 16°E, 39.38′) (fig. S1B). The reef complex is over 300 m thick and at least 7 km long (*18*, *22*). Here microbial reefs individually form elliptical mounds that reach up to 20 m in diameter, 5 to 10 m in width, and 5 m in height but coalesce to produce near-continuous structures with their long axes displaying a strong orientation parallel to the inferred paleoshoreline (now about northeast-southwest). Microbial reef cores were constructed by massive thrombolites, often with entrapped *Cloudina* and the skeletal metazoan *Namacalathus*; the outer (younger) layers often consist of stromatolites up to 0.75 m thick. A further skeletal metazoan, *Namapoikia*, encrusts the walls of vertical synsedimentary fissures, which formed perpendicular to bedding, and more rarely open reef surfaces (Fig. 2).

At Driedoornvlagte, *Cloudina* reefs grew in highly aggregating clusters, either as smaller coalescing thickets to create reef framework cavities (Fig. 1B), as single bioherms up to 1 to 1.5 m in diameter (fig. S3A), or in sheets on microbial bioherms (Fig. 1I and fig. S3I). Some bioherms show intermittent colonization by stromatolitic laminae and are subsequently encrusted by thick layers of stromatolite (fig. S3A). These laminae reveal the topographic relief of these bioherms to be up to 0.2 m.

Cloudina reefs grew in the absence of any internal microbial component. Remaining void spaces between aggregated *Cloudina* individuals (Fig. 1D), within individual skeletal elements (Fig. 1C), and within primary reef framework cavities between coalescing clusters (Fig. 1B) are dominantly filled with large botryoids up to 50 mm in radius that represent early marine aragonite cements now neomorphosed to calcite (Fig. 1H). These cements can fill framework cavities up to 0.15 m in diameter (Fig. 1B). There is limited geopetal micrite sediment but some late-burial calcite spar–filled remaining pore space (Fig. 1D), and *Cloudina* skeletons are often preferentially dolomitized (Fig. 1E).

We infer that colonizing *Cloudina* attached to a hard microbial substrate, initially subvertically (Fig. 1I). Most *Cloudina* individuals, however, show horizontal or subhorizontal sinuous growth. Some individuals show bifurcation to form two subhorizontal tubes 60° to 90° apart (Fig. 1, D and G, and fig. S3B). Previously, variable orientation of growth in *Cloudina* has been suggested to be a strategy to ensure high feeding efficiency (*12*) in settings of variable or limited food availability or living space or in interpopulation competition, but in our samples growth orientation is consistent and regular within communities (*23*) (figs. S3D and S4).

Cloudina individuals are attached to each other in two ways. Colonizing individuals settle on the outer walls of older individuals where the apical part of the tube (or cone) served as an attachment site (Fig. 1F), where subsequent growth is often perpendicular to the orientation of the host tube (Fig. 1F and fig. S3C) and shows an increase in tube diameter for the first 5 mm of extensional growth (Fig. 1F). Attachment appears to have been facilitated by some further precipitation of skeletal material, which is now preserved as neomorphosed calcite (Fig. 1F). Although such attachment is observed rarely, such colonization may in fact be a frequent occurrence. Similarly, *Cloudina* tubes in close proximity are also commonly cemented together by patch, or meniscus-like, cement features also now neomorphic calcite (Fig. 1A). These are interpreted as skeletal material between horizontally growing tubes, because cement botryoids are noted to nucleate on them or grow abutted against these features (Fig. 1C), testament to their presence before the onset of lithification. Similar early patchlike cements both between shell layers and within the central cavity of the tubes have been noted previously (*3*) and were suggested to be inorganic precipitation of calcareous cements between shell laminae that occurred during the lifetime of the organism, conveying robustness to the *Cloudina* tubes. Others have also noted the fusing of adjacent tubes

[1]School of GeoSciences, University of Edinburgh, West Mains Road, Edinburgh EH9 3JW, UK. [2]Department of Earth Sciences, University College London, Gower Street, London WC1E 6BT, UK. [3]Geological Survey of Namibia, Private Bag 13297, Windhoek, Namibia.
*Corresponding author. E-mail: a.m.penny@ed.ac.uk

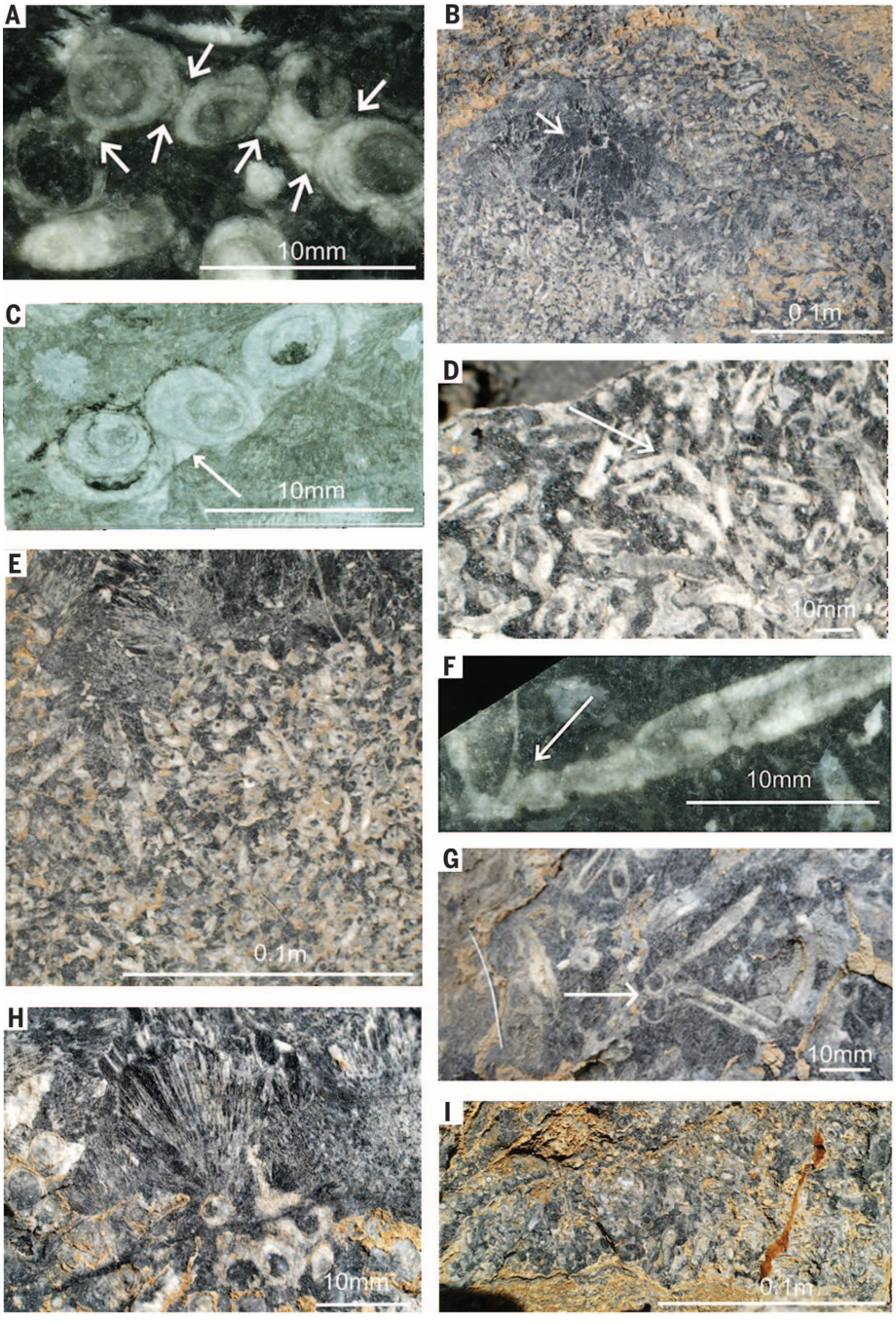

Fig. 1. *Cloudina* from the Omkyk Member, Nama Group, Namibia. (**A**) Transverse section across a number of *Cloudina* individuals showing meniscus-like calcite structures joining tubes together laterally (white arrows). (**B**) Coalescing thickets enclose primary reef cavity (white arrow). (**C**) Photomicrograph of thin section showing cementation of adjacent *Cloudina* by patch, meniscus-like neomorphosed calcite structures. Early marine cement botryoids abut against these; arrow shows nucleation of early marine botryoids on one example. (**D**) Abundant, aggregating *Cloudina* showing horizontal arrangement of tubes parallel to bedding, surrounded by early marine botryoidal fan cements. Internal void of tubes are filled by early marine botryoidal fan cements or late-burial spar. Bifurcating individual is arrowed. (**E**) Early marine botryoidal fan cements nucleating on *Cloudina* individuals. Some *Cloudina* skeletons are dolomitised. (**F**) Two *Cloudina* individuals attached to each other (at point indicated by white arrow). The shorter of the two tubes is interpreted as nucleating on a preexisting individual. (**G**) Aggregating *Cloudina* showing horizontal arrangement of tubes parallel to bedding, surrounded by botryoidal fan cements. Bifurcating individual showing marked growth reorientation is arrowed. (**H**) Neomorphosed early marine botryoidal fan cements infilling primary reef framework cavity between *Cloudina* clusters. (**I**) Growth of *Cloudina* from a microbial substrate.

during the life of *Cloudina* (*11*), although the cement present was interpreted as inorganic. Given their formation before any inorganic cementation, we suggest rather that these features were skeletal structures produced by *Cloudina*, similar to the mutual cementation of adjacent vermetid gastropods or calcareous polychaetes in formation and structure.

Many consider that the rise of predation pressure as a result of the radiation of bilaterians, particularly in the early Cambrian, promoted the first appearance of hard parts (*1*, *17*, *24*). The presence of metazoan on metazoan predation (carnivory) by the Ediacaran is in part corroborated by the finding of predatory boreholes in *Cloudina* individuals from China (*25*). Although most of these borings appear to have successfully penetrated the shell, the eccentrically stacked funnel-in-funnel structure of *Cloudina* may have been a defense strategy, and rugged shells with varying thickness have been shown to be more effective in hindering access to prey tissue (*26*). In addition, the relatively uniform distance of the borings from the shell apertures may indicate an avoidance response by the predator to protective measures near the aperture (*13*), where soft tissue was located.

Cloudina was aggregating and gregarious. An aggregating habit in solitary organisms assists the acquisition of favorable substrate for growth to maturity; affords protection from currents or high-energy events; and reduces susceptibility to overgrowth from competitors, larval invasion and infestation, and attack by predators (*27*). The aggregating habit has also been noted in the Ediacaran skeletal *Namacalathus* (*17*) and soft-bodied *Fusinia dorothea* (*28*).

Reef-building is facilitated by the ability to attach to a hard substrate and mutual cementation of individuals, enabling the formation of a stable, rigid reef framework and topographic relief and so creating a biologically controlled substrate for the successful fostering of future generations (*27*, *29*). Permanent, stable attachment also confers a selective advantage by inhibiting manipulability by predators, although drilling predation, which involves minimal manipulation, might not be hindered by attachment. The rarity of associated sediment and the abundance of early marine cements indicate that *Cloudina* grew elevated above a substrate, with further rigidity imparted by the presence of skeletal structures connecting adjacent individuals. Such a feature suggests that, as in many nonrelated modern and Phanerozoic reef benthos (*29*), aggregating individuals showed no competitive incompatibility. This could imply that the clusters of *Cloudina* represent substrates colonized by a limited number of larval spat falls. The aligned growth of horizontal tubes also suggests a passive suspension-feeding mode of life with tubes orientated into nutrient-rich currents.

Ediacaran reefs had been thought to be ecologically simple and of low biodiversity (*6*, *29*) but the presence of free-growing, reef-building *Cloudina*, as well as thrombolite-associated *Cloudina* and *Namacalathus* and fissure-dwelling *Namapoikia*, suggests a far more common metazoan component to these otherwise microbial communities and a

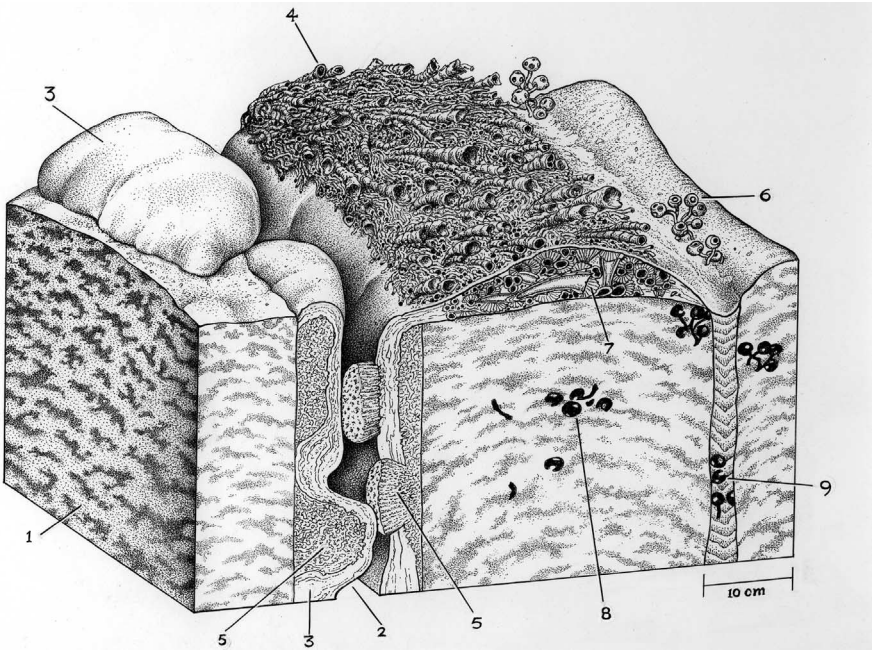

Fig. 2. Reconstruction of a late Ediacaran reef. 1, Thrombolite; **2**, Neptunian dyke; **3**, stromatolite; **4**, *Cloudina*; **5**, *Namapoikia*; **6**, *Namacalathus*; **7**, cement botryoids; **8**, trapped *Namacalathus*; **9**, sediment. [Image copyright: J. Sibbick]

differentiation of metazoans into the distinct open surface and cryptic biotas so characteristic of Phanerozoic and modern reefs (Fig. 2). *Cloudina* possessed additional features, such as the ability for interindividual skeletal cementation that enabled elevated growth above a substrate and mutual support to form an open framework with high mechanical strength and potential resistance to predation. These paleoecological characteristics are all consistent with competitive strategies and antipredation traits and support the views that both skeletonization and reef-building in metazoans was promoted by the rise of substrate competitors and bilaterian predators and that such a selective pressure was a strong driving evolutionary force by the Ediacaran.

REFERENCES AND NOTES

1. S. Bengtson, *Paleontol. Soc. Pap.* **10**, 67 (2004).
2. M. D. Brasier, in *The Precambrian-Cambrian Boundary*, J. W. Cowie, M. D. Brasier, Eds. (Oxford Univ. Press, Oxford, 1989), pp. 117–165.
3. S. W. F. Grant, *Am. J. Sci.* **290-A**, 261–294 (1990).
4. J. Gehling, J. K. Rigby, *J. Paleontol.* **70**, 185 (1996).
5. A. E. Kontorovich *et al.*, *Russ. Geol. Geophys.* **49**, 932–939 (2008).
6. J. P. Grotzinger, W. Watters, A. H. Knoll, *Paleobiology* **26**, 334–359 (2000).
7. R. A. Wood, J. P. Grotzinger, J. A. D. Dickson, *Science* **296**, 2383–2386 (2002).
8. P. D. Kruse, A. Yu. Zhuravlev, N. P. James, *Palaios* **10**, 291 (1995).
9. S. Bengtson, S. Conway Morris, *Topics in Geobiology* **20**, 447–481 (1992).
10. G. B. H. Germs, *Am. J. Sci.* **272**, 752–761 (1972).
11. I. Cortijo, M. M. Mus, S. Jensen, T. Palacios, *Precambrian Res.* **176**, 1–10 (2010).
12. L. V. Warren *et al.*, *Terra Nova* **23**, 382–389 (2011).
13. H. Hua, B. R. Pratt, L.-Z. Zhang, *Palaios* **18**, 454–459 (2003).
14. H. Hua, Z. Chen, X. L. Yuan, L.-Z. Zhang, S. H. Xiao, *Geology* **33**, 277 (2005).
15. A. Seilacher, *Palaios* **14**, 86 (1999).
16. Y. Cai *et al.*, *Gondwana Res.* **25**, 1008–1018 (2014).
17. R. A. Wood, *Earth Sci. Rev.* **106**, 184–190 (2011).
18. B. Z. Saylor, A. J. Kaufman, J. P. Grotzinger, F. Urban, *J. Sediment. Res.* **68**, 1223–1235 (1998).
19. J. P. Grotzinger, *Commun. Geol. Surv. Namibia* **11**, 77 (2002).
20. For details, see supplementary text on *Science* Online.
21. G. M. Narbonne, S. Xiao, G. Shields, "The Ediacaran Period," in *The Geologic Time Scale 2012*, F. Gradstein, J. Ogg, G. Ogg, Eds. (Elsevier, Boston, 2012), pp. 427–449.
22. G. M. Narbonne, B. Z. Saylor, J. P. Grotzinger, *J. Paleontol.* **71**, 953–967 (1997).
23. For details, see materials and methods on *Science* Online.
24. A. H. Knoll, *Rev. Mineral. Geochem.* **54**, 329–356 (2003).
25. S. Bengtson, Y. Zhao, *Science* **257**, 367–369 (1992).
26. G. J. Vermeij, *A Natural History of Shells* (Princeton Univ. Press, Princeton, NJ, 1993).
27. J. B. C. Jackson, in *Biotic Interactions in Recent and Fossil Benthic Communities*, M. Tevesz, P. W. McCall, Eds. (Plenum, New York, 1983), vol. 39.
28. M. L. Droser, J. G. Gehling, *Science* **319**, 1660–1662 (2008).
29. R. Wood, *Reef Evolution* (Oxford Univ. Press, Oxford, 1999).

ACKNOWLEDGMENTS

A.M.P. acknowledges funding from a University of Edinburgh, School of Geosciences Scholarship and the International Centre for Carbonate Reservoirs. R.W., R.T., and A.M.P. acknowledge support from Natural Environment Research Council (NERC) project "Re-inventing the planet: the Neoproterozoic revolution in oxygenation, biogeochemistry and biological complexity" (NE/I005978/1). F.B. thanks the Laidlaw Trust for fieldwork support. We thank the Geological Survey of Namibia; C. Husselmann for access to Driedoornvlagte; M. Hall for technical support; and A. Yu. Zhuravlev, B. MacGabhann, and S. Brusatte for comments and discussion. All data are available online in the supplementary materials on *Science* Online.

SUPPLEMENTARY MATERIALS

www.sciencemag.org/content/344/6191/1504/suppl/DC1
Materials and Methods
Supplementary Text
Figs. S1 to S4
References (*30*–*39*)

14 March 2014; accepted 2 June 2014
10.1126/science.1253393

VIRUS ENTRY

Lassa virus entry requires a trigger-induced receptor switch

Lucas T. Jae,[1] Matthijs Raaben,[1,2] Andrew S. Herbert,[3] Ana I. Kuehne,[3] Ariel S. Wirchnianski,[3] Timothy K. Soh,[2] Sarah H. Stubbs,[2] Hans Janssen,[1] Markus Damme,[4] Paul Saftig,[4] Sean P. Whelan,[2]* John M. Dye,[3]* Thijn R. Brummelkamp[1,5,6]*

Lassa virus spreads from a rodent to humans and can lead to lethal hemorrhagic fever. Despite its broad tropism, chicken cells were reported 30 years ago to resist infection. We found that Lassa virus readily engaged its cell-surface receptor α-dystroglycan in avian cells, but virus entry in susceptible species involved a pH-dependent switch to an intracellular receptor, the lysosome-resident protein LAMP1. Iterative haploid screens revealed that the sialyltransferase ST3GAL4 was required for the interaction of the virus glycoprotein with LAMP1. A single glycosylated residue in LAMP1, present in susceptible species but absent in birds, was essential for interaction with the Lassa virus envelope protein and subsequent infection. The resistance of *Lamp1*-deficient mice to Lassa virus highlights the relevance of this receptor switch in vivo.

Lassa virus binds to glycosylated α-dystroglycan (α-DG) at the cell surface to enter cells (*1*, *2*). Over 30 years ago, it was reported that Lassa virus infects a broad suite of cells from different species, with the exception of chicken (*3*). This was recapitulated by a recombinant vesicular stomatitis virus (VSV) that enters cells using the Lassa virus glycoprotein (rVSV-GP-LASV) (*4*). Because wild-type VSV was unaffected, this indicated a defect in Lassa glycoprotein (GP)–mediated entry (fig. S1A). Birds, however, generate glycosylated α-DG (*5*), and the Lassa envelope protein recognized avian α-DG (fig. S1, B and C).

To identify host factors affecting virus entry independent of α-DG binding, we carried out a haploid screen in receptor-deficient cells. For this, we made use of their incomplete resistance phenotype (fig. S2). This showed that neither α-DG nor factors glycosylating α-DG acted as host factors under these conditions (Fig. 1A; fig. S3, A and B; and tables S1 and S2) (*6*). Instead, we found genes involved in glycosylation, Golgi function, and heparan sulfate biosynthesis. The latter were not identified in wild-type cells (fig. S3C and tables S1 and S3) (*4*), suggesting that in the absence of α-DG, Lassa virus used heparan sulfate, a commonly used virus attachment factor (*7*). The lysosomal transmembrane protein LAMP1 and factors involved in *N*-glycosylation and sialylation, including the α-2,3-sialyltransferase ST3GAL4, stood out in both genotypes. Cells deficient for *LAMP1* or *ST3GAL4* were comparably resistant to wild-type Lassa virus as those lacking α-DG (Fig. 1B and fig. S4, A and B). Expression of human but not chicken LAMP1 sensitized chicken fibroblasts to infection with rVSV-GP-LASV (Fig. 1C and fig. S4C) and imposed virus susceptibility in *LAMP1*-deficient human cells (Fig. 1D and fig. S5). This requirement for LAMP1 was specific for Lassa virus and not shared by the related lymphocytic choriomeningitis virus (fig. S6). Thus, LAMP1 and ST3GAL4 were important for Lassa virus infection independent of α-DG, and host factor function of human LAMP1 was not shared by its chicken ortholog.

Because LAMP1 deficiency neither causes pronounced phenotypes in mice (*8*) nor detectably impaired the endo-lysosomal compartment in cultured cells (fig. S7), we asked whether the nuclease-generated mutations in the corresponding genes were exposed to wild-type Lassa virus and stained with antibodies specific for viral antigens to measure infected cells. *LAMP1*-deficient cells were complemented with human LAMP1 cDNA. (**C**) Chicken fibroblasts were transduced with retroviruses expressing chicken (c) or human (h) LAMP1 and challenged with rVSV-GP-LASV. Average number (±SD) of infected cells per field (eGFP-positive) is indicated. (**D**) Wild-type or *LAMP1*-deficient HAP1 cells transduced with retroviruses expressing cLAMP1 or hLAMP1 (L1) were exposed to rVSV-G or rVSV-GP-LASV. Percentage (±SD) of infected cells (expressing eGFP) is indicated. Scale bars, 50 μm.

[1]Netherlands Cancer Institute, Plesmanlaan 121, 1066 CX, Amsterdam, Netherlands. [2]Department of Microbiology and Immunobiology, Harvard Medical School, 77 Avenue Louis Pasteur, Boston, MA 02115, USA. [3]U.S. Army Medical Research Institute of Infectious Diseases, 1425 Porter Street, Fort Detrick, MD 21702–5011, USA. [4]Biochemisches Institut, Christian Albrechts-Universität Kiel, 24118 Kiel, Germany. [5]CeMM Research Center for Molecular Medicine of the Austrian Academy of Sciences, 1090 Vienna, Austria. [6]Cancer Genomics Center (CGC.nl), Plesmanlaan 121, 1066 CX, Amsterdam, Netherlands.
***Corresponding author. E-mail: t.brummelkamp@nki.nl (T.R.B.); john.m.dye1.civ@mail.mil (J.M.D.); sean_whelan@hms.harvard.edu (S.P.W.)**

Lassa virus envelope protein could bind to LAMP1. As the majority of LAMP1 is localized in the acidic interior of lysosomes (*9*, *10*), these experiments were carried out at neutral and acidic pH. Immobilized Flag-tagged Lassa-GP bound α-DG at neutral pH, but this interaction was lost at acidic pH, at which Lassa-GP instead strongly bound to LAMP1 (Fig. 2A and fig. S8, A and B). Lassa-GP molecules that had previously bound α-DG were capable of subsequent binding to LAMP1 (fig. S8C). Likewise, intact virions were captured by the luminal region of LAMP1 at acidic but not at neutral pH (fig. S9). Last, this interaction was observed for both human and mouse LAMP1 but not chicken LAMP1 or human LAMP2 (Fig. 2B and fig. S10).

Virus particles containing enhanced green fluorescent protein (eGFP) fused to the VSV matrix protein (MeGFP, allowing direct visualization of incoming fluorescent virions) were internalized in cells lacking *LAMP1* or *ST3GAL4* (fig. S11) but accumulated in vesicles of *LAMP1*-deficient cells (Fig. 2C). In wild-type cells, fusion of viral and cellular membranes leads to release of MeGFP protein into the cytoplasm (*11*), but in *LAMP1*-deficient cells, MeGFP remained localized to vesicles (figs. S12 and 13), suggesting that the association of Lassa-GP with LAMP1 precedes membrane fusion. In agreement with this, LAMP1 interacted with Lassa-GP in a prefusion configuration when the GP1 subunit of the viral envelope protein is still part of the complex (*12*, *13*) but not when GP1 was fully released from GP2 by low pH (Fig. 2D and fig. S14). To test whether Lassa-GP–mediated membrane fusion was affected by LAMP1, we carried out cell-cell fusion experiments in the presence of a LAMP1 mutant that localizes to the cell surface (LAMP1d384) (fig. S15A) (*9*). Expression of this mutant led to increased syncytia formation as a consequence of membrane fusion (Fig. 2E and fig. S15, B and C). This activity of LAMP1 was independent of α-DG (fig. S15D). Thus, Lassa virus likely engages α-DG at the cell surface, enters the endocytic pathway and binds to LAMP1 upon reaching the acidic interior of lysosomes, before membrane fusion.

To test this model, we engineered an artificial virus infection scenario. Cells in which α-DG was knocked out that expressed LAMP1d384 were largely resistant to rVSV-GP-LASV under normal conditions, but lowering the extracellular pH during virus exposure led to productive infection (fig. S16, A to E). Lassa virus entry normally depends on acidification of endosomes (*14*) and is sensitive to bafilomycin (*15*). The engineered entry route was, however, bafilomycin-insensitive (fig. S16, F and G). Thus, the requirement for α-DG could be bypassed by rerouting LAMP1 to the cell surface and triggering binding to Lassa-GP.

Besides LAMP1, the screens identified the α-2,3-sialyltransferase ST3GAL4 as an α-DG–independent host factor. Because targets modified by this enzyme could display genetic interactions, we searched for host factors depending on ST3GAL4. *ST3GAL4*-deficient cells were mutagenized and selected with rVSV-GP-LASV. Like experiments in wild-type cells, this screen identified *DAG1* and its modifiers (*4*). As expected, the disrupted *ST3GAL4* locus did not act as a host factor under

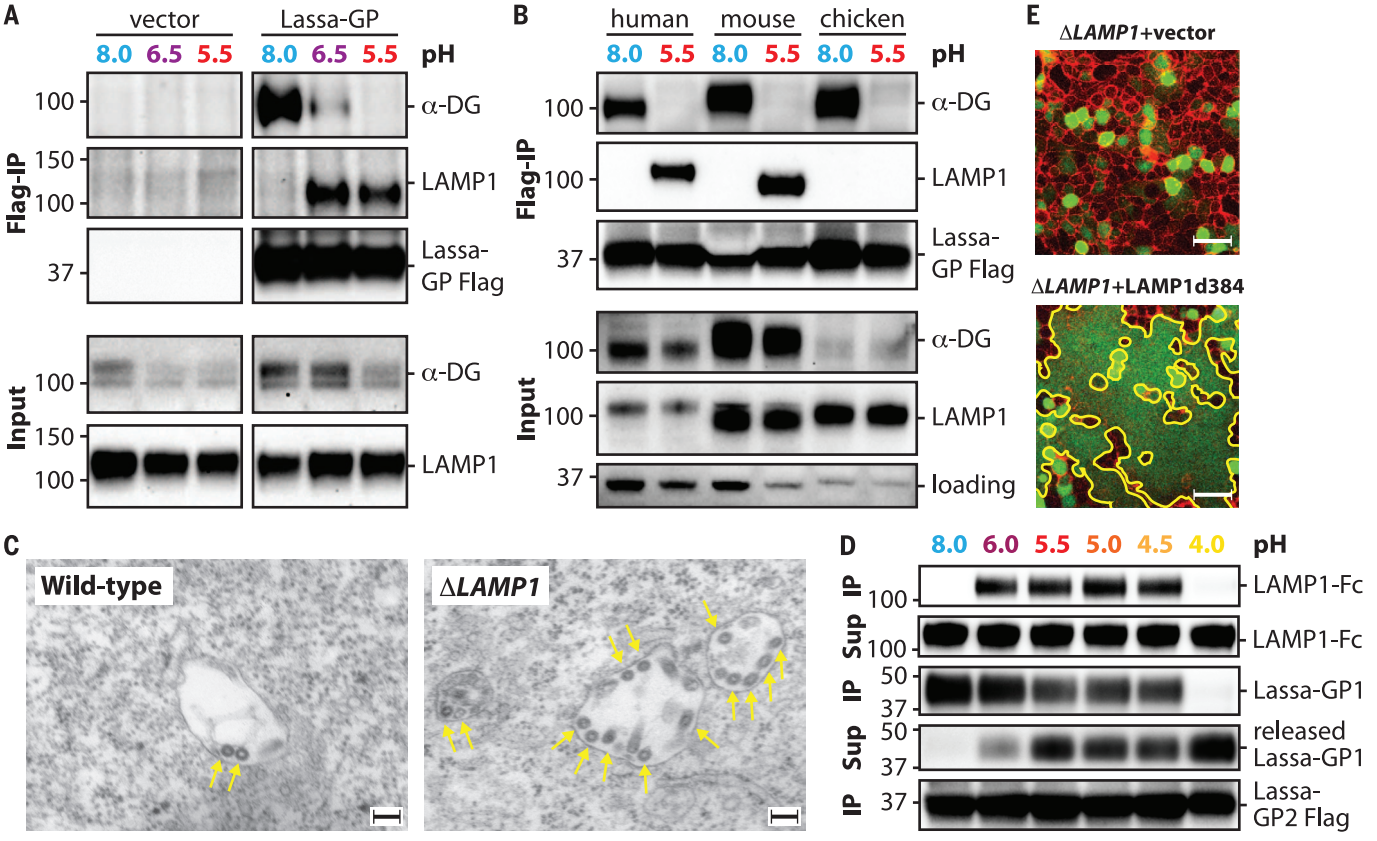

Fig. 2. Lassa-GP undergoes a pH-induced switch to engage LAMP1. (**A**) Flag-tagged Lassa-GP was immobilized on beads and incubated with cell lysates from human embryonic kidney (HEK) 293T cells at the indicated pH. Bound proteins were subjected to immunoblot analysis, and uncoated beads served as a control. IP, immunoprecipitation. (**B**) Flag-tagged Lassa-GP was immobilized on beads and incubated with lysates from human, mouse, and chicken cells at the indicated pH. Bound proteins were subjected to immunoblot analysis. (**C**) Electron micrographs of wild-type and *LAMP1*-deficient HEK-293T cells that were infected with rVSV-GP-LASV. *LAMP1*-deficient cells show an accumulation of the bullet-shaped viral particles (arrows) in intracellular vesicles. Scale bars, 100 nm. (**D**) Flag-tagged Lassa-GP was immobilized on beads and incubated with purified LAMP1-Fc at the indicated pH. Complexes (IP) were precipitated and subjected to immunoblot analysis. The supernatant (Sup) was analyzed for the release of Lassa-GP1. (**E**) *LAMP1*-deficient (top) or LAMP1d384-expressing HEK-293T cells (bottom) were transfected with expression vectors for Lassa-GP and GFP and exposed to pH 5.5. Cell boundaries were visualized with fluorescent wheat germ agglutinin (red). Large, homogenous green fluorescent area results from Lassa-GP–induced syncytia formation (yellow outline). Scale bars, 50 μm.

these conditions, but neither did *LAMP1* (Fig. 3A; figs. S3, C and D, and S17A, and tables S1 and S4). Therefore, we investigated a putative biochemical connection between them. LAMP1 is glycosylated (*16*) with both N- and O-glycans (*17*). LAMP1 derived from *ST3GAL4*-deficient cells showed reduced binding to lectins that preferentially capture α-2,3–linked sialic acid (fig. S17, B and C) (*18*) and lost its ability to bind to Lassa-GP (Fig. 3B). Thus, LAMP1 was only able to act as a host factor in the context of *ST3GAL4* proficiency.

LAMP1 consists of three luminal domains: a membrane-proximal domain, an O-glycosylated hinge region, and a distal domain. The distal domain contains 11 *N*-glycosylation sites (UniProt, P11279) and was sufficient to support rVSV-GP-LASV infection by itself (fig. S18). Reconciling that genes for *N*-glycosylation and sialylation acted as host factors and that LAMP1 derived from *ST3GAL4*-mutant cells was not recognized by Lassa-GP, we speculated that one of these glycosylation sites was important for host factor function. Indeed, we found that only Asn^{76} was essential for VSV-GP-LASV infectivity (Fig. 3C). This residue is present in LAMP1 from species susceptible to Lassa virus but absent in birds (Fig. 3D) (*16*). Substitution of this amino acid in human LAMP1 for the respective avian residue ($Asn^{76}Ser$) was sufficient to block infection (fig. S19) and binding to Lassa-GP (Fig. 3E). Reciprocally, insertion of a region surrounding human Asn^{76} into chicken LAMP1 converted the avian protein into a host factor (fig. S20). Thus, we identified the sialyltransferase ST3GAL4 as a critical enzyme required for LAMP1 to function as a host factor and mapped the interaction between sialylated LAMP1 and Lassa-GP to a single glycosylated amino acid present in sensitive species but absent in birds.

Because Lassa virus has a rodent reservoir, we examined whether LAMP1 is required for the propagation of wild-type Lassa virus in vivo. After intraperitoneal injection, virus was cleared in mice in which *Lamp1* was knocked out, whereas infection was manifest in all organ samples taken from wild-type or heterozygous animals (Fig. 4A and fig. S21).

Here, we have shown that Lassa virus entry requires a pH-regulated engagement of α-DG and LAMP1, both of which need to be glycosylated. However, the glycan structures that are needed for host factor function are unrelated and constructed by distinct enzymes (Fig. 4B and fig. S22). Unlike in rodents (*19*), the human upper airway mainly contains α-2,6–linked sialic acid moieties rather than α-2,3–linked sugars (*20*) generated by enzymes such as ST3GAL4. It has been proposed that this is an adaptation to evade pathogens like avian influenza (*21*), but it may also limit human-to-human spread of Lassa virus (*22*). Lassa virus has been described as a "late-penetrating"

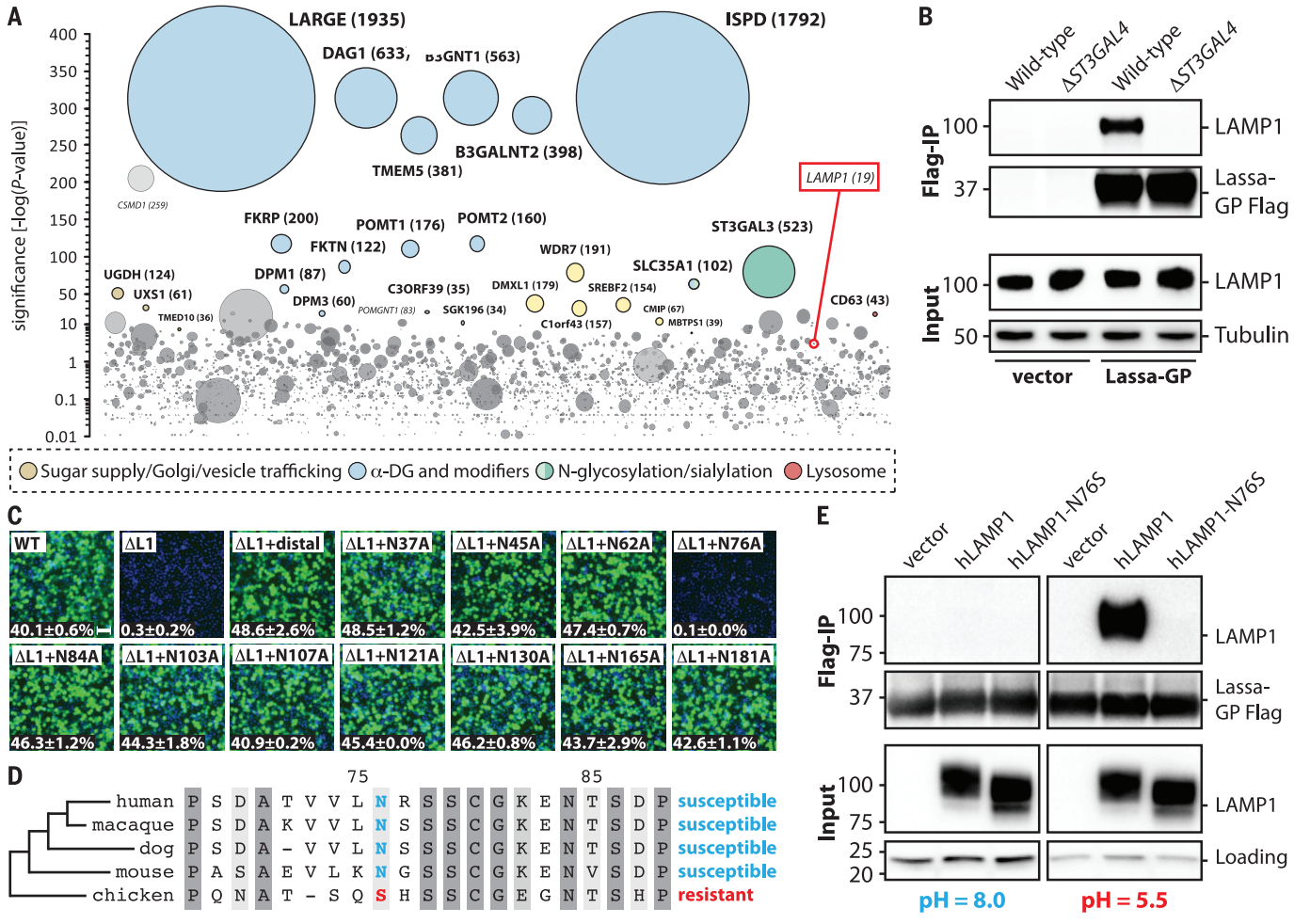

Fig. 3. Binding of Lassa-GP to LAMP1 depends on ST3GAL4, and LAMP1-Asn^{76} is critical for host factor function. (**A**) Haploid genetic screen pointing out genetic interactions between *ST3GAL4* and other Lassa entry factors. *ST3GAL4*-deficient cells were mutagenized and exposed to rVSV-GP-LASV. Gene-trap insertion sites were mapped in the resistant cell population, and data was analyzed as in Fig. 1A. (**B**) Flag-tagged Lassa-GP was immobilized on beads and incubated with cell lysates from wild-type and *ST3GAL4*-deficient HAP1 cells at pH 5.5. Bound proteins were subjected to immunoblot analysis. (**C**) Wild-type (WT) and *LAMP1*-deficient (ΔL1) HAP1 cells complemented with cDNAs expressing the distal domain of LAMP1 containing mutations at the indicated glycosylation sites were exposed to rVSV-GP-LASV. Percentage (±SD) of infected cells (eGFP-positive) is shown. (**D**) Comparison of LAMP1 polypeptides from indicated species highlights Asn^{76} as a marker of susceptibility to Lassa virus infection. (**E**) Flag-tagged Lassa-GP was immobilized on beads and incubated with lysates from *LAMP1*-deficient HEK-293T cells expressing human LAMP1 or "chickenized" LAMP1 carrying the $Asn^{76}Ser$ substitution at the indicated pH.

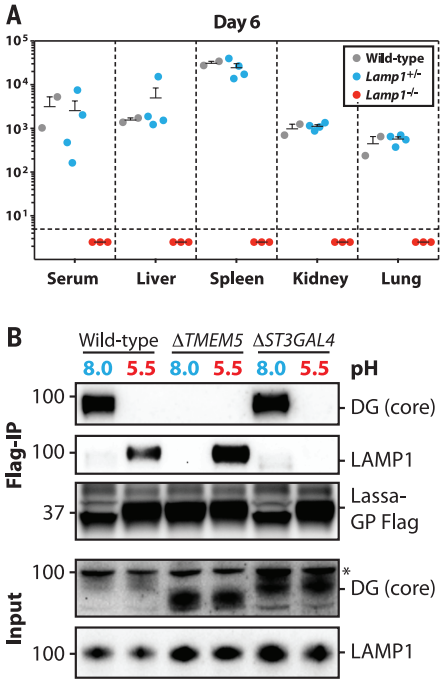

Fig. 4. *Lamp1* knockout mice are resistant to wild-type Lassa virus, and the receptors require distinct glycosyltransferases. (**A**) Lassa virus propagation in *Lamp1*$^{+/+}$, *Lamp1*$^{+/-}$, and *Lamp*$^{-/-}$ mice. Mice were injected intraperitoneally with wild-type Lassa virus, and viral titers (*y* axis, plaque-forming units/mL) were determined after 6 days in the indicated tissues. The horizontal line marks the detection limit. (**B**) Flag-tagged Lassa-GP was immobilized on beads and incubated with cell lysates from wild-type, *TMEM5*-, or *ST3GAL4*-deficient cells at the indicated pH. The glycosyltransferase TMEM5 is needed to generate an epitope on α-DG that is recognized by Lassa-GP (*4*). Bound proteins were subjected to immunoblot analysis. Asterisk indicates nonspecific background band.

virus (*23*) that requires low pH (*24*). Our findings rationalize these observations and emphasize the emergence of intracellular receptors for virus entry.

REFERENCES AND NOTES

1. S. Kunz *et al.*, *J. Virol.* **79**, 14282–14296 (2005).
2. W. Cao *et al.*, *Science* **282**, 2079–2081 (1998).
3. I. S. Lukashevich, R. F. Maryankova, F. M. Fidarov, *Acta Virol.* **27**, 282–285 (1983).
4. L. T. Jae *et al.*, *Science* **340**, 479–483 (2013).
5. F. Saito *et al.*, *FEBS Lett.* **579**, 2359–2363 (2005).
6. Materials and methods are available as supplementary materials on *Science* Online.
7. W. Zhu, J. Li, G. Liang, *Biomed. Environ. Sci.* **24**, 81–87 (2011).
8. N. Andrejewski *et al.*, *J. Biol. Chem.* **274**, 12692–12701 (1999).
9. J. Rohrer, A. Schweizer, D. Russell, S. Kornfeld, *J. Cell Biol.* **132**, 565–576 (1996).
10. T. Nishi, M. Forgac, *Nat. Rev. Mol. Cell Biol.* **3**, 94–103 (2002).
11. J. E. Carette *et al.*, *Nature* **477**, 340–343 (2011).
12. C. Di Simone, M. J. Buchmeier, *Virology* **209**, 3–9 (1995).
13. J. York, D. Dai, S. M. Amberg, J. H. Nunberg, *J. Virol.* **82**, 10932–10939 (2008).
14. J. H. Nunberg, J. York, *Viruses* **4**, 83–101 (2012).
15. E. J. Bowman, A. Siebers, K. Altendorf, *Proc. Natl. Acad. Sci. U.S.A.* **85**, 7972–7976 (1988).
16. M. Heffernan, S. Yousefi, J. W. Dennis, *Cancer Res.* **49**, 6077–6084 (1989).
17. S. R. Carlsson, P. O. Lycksell, M. Fukuda, *Arch. Biochem. Biophys.* **304**, 65–73 (1993).
18. W. C. Wang, R. D. Cummings, *J. Biol. Chem.* **263**, 4576–4585 (1988).
19. A. Ibricevic *et al.*, *J. Virol.* **80**, 7469–7480 (2006).
20. M. de Graaf, R. A. Fouchier, *EMBO J.* **33**, 823–841 (2014).
21. K. Shinya *et al.*, *Nature* **440**, 435–436 (2006).
22. W. H. Haas *et al.*, *Clin. Infect. Dis.* **36**, 1254–1258 (2003).
23. P. Y. Lozach, J. Huotari, A. Helenius, *Curr. Opin. Virol.* **1**, 35–43 (2011).
24. F. L. Cosset *et al.*, *J. Virol.* **83**, 3228–3237 (2009).

ACKNOWLEDGMENTS

We thank T. Sixma, A. Perrakis, E. von Castelmur, D. Lefeber, and members of the Brummelkamp group for discussion; M. Rusch for mouse breeding; S. Kunz for a plasmid encoding Lassa-GP; E. Ollmann-Saphire for an Fc-fusion vector; R. Schoepp for GP1 antibodies; and M. Verheije for DF1 cells. This work was supported by CGC.nl, Nederlandse Organisatie voor Wetenschappelijk Onderzoek Vidi grant 91711316, and European Research Council (ERC) Starting Grant (ERC-2012-StG 309634) to T.R.B.; Deutsche Forschungsgemeinschaft (DFG SPP1580 and GRK1459) to P.S.; and NIH grants AI081842 and AI109740 to S.P.W. J.M.D was supported by the Defense Threat Reduction Agency (CB3947). The HAP1 cells that were used are distributed under a materials transfer agreement. Opinions, interpretations, conclusions, and recommendations are those of the author and are not necessarily endorsed by the U.S. Army. T.R.B. is a cofounder and shareholder of Haplogen GmbH, a company involved in haploid genetics. Sequencing data are accessible at www.ncbi.nlm.nih.gov/sra (accession SRP041566).

SUPPLEMENTARY MATERIALS

www.sciencemag.org/content/344/6191/1506/suppl/DC1
Materials and Methods
Figs. S1 to S22
Tables S1 to S4
References (*25*–*44*)

20 February 2014; accepted 30 May 2014
10.1126/science.1252480

MEMBRANE TRAFFICKING

Nucleoside diphosphate kinases fuel dynamin superfamily proteins with GTP for membrane remodeling

Mathieu Boissan,[1,2,3,4]* Guillaume Montagnac,[1,2]† Qinfang Shen,[5] Lorena Griparic,[5] Jérôme Guitton,[6,7] Maryse Romao,[1,8] Nathalie Sauvonnet,[9] Thibault Lagache,[10] Ioan Lascu,[11] Graça Raposo,[1,8] Céline Desbourdes,[12,13] Uwe Schlattner,[12,13] Marie-Lise Lacombe,[3,4] Simona Polo,[14,15] Alexander M. van der Bliek,[5] Aurélien Roux,[16] Philippe Chavrier[1,2]*

Dynamin superfamily molecular motors use guanosine triphosphate (GTP) as a source of energy for membrane-remodeling events. We found that knockdown of nucleoside diphosphate kinases (NDPKs) NM23-H1/H2, which produce GTP through adenosine triphosphate (ATP)–driven conversion of guanosine diphosphate (GDP), inhibited dynamin-mediated endocytosis. NM23-H1/H2 localized at clathrin-coated pits and interacted with the proline-rich domain of dynamin. In vitro, NM23-H1/H2 were recruited to dynamin-induced tubules, stimulated GTP-loading on dynamin, and triggered fission in the presence of ATP and GDP. NM23-H4, a mitochondria-specific NDPK, colocalized with mitochondrial dynamin-like OPA1 involved in mitochondria inner membrane fusion and increased GTP-loading on OPA1. Like OPA1 loss of function, silencing of NM23-H4 but not NM23-H1/H2 resulted in mitochondrial fragmentation, reflecting fusion defects. Thus, NDPKs interact with and provide GTP to dynamins, allowing these motor proteins to work with high thermodynamic efficiency.

The 100-kD dynamin guanosine triphosphatase (GTPase) promotes uptake of cell-surface receptors both by clathrin-dependent and -independent pathways (*1*, *2*). Dynamin polymerizes into helix around the neck of endocytic pits and induces guanosine triphosphate (GTP) hydrolysis–driven membrane fission (*3*–*7*). Typical of molecular motors, dynamin has a low affinity for GTP and a high basal GTP-hydrolysis rate, which can be further stimulated by dynamin polymerization (*8*, *9*). This maximizes chemical energy gain and kinetics of hydrolysis, respectively, which in vivo depend on high concentration ratios of adenosine triphosphate/adenosine diphosphate (ATP/ADP) or GTP/guanosine diphosphate (GDP). The cellular concentrations of GTP and GDP are at least a factor of 10 lower than those of ATP and ADP, and GTP/GDP ratios could thus decrease much more rapidly at elevated workload, both of which make GTP not an ideal substrate for high-turnover, energy-dependent enzymes. Paradoxically, dynamin GTPases are among the most powerful molecular motors described (*7*).

Studies in *Drosophila* identified a genetic interaction between dynamin and *Awd* (*10*–*12*). Awd belongs to the family of nucleoside diphosphate kinases (NDPKs), which catalyze synthesis of nucleoside triphosphates, including GTP, from corresponding nucleoside diphosphates and ATP (*13*). The most abundant human NDPKs are the highly related cytosolic proteins NM23-H1 and -H2. NM23-H4, another NDPK-family member, localizes exclusively at the mitochondrial inner membrane (*14*, *15*). Mitochondrial

[1]Institut Curie, Research Center, Paris, France. [2]Membrane and Cytoskeleton Dynamics, CNRS UMR 144, Paris, France. [3]Université Pierre et Marie Curie, University Paris 06, Paris, France. [4]Saint-Antoine Research Center, INSERM UMR-S 938, Paris, France. [5]Department of Biological Chemistry, David Geffen School of Medicine at University of California, Los Angeles, Los Angeles, CA, USA. [6]Hospices Civils de Lyon, Pierre Bénite, France. [7]Université de Lyon, Lyon, France. [8]Structure and Membrane Compartments, CNRS UMR 144, Paris, France. [9]Institut Pasteur, Unité de Biologie des Interactions Cellulaires, Paris, France. [10]Quantitative Image Analysis Unit, Institut Pasteur, Paris, France. [11]Institut de Biochimie et Génétique Cellulaires-CNRS, Université Bordeaux 2, Bordeaux, France. [12]Université Grenoble Alpes, Laboratory of Fundamental and Applied Bioenergetics, Grenoble, France. [13]Inserm, U1055, Grenoble, France. [14]IFOM, Fondazione Istituto FIRC di Oncologia Molecolare, Milan, Italy. [15]Dipartimento di Scienze della Salute, Universita' degli Studi di Milano, Milan, Italy. [16]Biochemistry Department, University of Geneva, & Swiss National Center for Competence in Research Program Chemical Biology, Geneva, Switzerland.
***Corresponding author. E-mail: mathieu.boissan@inserm.fr (M.B.); philippe.chavrier@curie.fr (P.C.)** †Present address: Institut Gustave Roussy, Inserm U1009, Villejuif, France

membrane dynamics require dynamin-related GTPases (*16*). We hypothesized that NDPKs could influence the function of dynamin family members in membrane-remodeling events through spatially controlled GTP production and availability.

Knockdown of NM23-H1 and -H2 (fig. S1, A to E) reduced clathrin-dependent endocytosis of the transferrin (Tf) and epidermal growth factor (EGF) receptors (Fig. 1, A and B, and fig. S2, A to E) and clathrin-independent dynamin-dependent endocytosis of interleukin-2 receptor β subunit (Fig. 1C). The endocytic defect of EGF receptor was partially rescued by expression of wild-type, small interfering RNA (siRNA)–resistant NM23-H1, but not by kinase-dead NM23-$H1^{H118N}$ mutant (Fig. 1D). Thus, the function of Awd/NM23 in dynamin-mediated endocytosis is conserved from *Drosophila* to mammalian cells [(*10*) and this study].

Like in dynamin-null cells (*17*), NM23-H1/H2 depletion increased the density of clathrin-coated pits (CCPs) at the plasma membrane (Fig. 2, A and B, and fig. S3, A and B). Silencing of NM23-H1/H2 led to the accumulation of deeply invaginated CCPs, in contrast to control cells, where CCPs were rarely detected at the plasma membrane (Fig. 2, C to F). Scoring for Tf-positive CCPs and vesicles in the vicinity of the plasma membrane revealed an approximately threefold augmentation in the absence of NM23 (Fig. 2G), similar to the phenotype reported in dynamin-null cells (*17*), suggesting a role for NM23-H1/H2 in dynamin-mediated membrane fission at CCPs.

We examined the intracellular distribution of NM23-H1/H2 and confirmed that both isoforms were predominantly cytosolic, although a low but reproducible association of both isoforms with membranes was found (fig. S4, A and B). Total internal reflection fluorescence

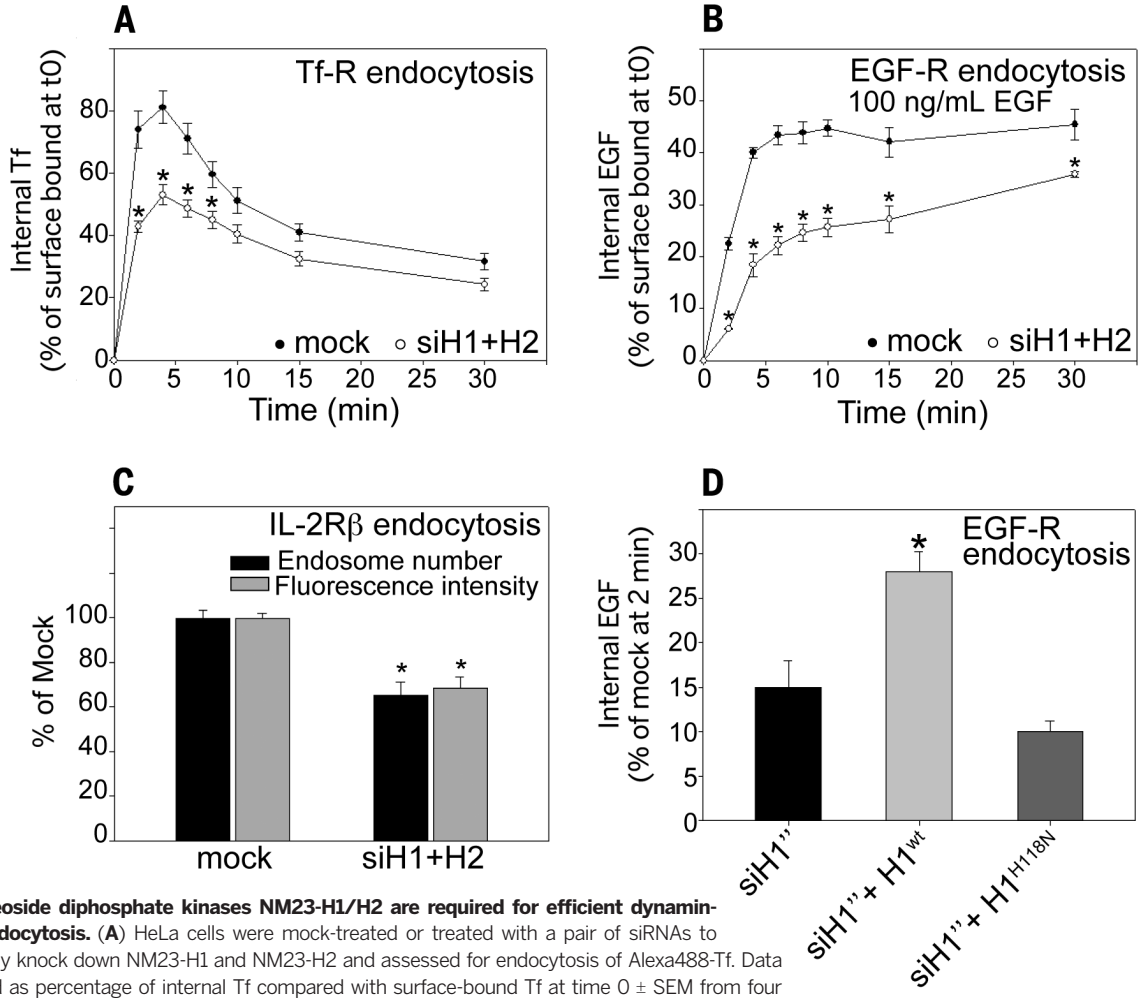

Fig. 1. Nucleoside diphosphate kinases NM23-H1/H2 are required for efficient dynamin-mediated endocytosis. (**A**) HeLa cells were mock-treated or treated with a pair of siRNAs to simultaneously knock down NM23-H1 and NM23-H2 and assessed for endocytosis of Alexa488-Tf. Data are expressed as percentage of internal Tf compared with surface-bound Tf at time 0 ± SEM from four independent experiments. **P* < 0.05 compared with mock-treated cells. (**B**) HeLa cells, either mock-treated or treated with NM23-H1/H2 siRNAs, were assessed for endocytosis of Alexa488-EGF (100 ng/ml). Data are expressed as percentage of internal EGF compared with surface-bound EGF at time 0 ± SEM from four independent experiments. **P* < 0.05 compared with mock-treated cells. (**C**) Hep2 cells stably expressing the interleukin-2 receptor β subunit (IL-2Rβ) were mock-treated or treated with siRNA for NM23-H1/H2 and incubated in the presence of Cy3-coupled antibody to IL-2Rβ for 5 min at 37°C. Data are expressed as average intracellular fluorescence intensity normalized to the intensity of mock-treated cells ± SEM and endosome number normalized to endosome number in mock-treated cells ± SEM. 100 cells were analyzed from three independent experiments. **P* < 0.05 compared with mock-treated cells. (**D**) HeLa cells mock-treated or treated with NM23-H1 siRNA were transfected with siRNA-resistant wild-type ($H1^{wt}$) or kinase-dead NM23-H1 ($H1^{H118N}$). EGF endocytosis after 2 min at 37°C was assessed as in (B). **P* < 0.05 compared with siH1''-treated cells.

(TIRF) microscopy analysis of cells labeled with antibody to NM23-H2 revealed the colocalization of NM23-H2 with AP-2 (α-adaptin) and dynamin-2 at CCPs (fig. S5, A to D), which was confirmed by means of proximity ligation assay (PLA), which showed a close proximity of NM23-H1/H2 with α-adaptin and dynamin-2 at CCPs (Fig. 2, H and I, and figs. S6 and S7). Furthermore, NM23-H1/H2 coimmunoprecipitated with dynamin-1 (Fig. 3A) and with dynamin-2 (Fig. 3B), and purified full-length recombinant NM23-H2 and dynamin-2 interacted directly in vitro (Fig. 3C). We investigated the contribution of the C-terminal proline-rich domain (PRD) of dynamin-2 to this interaction because this domain binds to several dynamin regulators and effectors (*18*). The dynamin-2 PRD domain fused to glutathione *S*-transferase (GST) pulled-down NM23-H1 and -H2, indicating that dynamin-2 physically interacts with both NM23-H1/H2 isoforms through its PRD (Fig. 3D). Thus, NM23-H1/H2 interact with endocytic dynamins at CCPs.

Next, we explored the role of NM23 NDPK activity in dynamin function. Whereas silencing of both NM23-H1 and -H2 isoforms caused a ~80% decrease of NDPK activity (fig. S8A), overall intracellular GTP levels were not affected by NM23 knockdown (fig. S8B) [nor were other nucleoside triphosphate levels affected (fig. S8C)]. Thus, decreased endocytic rate and increased CCP accumulation of NM23-depleted cells were not a consequence of a reduced bulk intracellular GTP concentration, but rather support a role of NM23-dynamin complexes in which NM23 generates GTP in the vicinity of dynamins to avoid a local drop in GTP/GDP ratio. Indeed, in the absence of added GTP and in the presence of NM23 substrates GDP (1 mM) and ATP (1 mM), catalytically active recombinant NM23-H1 and -H2 proteins triggered GTPase activity of dynamin-1 and -2 (Fig. 3E), whereas kinase-dead NM23-H1^{H118N} mutant did not (Fig. 3E). In the presence of nucleotide concentrations close to cellular levels—100 μM GTP, 10 μM GDP, and 1 mM ATP—NM23-H1 and -H2 were still able to enhance dynamin-1's GTPase activity by 30 to 35%, indicating that NM23 could stimulate dynamin activity further in the presence of physiological GTP level (Fig. 3F). This reflects the capacity of H1/H2 to directly provide GTP to dynamins within NM23/dynamin complexes.

Next, we monitored the capacity of NM23 to promote dynamin-mediated membrane fission in vitro. Classical dynamins can tubulate membrane sheets in the absence of GTP and then fragment the tubules depending on GTP hydrolysis (*6*). Dynamin-induced tubular networks remained stable in the presence of 1 mM ATP and 1 mM GDP and in the absence of NM23 (Fig. 3G and movie S1), and tubules were not altered by NM23-H1 or -H2 in the absence of nucleotides (Fig. 3G and movies S2 and S3, time 0). In contrast, in the presence of NM23, addition of 1 mM ATP and 1 mM GDP induced breakage and collapse of the tubule network (Fig. 3G and movies S2 and S3), with a fission density of 1 event per 8.3-μm tube length (n = 20 tubes). Most of the fission events occurred during the first 60 s after addition of ATP and GDP (fig. S9A). Immunogold electron microscopy (EM) on liposomes incubated in the presence of purified NM23-H2 and dynamin-1 revealed that NM23-H2 decorated the length of the membrane tubules (Fig. 3, H and I). In addition, EM of negatively stained preparations of membrane tubules confirmed the association of NM23-H2 to the surface of dynamin-1–coated tubules

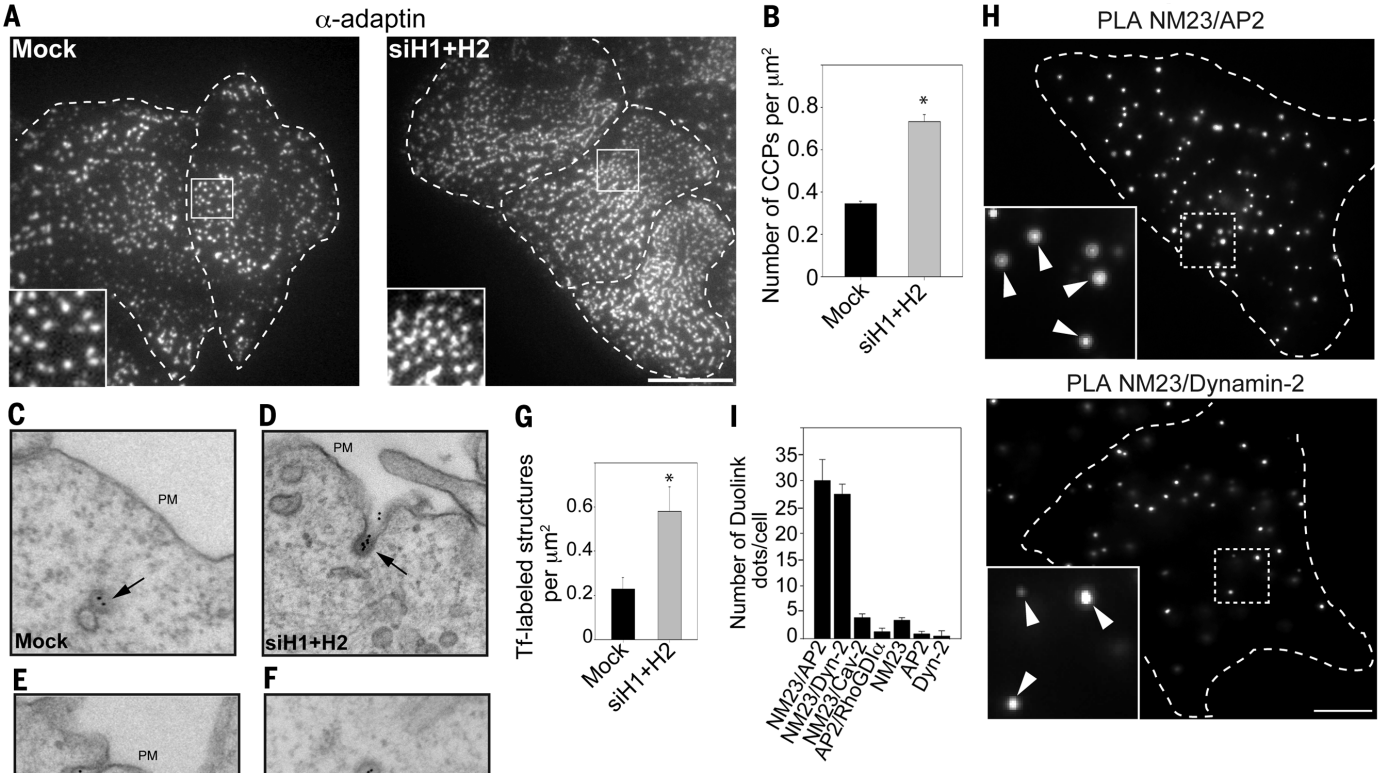

Fig. 2. Accumulation and tubulation of clathrin-coated pits in the absence of NM23-H1/H2. (**A** and **B**) AP-2 staining (α-adaptin) reveals higher CCP density in HeLa cells knocked down for NM23-H1/H2. Scale bar, 5 μm. Graph in (B) represents the mean CCP number/μm² ± SEM (n = 10 cells for each condition). *P < 0.05 compared with mock-treated cells. (**C** to **F**) HeLa cells mock-treated (C) or silenced for NM23-H1/H2 [(D) to (F)] were allowed to internalize Tf-Biotin for 4 min at 37°C and analyzed with electron microscopy by means of immunogold labeling with anti-Biotin antibodies and protein-A gold conjugates. Scale bar, 200 nm. (**G**) Number of Tf-positive structures (CCPs and vesicles)/μm² in a 1.9 μm-wide region, including the plasma membrane. *P < 0.05 compared with mock-treated cells. (**H**) PLA signal using combination of NM23 and AP-2 (α-adaptin) antibodies (top), or dynamin-2 antibodies (bottom). (Insets) Higher magnification of boxed regions. Scale bar, 5 μm. (**I**) Quantification of PLA dots per cell using different antibody pairs as indicated (mean ± SEM, n = 30 cells/condition from three independent experiments).

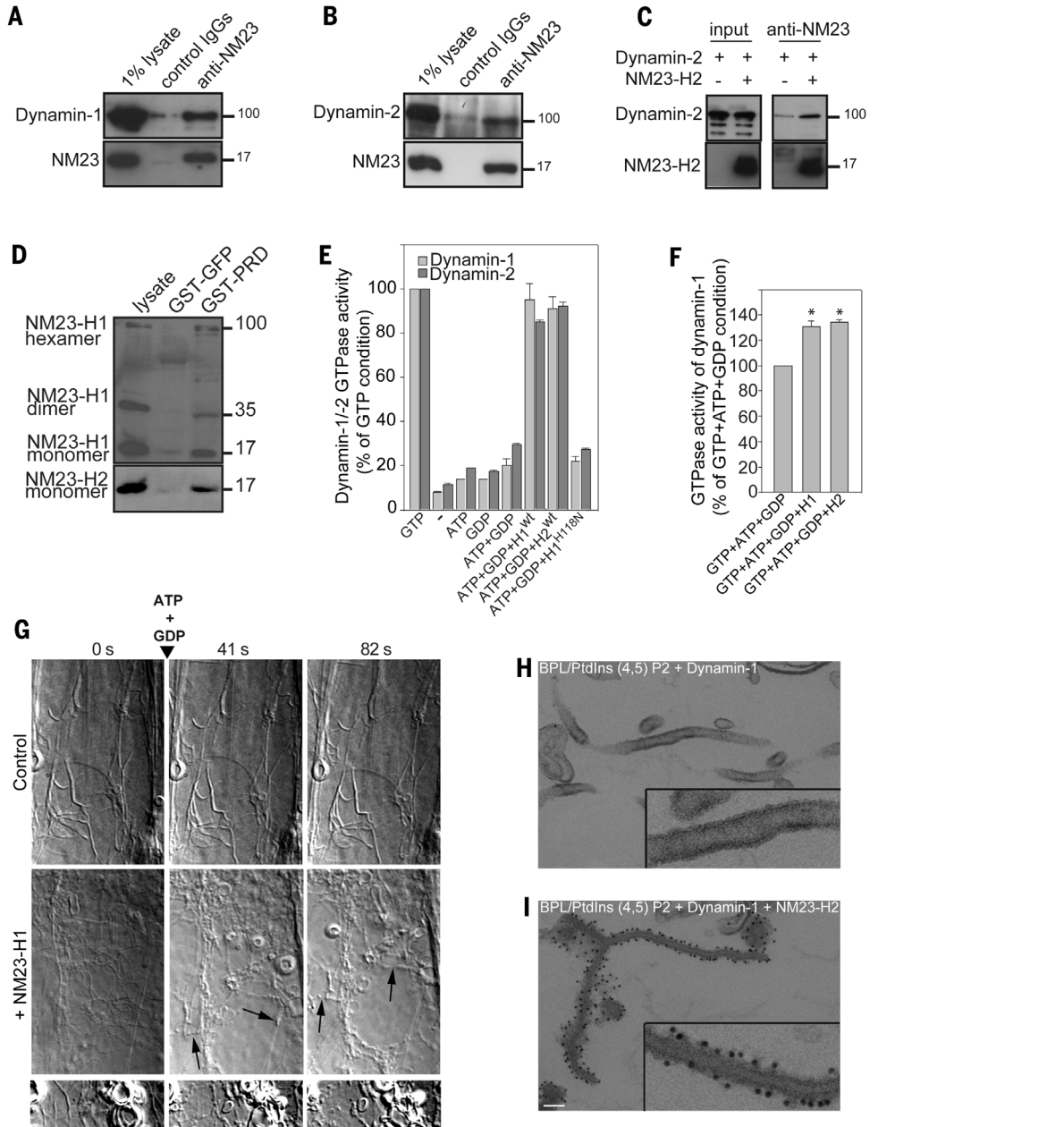

Fig. 3. NM23-H1/H2 promotes dynamin-mediated membrane fission by local GTP regeneration. (**A** and **B**) Lysates of (A) mouse brain or (B) HeLa cells immunoprecipitated with pan–NM23-H1/H2 antibodies and bound proteins analyzed with antibodies to dynamin-1 (A) and -dynamin-2 (B). One percent of total lysate was loaded as a control (input). (**C**) Purified recombinant human NM23-H2 and dynamin-2 were mixed and immunoprecipitated by using antibodies to NM23. Bound proteins were detected with dynamin-2 and NM23 antibodies as indicated. (**D**) Pull-down assays of NM23-H1/H2 from HeLa cell lysates with dynamin-2 GST-PRD or GST-GFP constructs. Bound proteins were detected with specific antibodies to NM23-H1 and -H2. Monomers and denaturation-resistant dimers and hexamers of NM23-H1 interact with dynamin-2 PRD domain. (**E**) GTPase activity of purified human dynamin-1 and -2 measured in the presence of 95% brain polar lipids (BPL)/5% PtdIns(4,5)P_2 liposomes, recombinant purified wild-type or catalytically dead (H118N) NM23-H1/H2 and nucleotides (1 mM) as indicated. Results are expressed as percentage of controls (1 mM GTP) from triplicate samples from four independent experiments. (**F**) GTPase activity of human dynamin-1 measured as in (E) in the absence or in the presence of NM23-H1 or -H2 and in the presence of physiological nucleotide concentrations (1 mM ATP, 100 μM GTP, and 10 μM GDP). Results are expressed as percent of control condition (ATP+GTP+GDP) from triplicate samples from two independent experiments. *$P < 0.05$ compared with control condition. (**G**) Selected frames from time-lapse sequences showing the effect of purified human NM23-H1/H2 on dynamin-induced membrane tubules after addition of 1 mM ATP and 1 mM GDP. Rat brain dynamin induces tubule formation from the 95% BPL/5% PtdIns (4,5) P_2 liposomes (time 0). Arrows point to tubule fission events in the presence of NM23-H1 or -H2. Representative frames from four independent experiments are shown. (**H** and **I**) Electron micrographs of liposomes incubated (H) with human dynamin-1 alone, which induced tubulation or (I) together with NM23-H2 and stained for NM23 by means of immunogold-labeling. (Insets) Higher magnification. Scale bar, 100 nm.

(fig. S9B). Thus, NM23 bound to membrane-associated dynamin affects dynamin function in membrane fission.

Given the efficiency of NM23-driven GTP supply to dynamins, we explored whether in another compartment, the mitochondria, mitochondrial NM23-H4 isoform was capable of supporting dynamin-related GTPase OPA1. In contrast to the typical tubular morphology of mitochondria in HeLa cells transfected with MitoDsRed, cells silenced for NM23-H4 showed abnormally fragmented and swollen mitochondria (Fig. 4, A and B). Depletion of NM23-H4 phenocopied the loss of OPA1 on mitochondrial morphology, whereas knockdown of NM23-H1/H2 did not alter mitochondrial morphology (Fig. 4, A and B). EM confirmed the severity of mitochondria alterations in NM23-H4–depleted cells (Fig. 4C), which is reminiscent of mitochondrial fusion defects as a result of OPA1 loss of function (*19*). Furthermore, immunofluorescence staining and PLA documented the colocalization and close proximity of NM23-H4 and OPA1 in mitochondria (Fig. 4D and fig. S10), which is in agreement with their reported interaction (*20*). To directly show the involvement of NM23-H4 in GTP fueling to OPA1, we determined the GTP hydrolysis rate of OPA1 reflecting GTP loading. Recombinant NM23-H4 triggered OPA1's GTPase activity in the presence of liposomes, mimicking the composition of the mitochondrial inner membrane (Fig. 4E). GTP loading on OPA1 was further increased by ~30% by NM23-H4 in the presence of native mitochondrial GTP concentration (Fig. 4F), which is similar to that observed for NM23-H1/H2 on classical dynamins (Fig. 3F).

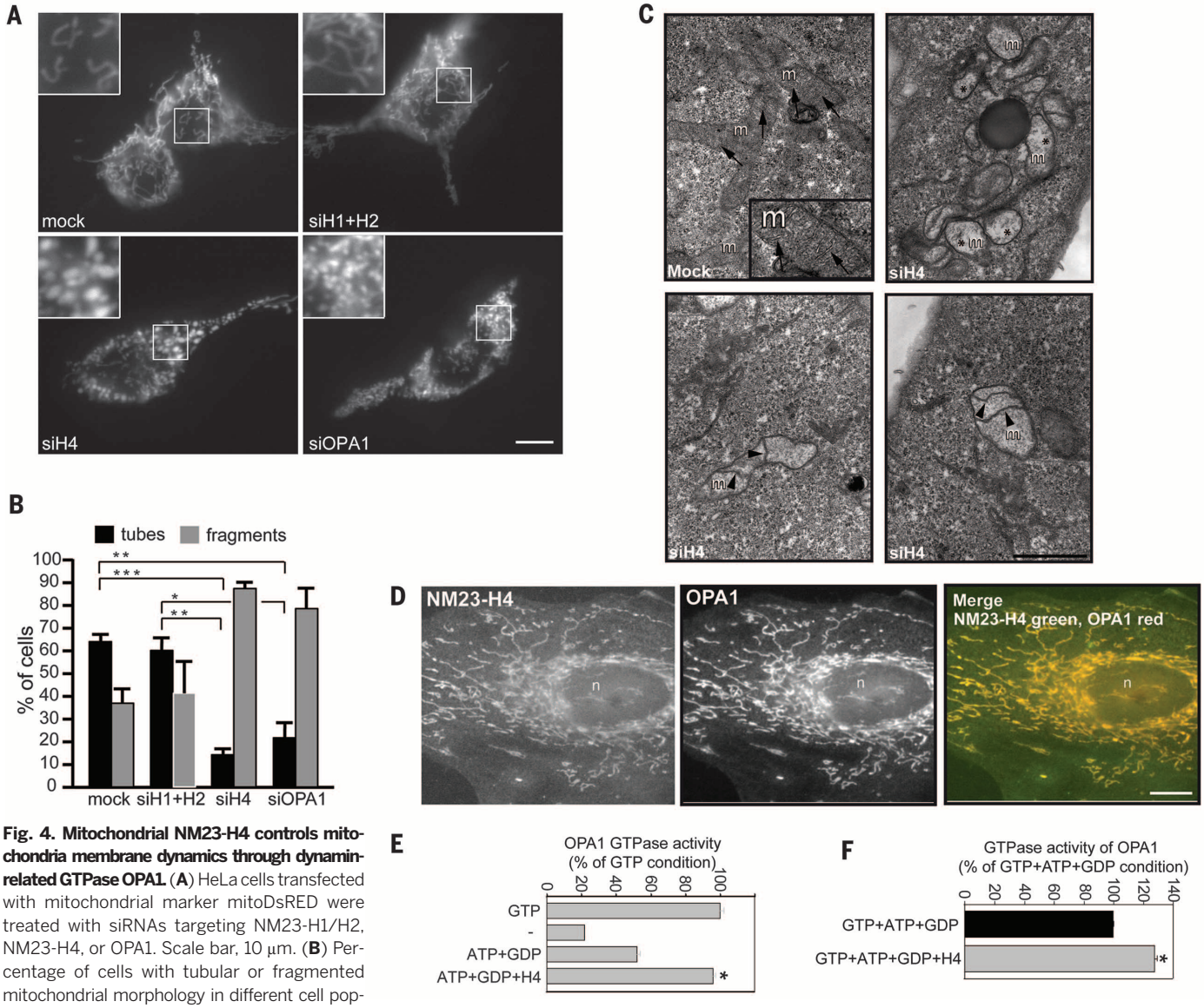

Fig. 4. Mitochondrial NM23-H4 controls mitochondria membrane dynamics through dynamin-related GTPase OPA1. (**A**) HeLa cells transfected with mitochondrial marker mitoDsRED were treated with siRNAs targeting NM23-H1/H2, NM23-H4, or OPA1. Scale bar, 10 μm. (**B**) Percentage of cells with tubular or fragmented mitochondrial morphology in different cell populations as in (A). Mean and SEM are shown for three independent experiments (>100 cells per experiment). ***$P < 0.001$; **$P < 0.01$; *$P < 0.05$. (**C**) EM of HeLa cells silenced for NM23-H4, showing alterations of mitochondrial morphology as compared with that in mock-treated cells. Arrows point to mitochondrial cristae in mock-treated cells. Asterisks indicate mitochondria with loss of cristae and electron-lucent matrix in cells knocked down for NM23-H4. Arrowheads point to internal septae, which appear to divide the inner membrane compartment in H4-KD cells. Scale bar, 1 μm. (**D**) Colocalization of NM23-H4 and OPA1 in mitochondria in HeLa cells. Scale bar, 10 μm. (**E**) GTPase activity of purified recombinant human OPA1 measured in the presence of 25% cardiolipin-enriched liposomes and purified NM23-H4 as in Fig. 3E. Results are expressed as percentage of control condition (1 mM GTP) from three independent experiments. *$P < 0.05$ compared with the ATP+GDP condition. (**F**) GTPase activity of human OPA1 in the presence of cardiolipin-enriched liposomes and NM23-H4 measured in the presence of physiological mitochondrial nucleotide concentration (1 mM ATP, 100 μM GTP, and 10 μM GDP). Results are expressed as percent of control (ATP+GTP+GDP) from duplicate samples from two independent experiments. *$P < 0.05$ compared with the control condition.

We have shown that members of the NM23/NDPK family interact directly and specifically with members of the dynamin superfamily and thus are positioned to maintain high local GTP concentrations and promote dynamin-dependent membrane remodeling. The role of NM23 is well supported by their high NDPK turnover number [k_{cat} 600 s^{-1} per active site (*21*)]. Furthermore, the localization of the NM23-H3 isoform at the mitochondrial outer membrane (fig. S11), where dynamin Drp1 is recruited to mediate mitochondrial fission, suggests that NM23-H3 could assist Drp1 in this process. These findings identify a general mechanism by which different NDPKs maintain high GTP concentration to high-turnover GTPase dynamins for efficient work in different membrane compartments.

REFERENCES AND NOTES

1. S. M. Ferguson, P. De Camilli, *Nat. Rev. Mol. Cell Biol.* **13**, 75–88 (2012).
2. S. L. Schmid, V. A. Frolov, *Annu. Rev. Cell Dev. Biol.* **27**, 79–105 (2011).
3. J. E. Hinshaw, S. L. Schmid, *Nature* **374**, 190–192 (1995).
4. K. Takei, P. S. McPherson, S. L. Schmid, P. De Camilli, *Nature* **374**, 186–190 (1995).
5. S. M. Sweitzer, J. E. Hinshaw, *Cell* **93**, 1021–1029 (1998).
6. A. Roux, K. Uyhazi, A. Frost, P. De Camilli, *Nature* **441**, 528–531 (2006).
7. S. Morlot *et al.*, *Cell* **151**, 619–629 (2012).
8. D. D. Binns *et al.*, *Biochemistry* **39**, 7188–7196 (2000).
9. B. Marks *et al.*, *Nature* **410**, 231–235 (2001).
10. K. S. Krishnan *et al.*, *Neuron* **30**, 197–210 (2001).
11. V. Dammai, B. Adryan, K. R. Lavenburg, T. Hsu, *Genes Dev.* **17**, 2812–2824 (2003).
12. G. Nallamothu, J. A. Woolworth, V. Dammai, T. Hsu, *Mol. Cell. Biol.* **28**, 1964–1973 (2008).
13. M. Boissan *et al.*, *Mol. Cell. Biochem.* **329**, 51–62 (2009).
14. L. Milon *et al.*, *J. Biol. Chem.* **275**, 14264–14272 (2000).
15. M. Tokarska-Schlattner *et al.*, *J. Biol. Chem.* **283**, 26198–26207 (2008).
16. A. M. van der Bliek, Q. Shen, S. Kawajiri, *Cold Spring Harb. Perspect. Biol.* **5**, a011072 (2013).
17. S. M. Ferguson *et al.*, *Dev. Cell* **17**, 811–822 (2009).
18. G. J. Praefcke, H. T. McMahon, *Nat. Rev. Mol. Cell Biol.* **5**, 133–147 (2004).
19. L. Griparic, N. N. van der Wel, I. J. Orozco, P. J. Peters, A. M. van der Bliek, *J. Biol. Chem.* **279**, 18792–18798 (2004).
20. U. Schlattner *et al.*, *J. Biol. Chem.* **288**, 111–121 (2013).
21. I. Lascu *et al.*, *J. Biol. Chem.* **272**, 15599–15602 (1997).

ACKNOWLEDGMENTS

We thank P. De Camilli, E. Smythe, and J. Bertoglio for reagents; S. L. Schmid and M. Mettlen for discussion; the Nikon Imaging Center@Institut Curie & Centre National de la Recherche Scientifique (CNRS) for image acquisition; and I. Hurbain for EM quantification. This work was supported by Institut Curie, CNRS, Fondation ARC pour la Recherche sur le Cancer, Groupement des Entreprises Françaises contre le Cancer, Fondation pour la Recherche Médicale, the Human Frontier Science Program, the Swiss National Fund for Research Grant, and the European Research Council.

SUPPLEMENTARY MATERIALS

www.sciencemag.org/content/344/6191/1510/suppl/DC1
Materials and Methods
Supplementary Text
Figs. S1 to S11
References (*22*–*33*)
Movies S1 to S3

24 March 2014; accepted 5 June 2014
10.1126/science.1253768

SENSORY BIOLOGY

Flower discrimination by pollinators in a dynamic chemical environment

Jeffrey A. Riffell,[1]* Eli Shlizerman,[2] Elischa Sanders,[1] Leif Abrell,[3] Billie Medina,[1] Armin J. Hinterwirth,[1] J. Nathan Kutz[2]

Pollinators use their sense of smell to locate flowers from long distances, but little is known about how they are able to discriminate their target odor from a mélange of other natural and anthropogenic odors. Here, we measured the plume from *Datura wrightii* flowers, a nectar resource for *Manduca sexta* moths, and show that the scent was dynamic and rapidly embedded among background odors. The moth's ability to track the odor was dependent on the background and odor frequency. By influencing the balance of excitation and inhibition in the antennal lobe, background odors altered the neuronal representation of the target odor and the ability of the moth to track the plume. These results show that the mix of odors present in the environment influences the pollinator's olfactory ability.

The olfactory environment is complex and rich, filled with natural, biogenically emitted volatile compounds (volatiles) and closely related volatiles from anthropogenic sources, such as those from combustion engines (*1*–*4*). Insects must successfully discriminate and locate biologically important scents, such as those emitted by food, mates, or hosts, from within this complex mixture (*5*–*8*). How does the insect olfactory system accomplish this task? Our understanding of these effects has been hampered by an inability to measure natural scents at time scales experienced by insects in nature and to link this information with an understanding of how the brain discriminates olfactory stimuli from the background odor landscape.

In the southwest USA, the *Manduca sexta* (hereafter, *Manduca*) moth navigates to, and pollinates, *Datura wrightii* flowers that are separated by hundreds of meters (*9*–*11*). *D. wrightii* (hereafter, *Datura*) often grow in dense stands of creosote bush (*Larrea tridentata*), which emit a high-intensity odor (>100 mg/h) that includes some of the same aromatic volatiles (e.g., benzaldehyde) as the scent of *Datura* (*9*, *12*).

A proton transfer–reaction mass spectrometer, which enables simultaneous measurement of multiple volatiles at subsecond time scales, allowed us to measure the scent plume from *Datura* flowers and characterize its dynamics (Fig. 1A). Measurement of ions from oxygenated aromatics (ARs, e.g., benzaldehyde) and monoterpenes (MOs, linalool and geraniol) showed that the floral plume increased in frequency and decreased in intermittency with increasing distance from the flower (Fig. 1, A to C). The ratio of volatiles in the plume also changed as the background volatiles from neighboring vegetation, including creosote bush plants, became intermixed with the plume (Fig. 1, D and E).

To determine how the changing frequency of the target odor influenced the moth's ability to locate the flower, we used a wind tunnel and a computer-controlled odor-stimulus system to test the moths' response to the *Datura* mixture at different frequencies (1 to 20 Hz) and embedded in different backgrounds [figs. S1 and S2; table S1; see supplementary materials (SM) for details]. Compared with the responses to a mineral oil (no-odor) control, moths exhibited the strongest response to odor pulses of 1 Hz (Fig. 2A_1) (2×2 χ^2 test, $P < 0.001$). However, frequencies higher than 1 to 2 Hz resulted in behavior similar to that displayed in response to the no-odor controls (Fig. 2, A_2 and B) (2×2 χ^2 test, $P > 0.33$).

We next tested the moths' ability to track the flower-odor plume at a frequency of 1 Hz among a background of different odors, ranging from volatiles that do not occur in the *Datura* mixture [nonoverlapping, ethyl sorbate] to those that do: for instance, (i) volatiles that occur in the flower odor and thereby change the constituent ratio (e.g., benzaldehyde) and (ii) the complex odor background of creosote bush (*L. tridentata*) that also shares volatiles with *Datura*. The volatile background significantly modified the moth's odor-tracking ability (Fig. 2, C and D). For example, when exposed to the *Datura* plume with a background of ethyl sorbate [a volatile that is not in the *Datura* floral odor and chemically dissimilar to constituents of the *Datura* mixture (*10*)], moths navigated to and located the odor source (Fig. 2, C_1 and D) (2×2 χ^2 test, $P < 0.001$). By contrast, when challenged with the *Datura* plume in a background of benzaldehyde (a volatile in creosote bush and *Datura* scents), the moth's ability to correctly navigate to the odor significantly decreased (Fig. 2C_2) (2×2 χ^2 test relative to *Datura* mixture, $P < 0.01$; χ^2 test relative to no odor control, $P = 0.44$). Similar results occurred

[1]Department of Biology, University of Washington, Seattle, WA 98195–1800, USA. [2]Department of Applied Mathematics, University of Washington, Seattle, WA 98195–3925, USA. [3]Department of Chemistry and Biochemistry and Department of Soil, Water, and Environmental Science, University of Arizona, AZ 85721–0077, USA
*Corresponding author. E-mail: jriffell@u.washington.edu

when the moth was exposed to the plume in the background of geraniol [a volatile that elicits strong antennal lobe (AL) responses (*13*)] or the complex creosote bush scent (Fig. 2D). Thus, altering the background can significantly modify the ability of the moth to discriminate and track the odor.

Neurons on the moth's antennae and in the AL, which is the site of combinatorial processing of olfactory information in the insect brain, are extremely sensitive to the *Datura* mixture (*13*, *14*). We investigated how peripheral and AL neurons processed the *Datura* mixture at different frequencies and how the volatile background modified the representation of the floral scent. Peripheral recordings from the moth's antennae showed that antennal responses were not modified when a background was presented simultaneously with the *Datura* mixture (fig. S3). We next examined whether the downstream AL neurons changed their activity in response to different odor frequencies and backgrounds. Inserting a 16-channel electrode into the moth's AL allowed recordings of neural ensemble activity in response to pulsed and background odor stimuli (Fig. 3A). Similar to the behavioral response, results at both the level of the single neuron and neuronal population showed that the greatest pulse-tracking occurred at a frequency of 1 Hz (fig. S4) (Kruskal-Wallis test, $P < 0.0001$), with higher frequencies not statistically different from the no-odor control (Fig. 3B and figs. S4 and S5) (Kruskal-Wallis test, $P > 0.05$). Similar results occurred when 1-Hz pulses of the *Datura* mixture were presented simultaneously with a background of benzaldehyde [Fig. 3B (middle trace) and fig. S6].

To gain further insight into how the neuronal population represented the odor, as well as how the frequency and background influenced perception, we used an odor-recognition classifier based on the *Datura* representation in the multivariate space (Fig. 3C and fig. S7; tables S2 and S3; see SM for details). In the multivariate space, when the dynamical trajectory representing the neural population responses reaches the prescribed neighborhood of the *Datura* representation, it is counted as evidence, or "recognition" of the given stimulus. We thus were able to compare the recognition scores between the *Datura* mixture at 1 Hz with the *Datura* mixture in different backgrounds or frequencies (Fig. 3C). This analysis showed similar results to those in the behavioral experiments: High odor frequencies (>5 Hz) and certain backgrounds (e.g., benzaldehyde) significantly modified the representation of the *Datura* mixture, which altered the perception of the flower (Fig. 3, D and E).

In addition to the interference caused by the plant volatile background, other volatiles could potentially modify the AL representation of the flower odor, including those that are commonly anthropogenic in origin such as toluene and *p*-xylene, which are chemically similar to benzaldehyde. We examined these effects by using volatile backgrounds at intensities equivalent to those found in urban environments (*1*, *2*) (fig. S2). Experiments showed that toluene and xylene elicited strong antennal responses and activated the same olfactory sensory neurons that responded to benzaldehyde and the *Datura* and creosote bush odors (fig. S8, A to F). Both volatiles influenced the AL representation of the *Datura* mixture (fig. S8, G to I) and significantly decreased the moth's ability to locate the *Datura* flower (fig. S8, J and K). When the moths were preexposed to the odor for 3 hours before testing, these results were exacerbated because of adaptation of these same olfactory "channels." Thus, biogenically or anthropogenically produced volatiles both play important roles in navigation by *Manduca* moths.

Inhibition in the AL is mediated by local interneurons that release γ-aminobutyric acid (GABA) onto projection neurons (PNs), and plays a profound role in odor representation and encoding odor pulses (*15*–*17*). To determine how altering the odor input into the AL (i.e., the composition and ratio of volatiles) also modified the balance of excitation and inhibition, we pharmacologically manipulated the inhibition by superfusing a GABA-receptor antagonist (50 μM CGP54626)

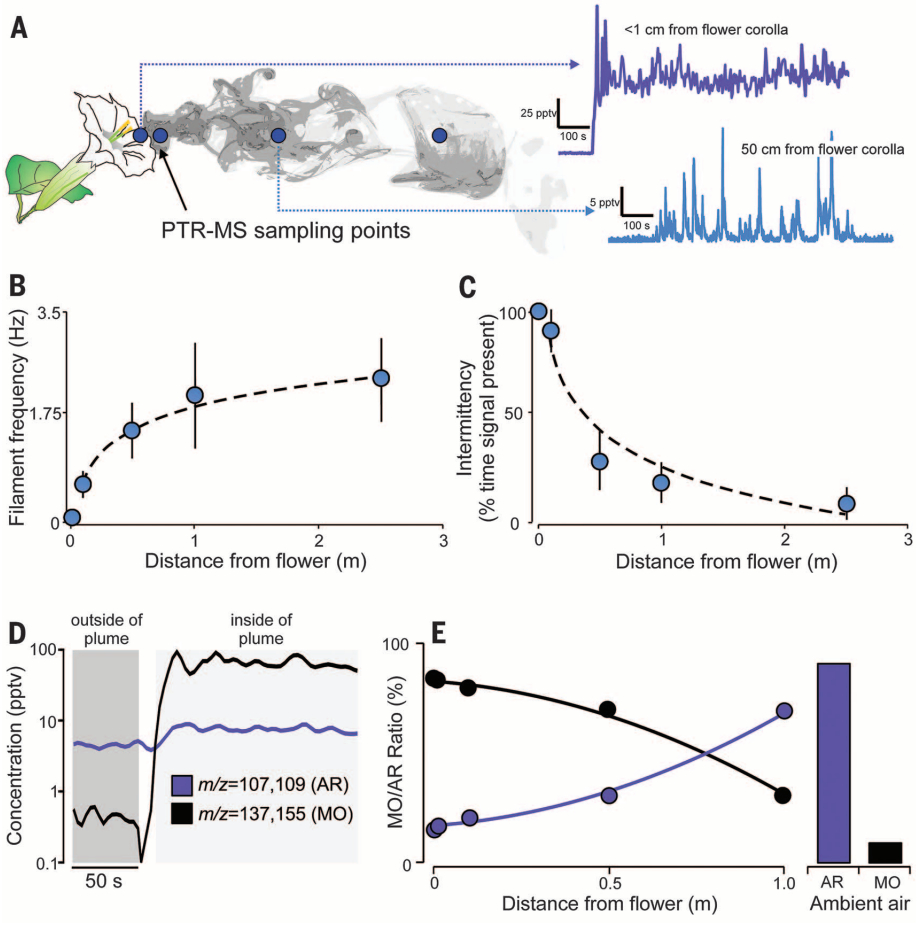

Fig. 1. The plume dynamics of a flower scent. (**A**) Single-ion monitoring (m/z = 137) from the *Datura* flower. (**B**) Odor frequency with increasing distance from the flower. (**C**) Intermittency (percent of time present) with increasing distance from the flower. Each symbol is the mean ± SEM; lines are the fitted regressions ($R^2 > 0.75$, $P < 0.001$). (**D**) Ions indicative of ARs (blue line) and monoterpenoids (black line) 1 cm from the flower. (**E**) (Left) Scatter plot showing the ratio of the percentage of monoterpene (black) and aromatic (blue) ions with increasing distance from the flower. Each symbol is the mean ± SEM; lines are the regressions (R^2 = 0.88, $P < 0.001$). (Right) The ions measured in the ambient environment outside of the plume.

onto the preparation during our experiments. When the vehicle control (saline) was superfused on the AL, neurons typically showed an excitatory response that was time-locked to the duration of the stimulus (Fig. 4A). By contrast, when the GABA-receptor antagonist was superfused, neurons showed a decreased ability to encode the pulses of odor, and the odor representation was significantly modified in a manner similar to that which occurred with the benzaldehyde background [Fig. 4, A (middle trace) and B]. These results were further validated by a computational model that allowed us to simulate different levels of inhibition in the AL (*18*): Decreasing inhibition by ~50% produced results similar to those of the *Datura* mixture embedded in benzaldehyde or those when the GABA antagonist was superfused on the preparation, which suggested a correlation between modifying the odor composition and modulation of the inhibitory circuitry (Fig. 4B and figs. S9 to S11).

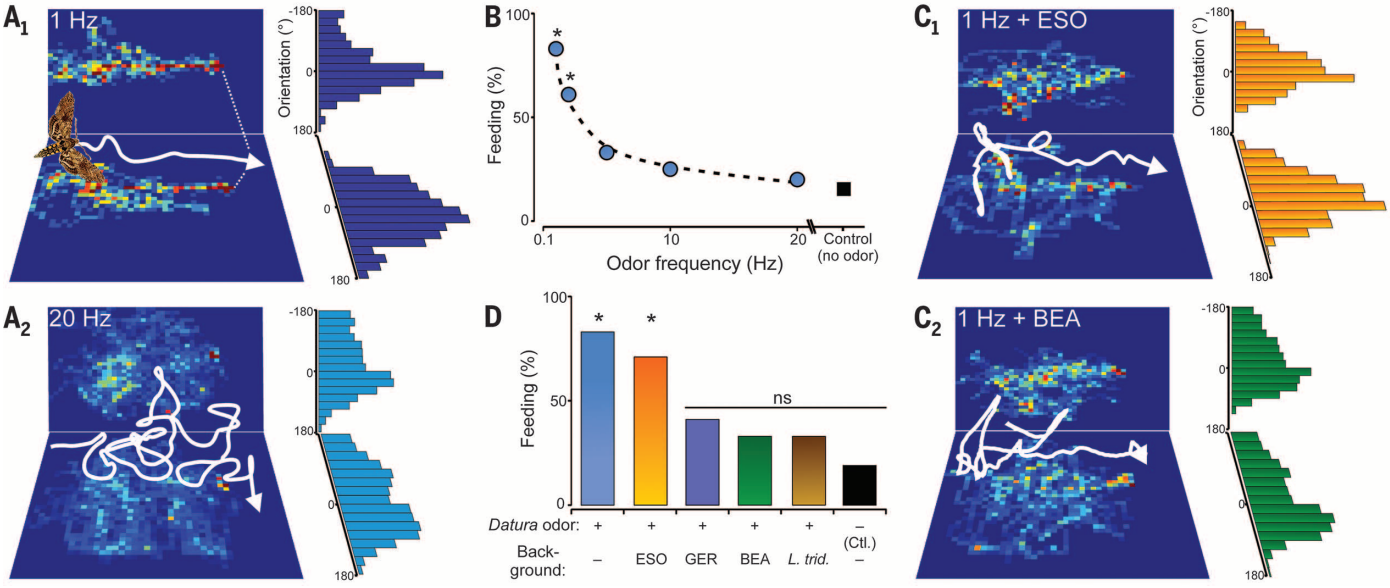

Fig. 2. Flower odor intermittency and background significantly modify moth behavior. (**A**) Flight tracks of moths navigating to an odor plume (white track) pulsed at 1 Hz (A_1) and 20 Hz (A_2). Moth trajectories were plotted as a transit probability plots in the *x*-*y* and *x*-*z* dimensions (left); orientations to the odor (0° origin) are shown as a track-angle distribution (right). (**B**) Increasing odor frequency caused a significant decrease in odor navigation and feeding (regression: $R^2 = 0.97$, $P < 0.01$) to levels not significantly different from control ($2 \times 2\ \chi^2$ test: $P > 0.48$). (**C**) Moth flight tracks to the *Datura* mixture embedded in different backgrounds [C_1: ethyl sorbate (ESO); C_2: benzaldehyde (BEA)]. (**D**) The percentage of moths that successfully navigated to the *Datura* mixture embedded in different backgrounds (N = 20 to 40 moths per treatment). ns indicates not significantly different from control ($P > 0.12$); *$P < 0.001$.

Fig. 3. Antennal-lobe neuronal response to *Datura* mixture at different frequencies and backgrounds. (**A**) Depiction of *Manduca* preparation and the odor delivery system (*Datura* mixture and background stimuli were presented by two solenoid valves). (**B**) Peristimulus time histogram (PSTH) of a single neuron response (B_1) to different stimuli (mean ± SEM from five stimulations). Rasters are plotted below the PSTHs. (B_2) Neural population response. Relative to the 1 Hz frequency, there was significant attenuation in response at the 20 Hz frequency and the BEA background (Kruskal-Wallis test: $P < 0.05$). (**C**) On the basis of the neural population response (10 preparations; N = 153 neurons) to the components in the *Datura* mixture [BEA and benzyl alcohol (BOL)] and 1-Hz pulses of the *Datura* mixture, a recognition region was calculated that describes the area that the trajectory returns to over the course of repeated stimulations. (**D** and **E**) Recognition scores computed as the percentage of time the trajectory spent in the *Datura* mixture recognition region. Increasing the odor frequency (D), or changing the background (E), caused a significant decrease in the recognition scores to levels approaching the control. Background volatiles included ESO, geraniol (GER), and BEA. Line is the regression fit ($R^2 = 0.91$, $P < 0.05$); asterisks denote responses significantly greater than control (Kruskal-Wallis test: $P < 0.05$).

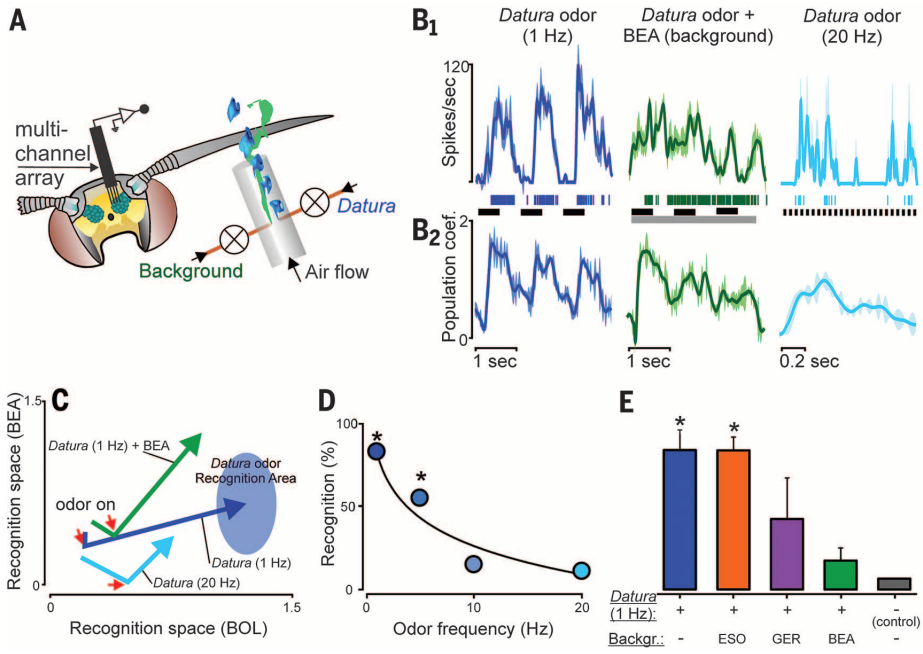

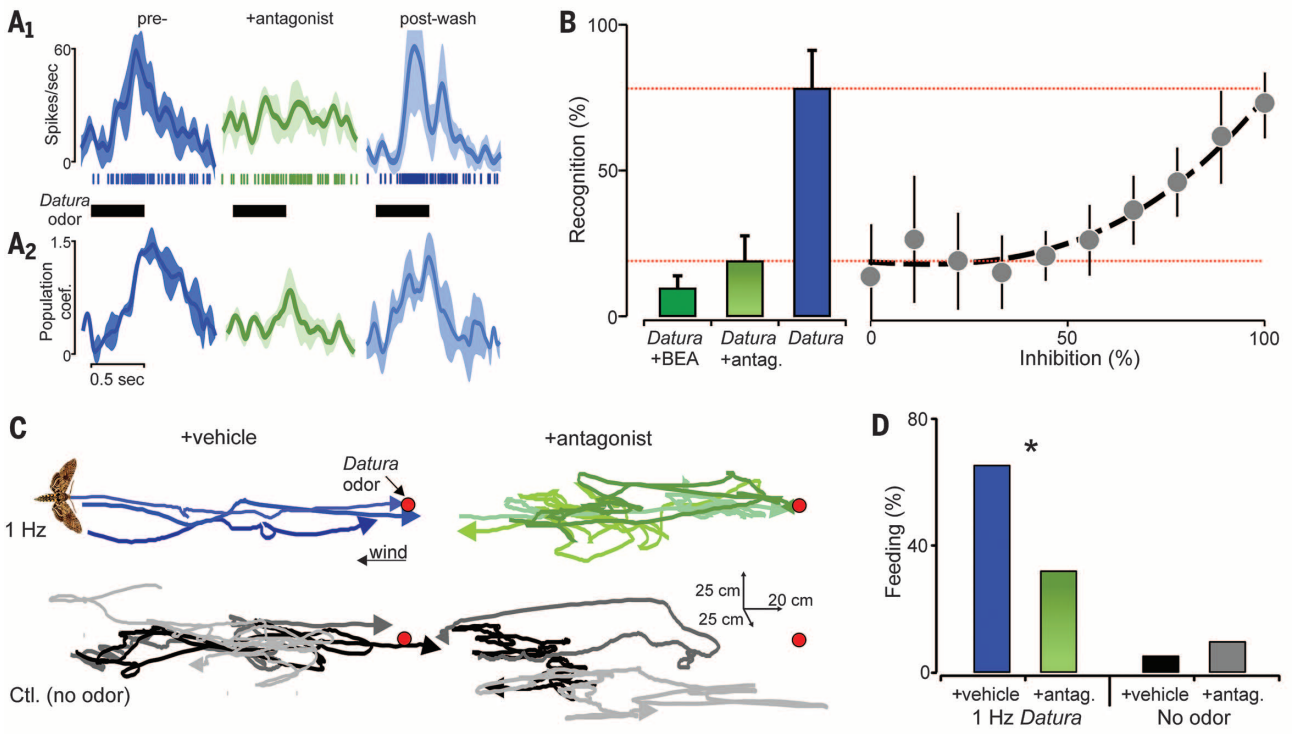

Fig. 4. The effects of inhibition in encoding the odor plume. (**A**) (A_1) PSTHs of a single neuron response and (A_2) population response (12 preparations, $N = 172$ neurons) to the *Datura* mixture (left, blue). Superfusion of the GABA receptor antagonist, (middle, green line), modifies the response to the *Datura* mixture relative to the pre- and postantagonist controls (left and right blue lines; paired *t* tests: $P < 0.05$). Rasters are plotted below the PSTHs; PSTHs are the average ± SEM of five stimulations. (**B**) The recognition scores for the recorded responses (left) in comparison with the model simulated under decreasing inhibition (right). Red lines denote the upper and lower bounds of the experimental manipulations of inhibition. (**C**) Behavioral flight tracks of saline- (left, blue lines) and antagonist-injected moths (right, green lines) to the *Datura* mixture or control (bottom, grey lines). (**D**) Percentage of moths that attempted to feed from the odor source. Asterisks denote a significant difference between saline- (blue bars) and antagonist-injected (green bars) moths (2×2 χ^2-test: $P < 0.05$). Each bar represents 20 to 30 moths.

Modification of the levels of excitation and inhibition in the AL need not indicate that odor navigation is altered or that moths are unable to locate flowers. Thus, we performed wind-tunnel experiments with moths that had either saline (vehicle control) or the GABA-receptor antagonist (CGP54626) microinjected into their ALs. Saline-injected moths navigated to the *Datura* mixture at a stimulus frequency of 1 Hz (Fig. 4, C and D). By contrast, antagonist-injected moths exhibited increased frequencies of cross-wind casting and a lower percentage of moths navigating to the odor (Figs. 4, C and D; fig. S11, C and D). Taken together, these results support the hypothesis that modifying AL inhibition severely alters the perception of the odor and disrupts the moth's ability to successfully navigate to the plume.

Together, our results show that the olfactory background can have important effects on the moth's ability to locate an odor source. At the neuronal level, odor backgrounds affect the ability of neurons to track the odor frequency and interfere with the odor representation through the alteration of the balance of excitation and inhibition. Our results have implications for ecological interactions among plants and their pollinators at the level of the individual flower, where the visual and morphological displays might offset the change of the odor (*19*). Additionally, these results have implications locally, where the plant community might have strong, indirect effects on the distances at which pollinators can recognize certain flowers (*6*, *20*), and, potentially, at larger scales because of the transport of volatiles from urban environments (*21*, *22*).

REFERENCES AND NOTES

1. A. Dorsey, P. McClure, A. McDonald, M. Singh, *Toxicological Profile for Toluene* (U.S. Department of Health and Human Services, Washington, DC, 2000).
2. D. Helmig, J. Arey, *Sci. Total Environ.* **112**, 233–250 (1992).
3. A. Herrmann, *The Chemistry and Biology of Volatiles* (Wiley Online Library, New York, 2010).
4. J. A. Riffell, L. Abrell, J. G. Hildebrand, *J. Chem. Ecol.* **34**, 837–853 (2008).
5. J. Murlis, J. S. Elkinton, R. T. Cardé, *Annu. Rev. Entomol.* **37**, 505–532 (1992).
6. R. Schröder, M. Hilker, *Bioscience* **58**, 308–316 (2008).
7. N. J. Vickers, T. A. Christensen, T. C. Baker, J. G. Hildebrand, *Nature* **410**, 466–470 (2001).
8. R. K. Zimmer, C. A. Zimmer, *J. Chem. Ecol.* **34**, 822–836 (2008).
9. R. A. Raguso, C. Henzel, S. L. Buchmann, G. P. Nabhan, *Int. J. Plant Sci.* **164**, 877–892 (2003).
10. J. A. Riffell *et al.*, *Proc. Natl. Acad. Sci. U.S.A.* **105**, 3404–3409 (2008).
11. R. E. Stockhouse II, *Am. Midl. Nat.* **96**, 241–245 (1976).
12. K. Jardine *et al.*, *Atmos. Chem. Phys.* **10**, 12191–12206 (2010).
13. J. A. Riffell, H. Lei, T. A. Christensen, J. G. Hildebrand, *Curr. Biol.* **19**, 335–340 (2009).
14. J. A. Riffell, H. Lei, L. Abrell, J. G. Hildebrand, *Science* **339**, 200–204 (2013).
15. T. A. Christensen, B. R. Waldrop, J. G. Hildebrand, *J. Neurosci.* **18**, 5999–6008 (1998).
16. T. Heinbockel, T. A. Christensen, J. G. Hildebrand, *J. Comp. Neurol.* **409**, 1–12 (1999).
17. S. R. Olsen, R. I. Wilson, *Nature* **452**, 956–960 (2008).
18. E. Shlizerman, J. A. Riffell, J. N. Kutz, *Front. Comput. Neurosci.*, in press; preprint available at http://arxiv.org/abs/1311.7450.
19. A. S. Leonard, A. Dornhaus, D. R. Papaj, *J. Exp. Biol.* **214**, 113–121 (2011).
20. D. Thiery, J. Visser, *Entomol. Exp. Appl.* **41**, 165–172 (1986).
21. R. D. Girling, I. Lusebrink, E. Farthing, T. A. Newman, G. M. Poppy, *Sci. Rep.* **3**, 2779 (2013).
22. R. A. Field, M. E. Goldstone, J. N. Lester, R. Perry, *Atmos. Environ. A-Gen.* **26**, 2983–2996 (1992).

ACKNOWLEDGMENTS

The authors thank B. Nguyen, W. Chan, K. Jardine, and J. Thornton for their assistance. This work was supported by funds from the University of Washington (J.A.R.). The electrophysiology data reported in this paper are tabulated in the supplementary materials (database S1).

SUPPLEMENTARY MATERIALS

www.sciencemag.org/content/344/6191/1515/suppl/DC1
Materials and Methods
Figs. S1 to S12
Tables S1 to S3
References (*23*–*47*)
Database S1

20 January 2014; accepted 22 May 2014
10.1126/science.1251041

MICROBIAL EVOLUTION

Global epistasis makes adaptation predictable despite sequence-level stochasticity

Sergey Kryazhimskiy,[1,3]*† Daniel P. Rice,[1,3]* Elizabeth R. Jerison,[2,3] Michael M. Desai[1,2,3]†

Epistatic interactions between mutations can make evolutionary trajectories contingent on the chance occurrence of initial mutations. We used experimental evolution in *Saccharomyces cerevisiae* to quantify this contingency, finding differences in adaptability among 64 closely related genotypes. Despite these differences, sequencing of 104 evolved clones showed that initial genotype did not constrain future mutational trajectories. Instead, reconstructed combinations of mutations revealed a pattern of diminishing-returns epistasis: Beneficial mutations have consistently smaller effects in fitter backgrounds. Taken together, these results show that beneficial mutations affecting a variety of biological processes are globally coupled; they interact strongly, but only through their combined effect on fitness. As a consequence, fitness evolution follows a predictable trajectory even though sequence-level adaptation is stochastic.

Epistatic interactions between mutations are pervasive in microbial and viral systems (*1*–*6*). In some cases, a single mutation can open up previously unavailable opportunities for a population to colonize a new metabolic niche (*2*) or survive in a previously intolerable drug concentration (*3*). Such idiosyncratic epistasis makes evolutionary trajectories dependent on the chance occurrence of initial mutations that constrain or potentiate future adaptation. This historical contingency can render adaptation fundamentally unpredictable (*7*). However, recent work has also provided evidence for more systematic patterns of epistasis (*8*–*10*), which can drive convergent phenotypic evolution (*11*–*13*) or can lead to parallel adaptation at the sequence level (*14*). These observations suggest that evolutionary outcomes may be statistically predictable if mutations causing idiosyncratic changes in adaptability are rare, and if epistasis instead channels evolution into convergent phenotypic or genotypic pathways.

To test how epistasis and historical contingency affect the predictability of adaptation, we conducted a hierarchical laboratory evolution experiment in *S. cerevisiae* (fig. S1). In the first phase of the experiment ("diversification"), we created 432 independent lines from a single haploid clone (the diversification ancestor, DivAnc) isolated from an earlier long-term evolution experiment (*15*). We evolved each line independently, half at large and half at small population size, in rich media in 96-well microplates for 240 generations (*16*). We then selected 64 clones ("founders"), each from a different line, chosen to span a range of fitness relative to the DivAnc (*16*) (table S1). Founders differed from the DivAnc by 4.2 mutations on average (*16*). In the second phase of the experiment ("adaptation"), we founded 10 independent replicate populations with each founder and then allowed each of the resulting 640 lines to adapt at large population size for 500 generations. This enabled us to compare variation among lines descended from the same founder (which reflects the inherent stochasticity of evolution) to variation between lines descended from different founders, thereby providing an assessment of the extent to which genetic background influences evolution.

The competitive fitness of each population after 250 and 500 generations of the adaptation phase increased on average by 3.3% and 6.6%, respectively (Fig. 1A and table S2). However, not all populations adapted at the same rate. Instead, the initially large variation in fitness between lines declined with time (Fig. 1A). We carried out an analysis of variance (ANOVA) to partition observed variance in fitness increase during the adaptation phase into contributions from measurement noise, inherent stochasticity of the evolutionary process, and the identity of the founder (*16*, *17*). After 250 generations of adaptation, 49% of the variance in fitness increment was attributed to inherent evolutionary stochasticity, 17% to measurement error, and 34% to founder identity; after 500 generations, 29% of the variance in fitness increment was attributed to inherent stochasticity, 21% to measurement error, and 50% to founder identity (Fig. 1B and table S3). This demonstrates that genetic background is a key determinant of how rapidly a population will adapt.

These differences in adaptability are not random: Populations with lower initial fitness systematically adapt more rapidly than populations with higher initial fitness, driving the overall pattern of convergent evolution in fitness (Fig. 1C). We further partitioned the variation in fitness increment attributed to founder identity and found that after 250 generations of adaptation, 31% of this variation was explained by the fitness of the founder, whereas 3% was determined by its specific genotype; for 500 generations, these percentages rose to 46% and 4%, respectively (Fig. 1B and table S3). Thus, the differences in adaptability between founders are almost entirely predicted by their differences in fitness and are independent of the specific mutations underlying this fitness. The initial fitness of the founder therefore predicts the average rate of adaptation in its descendant lines (Fig. 1D). Although the effects of specific genotype on adaptability are rare or weak, they are significant (fig. S2 and tables S3 and S4).

A negative correlation between fitness and adaptability has also been observed in prokaryotes (*11*, *12*), and it is consistent with the common observation in evolution experiments that the rate of increase in fitness slows down over time (*13*, *18*). Combined with this earlier work, our results suggest a general "rule of declining adaptability" that holds for prokaryotes and eukaryotes adapting to rich and minimal media. Further, our observations support a stronger version of this rule: Genotypes with lower fitness are more adaptable than those with higher fitness, and distinct genotypes with identical fitness are equally adaptable (up to the rare or weak exceptions noted above). This is consistent with the argument recently presented in (*13*).

The rule of declining adaptability could arise for two non-exclusive reasons. First, there could be only a few ways to increase in fitness. In this model, high-fitness founders have lower adaptability because they have already acquired all or most of the possible strong-effect beneficial mutations: They are "running out" of beneficial mutations. In contrast, low-fitness founders adapt more quickly because they have not yet acquired these mutations. More generally, some groups of mutations may have redundant functional effects (e.g., those that knock out a given pathway). In this case, the number of nonredundant ways to increase fitness would be much smaller than the number of distinct beneficial mutations. We refer to this general form of the running-out-of-mutations hypothesis as the "modular epistasis" model [inspired by (*14*)]: Each beneficial mutation improves a single module, mutations within each module are redundant, and high-fitness founders adapt more slowly because they have fewer remaining modules to improve, especially among those modules that confer the largest fitness gains (*16*).

Alternatively, mutations arising in higher-fitness backgrounds may be less beneficial than those arising in lower-fitness backgrounds; that is, diminishing-returns epistasis may be pervasive among adaptive mutations, as suggested by (*8*–*10*). This epistasis could have two forms. If epistasis is idiosyncratic, mutations may often have widely different effects in different genetic backgrounds (possibly including sign epistasis, where the sign of the fitness effect depends on genetic background), but the average effect of a beneficial mutation is smaller in fitter backgrounds. On the

[1]Department of Organismic and Evolutionary Biology, Harvard University, Cambridge, MA 02138, USA. [2]Department of Physics, Harvard University, Cambridge, MA 02138, USA. [3]FAS Center for Systems Biology, Harvard University, Cambridge, MA 02138, USA.
*These authors contributed equally to this work. †Corresponding author. E-mail: skryazhi@oeb.harvard.edu (S.K.); mdesai@oeb.harvard.edu (M.M.D.)

other hand, if epistasis is global, each individual beneficial mutation provides a smaller advantage in a fitter genetic background. This latter model implies that the effect of each mutation depends on all other mutations, but only through their combined effect on fitness.

In the modular and idiosyncratic epistasis models, different founders have different sets of beneficial mutations available to them. Hence, in both models we expect lines descended from the same founder to take more similar mutational trajectories than lines descended from different founders. In the modular model, we expect each mutation to either confer some fixed advantage (in genotypes lacking mutations in that module) or be neutral (in genotypes that already have a mutation in that module). In the idiosyncratic epistasis model, we expect individual mutations to have a variety of different fitness effects in different genetic backgrounds. In contrast to these two models, in the global epistasis model all genotypes acquire beneficial mutations from the same pool, but the advantage conferred by each mutation consistently declines with the fitness of the genetic background. In this model, founder identity should not affect subsequent mutational trajectories.

To assess the extent to which these three types of epistasis contribute to the rule of declining adaptability, we sampled one clone from each population descended from 15 founders at generation 500 of the adaptation phase and sequenced their complete genomes (*16*, *19*). We found that four sequenced clones acquired a mutator phenotype during the adaptation phase, and two founders and all their descendants became diploid (fig. S3). We excluded these from further analysis, leaving a total of 104 sequenced clones descended from 13 founders (*16*). We identified a total of 55 mutations that occurred in these founders during diversification and 1149 mutations that occurred in their descendants during adaptation. We annotated each mutation to a gene or intergenic region and classified coding mutations as synonymous or nonsynonymous (Fig. 2A and table S5). Because most synonymous and intergenic mutations are likely neutral hitchhikers, we restricted analysis to putatively functional nonsense, frameshift, nonsynonymous, and promoter mutations (818 total mutations).

In contrast to experiments in bacteria and viruses (*14*, *20*), all but four mutations are unique at the nucleotide level, consistent with earlier work in *S. cerevisiae* (*21*). However, we found significant gene-level convergent evolution. For example, 24 genes had mutations in at least three replicate lines [versus 2.7 genes expected by chance; multinomial test, $P < 0.01$ (*16*) (tables S6 and S7)], indicating that most mutations observed in these "multi-hit" genes are likely beneficial. Moreover, mutations in genes involved in negative regulation of Ras, cell cycle regulation, and filamentous growth were enriched (table S8), demonstrating convergence at higher levels of biological organization.

We next compared the total number of mutations observed in different evolved lines. Among lines descended from a given founder, the lines that increased most in fitness acquired more mutations on average in multi-hit genes, as we would expect if these mutations are beneficial (fig. S4). The modular epistasis model predicts that lines descended from high-fitness founders should acquire fewer beneficial mutations than those descended from low-fitness founders, because the former have fewer ways to improve. However, this is not the case: The numbers of putatively functional mutations in lines descended from different founders are not significantly different (Fig. 2B and table S9). This result is also surprising under the diminishing-returns epistasis models, although not strictly inconsistent with them (*22*). Because neutral hitchhiker mutations could mask differences in numbers of beneficial mutations between lines (*23*), we repeated this analysis on more restricted sets of "putatively beneficial mutations" [e.g., those in multi-hit genes (*24*)]. We found similar results in all cases (figs. S5 and S6).

In the modular and idiosyncratic epistasis models, many mutations are beneficial only in particular genetic backgrounds. Hence, these models predict that clones descended from the same founder should on average have more mutations in common (parallelism) than expected by chance, given the observed degree of overall convergence. However, this is not the case. Instead, clones descended from the same founder are not significantly more likely to share mutations than clones descended from different founders (Fig. 2, C and D, and fig. S7), as expected in the global diminishing-returns epistasis model. This pattern holds regardless of the level at which we define parallelism and convergence (genes or GO Slim categories).

We next selected three genes (*SFL1*, *WHI2*, and *GAT2*) in which we found putative loss-of-function (nonsense or frameshift) mutations in three or

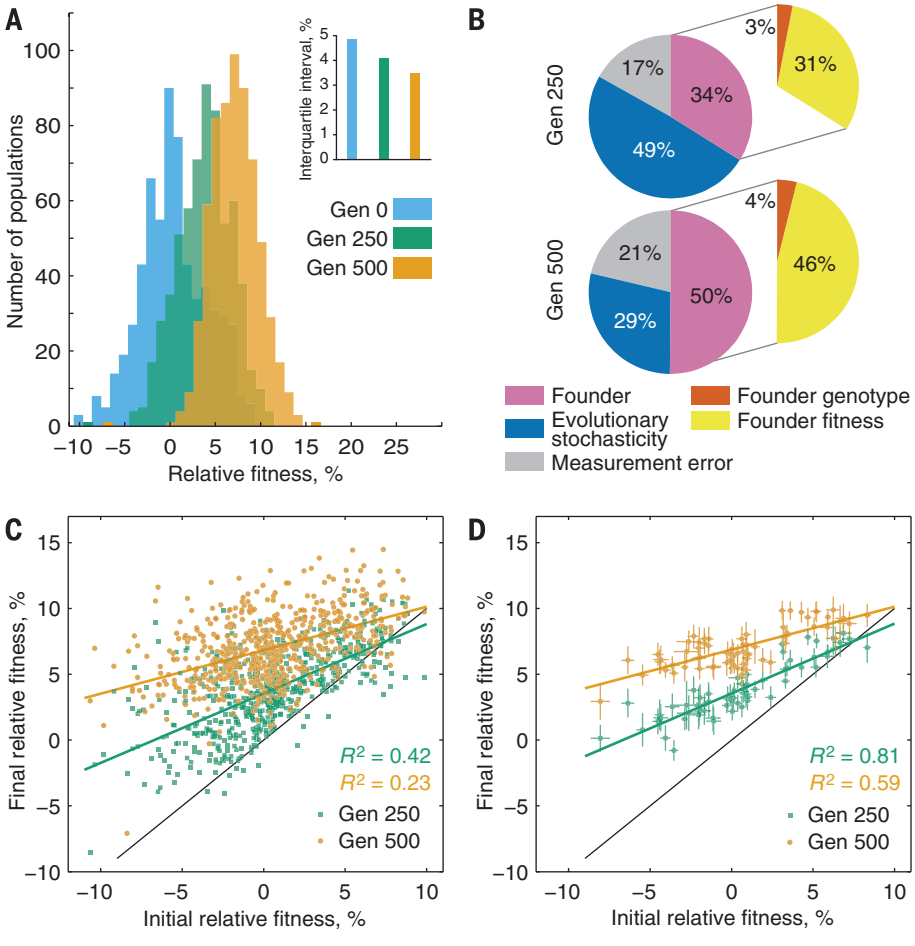

Fig. 1. Fitness evolution. (**A**) Distribution of mean population fitness over time, relative to the diversification ancestor (DivAnc). Inset shows interpopulation fitness variation over time. (**B**) Fraction of the variance between lines in fitness increment that is attributable to each indicated component after 250 and 500 generations of the adaptation phase. All variance components are significant (table S3). (**C**) Relationship between founder fitness and population fitness after 250 and 500 generations of adaptation. (**D**) Relationship between founder fitness and the mean fitness of the 10 independent lines descended from that founder, after 250 and 500 generations of adaptation. Error bars denote SEM.

more lines, suggesting that knockouts of these genes are beneficial in our system. *GAT2* displays the strongest signature of parallel evolution in our data (Fig. 2D) and therefore represents the strongest candidate for idiosyncratic epistasis. We constructed separate targeted knockouts of each of these genes, along with one control gene, *HO*, in several replicates into all 13 founders, DivAnc, and four additional clones (*16*) (table S1). We measured the fitness effects of each knockout in each background, and found a negative correlation between the fitness effect of the *gat2*Δ, *whi2*Δ, and *sfl1*Δ gene deletions and the fitness of the background strain (Fig. 3). Furthermore, there were no idiosyncratic epistatic interactions specific to particular genotypes: Up to small deviations, the fitness effect of each knockout depends only on the fitness of the genetic background and not on the specific mutations present in that background.

Taken together, these results support the global diminishing-returns epistasis model as the dominant explanation for declining adaptability with increasing fitness, and paint a surprisingly simple picture of adaptation in our system. Many mutations scattered across many biological processes appear to be beneficial. Yet despite their lack of apparent functional relationship, these mutations are globally coupled by diminishing-returns epistasis; their effects are strongly mediated by background fitness but are otherwise essentially independent of the specific identity of mutations present in the background. The biological basis of this global coupling remains unknown. Nonetheless, it

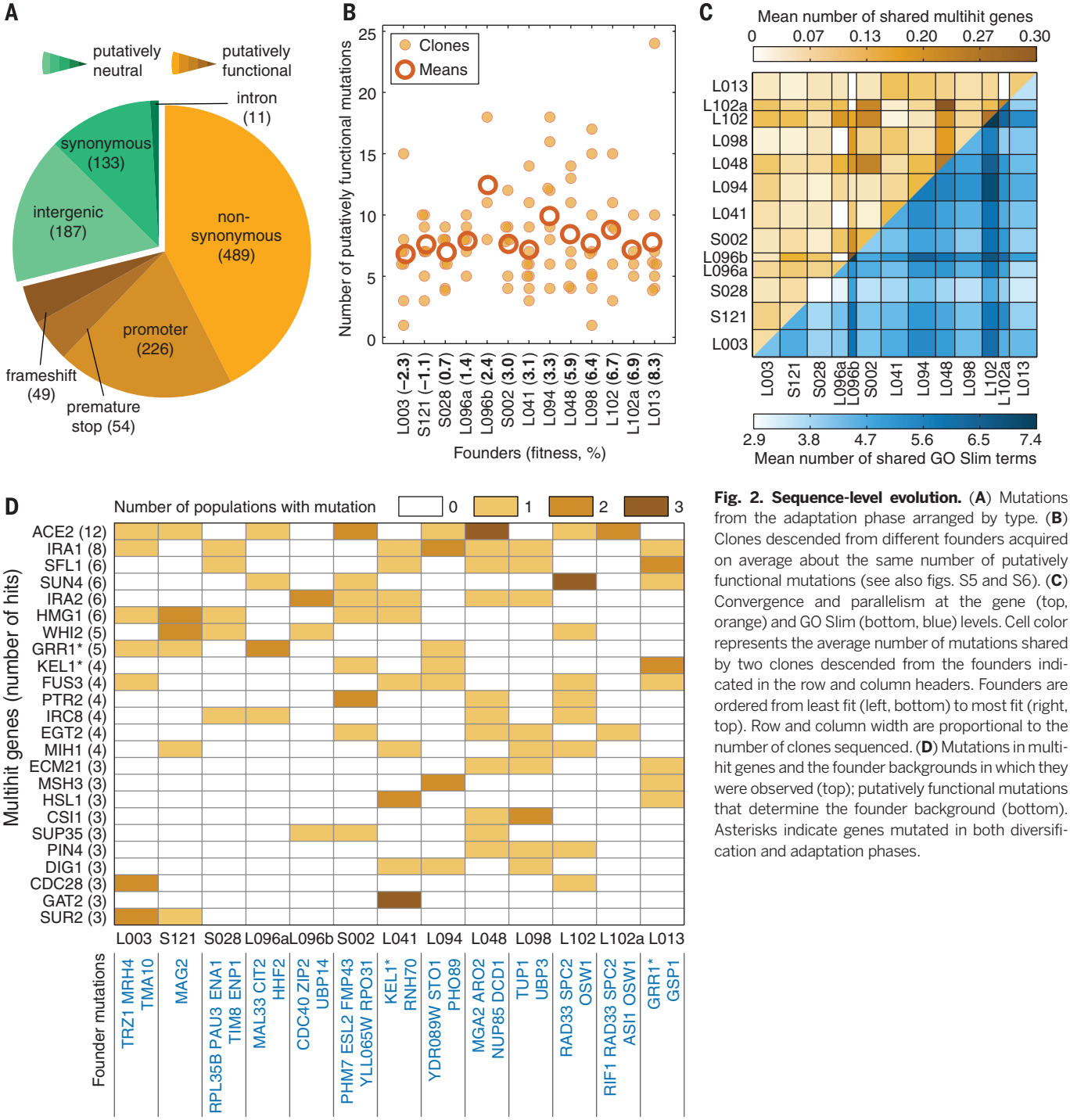

Fig. 2. Sequence-level evolution. (**A**) Mutations from the adaptation phase arranged by type. (**B**) Clones descended from different founders acquired on average about the same number of putatively functional mutations (see also figs. S5 and S6). (**C**) Convergence and parallelism at the gene (top, orange) and GO Slim (bottom, blue) levels. Cell color represents the average number of mutations shared by two clones descended from the founders indicated in the row and column headers. Founders are ordered from least fit (left, bottom) to most fit (right, top). Row and column width are proportional to the number of clones sequenced. (**D**) Mutations in multihit genes and the founder backgrounds in which they were observed (top); putatively functional mutations that determine the founder background (bottom). Asterisks indicate genes mutated in both diversification and adaptation phases.

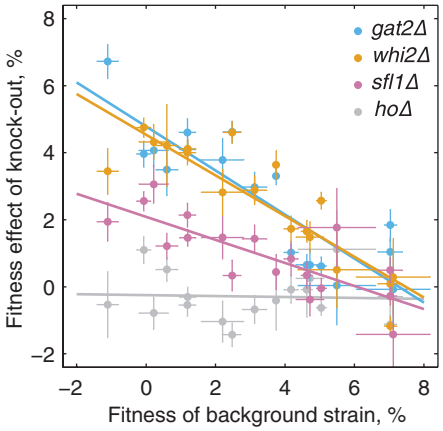

Fig. 3. Diminishing-returns epistasis among specific mutations. The fitness effect of knocking out genes *gat2*, *whi2*, and *sfl1* declines with the fitness of the background strain. The *ho* knockout is a negative control. Error bars are SEM over biological replicates.

leads to a striking pattern of convergent evolution, making fitness evolution relatively predictable. Despite this fitness-level convergence, evolution remains highly stochastic at the genotype level, likely because many distinct mutational paths can lead a population to any given fitness.

REFERENCES AND NOTES

1. R. J. Woods *et al.*, *Science* **331**, 1433–1436 (2011).
2. Z. D. Blount, C. Z. Borland, R. E. Lenski, *Proc. Natl. Acad. Sci. U.S.A.* **105**, 7899–7906 (2008).
3. J. D. Bloom, L. I. Gong, D. Baltimore, *Science* **328**, 1272–1275 (2010).
4. D. R. Rokyta *et al.*, *PLOS Genet.* **7**, e1002075 (2011).
5. C. L. Burch, L. Chao, *Nature* **406**, 625–628 (2000).
6. D. M. Weinreich, N. F. Delaney, M. A. Depristo, D. L. Hartl, *Science* **312**, 111–114 (2006).
7. S. J. Gould, *Wonderful Life* (Norton, New York, 1989).
8. A. I. Khan, D. M. Dinh, D. Schneider, R. E. Lenski, T. F. Cooper, *Science* **332**, 1193–1196 (2011).
9. H.-H. Chou, H.-C. Chiu, N. F. Delaney, D. Segrè, C. J. Marx, *Science* **332**, 1190–1192 (2011).
10. H.-H. Chou, J. Berthet, C. J. Marx, *PLOS Genet.* **5**, e1000652 (2009).
11. J. E. Barrick, M. R. Kauth, C. C. Strelioff, R. E. Lenski, *Mol. Biol. Evol.* **27**, 1338–1347 (2010).
12. L. Perfeito, A. Sousa, T. Bataillon, I. Gordo, *Evolution* **68**, 150–162 (2014).
13. M. J. Wiser, N. Ribeck, R. E. Lenski, *Science* **342**, 1364–1367 (2013).
14. O. Tenaillon *et al.*, *Science* **335**, 457–461 (2012).
15. G. I. Lang, D. Botstein, M. M. Desai, *Genetics* **188**, 647–661 (2011).
16. See supplementary materials on *Science* Online.
17. M. Travisano, J. A. Mongold, A. F. Bennett, R. E. Lenski, *Science* **267**, 87–90 (1995).
18. S. Kryazhimskiy, G. Tkačik, J. B. Plotkin, *Proc. Natl. Acad. Sci. U.S.A.* **106**, 18638–18643 (2009).
19. Note that this includes two founders inadvertently picked from the same diversified population (*16*).
20. J. P. Bollback, J. P. Huelsenbeck, *Mol. Biol. Evol.* **24**, 1397–1406 (2007).
21. G. I. Lang *et al.*, *Nature* **500**, 571–574 (2013).
22. This result is also surprising in the diminishing-returns models because we expect fewer beneficial mutations to fix in high-fitness backgrounds where they provide a smaller selective advantage. This puzzle is related to the observation (*25*) that fixation rates in long-term evolution of *E. coli* are constant through time despite a declining rate of fitness increase. However, our result would be consistent with the diminishing-returns models if the beneficial mutation rate is also higher in high-fitness backgrounds.
23. See (*16*) for a power analysis.
24. These are likely enriched for the most strongly beneficial mutations. Hence, if modular epistasis is prevalent, it is among these mutations that we expect the strongest trend.
25. J. E. Barrick *et al.*, *Nature* **461**, 1243–1247 (2009).

ACKNOWLEDGMENTS

We thank A. Murray, Q. Justman, B. Good, D. van Dyken, M. McDonald for useful discussions; A. Subramaniam, G. Lang, M. Müller, and J. Koschwanez for experimental advice and strains; and P. Rogers and C. Daly for technical support. Supported by the Burroughs Wellcome Foundation (S.K.), NSF graduate research fellowships (D.P.R., E.R.J.), and the James S. McDonnell Foundation, the Alfred P. Sloan Foundation, the Harvard Milton Fund, NSF grant PHY 1313638, and NIH grant GM104239 (M.M.D.). Sequence data have been deposited to GenBank under BioProject identifier PRJNA242140.

SUPPLEMENTARY MATERIALS

www.sciencemag.org/content/344/6191/1519/suppl/DC1
Materials and Methods
Figs. S1 to S12
Tables S1 to S12
References (*26*–*34*)

16 January 2014; accepted 28 May 2014
10.1126/science.1250939

NONHUMAN GENETICS

Genomic basis for the convergent evolution of electric organs

Jason R. Gallant,[1,2]* Lindsay L. Traeger,[3,4]* Jeremy D. Volkening,[4,5] Howell Moffett,[6,7] Po-Hao Chen,[6,7,8] Carl D. Novina,[6,7,8] George N. Phillips Jr.,[9] Rene Anand,[10] Gregg B. Wells,[11] Matthew Pinch,[12] Robert Güth,[12] Graciela A. Unguez,[12] James S. Albert,[13] Harold H. Zakon,[2,14,15]† Manoj P. Samanta,[16]† Michael R. Sussman[4,5]†

Little is known about the genetic basis of convergent traits that originate repeatedly over broad taxonomic scales. The myogenic electric organ has evolved six times in fishes to produce electric fields used in communication, navigation, predation, or defense. We have examined the genomic basis of the convergent anatomical and physiological origins of these organs by assembling the genome of the electric eel (*Electrophorus electricus*) and sequencing electric organ and skeletal muscle transcriptomes from three lineages that have independently evolved electric organs. Our results indicate that, despite millions of years of evolution and large differences in the morphology of electric organ cells, independent lineages have leveraged similar transcription factors and developmental and cellular pathways in the evolution of electric organs.

Electric fishes use electric organs (EOs) to produce electricity for the purposes of communication; navigation; and, in extreme cases, predation and defense (*1*). EOs are a distinct vertebrate trait that has evolved at least six times independently (Fig. 1A). The taxonomic diversity of fishes that generate electricity is so profound that Darwin specifically cited them as an important example of convergent evolution (*2*). EOs benefit as a model for understanding general principles of the evolution of complex traits, as fish have evolved other specialized noncontractile muscle-derived organs (*3*). Furthermore, EOs provide a basis to assess whether similar mechanisms underlie the evolution of other specialized noncontractile muscle derivatives, such as the cardiac conduction system (*4*).

Electric organs are composed of cells called electrocytes (Fig. 1B). All electrocytes have an innervated surface enriched in cation-specific ion channels and, on the opposite surface, an invaginated plasma membrane enriched in sodium pumps, and, in some species, ion channels as well. The functional asymmetry of these cells, and their "in-series" arrangement within each organ, allows for the summation of voltages, much like batteries stacked in series in a flashlight. Although EOs originate developmentally from myogenic precursors, they are notably larger than muscle fibers (*5*). Further, they either lack the contractile machinery clearly evident in electron

[1]Department of Zoology, Michigan State University, East Lansing, MI 48824, USA. [2]BEACON Center for the Study of Evolution in Action, Michigan State University, East Lansing, MI 48824, USA. [3]Department of Genetics, University of Wisconsin, Madison, WI 53706, USA. [4]Biotechnology Center, University of Wisconsin, Madison, WI 53706, USA. [5]Department of Biochemistry, University of Wisconsin, Madison, WI 53706, USA. [6]Department of Cancer Immunology and AIDS, Dana-Farber Cancer Institute, Boston, MA 02115, USA. [7]Department of Microbiology and Immunobiology, Harvard Medical School, Boston, MA 02115, USA. [8]Broad Institute of Harvard and MIT, Cambridge, MA 02141, USA. [9]Department of Biochemistry and Cell Biology and Department of Chemistry, Rice University, Houston, TX 77005, USA. [10]Department of Pharmacology and Department of Neuroscience, College of Medicine, The Ohio State University Wexner Medical Center, Columbus, OH 43210, USA. [11]Department of Molecular and Cellular Medicine, Texas A&M University, College Station, TX 77843, USA. [12]Department of Biology, New Mexico State University, Las Cruces, NM 88003, USA. [13]Department of Biology, University of Louisiana, Lafayette, LA 70503, USA. [14]University of Texas, Austin, TX 78712, USA. [15]The Josephine Bay Paul Center for Comparative Molecular Biology and Evolution, The Marine Biological Laboratory, Woods Hole, MA 02543, USA. [16]Systemix Institute, Redmond, WA 98053, USA.
*These authors contributed equally to this work. **†Corresponding author. E-mail: msussman@wisc.edu (M.R.S.); manoj.samanta@systemix.org (M.P.S.); h.zakon@austin.utexas.edu (H.H.Z.)**

micrographs of muscle cells (Fig. 1B) or, if sarcomeres are present, as in mormyroid fish, they are disarrayed and noncontractile (Fig. 1B). Finally, electrocyte morphology varies widely: they can be long and slender, box-like, or flattened and pancake-like (Fig. 1B). Despite these differences in morphology, the three lineages of electric fish studied here share patterns of gene expression in transcription factors and pathways contributing to increased cell size, increased excitability, and decreased contractility.

We used next-generation sequencing technologies to construct a draft assembly of the *Electrophorus electricus* genome. Like all Gymnotiformes, *E. electricus* has a weak EO but is most famous for its distinct strong voltage EO. To inform gene predictions in the genome assembly, we generated short-read mRNA sequences from the main, Sachs', and Hunter's EOs, as well as the kidney, brain, spinal cord, skeletal muscle, and heart (*6*). This resulted in 29,363 gene models representing an estimated 22,000 protein-coding genes (table S1). Variance filtering of the gene models removed genes with low covariance among tissues, and

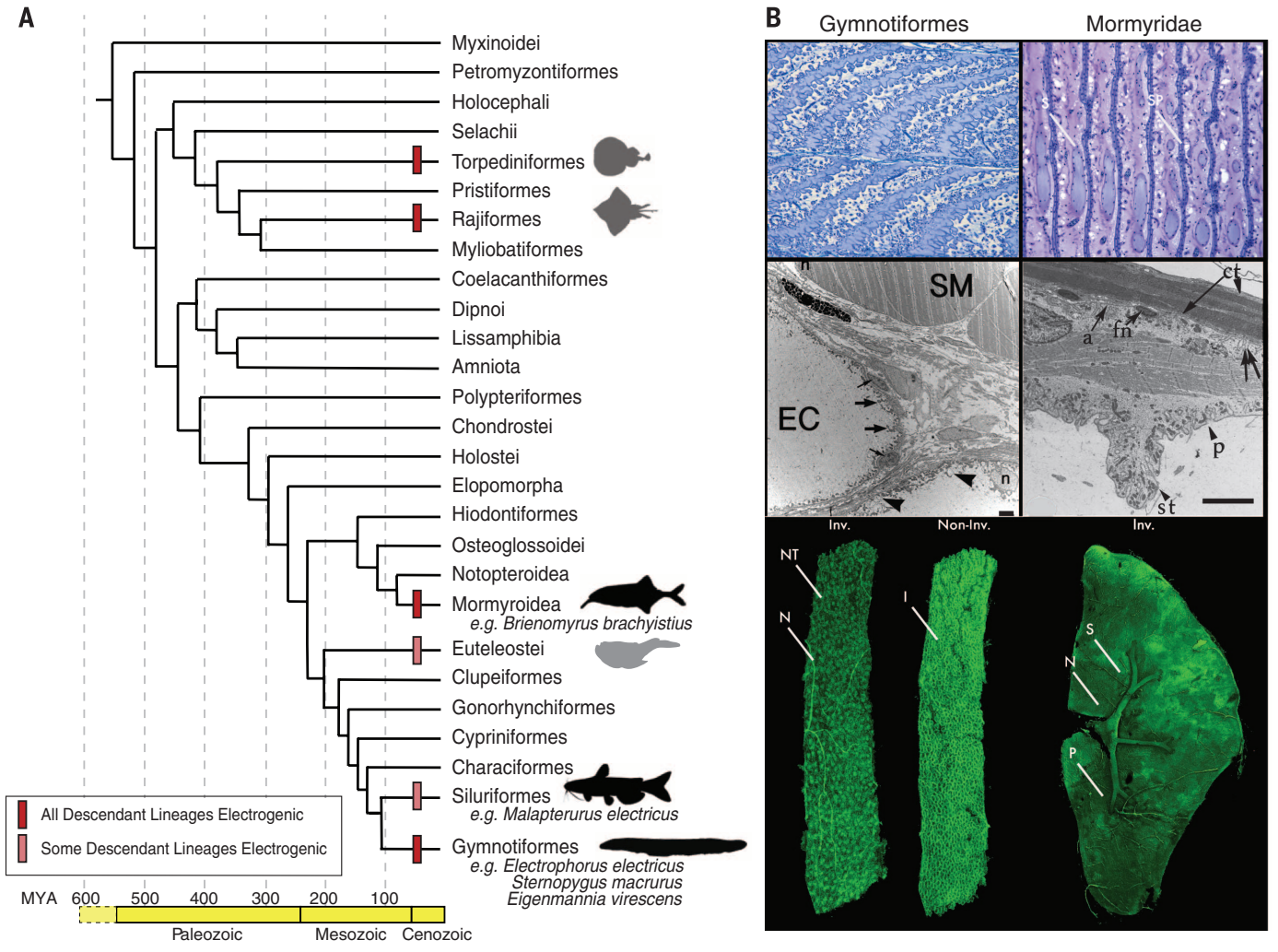

Fig. 1. Origins and diversity of EOs in vertebrates. (**A**) Phylogenetic tree of vertebrate orders and major groups of electric fishes, after (*25*). Geological periods and ages [in million years ago (MYA)] are shown at bottom. The origins of electrogenesis are indicated with bars (see legend) at internal branches. Black silhouettes denote lineages surveyed in the present study; gray silhouettes represent electrogenic lineages that were not surveyed. (**B**) (Top left) Sagittal sections through the *E. electricus* EO for the innervated, invaginated face and uninnervated smooth faces of the electrocyte and their in-series arrangement. (Top right) Sagittal section through the EO of the mormyroid *Paramormyrops kingsleyae*. Anterior is left; posterior is right. In mormyroids, innervation is restricted to a narrow region of the stalk system (S) protruding from the innervated, anterior face of the electrocyte. Also note the central filament of sarcomeric proteins (SP) between the multinucleated electrocyte faces. (Middle left) An electron micrograph of both skeletal muscle (SM) and electrocytes (EC) from the gymnotiform *S. macrurus*, which contain an amorphous cytoplasm devoid of sarcomeres: the striated, contractile structures that fill the cytosol of muscle cells. Peripheral nuclei (n) are marked in both electrocyte and muscle cells. In electrocytes, thick arrows point to mitochondria, thin arrows point to satellite cells, and arrowheads mark membrane-bound vesicular structures. Scale bar, 2 μm. (Middle right) An electron micrograph of an electrocyte of the mormyroid *P. kingsleyae*, illustrating the disorganized sarcomeric proteins in the center of the electrocyte. The outer edge of an electrocyte forms a "footplate" that apposes the connective tissue sheath (ct) surrounding the EO. The anterior face (a) of the electrocyte forms the major surface of the plate lying against the connective tissue surface. Fibroblast nuclei (fn), papillae (p), and stalk (st) are also indicated. Double arrows correspond to invaginations of the posterior face. Scale bar, 4 μm. [Image provided by Andrew Bass (Cornell University)] (Bottom left) A confocal reconstruction of an *E. electricus* electrocyte from anterior and posterior views. The nerve (N) innervating the innervated (Inv.) face is clearly visible, along with the many cholinergic nerve terminals (NT). The numerous invaginations (I) of the noninnervated (Non-Inv.) face are visible. (Bottom right) A confocal reconstruction of a *P. kingsleyae* electrocyte, clearly showing the protruding stalk system (S) from the anterior face. The stalk junction is innervated by motoneurons (N) in a highly localized fashion to contrast with *E. electricus*. Penetrations (P) are also visible in the electrocyte face.

subsequent *k*-means clustering (k = 12) revealed sets of tissue-specific cotranscriptionally regulated genes (*6*) (fig. S1). We focused primarily on a reduced set of genes that were highly up-regulated only in EOs (cluster 9, 211 genes) or down-regulated in EOs compared with skeletal and heart muscle (cluster 1, 186 genes).

Next, we sequenced and performed de novo assembly of the transcriptomes from EOs and skeletal muscles in two other Gymnotiformes from South America (*Sternopygus macrurus* and *Eigenmannia virescens*), as well as in two other species with independently evolved EOs, a mormyroid from Africa (*Brienomyrus brachyistius*) and the electric catfish from Africa (*Malapterurus electricus*). For each species, we assigned orthology between transcripts by reciprocal BLAST searching of the set of *E. electricus* genes followed by manual confirmation of the matches (*6*). We focused on convergent properties of EOs versus skeletal muscle among lineages, and we then examined patterns of gene expression in transcription factors and developmental pathways to determine candidate mechanisms underlying these similarities (Fig. 2). We highlighted genes likely to be involved in phenotypic characteristics of electrocytes relative to muscle, including (i) down-regulation of myogenic transcriptional "profile," (ii) increased excitability, (iii) enhanced insulation, (iv) elimination of excitation-contraction coupling, and (v) large size.

We found elevated expression of several transcription factors (Fig. 2 and fig. S2) expressed early in muscle differentiation (*7*) that are typically down-regulated in skeletal muscle after differentiation. *Six2a* is of particular interest, given that it is known to target ARE promoter elements in Na^+/K^+ adenosine triphosphatases (*8*, *9*). Concordant with the expression of early muscle transcription factors is the down-regulation of some transcription factors involved in muscle differentiation (e.g., *myogenin* and *six4b*) in *E. electricus*, *B. brachyistius*, and *M. electricus*, although not in the gymnotiform *S. macrurus*. Interestingly, *hey1*, which is one of the most consistent highly up-regulated genes in the EOs across all groups of electric fishes, is abundant in zebrafish somites and down-regulated in mature muscle, and its overexpression in mammalian muscle precursor cells prevents their

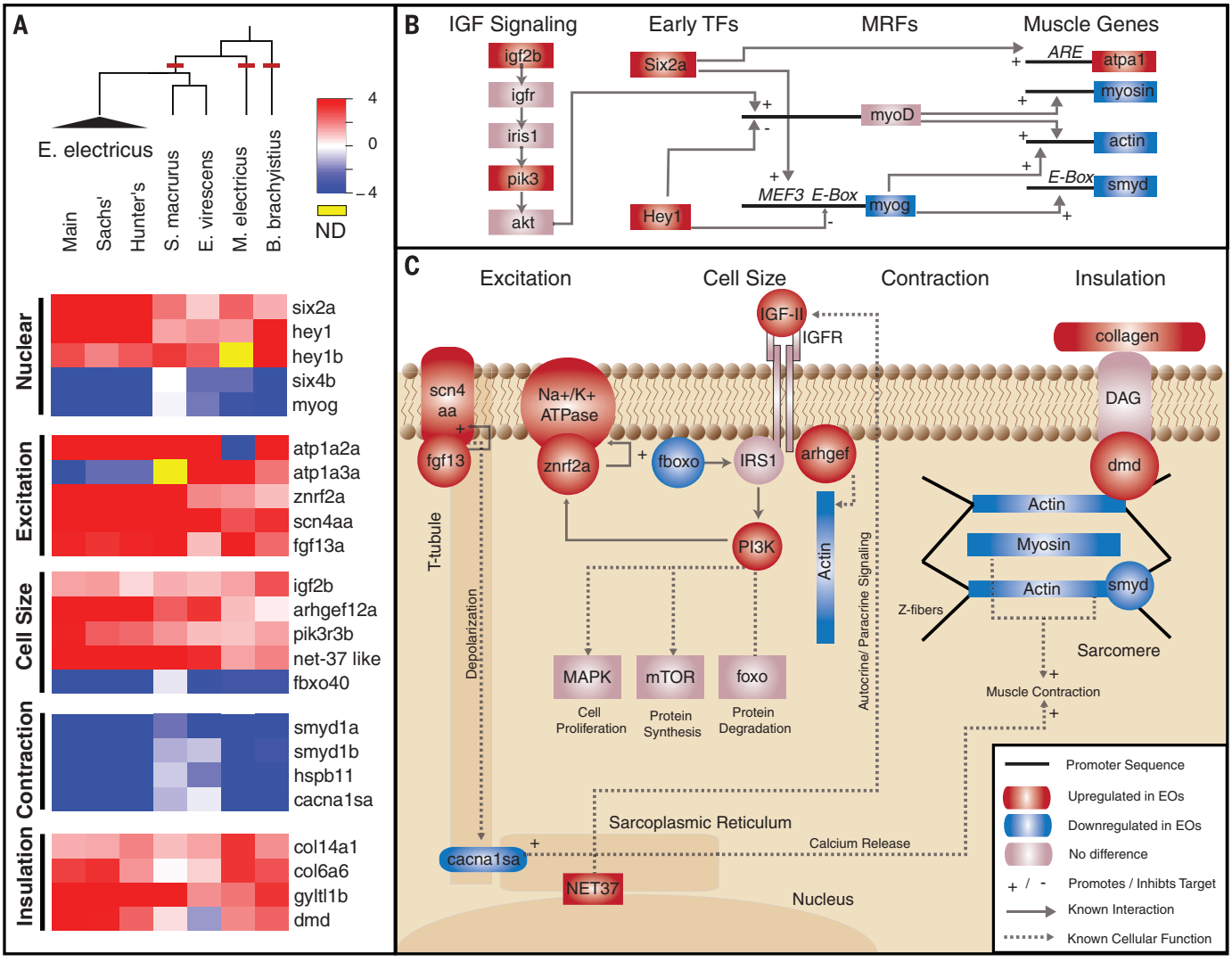

Fig. 2. Common toolkit for convergent evolution of EOs. (**A**) RNA-Seq was performed on five species, representing three independent origins of electrogenesis (cladogram, red lines). Also shown are plots of the log-transformed ratio of EO to skeletal muscle expression genes (red, up-regulated in EO; blue, down-regulated in EO) in several categories of function, including (i) nuclear transcription factors, (ii) genes that regulate cell excitation, (iii) genes that regulate cell size, (iv) genes involved in contraction and excitation contraction coupling, and (v) genes encoding proteins that surround individual electrocytes to provide the scaffold for insulation. *hey1b* data for *E. electricus* was derived from the Trinity transcriptome assembly (*6*). (**B**) Interaction of identified IGF signaling and transcription factors (TFs). IGF signaling pathway genes and early TFs influence the expression of muscle regulatory factors (MRFs), which ultimately lead to the expression of muscle-specific effector genes (table S3). (**C**) Interactions of genes identified in (A) are shown, grouped by function. For each, we list known patterns of expression in electric fish or the result of knockout studies in other vertebrates (table S4). IGFR, IGF receptor; MAPK, mitogen-activated protein kinase.

differentiation into muscle (*10*). Furthermore, *hey1* is transiently expressed in the developing cardiac conduction pathway, and its overexpression in the heart prevents assembly of the sarcomeres (*4*).

A key feature of EOs is that current dissipation must be minimized and conducted unidirectionally from the EOs through the body of the fish and into the water. We noted two collagen genes, *col6a6* and *col14a1*, that are up-regulated in EOs. The first is associated with muscle fibers, and the second is more generally expressed and ties the collagen fibers together. Collagen is deposited in the extracellular domain of basal lamina and is maintained by a cluster of molecules that span the membrane and attach to the cytoskeleton. Two of these membrane-spanning proteins, including a glycosyltransferase (*gyltl1b*) and dystrophin (mutations of which cause muscular dystrophy) (*11*), are also up-regulated in EOs and are probably involved in assembling the components that direct the flow of current.

Also, as expected, several transporters (*atp1a2a* or *atp1a3a*) and voltage-dependent ion channels (*scn4aa*) were highly expressed in all EOs, along with molecules that regulate them (*znrf2a* and *fgf13a*, respectively). Interestingly, the highly expressed gene encoding the α subunit of the sodium pump (*atp1a2a*) most closely resembles the isoform also expressed in transverse tubules (T-tubules) of muscle (*12*) and is abundant in the villi located within the invaginated side of the *E. electricus* electrocyte (*13*), suggesting that the uninnervated face of the electrocyte is derived from the T-tubule membrane.

A key step in the evolution of electrocytes requires disabling the excitation-contraction pathway. We noted variation in the extent to which genes for sarcomeric and sarcoplasmic reticulum–associated proteins are down-regulated in different species (Fig. 2, fig. S3, and table S2). Furthermore, mormyroid electrocytes still have sarcomere-like structures, although they appear disrupted (Fig. 1B). Despite these differences, the gene encoding the L-type calcium channel, or dihydropyridine receptor (*cacna1s*), which is localized in T-tubules and associated with excitation-contraction coupling in muscle, is down-regulated in all lineages. The *smyds* and *hspb11* genes are also down-regulated in all lineages. These proteins associate with the sarcomeres, and zebrafish and mice with reduced expression or mutant gene copies have disrupted sarcomeres (*14*). The observed low levels of these genes in EOs suggest that they may promote disassembly of the sarcomeres, and we hypothesize that the early evolution of the EO included the down-regulation of this suite of genes, disabling contraction.

As electrocytes are much larger than muscle fibers, we hypothesized that this might be due to changes in insulin-like growth factor (IGF) signaling pathway genes (Fig. 2 and fig. S4). IGF signaling enhances body size and developmental rate in an organism-wide and tissue-specific fashion (*15*–*18*). IGF ligands are produced and released by muscle in an autocrine fashion (*19*), and differences in IGF signaling may result in differential growth of muscles. IGF signaling activates the insulin receptor substrate 1 protein (IRS1), which then binds to the regulatory subunit of phosphoinositide 3 kinase (PIK3) (*20*). PIK3 acts through distinct signaling targets to regulate cell size, cell proliferation, and protein synthesis and degradation (*21*). The IGF pathway is also autoregulated by a muscle-specific protein, Fbxo40, which brings IRS1 to an E3 ligase complex. Thus, up-regulation of IRS1 is likely a key step in increasing IGF signaling activity in electrocytes.

Finally, the nuclear-envelope–related protein (Net37), abundant in cardiac and skeletal muscle tissues (*22*), regulates autocrine and/or paracrine release of IGF signaling and is required for myogenic differentiation of mouse myoblast cells (*23*). We detected electrocyte-specific up-regulation of *igf1l*, a gene for PI3K (*pik3r3b*) and a *net37*-like gene in all lineages, as well as down-regulation of the negative inhibitor *fbxo40*. The *net37*-like protein was also recently reported to be highly expressed in the EO of another electric fish, the *Torpedo* ray (*24*). Together, the observed changes in expression in these key IGF signaling pathway genes suggest a conserved pathway among electrocytes that contributes to their increased size. The independent changes and the resulting enhancement in cell size highlight these genes as possible intracellular effectors in other insulin- or IGF-sensitive systems, as observed in male horned beetles (*18*).

Our analysis suggests that a common regulatory network of transcription factors and developmental pathways may have been repeatedly targeted by selection in the evolution of EOs, despite their very different morphologies. Moreover, our work illuminates convergent evolution of EOs and emphasizes key signaling steps that may be foci for the evolution of tissues and organs in other organisms.

REFERENCES AND NOTES

1. J. S. Albert, W. G. R. Crampton, in *The Physiology of Fishes* (Springer, New York, ed. 3, 2005), pp. 431–472.
2. C. Darwin, in *On the Origin of Species by Means of Natural Selection* (J. Murray, London, 1859), pp. ix, 1.
3. B. A. Block, *Am. Zool.* **31**, 726–742 (1991).
4. H. Kokubo, S. Tomita-Miyagawa, Y. Hamada, Y. Saga, *Development* **134**, 747–755 (2007).
5. G. A. Unguez, H. H. Zakon, *J. Neurosci.* **18**, 9924–9935 (1998).
6. Materials and methods are available as supplementary materials on *Science* Online.
7. H. Ghanbari, H. C. Seo, A. Fjose, A. W. Brändli, *Mech. Dev.* **101**, 271–277 (2001).
8. F. Spitz *et al.*, *Proc. Natl. Acad. Sci. U.S.A.* **95**, 14220–14225 (1998).
9. K. Kawakami *et al.*, *Nature* **316**, 733–736 (1985).
10. M. F. Buas, S. Kabak, T. Kadesch, *J. Biol. Chem.* **285**, 1249–1258 (2010).
11. K. J. Nowak, K. E. Davies, *EMBO Rep.* **5**, 872–876 (2004).
12. R. G. Berry, S. Despa, W. Fuller, D. M. Bers, M. J. Shattock, *Cardiovasc. Res.* **73**, 92–100 (2007).
13. J. Lowe *et al.*, *Biochim. Biophys. Acta* **1661**, 40–46 (2004).
14. N. Klüver *et al.*, *PLOS ONE* **6**, e29063 (2011).
15. C. Duan, H. Ren, S. Gao, *Gen. Comp. Endocrinol.* **167**, 344–351 (2010).
16. B. C. Hoopes, M. Rimbault, D. Liebers, E. A. Ostrander, N. B. Sutter, *Mamm. Genome* **23**, 780–790 (2012).
17. N. B. Sutter *et al.*, *Science* **316**, 112–115 (2007).
18. D. J. Emlen, I. A. Warren, A. Johns, I. Dworkin, L. C. Lavine, *Science* **337**, 860–864 (2012).
19. A. S. Van Laere *et al.*, *Nature* **425**, 832–836 (2003).
20. I. Mothe *et al.*, *Mol. Endocrinol.* **11**, 1911–1923 (1997).
21. A. Otto, K. Patel, *Exp. Cell Res.* **316**, 3059–3066 (2010).
22. I. H. Chen, M. Huber, T. Guan, A. Bubeck, L. Gerace, *BMC Cell Biol.* **7**, 38 (2006).
23. K. Datta, T. Guan, L. Gerace, *J. Biol. Chem.* **284**, 29666–29676 (2009).
24. S. E. Mate, K. J. Brown, E. P. Hoffman, *Skeletal Muscle* **1**, 20 (2011).
25. M. E. Alfaro *et al.*, *Proc. Natl. Acad. Sci. U.S.A.* **106**, 13410–13414 (2009).

ACKNOWLEDGMENTS

This project has been funded in part by NSF grants MCB no. 1144012 (M.R.S.), CNS no. 1248109 (G.A.U.), and DEB no. 0741450 (J.S.A.); the W.M. Keck Foundation Distinguished Young Scholars in Medical Research (C.D.N.); NIH grants R01 GM084879 (H.H.Z.), R01 GM088670 (R.A.), and 1SC1GM092297-01A1 (G.A.U.); the Texas A&M University Health Science Center College of Medicine (G.B.W.); the Cornell University Center for Vertebrate Genomics (J.R.G.); the University of Wisconsin Genetics NIH Graduate Training Grant (L.L.T.); and the Morgridge Graduate Fellowship (J.D.V.). E. V. Armbrust provided computing assistance, and S. B. McKay assisted with data analysis. M.P.S. acknowledges useful discussions with R. Chikhi, R. Luo, and J. Simpson. We thank J. Bayliss for dissection of *E. electricus* and R. Amasino for help in preparing this manuscript. M.R.S. and L.L.T. acknowledge the guidance of J. Hyman, M. Adams, and J. Speers from the University of Wisconsin Biotechnology Center for their excellent assistance in *E. electricus* sequencing. The raw sequencing reads have been deposited in the National Center for Biotechnology Information short-read archive for the *E. electricus* genome (BioProject ID: PRJNA249073) and transcriptome sequences of *E. electricus*, *S. macrurus*, *E. virescens*, *M. electricus*, and *B. brachyistius* (BioProject ID: PRJNA248545). The whole-genome assemblies and annotation, together with the transcriptome assemblies, are available at http://efishgenomics.zoology.msu.edu, along with BLAST and genome-browsing services.

SUPPLEMENTARY MATERIALS

www.sciencemag.org/content/344/6191/1522/suppl/DC1
Materials and Methods
Supplementary Text
Figs. S1 to S6
Tables S1 to S7
References (*26*–*91*)

7 April 2014; accepted 6 June 2014
10.1126/science.1254432

Capacitance Manometer

The *a*-Baratron Capacitance Manometer is an advanced high-performance, heated absolute capacitance manometer with better accuracy, higher tolerance to ambient temperature changes, and excellent repeatability. The *a*-Baratron manometer is internally heated to 45°C, 80°C, or 100°C, and has a pushbutton zero that allows service intervals up to four times longer than earlier models. The manometer offers full-scale measurement ranges from 0.1 Torr to 1,000 Torr (13.3 Pa to 133.3 kPa). Its all-digital architecture and advanced new sensor heating system provide long-term performance and reliability. As with previous Baratron manometers, the sensor is made from Inconel and Incoloy nickel alloys for the same superior corrosion resistance. The *a*-Baratron manometer can be equipped with the standard sensor or MKS' patented Etch Baffle sensor technology that greatly reduces process contamination. It can be configured for both new and existing processing systems. It operates on ±15VDC input voltage and has a standard 0–10VDC analog output signal.

MKS Instruments
For info: 978-645-5500
www.mksinst.com

Evaporation Technology

eXalt is an exciting new nondestructive evaporation technology with applications such as first time crystallizations of amorphous forms, recrystallization of samples which have only a few known forms, removing a hydrate, solvent screening studies to find the most suitable conditions to take forward in development, high throughput co-crystallization screens, and studies to confirm stable isoforms. eXalt enables a wide range of solvents and multiple actives to be evaporated all at the same slow rate, and under the same conditions, giving the user unprecedented control of the crystallization process. This is achieved using a special holder which can be configured to slow the evaporation rate of each solvent, i.e., the more volatile solvents are impeded more, and some solvents such as water, need no restriction. The holder is then placed in the controlled conditions of a Genevac HT Series Evaporator which cycles the pressure over the samples to create a draw, achieving controlled, even evaporation.

Genevac
For info: +44-(0)-1473-240000
www.genevac.com/exalt

Automated Tube Capper/DeCapper

The LabElite line of benchtop devices provide laboratories with flexible solutions for sample processing, tracking, and security. For manual workflows that need high-speed 2-D barcode reading of tube racks, the LabElite I.D. Reader is the ideal choice. It decodes tubes in all common 12-, 24-, 48-, 96-, and 384-tube racks including honeycomb-shaped racks. The LabElite DeCapper can decap and recap tubes in 48-cryovial or 96-microtube racks in portrait or landscape formats, one row at a time, to minimize the time tubes are open and eliminate the risk of cross-contamination. Rows can be paused for "point-of-use" manual pipetting. The all-in-one LabElite I.D. Capper combines decapping and recapping and high-speed barcode reading in one small device. The I.D. Capper includes all of the standard features and benefits of the I.D. Reader and DeCapper.

Hamilton Storage Technologies
For info: 508-544-7000
www.hamilton-storage.com

Benchtop Cell Analysis System

The guava easyCyte 12 flow cytometry system provides a simple benchtop method for multicolor flow cytometry. The new platform consumes less sample, generates less waste, and is easier to maintain than traditional systems. The guava easyCyte 12 flow cytometer uses three excitation lasers to provide up to 12 simultaneous detection parameters, including 10 fluorescent colors plus forward and side scatter for size and granularity determination. Single-sample and multisample processing options are offered, and high throughput analysis is possible with robotic sample trays that automatically handle 96-well microplates and up to 10 sample tubes. The new system, capable of detecting mammalian and microbial cells and beads, offers an intuitive interface and is priced to be affordable for every laboratory budget. The new guava easyCyte cytometer offers researchers a simple, flexible option for a variety of applications, including easy identification of subpopulations in a heterogeneous sample and multiplexing cell health parameters to study cell function pathways.

EMD Millipore
For info: 800-645-5476
www.emdmillipore.com/guava

Low-Temperature Control System

The DrySyn SnowStorm system enables low-temperature reactions which have traditionally been difficult to undertake reproducibly on a small to medium scale. The DrySyn SnowStorm offers an attractive solution to laboratories undertaking low-temperature reaction chemistries. Available in a choice of configurations, the DrySyn SnowStorm system provides controlled cooling and heating for sub-ambient parallel chemistry without the need for jacketed reaction vessels or ice baths. Operating with a suitable chiller/circulator, a DrySyn SnowStorm system provides accurate, stable temperature control down to -50°C and up to +150°C. The DrySyn SnowStorm connects to an external chiller unit and holds temperatures at a set-point for as long as is required. Setting temperature ramping profiles is also possible which is important in optimization studies.

Asynt
For info: +44-(0)-1638-781709
www.asynt.com

Electronically submit your new product description or product literature information! Go to www.sciencemag.org/products/newproducts.dtl for more information.

Newly offered instrumentation, apparatus, and laboratory materials of interest to researchers in all disciplines in academic, industrial, and governmental organizations are featured in this space. Emphasis is given to purpose, chief characteristics, and availability of products and materials. Endorsement by *Science* or AAAS of any products or materials mentioned is not implied. Additional information may be obtained from the manufacturer or supplier.

Downloaded from www.sciencemag.org on June 28, 2014

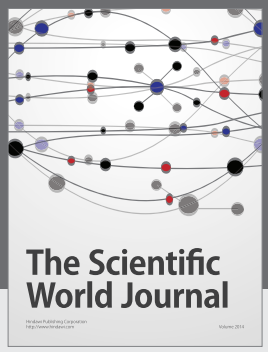

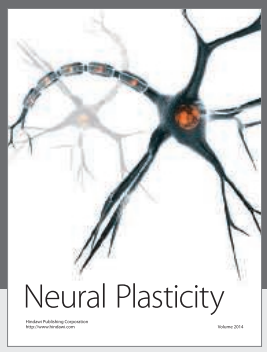

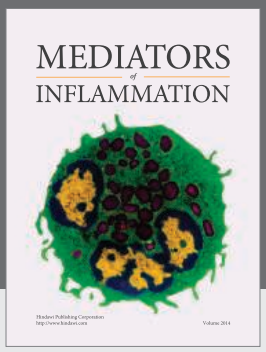

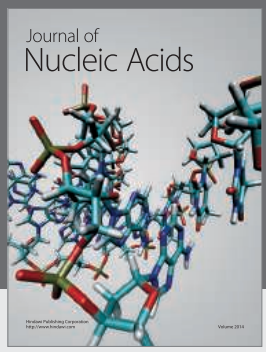

Hindawi

Submit your manuscripts at
http://www.hindawi.com

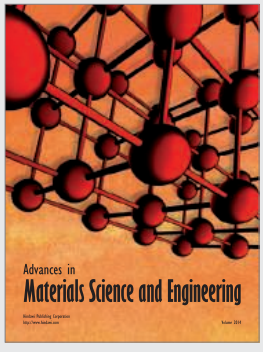

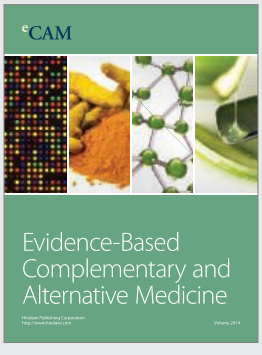

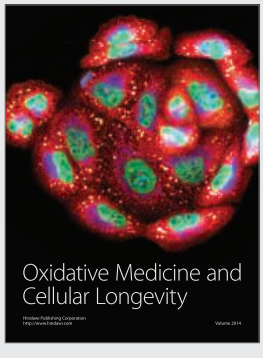

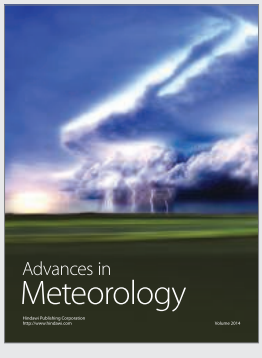

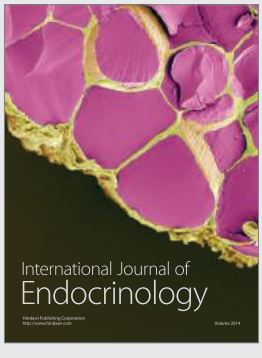

Quick-RNA™ Kits

Purify small, large, or total RNA... You decide!

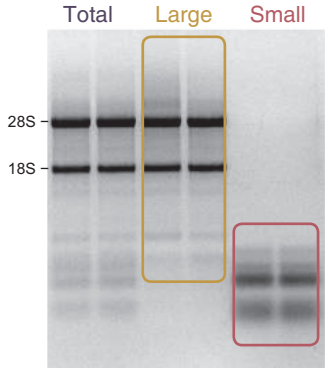

DNA-free RNA
(DNase I included)

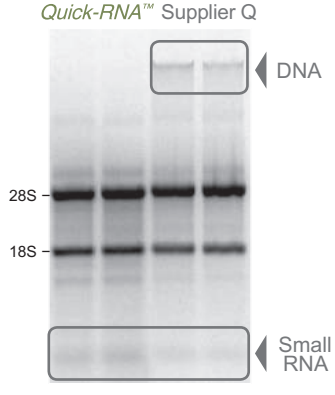

RNA is ideal for RT-PCR, RNA-Seq, arrays, etc.

For Special Offers Visit
www.zymoresearch.com

ZYMO RESEARCH
The Beauty of Science is to Make Things Simple

APERTO
Protein Extraction Buffer for *E.coli*

Solubilizes proteins that the top 3 lysis buffers do not!

Gentle • Rapid • Active Enzymes

Competing Product Aperto

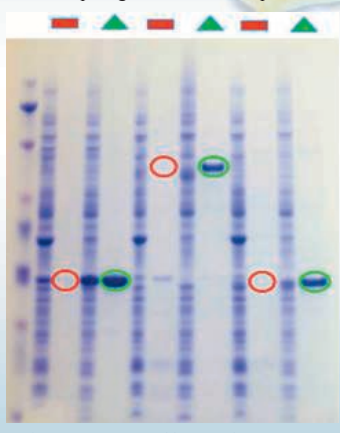

Can you afford for your protien to go undetected?

phone: 1-855-242-0011
www.TEKnova.com

enfold by TEKnova

Science Signaling

Publishing key findings in cell signaling in all areas of biology

Submit your research
ScienceSignaling.org

Science Signaling AAAS

sciencesignalingeditors@aaas.org

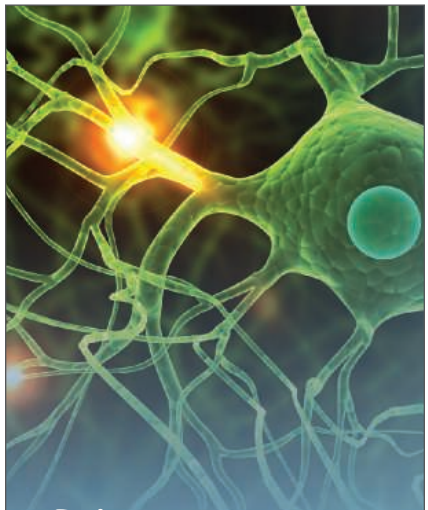

Science Translational Medicine

Integrating Science, Engineering, and Medicine

Publishing results that harness the basic sciences to advance human health in all areas of medicine

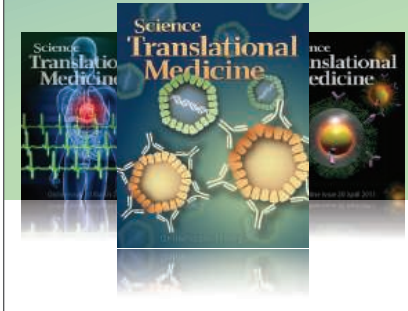

Submit your research
ScienceTranslationalMedicine.org

Recommend to your library
ScienceOnline.org/recommend

Science Translational Medicine AAAS

scitranslmededitors@aaas.org

immunogenomics 2014

September 29 - October 1, 2014

HudsonAlpha Biotechnology Campus
Huntsville, Alabama, USA

Join us at the intersection of Immunology and Genomics!

Keynote Speakers

Christophe Benoist, Harvard Medical School
Mary Ellen Conley, University of Tennessee, College of Medicine, Memphis
Mark Davis, Howard Hughes Medical Institute; Stanford University School of Medicine

Session Chairs

Lou Bridges, University of Alabama at Birmingham, AL, USA • **Jean-Laurent Casanova**, Howard Hughes Medical Institute, Rockefeller • **Alain Fischer**, Imagine Institute, Necker Hospital, Paris, France • **Dan Littman**, New York University, NY, USA • **Sara Marsal**, University of Barcelona, Spain • **Kristen Mueller**, *Science* • **Harlan Robins**, University of Washington/Fred Hutchinson Cancer Research Center

Session Speakers

Scott Boyd, Stanford University School of Medicine, CA • **Zhijian James Chen**, UT Southwestern, TX • **Yanick Crow**, University of Manchester, UK • **Malek Faham**, Sequenta, CA • **Wendy Garrett**, Harvard University School of Public Health, MA • **Peter Gregersen**, Feinstein Institute for Medical Research, NY • **Jian Han**, HudsonAlpha Institute for Biotechnology, AL • **Lionel Ivashkiv**, Hospital for Special Surgery, NY • **Thirumala-Devi Kanneganti**, St. Jude Children's Research Hosp. • **Julian Knight**, Merton College , University of Oxford, UK • **Mike Lenardo**, National Institutes of Health, Washington D.C. • **Xochitl Morgan**, Harvard University School of Public Health, MA • **Barbara Methe**, J. Craig Venter Institute, MD • **Kees Murre**, University of California, San Diego, CA • **Richard M. Myers**, HudsonAlpha Institute for Biotechnology, AL • **Soumya Raychaudhuri**, Broad Institute, MA • **Lars Steinmetz**, European Molecular Biology Laboratory, Germany • **Barbara Stranger**, University of Chicago, IL USA

Platinum Sponsors

BAY CITY CAPITAL

iRepertoire, Inc.

Gold Sponsors

UAB COMPREHENSIVE ARTHRITIS, MUSCULOSKELETAL, AND AUTOIMMUNITY CENTER

Silver Sponsors

GenapSys

illumina®

Bronze Sponsors

SEQUENTA

follow @immunogenomics on twitter

Register today at immunogenomics.com

presented by

HUDSONALPHA INSTITUTE FOR BIOTECHNOLOGY

Science AAAS

Capacitance Manometer

The *a*-Baratron Capacitance Manometer is an advanced high-performance, heated absolute capacitance manometer with better accuracy, higher tolerance to ambient temperature changes, and excellent repeatability. The *a*-Baratron manometer is internally heated to 45°C, 80°C, or 100°C, and has a pushbutton zero that allows service intervals up to four times longer than earlier models. The manometer offers full-scale measurement ranges from 0.1 Torr to 1,000 Torr (13.3 Pa to 133.3 kPa). Its all-digital architecture and advanced new sensor heating system provide long-term performance and reliability. As with previous Baratron manometers, the sensor is made from Inconel and Incoloy nickel alloys for the same superior corrosion resistance. The *a*-Baratron manometer can be equipped with the standard sensor or MKS' patented Etch Baffle sensor technology that greatly reduces process contamination. It can be configured for both new and existing processing systems. It operates on ±15VDC input voltage and has a standard 0–10VDC analog output signal.

MKS Instruments
For info: 978-645-5500
www.mksinst.com

Evaporation Technology

eXalt is an exciting new nondestructive evaporation technology with applications such as first time crystallizations of amorphous forms, recrystallization of samples which have only a few known forms, removing a hydrate, solvent screening studies to find the most suitable conditions to take forward in development, high throughput co-crystallization screens, and studies to confirm stable isoforms. eXalt enables a wide range of solvents and multiple actives to be evaporated all at the same slow rate, and under the same conditions, giving the user unprecedented control of the crystallization process. This is achieved using a special holder which can be configured to slow the evaporation rate of each solvent, i.e., the more volatile solvents are impeded more, and some solvents such as water, need no restriction. The holder is then placed in the controlled conditions of a Genevac HT Series Evaporator which cycles the pressure over the samples to create a draw, achieving controlled, even evaporation.

Genevac
For info: +44-(0)-1473-240000
www.genevac.com/exalt

Automated Tube Capper/DeCapper

The LabElite line of benchtop devices provide laboratories with flexible solutions for sample processing, tracking, and security. For manual workflows that need high-speed 2-D barcode reading of tube racks, the LabElite I.D. Reader is the ideal choice. It decodes tubes in all common 12-, 24-, 48-, 96-, and 384-tube racks including honeycomb-shaped racks. The LabElite DeCapper can decap and recap tubes in 48-cryovial or 96-microtube racks in portrait or landscape formats, one row at a time, to minimize the time tubes are open and eliminate the risk of cross-contamination. Rows can be paused for "point-of-use" manual pipetting. The all-in-one LabElite I.D. Capper combines decapping and recapping and high-speed barcode reading in one small device. The I.D. Capper includes all of the standard features and benefits of the I.D. Reader and DeCapper.

Hamilton Storage Technologies
For info: 508-544-7000
www.hamilton-storage.com

Benchtop Cell Analysis System

The guava easyCyte 12 flow cytometry system provides a simple benchtop method for multicolor flow cytometry. The new platform consumes less sample, generates less waste, and is easier to maintain than traditional systems. The guava easyCyte 12 flow cytometer uses three excitation lasers to provide up to 12 simultaneous detection parameters, including 10 fluorescent colors plus forward and side scatter for size and granularity determination. Single-sample and multisample processing options are offered, and high throughput analysis is possible with robotic sample trays that automatically handle 96-well microplates and up to 10 sample tubes. The new system, capable of detecting mammalian and microbial cells and beads, offers an intuitive interface and is priced to be affordable for every laboratory budget. The new guava easyCyte cytometer offers researchers a simple, flexible option for a variety of applications, including easy identification of subpopulations in a heterogeneous sample and multiplexing cell health parameters to study cell function pathways.

EMD Millipore
For info: 800-645-5476
www.emdmillipore.com/guava

Low-Temperature Control System

The DrySyn SnowStorm system enables low-temperature reactions which have traditionally been difficult to undertake reproducibly on a small to medium scale. The DrySyn SnowStorm offers an attractive solution to laboratories undertaking low-temperature reaction chemistries. Available in a choice of configurations, the DrySyn SnowStorm system provides controlled cooling and heating for sub-ambient parallel chemistry without the need for jacketed reaction vessels or ice baths. Operating with a suitable chiller/circulator, a DrySyn SnowStorm system provides accurate, stable temperature control down to -50°C and up to +150°C. The DrySyn SnowStorm connects to an external chiller unit and holds temperatures at a set-point for as long as is required. Setting temperature ramping profiles is also possible which is important in optimization studies.

Asynt
For info: +44-(0)-1638-781709
www.asynt.com

Electronically submit your new product description or product literature information! Go to www.sciencemag.org/products/newproducts.dtl for more information.

Newly offered instrumentation, apparatus, and laboratory materials of interest to researchers in all disciplines in academic, industrial, and governmental organizations are featured in this space. Emphasis is given to purpose, chief characteristics, and availability of products and materials. Endorsement by *Science* or AAAS of any products or materials mentioned is not implied. Additional information may be obtained from the manufacturer or supplier.

Bat man wins young scientist prize in Stockholm. Are you next?

Science & SciLifeLab PRIZE FOR YOUNG SCIENTISTS

Photo: Nancy Evelyn - UGA

The 2014 *Science* and SciLifeLab Prize is now open and we are looking for new bright ideas. Are you like Daniel Streicker? Are you a recent PhD graduate eager to win a prize? Daniel is a true "bat man" having spent many hours in dark caves studying bats, to better understand how infectious diseases emerge and establish in new host species. It is for this work that Daniel was published in the journal *Science*, December 6, 2013, as the Grand Prize winner of the 2013 *Science* & SciLifeLab Prize for Young Scientists.

The journal *Science* and SciLifeLab have come together to recognize and celebrate excellence in PhD Research. The *Science* & SciLifeLab Prize has been established to support young scientists at the start of their career.

The four categories for the 2014 prize are: Cell and Developmental Biology; Genomics and Proteomics; Environment; and Translational Medicine. The Grand Prize winner will receive 25,000USD and the other three Category Prize winners will receive 3,000USD each. The Grand Prize winning essay will be published in *Science* and the Category Prize winners will be published in *Science* online.

The deadline for submissions is August 1, 2014.
For further details and to enter, please visit: www.sciencemag.org/scilifelabprize

For over 130 years the journal Science has been the world's leading journal of original scientific research, global news and commentary.

SciLifeLab is a collaboration among four universities in Stockholm and Uppsala, Sweden, and is a national center for molecular biosciences with focus on health and environmental research.

This prize is made possible with the kind support of the Knut and Alice Wallenberg Foundation.

Science AAAS

SciLifeLab

Knut och Alice Wallenbergs Stiftelse

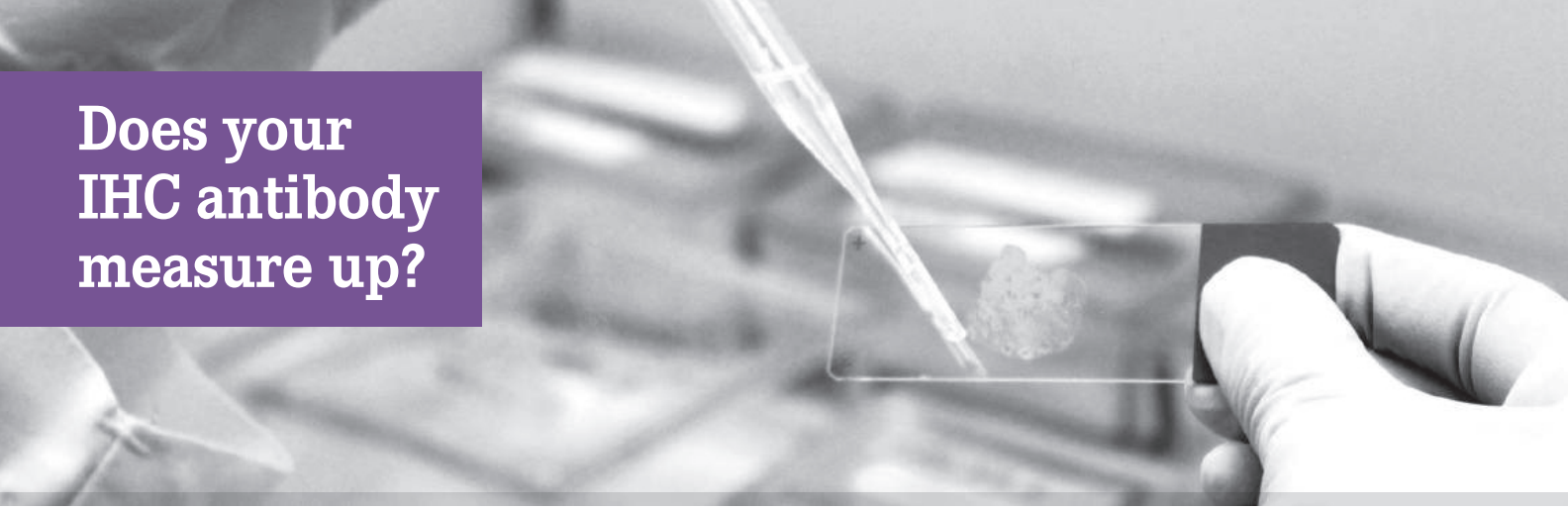

Does your IHC antibody measure up?

Rigorously Validated IHC Antibodies Against High Impact Research Targets

from Cell Signaling Technology

Paraffin-embedded human lung and ovarian carcinoma tissues using CST™ HER3/ErbB3 (D22C5) XP® Rabbit mAb #12708 or Company 2 mouse monoclonal antibody.

CST HER3/ErbB3 (D22C5) XP® Rabbit mAb #12708

Company 2 Mouse Antibody

Lung Carcinoma

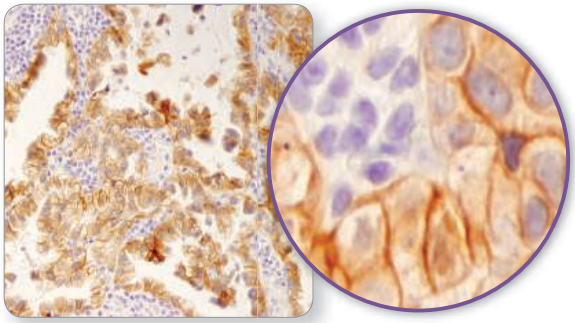

Strong, specific plasma membrane-associated HER3 staining in the epithelium

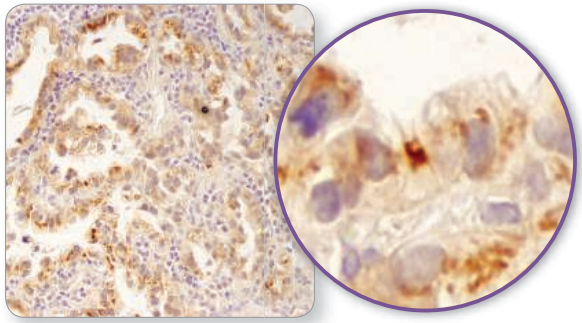

Non-specific, non-membranous staining in the epithelium

Ovarian Carcinoma

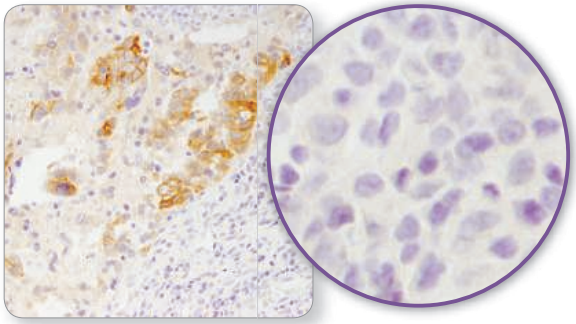

Strong, specific signal in tumor cells, and no staining seen in stromal cells

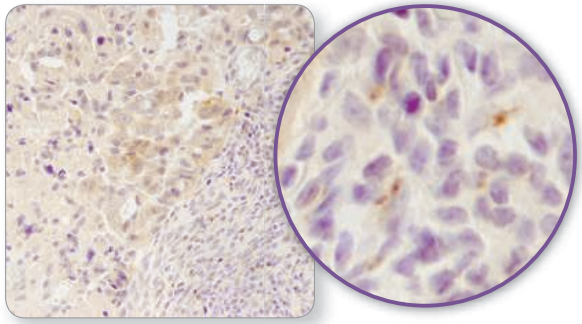

Weak, signal in tumor cells, and non-specific staining in stromal cells

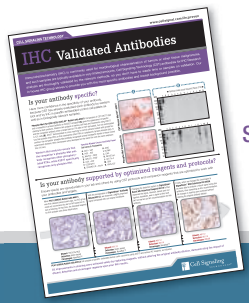

WB IP IHC IF F ChIP

For Research Use Only. Not For Use In Diagnostic Procedures.

Skeptical? Go to **www.cellsignal.com/ihcscience** to see more

© 2014 Cell Signaling Technology, Inc. Cell Signaling Technology®, CST™, and XP® are trademarks of Cell Signaling Technology, Inc.

14PADIHC_NONE0152ENG_00

Cell Signaling TECHNOLOGY®

By **Trisha Gura**

Brewing a career

Protein engineer Jasper Akerboom left his job as a research specialist at the Howard Hughes Medical Institute's (HHMI's) Janelia Farm Research Campus in Virginia to pursue a career as a brewmeister. In this interview (edited for brevity and clarity), Akerboom discusses the Janelia Farm experience, yeast, and what it's like to follow one's microbiological bliss.

Q: What brought you to Janelia Farm?
A: I was doing my Ph.D. in microbiology at Wageningen University in the Netherlands. The focus was on extreme life, organisms living in very hot locations. I was studying the molecular biology and biochemistry of these organisms because their proteins had to be very stable to withstand very high temperatures and salt concentrations. We were collaborating with a postdoc at Stanford, who later moved to HHMI. He asked me if I wanted to postdoc in his lab.

Q: Tell us about Janelia Farm.
A: It's a pretty incredible institution. Principal investigators come in for short-term contracts. They can hire people—but not too many, so the groups are small. After 5 or 6 years, these group leaders are reviewed, and they might not be renewed, so new people come in. There is no teaching. Every year, there is a large amount of funding available, so it is a nice place to be.

Q: How did you get from tracking neurons to brewing beer?
A: I started home brewing in the Netherlands. Lots of us were doing yeast research. When I came to the United States, I began isolating strains from the local area. In 2007, I approached these guys who had just started a local brewery, Lost Rhino Brewing Company, and I said, "I have these local yeast strains. It would be great to collaborate." I gave them a few tasters of my test batches. They were super excited, and so we did this together. It was a great success.

Q: What made you decide to go from brewing as a hobby to brewmeister as a career?
A: Eventually, every postdoc has to decide, "What are you going to do?" Janelia Farm is a very prestigious institution, so people often get very good jobs afterward. But I wanted to do something else. I saw people around me who were all very stressed. It was just very hard for them to get these papers published, as it was for me. I had been scooped many times, competing with people outside and maybe even inside the institution. And I was like, "This is not something I would like to do forever." I thought, "Maybe I can just take my success with yeast and get some experience at this brewery, and then take that experience and maybe move somewhere else in the future."

Eventually, every postdoc has to decide, "What are you going to do?"

Q: Would you say the demands at Janelia Farm are too high?
A: This is of course the top. I would compare it to doing a postdoc at Harvard or Stanford. Some people thrive in that environment. The good side is that Janelia pushes people to the limit. You will enrich a whole group of people who are very smart. But the downside is that it can be a very hard environment.

Q: Do you have any regrets about leaving?
A: At first, I felt like I let myself down. When you deviate from the path, you are breaking with what you were always planning on doing. But if I can say one thing that may be of interest to your readers, it is that they shouldn't feel bad about themselves if they make the decision to step off the path, because it might be the right decision, although it might not feel right at the time.

Q: Any other advice for scientists who want to pursue an alternate career path?
A: Take advantage of the freedom that comes with being a postdoc. Use that period to think about what you want. Everyone congratulates the person who gets the professorship at a big-name university or a huge grant. But that is not for everybody, and there is nothing wrong with that.

Trisha Gura is a freelance writer in Boston. For more on life and career issues, visit http://www.sciencecareers.org.

ILLUSTRATION: ROBERT NEUBECKER

Downloaded from www.sciencemag.org on June 28, 2014

Published by AAAS

Department of Veterans Affairs
Puget Sound Health Care System
American Lake & Seattle

UNIVERSITY of WASHINGTON

Jointly Announce a Career Opportunity in Research and Development

Associate Chief of Staff for Research and Development (ACOS for R&D)

The ACOS for R&D is Chief of the Research Service with responsibility for the administration of the Seattle VA Medical Center's internationally renowned $38 million research program. The ACOS for R&D maintains close ties to the VA academic affiliate, the University of Washington and UW School of Medicine; advises research investigators on administrative, scientific and professional matters; ensures communication; and effectively administers research program funds, R&D staff, and other research resources. In these roles, the ACOS for R&D is responsible for: developing administrative procedures and core facilities to support the research efforts; providing research and administrative guidance to researchers; ensuring the research complies with VA and other Federal regulations, policies and directives; serving as the official liaison with VA Central Office and other agencies on all research matters; and participating in management of the VA-affiliated research nonprofit, Seattle Institute for Biomedical and Clinical Research (SIBCR), by serving as a statutory member of its Board of Directors.

The successful candidate will have the opportunity to recruit a Deputy Director to assist in the administrative functions of this position, and is expected to qualify for a full-time faculty appointment at the University of Washington School of Medicine at the Associate or Full Professor level without tenure due to funding. Competitive candidates must be US citizens, hold the M.D or Ph.D. degree or foreign equivalent, and should have a vibrant, independent research program including a solid record of successful, extramurally-funded research. Experience in the management of medical research is desirable.

Interested applicants should submit a letter of inquiry and curriculum vitae to **Henry Laguatan, Physician Recruiter**, via **FAX (1-478-757-3144)**, using the cover page accessible at **http://staffing.opm.gov/pdf/usascover.pdf**. Mr. Laguatan is also available at **Henry.Laguatan@va.gov** or by phone **(206) 658-4289**. For additional information please contact **Roberto F. Nicosia, M.D. , Ph.D., Chair, ACOS for R&D Search Committee/ Director, Pathology and Laboratory Medicine (S-113-Lab) / 1660 S. Columbian Way, Seattle, WA 98108** (phone: **1-206-764-2284**; email: **Roberto.Nicosia@va.gov**).

The VA Puget Sound Health Care System and UW are Equal Opportunity/Affirmative Action Employers. UW faculty engage in teaching, research, and service.

Immunology
UNIVERSITY OF TORONTO

DEPARTMENT OF IMMUNOLOGY TENURE STREAM POSITION
Assistant Professor - 1401077

The Department of Immunology, University of Toronto invites applications for a tenure-stream appointment. The appointment will be at the rank of Assistant Professor and will begin on July 1, 2015 or shortly thereafter.

As part of a continuing program to build on strength in Immunology, the University of Toronto is recruiting for a tenure track position. Outstanding applicants working in any area of Immunology complementary to our existing faculty (**www.immunology.utoronto.ca**) will be considered.

The successful candidate must have a Ph.D. or equivalent degree, postdoctoral experience, and will be expected to mount an original, competitive and independently funded research program, and to have a commitment to excellence in teaching at the undergraduate, medical and graduate level in Immunology. Salary will be commensurate with qualifications and experience. The position will be located in the Medical Sciences Building on the downtown St. George campus of the University of Toronto. All qualified candidates are invited to apply by visiting us at **www.uoft.me/facultycareers**. Please see Job **#1401077**. Applications should include a cover letter, curriculum vitae, and a statement outlining current and future research. If you have questions about this position, please contact **immunology.search@utoronto.ca**. All application materials should be submitted online. Submission guidelines can be found at: **http://uoft.me/how-to-apply**. We recommend combining attached documents into one or two files in PDF/MS Word format.

Applicants should also ask three referees to send letters directly to the department via e-mail to **immunology.search@utoronto.ca** by the closing date, **August 17, 2014**.

All application materials should be submitted online by closing date, **August 17, 2014**.

For details about the Department of Immunology see **http://www.immunology.utoronto.ca**

The University of Toronto is strongly committed to diversity within its community and especially welcomes applications from visible minority group members, women, Aboriginal persons, persons with disabilities, members of sexual minority groups, and others who may contribute to the further diversification of ideas. All qualified candidates are encouraged to apply; however, Canadians and permanent residents will be given priority.

Science Careers Advertising

For full advertising details, go to ScienceCareers.org and click For Employers, or call one of our representatives.

Tracy Holmes
Worldwide Associate Director
Science Careers
Phone: +44 (0) 1223 326525

THE AMERICAS

E-mail: advertise@sciencecareers.org
Fax: 202-289-6742

Tina Burks
Phone: 202-326-6577

Nancy Toema
Phone: 202-326-6578

Marci Gallun
Sales Administrator
Phone: 202-326-6582

Online Job Posting Questions
Phone: 202-312-6375

EUROPE / INDIA / AUSTRALIA / NEW ZEALAND / REST OF WORLD

E-mail: ads@science-int.co.uk
Fax: +44 (0) 1223 326532

Axel Gesatzki
Phone: +44 (0)1223 326529

Sarah Lelarge
Phone: +44 (0) 1223 326527

Kelly Grace
Phone: +44 (0) 1223 326528

JAPAN

Yuri Kobayashi
Phone: +81-(0)90-9110-1719
E-mail: ykobayas@aaas.org

CHINA / KOREA / SINGAPORE / TAIWAN / THAILAND

Ruolei Wu
Phone: +86-186-0082-9345
E-mail: rwu@aaas.org

All ads submitted for publication must comply with applicable U.S. and non-U.S. laws. *Science* reserves the right to refuse any advertisement at its sole discretion for any reason, including without limitation for offensive language or inappropriate content, and all advertising is subject to publisher approval. *Science* encourages our readers to alert us to any ads that they feel may be discriminatory or offensive.

Science Careers
From the journal *Science* AAAS

ScienceCareers.org

University of Zurich[UZH]

Faculty of Science

The Faculty of Science of the University of Zurich invites applications for a

Professorship in Developmental Biology

at the Institute of Molecular Life Sciences.

The Institute of Molecular Life Sciences conducts cutting-edge basic research in the areas of Molecular, Cellular and Developmental Biology. We seek an innovative scientist with an outstanding track record in research and teaching, as well as the leadership skills and enthusiasm to build on the strength of the Institute in the field of Molecular Developmental Biology. The successful candidate will establish a strong, independent research group and contribute to graduate and undergraduate education (in English or German) in Molecular and Developmental Biology.

The position will be filled preferentially at the level of Associate or Full Professor. The position may be occupied with a part-time or shared professorship. The University of Zurich is an equal opportunity employer.

The University of Zurich provides generous research support, including earmarked funds for personnel and running expenses, and competitive start-up packages. Zurich offers a stimulating scientific environment and extensive opportunities for collaborations within the University and with the ETH Zurich. Switzerland provides excellent opportunities for external funding of research.

Candidates are invited to submit an application package including curriculum vitae, list of publications and personal conference contributions, outline of current and future research interests, teaching philosophy and names and addresses of three potential referees. Documents should be addressed to Prof. Dr. Bernhard Schmid, Dean of the Faculty of Science, University of Zurich, and uploaded as a single PDF file at www.mnf.uzh.ch/mdb by 15 August 2014. For further information, please contact Prof. Dr. Alex Hajnal via alex.hajnal@imls.uzh.ch.

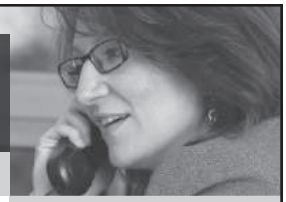

HEAD OF USER SUPPORT AND CLIMATE SERVICES DIVISION

DARMSTADT, GERMANY

Taking responsibility for our User Support and Climate Services Division, you will manage teams responsible for the delivery of all support services to users (including user registration, notification and information services, cataloguing/browsing, data ordering and access, help desk services, training and feedback mechanisms), the production of Climate Data Records and the operations of all dedicated infrastructure and system. You champion a responsive approach to meeting user needs. Your goal will be to facilitate the widest possible use of EUMETSAT real time and off line data services for a growing spectrum of applications.

To this end, you will support the implementation of upgrades for user interfaces and operational validation, co-ordinate the standardisation of data access, and partner colleagues across the organisation in releasing new products and services. At the same time, you will plan training activities for our users across Europe, Africa and other areas, giving you high visibility with our stakeholders.

Qualified to degree level in a relevant discipline, you will possess extensive experience of supporting scientific data users in an operational environment. Equally important, you will bring knowledge of meteorological and/or climate services, exposure to appropriate satellite data and awareness of the needs of our product and service users. Finally, you will be skilled in capacity building and training, capable of operating effectively in an international environment, and fluent in English with a working knowledge of French.

Attractive employment conditions are offered, in terms of salary, comprehensive benefits including health and social welfare provision, and extensive relocation assistance if applicable.

EUMETSAT is the European satellite agency for monitoring weather and climate. Bringing together the resources of 30 Member States, we develop and operate a range of satellite systems surveying the atmosphere, land and ocean that deliver vital data 24 hours a day, 365 days a year. Our data contribute to weather forecasts that protect lives and property across Europe and to monitoring of our changing climate. EUMETSAT is now embarking on new and challenging satellite development programmes, shaping its long-term future.

EUMETSAT is committed to providing an equal opportunities work environment for men and women and is seeking to recruit nationals from its Member States. Please see our website for further details.

Closing date:
22 July 2014 (Ref: VN 14/31)

To learn more and apply online, please visit:
www.eumetsat.int

EUMETSAT

Faculty Positions in Translational Tumor Immunology

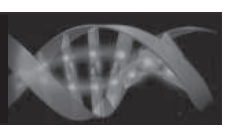

The Wistar Institute is seeking outstanding candidates at all ranks for faculty positions in the newly created program in Translational Tumor Immunology, where they will be expected to develop or expand their extramurally-funded research programs in different areas of tumor immunology and tumor microenvironment.

Specific areas of interest include and are not limited to: molecular and cellular mechanisms regulating immune responses in cancer; novel approaches to therapeutic manipulation of the immune system in cancer; the role of metabolic changes in the function of the immune system in cancer; the impact of conventional and targeted cancer therapeutics on the immune system; interaction between cells of the immune system and epithelium/endothelium/stroma. Interest in translational research is desirable.

The Wistar Institute, an NCI-designated Cancer Center and independent research institute in Philadelphia, offers highly competitive start-up support packages including salary and fringe benefits, a superb and interactive research environment in a newly constructed state-of-the-art research tower and animal facility, and outstanding core facilities in proteomics, genomics, microscopy, high-throughput molecular screening, bioinformatics, and flow cytometry. Investigators have access to a wide range of clinical materials through a partnership with the Helen F. Graham Cancer Center, Newark, DE. The Institute's location, near the University of Pennsylvania campus, provides opportunities for academic and clinical collaborations. Graduate students at Philadelphia academic institutions frequently receive training at The Wistar Institute.

Applications will be reviewed as received and will be accepted until the positions are filled. To ensure timely consideration, applications should be submitted before **September 1, 2014**. The application should include: a curriculum vitae, a brief summary of past and future research interests, a history of research funding support (if applicable), and the names of three referees (submitted as a single PDF). Applications should be sent by e-mail to: Dmitry Gabrilovich, Search Committee Chair, **c/o Maria Colelli (colelli@wistar.org)**, The Wistar Institute, 3601 Spruce Street, Philadelphia, PA 19104.

THE WISTAR INSTITUTE

An NCI-designated Cancer Center

For more information about us, visit our web site at

www.wistar.org

Bloomsbury Research Institute

UCL

LONDON SCHOOL of HYGIENE &TROPICAL MEDICINE

Director, Bloomsbury Research Institute

Professorial scale: competitive salary

The London School of Hygiene & Tropical Medicine and University College London have entered into an exciting partnership to create a centre of excellence in infectious disease research, the Bloomsbury Research Institute, and we are now seeking to appoint a Director to lead and develop the Institute as an international beacon of outstanding scientific research in this pivotal London-based role.

The Bloomsbury Research Institute will be a dedicated research facility that will host some of the world's leading infectious disease researchers, and form a critical part of the largest biosciences hub in Europe. The Institute will undertake knowledge exchange and accelerate translational research, working with the National Health Service partners, the healthcare industry, and the global collaborative network of the School and UCL. The Institute will be ideally placed to move new treatments and solutions for prevention and control of infectious diseases from the laboratory to real world applications, from bench to bedside and populations.

Educated to PhD level, and with previous experience of running a substantial research department or institute, the successful post-holder will be responsible for developing, implementing and delivering the strategic plan for the Institute, in collaboration with the partners and other stakeholders; guiding the development of the institute through design and construction through to operational management and leadership.

We invite applications from research with an international track record of leadership and innovation in infectious diseases with the ambition and vision to help us to create this world leading institute.

Full particulars and application forms are on our website http://jobs.lshtm.ac.uk. For more information and to express interest, potential candidates are encouraged to contact Professor Peter Piot, Director, London School of Hygiene & Tropical Medicine via director@lshtm.ac.uk or tel: +44 (0) 20 7927 2278.

Closing date for applications: 10 pm, Thursday 7 August 2014

The London School of Hygiene & Tropical Medicine is an equal opportunities employer

Athena SWAN Bronze Award

Stonewall DIVERSITY CHAMPION

Improving health worldwide

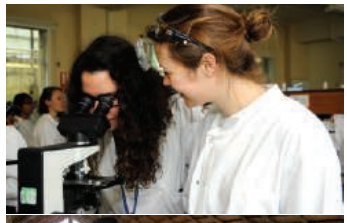

www.lshtm.ac.uk

Universität Konstanz

The University of Konstanz with its »Institutional Strategy to promote Top-Level Research« has been receiving continuous funding since 2007 within the framework of the Excellence Initiative by the German Federal and State Governments.

The Faculty of Sciences, Department of Chemistry, announces an opening for a

W1-Professorship of Inorganic Chemistry

to be filled as soon as possible. The initial appointment as a junior professor is for three years and can be extended to six years after positive evaluation. There is no option for tenure track.

The new professorship is intended to enrich and to enforce the present research activities of the Department with a modern, preparative chemistry. Willingness to contribute to existing cooperative research programs of the department is highly welcome. Teaching activity of 4 hours/week during the semester term is expected.

Prerequisites for a successful application are recommendations which mirror the ability to conduct high quality research of the applicant. In addition, an academic degree, a doctoral degree received within the past five years, experiences as post-doc as well as publications in international scientific journals are required. Experiences as independent project leader and in the acquisition of extramural funding are welcome.

Further information can be obtained by contacting Prof. Rainer Winter, e-mail: rainer.winter@uni-konstanz.de. Please send your digital application comprising a cover letter, curriculum vitae, publication list, a list of grants and awards, copies of academic degrees as well as statements of current research topics, future research directions and a statement of how the intended research connects with the department´s **until 25 July 2014 under the reference number 2014/115** formatted into *one pdf-file* to: Prof-2014-115@uni-konstanz.de. If you have questions about the procedure please contact Hanns Fahlbusch Tel. +49(0) 7531/88-2413.

Argonne NATIONAL LABORATORY

DIRECTOR

Nanoscience and Technology Division

Argonne National Laboratory invites applications for the position of Director of the Nanoscience and Technology Division (NST) to lead the division's multidisciplinary science and user research programs. NST's mission includes the development of advanced concepts and instrumentation that will lead to breakthroughs in fabricating and exploring novel nanoscale materials and tailoring and discoveries of nanoscale phenomena. NST includes the Center for Nanoscale Materials (CNM) and the Electron Microscopy Center (EMC). The CNM is a Department of Energy (DOE) national user facility that provides the expertise and capabilities for the synthesis, fabrication, characterization, and theory of materials at the nanoscale. The CNM also operates a nanoprobe beamline at the Advanced Photon Source for characterization of nanomaterials with hard X-rays. The CNM is one of five U.S. Nanoscale Science Research Centers and host to over 400 external users per year. NST also manages the EMC, a DOE national user facility that offers unique capabilities for electron beam characterization of energy materials and processes.

The Division Director will be expected to work with NST scientific and management staff to: (1) enhance the strengths and visibility of existing multidisciplinary staff and user research programs, and identify new research directions that are strategically aligned with DOE's missions; (2) enable a world-class user program with an engaged, satisfied and diverse user community; (3) recruit, hire, and retain world-class researchers; (4) promote interactions with other programmatic directorates and user facilities; (5) interface with facility and programmatic sponsors at DOE; and (6) foster and maintain high standards in Environmental, Safety, and Health and quality assurance for all of the Division's activities.

The successful candidate should have a Ph.D., an internationally recognized research stature, 10+ years of scientific leadership in the physical sciences with experience in nanoscience, and a proven track record of managing multidisciplinary research programs. For a description of Divisional programs, please visit NST's Home Page at **http://www.nano.anl.gov**.

Argonne offers an excellent compensation and benefits package. For full consideration, please apply by **July 31, 2014** at **www.anl.gov/careers** to **Requisition 322255**. Interested candidates should include a curriculum vitae, list of publications, awards, patents, etc., and salary history. In addition please include 4 names that can provide a professional reference.

Argonne National Laboratory is a multi-program laboratory managed by UChicago Argonne, LLC for the U.S. Department of Energy's Office of Science. We are an equal opportunity employer and value diversity in our workforce. Argonne's site is located about 25 miles southwest of Chicago on a beautiful 1500 acre campus. For additional information, please refer to Argonne's Home Page at **http://www.anl.gov**.

UNIVERSITY of HOUSTON

DEAN
COLLEGE OF NATURAL SCIENCES AND MATHEMATICS

The University of Houston (UH) requests nominations and applications for the Dean, College of Natural Sciences and Mathematics (NSM).

Founded in 1927, the University of Houston is the leading urban public research university in Texas. UH is a 'Tier-One' research university that enrolls over 40,000 students. UH is the flagship of The University of Houston System which serves more than 65,000 students enrolled in four universities, two branch campuses and four regional teaching centers.

The College of Natural Sciences and Mathematics (NSM) is one of twelve colleges in the University and is comprised of six departments: Biology and Biochemistry; Chemistry; Computer Science; Earth & Atmospheric Sciences; Mathematics; and Physics. NSM has a number of centers and institutes to foster interdisciplinary research across the university. The College enrolls approximately 5,300 Science majors (about 4,300 undergraduates and 1,050 graduate students) and has annual research expenditures of $31 million. For more information about the College, please visit **http://nsm.uh.edu/**.

The Dean is the chief academic and administrative officer of the College and is responsible for the energetic, visionary, and effective leadership of NSM. The successful candidate will be an engaging and charismatic leader among the faculty, a strong advocate for the teaching and research mission of the College, a preeminent university citizen, and an energetic and conscientious administrator committed to collegiality and inclusivity. Most of all, the candidate will provide leadership in addressing the evolving challenges that face students and faculty alike in higher education, science, mathematics, and other related fields. The next Dean will be an energetic and visionary leader who will make a real difference in the future of the College and play a lead role in supporting and strengthening UH's position as a 'Tier One' research university.

The Search Committee will continue to accept applications and nominations until the position is filled. Applicants must submit a current curriculum vitae and a letter describing relevant experience and interest in the position. Submission of materials via e-mail is strongly encouraged. Nomination letters should include the name, position, address and telephone number of the nominee. All applications and nominations will be handled in confidence.

storbeck / pimentel
executive search consultants

Applications and letters of nomination should be submitted to:
Alberto Pimentel
Managing Partner
Storbeck/Pimentel & Associates
1111 Corporate Center Drive, Suite 106
Monterey Park, CA 91754
323-260-7889 (FAX)
Email: apsearch@storbeckpimentel.com
Refer to code "UH-NSM" in subject line

~The University of Houston is an affirmative action/equal employment opportunity employer~

AAAS is here – helping scientists achieve career success.

Every month, over 400,000 students and scientists visit ScienceCareers.org in search of the information, advice, and opportunities they need to take the next step in their careers.

A complete career resource, free to the public, *Science* Careers offers a suite of tools and services developed specifically for scientists. With hundreds of career development articles, webinars and downloadable booklets filled with practical advice, a community forum providing answers to career questions, and thousands of job listings in academia, government, and industry, *Science* Careers has helped countless individuals prepare themselves for successful careers.

As a AAAS member, your dues help AAAS make this service freely available to the scientific community. If you're not a member, join us. Together we can make a difference.

To learn more, visit
aaas.org/plusyou/sciencecareers

AAAS + U = Δ

Weill Cornell Medical College

Postdoctoral Associate Positions
Molecular Imaging Innovations Institute
Department of Radiology

The Molecular Imaging Innovations Institute (MI^3) in the Department of Radiology at Weill Cornell Medical College is seeking highly motivated applicants to join our newly established institute. MI^3 is located in the brand new state-of-the-art Belfer Research Building, on the upper east side of Manhattan in New York City. MI^3 is committed to becoming an internationally recognized institute of excellence in discovery and development of new molecular imaging technologies for use in basic and translational research as well as in clinical care.

MI^3 seeks both biologists and chemists who are creative, motivated, and enjoy working independently as well as in a collaborative environment. Research experience in, cellular microscopy, animal tumor models, nanoparticle and small molecule chemical synthesis, photodynamic therapy, or drug delivery, are preferred. Applicants must have a doctoral degree, possess excellent communication and writing skills, and be fluent in English.

To apply, please email a cover letter, research interests, CV, and names of three references to the Director of MI^3, **Dr. Ching Tung** at **mi3@med.cornell.edu**.

Weill Cornell Medical College is an employer and educator recognized for valuing AA/EOE/M/F/Protected Veterans, and Individuals with Disabilities.

| le savoir vivant |

UNIL | Université de Lausanne
Faculty of Biology and Medicine

UNIL | Université de Lausanne
HEC Lausanne

THE FACULTY OF BIOLOGY AND MEDICINE (FBM) AND THE FACULTY OF BUSINESS AND ECONOMICS (HEC) OF THE UNIVERSITY OF LAUSANNE, SWITZERLAND INVITE APPLICATIONS FOR THE FOLLOWING POSITION:

FULL PROFESSOR DIRECTOR OF THE PROGRAMME IN BEHAVIOR, ECONOMICS, AND EVOLUTION

The Department of Ecology and Evolution of FBM and the Departments of Economics, Organizational Behavior, and Information Systems of HEC have developed a new interdisciplinary Master of Science major in Behavior, Economics, and Evolution. This major can be taken by students enrolled in the Master of Science programmes in Economics or in Management (in HEC), as well as students in the Master in Behavior, Evolution and Conservation (in FBM). The programme intends to develop teaching and research connections between evolutionary biology and behavioral economics.

We therefore seek an outstanding researcher as full professor and director of the programme with a track record in Sociobiology, Social Evolution, Human Behavioral Ecology, Evolutionary Psychology, Biological Psychology, Neuroeconomics, Evolutionary Economics, or Behavioral Economics (or related areas). The position requires a record of scientific excellence, administrative experience, the motivation to lead a MSc programme, as well as a scientific interest in both evolution and economics.

The Professor is expected to lead the programme and an internationally competitive research programme on proximate and/or ultimate questions pertaining to social decision-making and behavior. She/he is expected to attract external funding and to promote an interactive and synergistic research environment between the Faculty of Business and Economics, and the Faculty of Biology and Medicine.

A start-up package, a state-of-the-art research infrastructure as well as a yearly research allowance for positions and consumables will be available within an environment that has a long track record of excellence in research (http://www.unil.ch/dee; http://www.hec.unil.ch/ob; http://www.hec.unil.ch/deep; www.hec.unil.ch/isi).

The job description is available on the Internet site http://www.unil.ch/emplois or http://www.unil.ch/fbm/page64812.html.

Further information may be obtained from Prof. Andreas Mayer (Andreas.Mayer@unil.ch), Chairman of the search committee.

The application, in English, must include a full CV (indicating previous positions, teaching experience, list of grants received, publication record), a motivation letter, future research interests, and representative publications, as well as names and contact information of three referees. Applications are received electronically at this address: www.unil.ch/iafbm/application. They should be submitted by August 27th, 2014.

Seeking to promote an equitable representation of women and men among its staff, the University encourages applications from women.

MEET THE "BRIGHTEST MINDS ON THE PLANET" BBC

and celebrate the 25th anniversary of the Fall of the Berlin Wall.

FALLING WALLS is a unique international platform for leaders from the worlds of science, business, politics, the arts and society.

THE FALLING WALLS CONFERENCE (9 November, 9 am - 7 pm) is at the heart of the Falling Walls days in Berlin. 20 world-class scientists from top institutions around the globe present in only 15 minutes each the breakthroughs they are working on.

FALLING WALLS VENTURE (8 November, 11 am - 6 pm) is an international forum for outstanding science based start-up companies, venture capital companies and strategic investors. It is supported by the European Private Equity and Venture Capital Association (EVCA).

Falling Walls attracts an audience from more than 80 nations and is covered by media globally.

More information and registration: **www.falling-walls.com**

REGISTER NOW!

REGISTER BEFORE 31 AUGUST 2014
to take advantage of the Early Bird Ticket
www.falling-walls.com/registration

SPONSORED BY THE Federal Ministry of Education and Research · HELMHOLTZ ASSOCIATION · acatech · Alexander von Humboldt Stiftung/Foundation · ATKearney · Senate Department for Economics, Technology and Research · be Berlin · Robert Bosch Stiftung · DAAD · DFG · European Research Council · erc · EVCA · Fraunhofer · Leibniz · Leopoldina · Science AAAS · Stifterverband für die Deutsche Wissenschaft · STS · FALLING WALLS

For your career in science, there's only one **Science**

A career plan customized *for* you, *by* you.

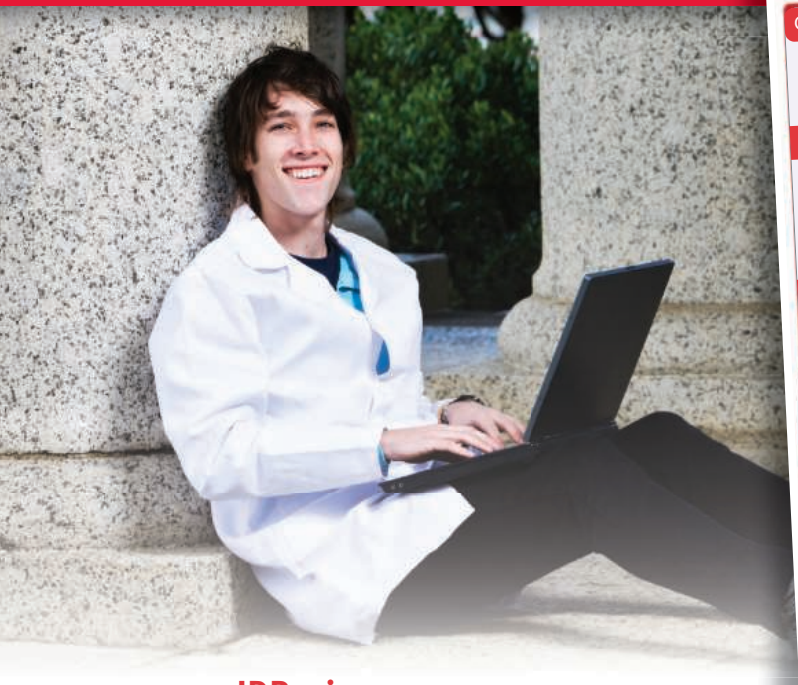

myIDP.sciencecareers.org

Recommended by leading professional societies and endorsed by the National Institutes of Health, an individual development plan will help you prepare for a successful and satisfying scientific career.

my IDP Science Careers

In collaboration with FASEB, UCSF, and the Medical College of Wisconsin and with support from the Burroughs Wellcome Fund, AAAS and *Science* Careers present the first and only online app that helps scientists prepare their very own individual development plan.

Visit the website and start planning today!
myIDP.sciencecareers.org

In partnership with:

advancing the life sciences 1912-2012 FASEB Federation of American Societies for Experimental Biology

UCSF University of California San Francisco

Medical College of Wisconsin

Burroughs Wellcome Fund

湖南大学
HUNAN UNIVERSITY

Hunan University Hunting for Talents from home and abroad

Hunan University （http://www.hnu.edu.cn）is located in Changsha, a historically and culturally renowned city in China. Situated at the foot of the picturesque Yuelu hill and on the west bank of the rippling Xiang River, it has a beautiful campus. It is a key comprehensive university affiliated with the Ministry of Education, China and included in China's "211 Project" and "985 Project" for priority investment and construction. The university, dating back to Yuelu Academy founded in 976 A.D, experienced the time changes of the Song, Yuan, Ming and Qing Dynasties for more than one thousand years and has committed itself to fostering talent people for the society.

The university now has 23 colleges, covering 11 disciplines as Philosophy, Economics, Law, Education, Literature, History, Nature Science, Engineering, Management, Medicine, and Art. It also has 25 first-level discipline doctorate degree awarding stations, 41 first-level disciplinemaster's degree awarding stations, and 20 professional degree awarding stations. 14 programs were recognized as national key discipline (second-level), come with 21 post-doctoral research stations. The university has more than 4,000 staff members, 1900 of them are full-time faculties, and 1200 are professors and associate professors. There are approximately 20,700 undergraduates and 14,000 postgraduates study and research in the campus as well.

Alldisciplines mentioned above were needed for this recruitment with negotiable salary, particularly Mathematics, Physics, Biology, Environmental Science, Material Science and Chemistry. Please feel free to contact us if there is any question.

For more information, please check the link :http://rsc.hnu.cn/

Contact us:
Wang Qian
TEL: +86-731-8882-2723
E-mail:szgl@hnu.edu.cn
Address: No.2 Lushan South Street,Yuelu District, Changsha City, Hunan Province, China
Human Resource Department of Hunan University
Zip Code: 410082

南京理工大学
NANJING UNIVERSITY OF SCIENCE & TECHNOLOGY

Recruitments of talents abroad by Nanjing University of Science and Technology

http://rczp.njust.edu.cn/urp-portal/portal/group/Recruit

Nanjing University of Science and Technology (NUST) is one of the first national "211 Project" universities affiliated with the Ministry of Industry and Information Technology. It has become a multi-disciplinary and coordinated developing engineering-based university along with science, liberal arts, economics, management, law, education, etc. It is an ideal place for research work for its strong scientific research ability, prominent advantages, perfect construction of infrastructural facilities and it's also a pleasant place to live in since the beautiful scenery of Dr. Sun Yat-sen's Mausoleum which is only less than one mile away.

Please refer to the following application guidelines and we welcome your applications.

Majors for recruitment:

Related disciplines of Ordnance Science and Technology, Mechanical Engineering, Instrumentation Science and Technology, Chemical Engineering and Technology, Chemical, Electronic Science and Technology, Information and Communication Engineering, Optics, Optical Engineering, Computer Science and Technology, Control Science and Technology, Electrical Engineering, Transportation Engineering, Aerospace Science and Technology, Power Engineering and Thermal Physics, New Energy, Mechanics, Mathematics, Physics, Civil Engineering, Materials Science and Engineering, Environmental Science and Engineering, Biomedical Engineering, Law, Intellectual Property, Public Administration, Sociology, Economics, Management Science, (Applied) Linguistics and Literature, Art and Design.

Position and requirements:

Recruiting position: "Zijin scholars" distinguished professor, "Young Talents Professors", Professor, Associate Professor, Assistant Professor.

Basic qualities: Overseas talents with a doctorate degree, passion for education, high academic achievement and strong research capability and, good professionalism, academic character and team spirit as well. Among them, the candidates for "Young Talent Professor" staff position should be under 35 years old.

Related treatment:

The full-time employed teachers will be directly categorized into national institution, enjoying free medical care, pensions and other state welfare, and the family issues such as children's nursery and schooling will be addressed. We provide the high-level personnel and young talents with transitional housing, financial relief, research funding and other supports with generous salaries, comfortable working and living conditions. For high-level talents, we help settle down in terms of team building, work, housing, etc. Specific treatment will be determined by personal discussion.

1. For the full-time "Thousands of Plans" and other leading talents, NUST will provide 600 thousand to 1 million RMB annual salary and no less than 8 million RMB research start-up funds.
2. For the "Thousands Youth Talents" and other related talents, we provide no less than 300 thousand RMB annual salary, 1 million RMB financial relief and 2-4 million RMB research start-up funds.
3. For the "Zijin scholars" distinguished professor, we provide 500 thousand to 2 million RMB financial relief, 1 to 5 million RMB research funds and stipulated wages and other benefits along with certain amount of professor allowances per year.
4. For the "Young Talented Professors", we provide 300 thousand RMB annual salary, with certain financial relief and start-up funds.
5. For the professor, associate professor, assistant professor, we will provide salary and financial relief which is competitive in the same region, as well as starter home, and provide appropriate amount of research funds.

Way for recruitment:

The recruitments of talents abroad by NUST is under way regularly, please log in NUST Recruitment Network http://rczp.njust.edu.cn/urp-portal/portal/group/Recruit to have a registration, or contact us directly.

Contact us:
JI Wenchao Meng Yang
Tel: 86-25-84316943
Mail: rcb@njust.edu.cn
NUST website: www.njust.edu.cn